

Czech Technical University in Prague
Faculty of Biomedical Engineering

Doctoral Thesis

September 2019

Ing. Jan Dudák

Czech Technical University in Prague
Faculty of Biomedical Engineering
Department of Natural Sciences

***ENERGY SENSITIVE X-RAY RADIOGRAPHY
AND TOMOGRAPHY OPTIMIZED FOR
SMALL ANIMAL IMAGING***

Doctoral Thesis

Ing. Jan Dudák

Kladno, September 2019

Ph.D. Programme: Biomedical and Clinical Technology
Branch of Study: Biomedical and Clinical Technology

Supervisor: Ing. Stanislav Pispíšil, DrSc.

Supervisor-Specialist: Ing. Jan Jakůbek, Ph.D.

Statement of authorship

I declare, that I conducted the research described in the submitted doctoral thesis entitled “*Energy sensitive X-ray radiography and tomography optimized for small animal imaging*” myself. All used sources of information are acknowledged in the attached list of references. I do not have a compelling reason against the use of the thesis within the meaning of Section 60 of the Act No.121 / 2000 Coll., on copyright, rights related to copyright and amending some laws (Copyright Act).

Prohlašuji, že jsem svou dizertační práci „*Optimalizace energeticky citlivé rentgenové radiografie a tomografie pro zobrazování malých zvířat*“ vypracoval samostatně a použil jsem úplný výčet pramenů uvedený v přiloženém seznamu. Nemám závažný důvod proti užití tohoto školního díla ve smyslu § 60 Zákona 4. 121/2000 Sb., o právu autorském, o právech souvisejících s právem autorským a o změně některých zákonů (autorský zákon).

Kladno, September 2019

Jan Dudák

Acknowledgements

I would like to express my gratitude to the people who helped me while I was working on this doctoral thesis. First of all, I would like to thank my supervisor Dr. Stanislav Pospíšil and supervisor-specialist Dr. Jan Jakůbek for providing me the opportunity to take a part in research of hybrid-pixel photon-counting detectors Timepix and for their support, valuable advices and professional guidance. Further, I would like to thank to the Medipix Collaboration that, as an inventor of Medipix technology, enabled the research carried out within this thesis.

I would like to thank to my colleagues Dr. Jan Žemlička, Dr. František Krejčí and Jakub Karch from the Institute of Experimental and Applied Physics who were constantly ready to help me with experimental setup and who spent a reasonable amount of time discussing the topic of my research work with me. Special thanks belong to Dr. Jan Žemlička for his sharp and honest criticism which I hated but which eventually significantly improved both the experimental results and the manuscript of the thesis.

I would like to thank all colleagues from partner facilities who cooperated with me on experimental measurements. Namely I would like to express my gratitude to Dr. Jana Mrzílková, Dr. Katarína Holcová and Dr. Jana Bulantová for providing the biological samples presented in this thesis and who interpreted the obtained results. I would like to thank to Daniela Ekendahl, Dr. Libor Judas and Dr. Peter Rubovič for analysis of the dose rate of the small animal scanner. Further, I would like to thank Dr. Zuzana Heřmanová and Dr. Jiří Kvaček who provided me an access to micro-CT laboratory of National Museum in Prague and allowed me performing a set of reference measurements using a local micro-CT scanner.

I would like to thank for financial support from the Institute of Experimental and Applied Physics originating from grant projects of Czech Science Foundation and Technology Agency of Czech Republic. Also for support from Ministry of Education, Youth and Sports of the Czech Republic and for grant support provided by European Union.

Finally, I would like to thank to my beloved wife Anička for her support, tolerance and understanding during this long-way run.

Abstract

X-ray micro-CT (micro computed tomography), a non-destructive imaging modality providing 3D information on inner structures of an investigated object, has recently become a valuable tool that is widely used in scientific research. The current state-of-the-art laboratory micro-CT systems routinely provide spatial resolution of several micrometers; however, even sub-micron resolution can be nowadays achieved. Small animal X-ray imaging has enabled new approaches of research in biology and pre-clinical field.

Despite the high level of state-of-the-art technologies, several known technology limitations are permanently subjects of continuous development. The conventional X-ray detection technologies suffer from the presence of so called-dark current that reduces the contrast-to-noise ratio of the data and consequently degrades the detectability of fine structures within the data. Furthermore, micro-CT or computed tomography in general, is not capable of quantitative measurements.

This thesis addresses both mentioned drawbacks by utilizing a novel technology of photon-counting detectors for micro-CT imaging. The key advantages of photon-counting technology concerning X-ray imaging are based on dark-current-free operation and energy-resolving capabilities. Dark-current-free photon-counting provides an enhanced contrast of the obtained data, while the energy-resolving capability enables quantitative CT measurements by means of energy-sensitive or so-called spectral radiography and CT.

The thesis focuses on the development of methods, data processing algorithms and associated equipment for high-resolution and energy sensitive X-ray micro-CT of biological samples using photon-counting detectors Timepix. The thesis characterizes the technology of photon-counting detectors and compares it with conventional X-ray imaging cameras. Furthermore, it introduces techniques for data acquisition, processing and hardware accessories developed within the thesis. The key results are based on the applied use of Timepix detectors for micro-CT imaging of diverse biological samples ranging from whole small animals to single-cell organisms. CT measurements with voxel size smaller than 600 nm have been carried out. Important results have been achieved especially in the case of micro-CT of *ex vivo* soft biology tissue.

The thesis further presents unique results of spectral micro-CT measurements of a phantom object. Experimental results have proven the capability of simultaneous identification and quantification of multiple materials within the scanned object, by using self-implemented four-channel basis material decomposition. Such results achieved using large-area Timepix detectors have not been published so far. The ability of quantitative estimation of content of a target element can potentially open new application areas of CT imaging towards molecular imaging or simultaneous imaging of multiple contrast agents in a single scan.

Abstract (in Czech)

Rentgenová mikrotomografie (mikro-CT) je nedestruktivní zobrazovací metoda umožňující získání informací o vnitřních strukturách zkoumaného objektu ve formě virtuálního 3D modelu. Tato moderní zobrazovací metoda je neustále dostupnější a stává se široce využívaným nástrojem vědeckého výzkumu. Současná zařízení poskytují rutinně prostorové rozlišení v řádu mikrometrů, nicméně lze již dosáhnout i rozlišení v řádu stovek nanometrů. Využití mikro-CT pro zobrazování malých zvířat přinesla řadu nových možností v biologickém a preklinickém výzkumu.

Navzdory vysoké úrovni současných mikro-CT zařízení stále existují technologická omezení, která jsou předmětem nepřetržitého výzkumu. Kontrast obrazu poskytovaný běžně využívanými detektory je bohužel omezen přítomností takzvaného temného proudu, který je vedlejším produktem činnosti elektroniky detektoru. Dalším omezením mikro-CT zařízení, ale i klinických CT systémů, je neschopnost kvantitativního vyhodnocení získaných dat.

Předkládaná dizertační se zabývá řešením obou zmíněných omezení využitím nové generace polovodičových detektorů počítajících jednotlivé fotony. Klíčovými parametry těchto detektorů je provoz s potlačeným temným proudem a schopnost měřit a rozlišit energii detekovaných fotonů. Potlačení temného proudu zvyšuje v datech odstup signálu od šumu a tím zvyšuje schopnost zachytit drobné detaily s malým kontrastem. Schopnost kategorizovat detekované fotony na základě jejich energií je základem tzv. spektrální (energeticky citlivé) radiografie a tomografie.

Dizertační práce se zabývá vývojem metodiky měření, algoritmů zpracování dat a souvisejícího vybavení pro mikro-CT biologických vzorků s vysokým rozlišením a energetickou citlivostí s využitím polovodičových detektorů Timepix. Charakterizuje technologii Timepix ve vztahu k radiografickému zobrazování a prezentuje přímé srovnání vlastností detektorů Timepix s běžně používanými technologiemi určenými pro radiografické zobrazování s vysokým rozlišením. Klíčové výsledky jsou založeny na aplikovaném užití detektorů Timepix pro mikro-CT zobrazování širokého spektra biologických vzorků od celých laboratorních myší po jednobuněčné organismy. V některých případech bylo dosaženo velikosti voxelu menší než 600 nm. Hodnotné výsledky byly dosaženy zejména v případě snímání *ex vivo* vzorků biologických tkání.

Dále jsou prezentovány unikátní výsledky spektrální mikrotomografie provedené na fantomovém objektu. Experimentálně získané výsledky potvrzují schopnost jednoznačné identifikace a kvantifikace několika materiálů současně díky algoritmu čtyř-kanálové materiálové dekompozice implementované v rámci dizertační práce. Podobné výsledky s využitím velkoplošných detektorů Timepix dosud nebyly zveřejněny. Schopnost kvantitativního měření v rámci výpočetní tomografie umožňují zcela nové aplikace radiografie a CT jako například molekulární zobrazování nebo současné zobrazování různých orgánových struktur s využitím několika dedikovaných kontrastních látek v rámci jediného CT skenu.

Table of Content

Introduction.....	11
1 Principles of transmission X-ray imaging.....	16
1.1 Photoelectric absorption.....	16
1.2 Compton scattering.....	17
1.3 Rayleigh scattering.....	18
1.4 X-ray transmission radiography.....	18
1.5 Computed tomography.....	19
1.6 Principles of high-resolution X-ray imaging.....	22
1.7 Construction of a micro-CT imaging systems.....	23
1.8 X-ray sources.....	24
1.8.1 X-ray tube construction.....	25
1.9 Dual-energy CT.....	27
1.9.1 Technical approaches of dual-energy CT.....	28
1.9.2 Processing and interpretation of DECT data.....	30
1.10 X-ray spectral radiography and CT.....	32
2 Digital X-ray imaging detectors for high-resolution X-ray imaging.....	35
2.1 Energy-integrating detectors.....	36
2.1.1 CCD-based detectors.....	36
2.1.2 Flat-panel detectors.....	37
2.2 Photon-counting detectors.....	38
2.2.1 PCD anatomy.....	38
2.2.2 Sensor materials available for hybrid-pixel PCD.....	39
2.3 Hybrid-pixel PCDs convenient for high-resolution X-ray imaging.....	39
2.3.1 Medipix.....	40
2.3.2 PILATUS, EIGER.....	42
2.3.3 PiXirad.....	42
2.3.4 XPAD.....	42
2.3.5 UFXC32K.....	43
3 Applications of micro-CT in biology and pre-clinical research.....	44
3.1 <i>In vivo</i> small animal imaging.....	44
3.2 Ex-vivo imaging.....	45
3.3 Energy-sensitive micro-CT.....	47

4	Operation of Timepix detectors	49
4.1	Detector configuration	49
4.1.1	Threshold equalization	49
4.1.2	Energy calibration of Timepix detector	50
4.1.3	Detector threshold calibration	50
4.2	Detector operation.....	52
4.2.1	Flat field correction.....	52
4.2.2	Beam hardening correction	53
4.2.3	WidePIX detector geometry correction.....	55
5	The micro-CT apparatus used in the thesis	58
6	Imaging performance of Timepix detectors compared to EID technology.....	61
7	Upgrades of the MARS micro-CT Scanner	66
7.1	Evaluation of the gantry movement precision.....	66
7.2	Improvement of the spatial resolution.....	69
8	SW and HW tools developed for high-resolution X-ray imaging with large area Timepix detectors	70
8.1	Calibration CBCT geometry	70
8.2	Sample projection trajectory drift compensation.	72
8.2.1	Systematic SPD.....	73
8.2.2	Random SPD.....	74
8.3	Adapter system for soft tissue sample stabilization during micro-CT scan	77
8.4	Matlab-based application for micro-CT projections pre-processing.....	79
8.5	Automated acquisition of BHC data for the MARS scanner	80
9	High-resolution X-ray imaging using Timepix detectors in biology and medicine	82
9.1	Sub-micron resolution micro-CT	82
9.2	Small-animal imaging	85
9.3	Ex-vivo soft tissue imaging.....	87
9.4	Considerations towards in-vivo imaging with available devices	93
9.4.1	Acceptable radiation dose for micro-CT of rodents.....	94
9.4.2	Parameters of the available small animal scanner.....	95
9.4.3	Experimental evaluation of achievable data quality with respect to radiation dose and data sampling strategy.....	96
9.4.4	<i>In vivo</i> considerations summary.....	99
10	Spectral micro-CT using large area Timepix detectors.....	100
10.1	ToT vs. threshold scan	101

10.2	Simulation of X-ray transmission near an absorption edge	102
10.2.1	Modelling of X-ray beam and detector response	102
10.2.2	Occupancy of energy bins with respect to its width and mean energy	104
10.2.3	Radio-density increase above the absorption edge.....	105
10.2.4	Contrast-to-noise ratio of the data.....	108
10.2.5	Simulation summary	110
10.3	Spectral CT of multi-material phantom object.....	110
10.3.1	Material decomposition.....	112
10.4	Spectral micro-CT with WidePIX 3D detector	113
	Conclusions.....	117
	Author's publications	120
	List of References	124

List of abbreviations

3FM	The Third Faculty of Medicine, Charles University
ASIC	application-specific circuit
BHC	beam hardening correction
BMD	basis material decomposition
CB	cone-beam
CBCT	cone-beam computed tomography
CERN	European Organization for Nuclear Research (from French Conseil Européen pour la Recherche Nucléaire)
CHP	central-horizontal plane
COG	center of gravity
CT	computed tomography
DAC	digital to analog convertor
DE	dual energy
Δ SOD	distance between two different source-detector-distances
Δ SOD	distance between two different source-object-distances
EID	energy-integrating detector
EPS	effective pixel size
FF	flat-field
FOV	field of view
FWHM	full-width at half-maximum
HE	high energy
HU	Hounsfield units
IEAP	Institute of Experimental and Applied Physics, Czech Technical University in Prague
IKI	solution of atomic iodine and potassium iodine on water or ethanol
JLEI	Joint Laboratory for Experimental Imaging
LAD	large area detector
LE	low energy
M	magnification factor
NRPI	National Radiation Protection Institute
PCD	photon counting detector
PE	polyethylene
PSF	point-spread-function

PTA	phosphotungstic acid
SDD	source-detector-distance
SOD	source-object-distance
SPD	sample projection drift
TAT	total acquisition time
THL	threshold
ToT	time-over-threshold
TST	total scan time
Z	atomic number

Introduction

The discovery of X-rays was made, as many other significant findings in science, by coincidence. W. C. Roentgen noticed a new and unknown type of highly-penetrating radiation while he had been studying the cathode rays [1]. As the origin and properties of the rays were unclear, he coined the term “X-rays”. The discovery was made in November 1895 and it was introduced to academia in January 1896. The huge potential of X-rays was immediately recognized. The first medical application appeared soon after the official introduction. X-rays were used of localization for bullets after gunshot wounds and even a laboratory of dental radiology was established still during 1896 [2]. W. C. Roentgen became the first laureate of the Nobel Prize in Physics in 1901 [3].

The present state of X-ray imaging is based on more than 120 years of development. Aside profitable properties of X-rays also its harmful effects have been recognized. The technology – radiation sources and suitable detectors – as well as the methodology approaches have undergone huge progress. X-ray radiography and CT are widely known from clinical practices. However, nowadays it is applied in industry, for homeland security applications, and it is also widely used for the purposes of scientific research.

The new application fields with their specific demands gave birth to a new branch of X-ray imaging – micro-computed-tomography (micro-CT). Micro-CT is an advanced radiographic technique capable of visualizing the investigated object in the form of a 3D model with spatial resolution of tens of micrometers or better. Nowadays, some laboratory setups are capable of reaching a resolution that is even below micrometer level [4; 5]. Micro-CT was quickly recognized as a versatile and valuable tool with a wide application range in biology or pre-clinical research – especially for imaging of small animals. Small animals, typically rodents, serve as a model of a human organism and allow indirect study of processes occurring in human body. Micro-CT data provide valuable information useful for phenotyping, drug discovery or understanding of mechanics of a disease [6].

The contrast of certain material in CT data is given by its radio-density. Radio-density, which can be understood as opacity of a material for X-ray beam, is given from combination of effective atomic number of the material and its density. For that reason reason, cortical bone (effective $Z \approx 12$, density $\approx 1.9 \text{ g}\cdot\text{cm}^3$) provides much higher contrast compared to soft tissue (effective Z approx. ≈ 6 , density $\approx 1 \text{ g}\cdot\text{cm}^3$) [7]. Generally, high radio-density of mineralized structured makes them easy to visualize using X-rays while imaging of soft tissue and especially distinction of different soft tissue types is a highly challenging task. To enhance soft tissue radio-density, a number of contrast agents have been introduced [8; 9]. Therefore, micro-CT has become useful for vascular imaging, cardiac imaging, imaging of liver and spleen, or characterization of tumors [6].

Although the current state-of-the-art micro-CT technology is on a high technology level, it still has some known limitations that are the subject of constant development. One of the known issues is that a conventional CT system is not capable of clearly identifying or quantification of certain material. It often happens that two different materials or structures within an investigated object have the same radio-density. Under such circumstances, it is not possible to differentiate between those two although it might be highly demanded. Typically, this is a case of bone and an intravenous contrast agent.

This issue is addressed by energy-sensitive CT approaches. Both clinical and micro-CT rely on the use of broad polychromatic X-ray spectrum generated by an X-ray tube. Radio-density of a material is

a function of photon energy; however, conventional CT systems are not capable of utilizing this fact. A conventional CT system just detects the overall intensity of the beam. A material is, therefore, represented by one radio-density value proportional to the mean energy of used X-ray spectrum. On the other hand, the energy-sensitive approaches provide at least two radio-density values related to different beam energies. The energy dependence of radio-density provides additional information and extends the possibilities of CT data interpretation.

Energy-sensitive CT has been already introduced in clinical field in the form of dual-energy CT (DECT). DECT is the simplest energy-sensitive approach based on the use of two energy-dependent measurements. As mentioned earlier, conventional X-ray imaging detectors are not capable of resolving energy of incoming photons. The spectral separation of the two measurements is, therefore, achieved by alternating parameters of the X-ray source.

A significant progress in energy-sensitive X-ray imaging started with the introduction of technology of photon-counting detectors (PCD). PCD is considered as an extremely promising new technology with a potential to open a new era of X-ray radiography and CT [10]. PCD technology provides higher contrast and higher spatial resolution compared to standard detectors. Moreover, PCD technology resolves the energy of incoming photons. Therefore, it is possible to separate the broad X-ray spectrum generated by an X-ray tube into a set of energy bins. The multi-bin or so-called spectral CT has a potential to significantly exceed the capabilities of already known DECT. Higher number of energy bins means higher number of energy-dependent measurements, and consequently higher precision in material identification and quantification. Simultaneous imaging of multiple contrast agents targeted to different structures of organ systems becomes feasible. Generally, the spectral CT promises more information contained in a single scan while the patient dose is conserved or potentially even reduced.

The aim of this thesis is in the development of methods, data processing techniques and associated equipment for high-resolution and energy sensitive radiography and computed tomography of biologic samples using Timepix detectors. Timepix is a photon-counting detector technology that has been developed in the frame of Medipix Collaboration at CERN [11]. The Medipix Collaboration associated a number of research facilities worldwide. Institute of Experimental and Applied Physics of the Czech Technical University in Prague (IEAP), where this thesis has been carried out, is one of the collaborating members. The thesis demonstrates data processing techniques specifically dedicated for high-resolution X-ray imaging with large-area Timepix devices. It introduces software and hardware tools developed within the frame of this thesis to enhance the achievable quality of acquired CT data. Upgrades of available X-ray imaging systems leading to improved performance are mentioned. Furthermore, the thesis evaluates the imaging performance of Timepix devices compared to energy-integrating detectors widely used in state-of-the-art micro-CT systems. The key part of the thesis demonstrates the applied results of micro-CT with large-area Timepix detectors at a diverse set of biological samples. It was successfully used for micro-CT scans with sub-micron resolution. Results from field of virtual histology – 3D imaging of *ex vivo* samples of soft biology tissue – are presented. CT scans of whole mice are demonstrated and potential *in vivo* use is discussed. Finally, the applicability of large-area Timepix detectors for spectral micro-CT is addressed and experimental results that prove the capability of resolving multiple-materials within a single CT scan are presented.

Goals of the Thesis

The main goal of the thesis is the development of methods and associated equipment for high-resolution and energy sensitive X-ray micro-CT of biological samples using large area photon-counting Timepix detectors.

Partial objectives of the thesis are:

Evaluation of imaging performance of Timepix detectors

- An objective evaluation of the benefits of photon-counting technology for X-ray imaging in comparison to state-of-the-art scintillator-based X-ray cameras

Micro-CT with Timepix detectors for applications in biology and pre-clinical research

- Development and testing of micro-CT methodology for scanning small animals and other biological samples
- Development and implementation of custom tools dedicated for data processing of micro-CT data acquired with large-area Timepix detectors.
- Utilization of enhanced contrast-to-noise ratio provided by photon-counting detector technology for X-ray imaging of soft tissue samples
- Utilization of steep point-spread-function of Timepix detector for micro-CT with sub-micrometer resolution

Spectral micro-CT with Timepix detectors

- Testing of energy-resolving capabilities of large-area Timepix detectors for multiple-bin energy-sensitive micro-CT.
- Implementation of data processing techniques for identification and quantification of material composition of scanned objects

Thesis outline

The thesis consists of ten chapters. The first three chapters provide an introduction to the field of high resolution and energy sensitive X-ray imaging. Chapters 4 and 5 are focused on the apparatus used for experimental measurements. The rest of the thesis summarizes the experimental results achieved with large-area photon-counting detectors Timepix applied for micro-radiography and micro-CT of biological samples. The content of each chapter is detailed in the following paragraphs.

Chapter 1 summarizes the physical background and it introduces the technical approaches connected with X-ray imaging. It briefly describes the photon interactions contributing to production of a radiographic image. Principles of X-ray radiography and computer tomography are introduced. Production of X-rays in laboratory conditions is discussed and the construction of X-ray tubes and X-ray imaging systems are introduced. The text further explains principles of high-resolution X-ray imaging in cone beam geometry using laboratory-scale apparatus. Lastly, the chapter introduces the terms dual-energy CT and spectral CT. Principles of both approaches are explained together with the description of technical solutions and processing of energy-sensitive data.

Chapter 2 focuses on the state-of-the-art detection technologies suitable for high-resolution X-ray imaging. The available detector technologies are categorized into several classes and their advantages and disadvantages are discussed. The emphasis is put on the overview of different detector types based on hybrid-pixel photon counting technology, as it is closely related to the topic of this thesis.

Chapter 3 brings a review of interesting applications of micro-CT in biology and pre-clinical research. The aim of this chapter is to provide a comprehensive summary about the range of possible applications and to demonstrate image quality achievable by means of X-ray micro-CT. Both *in vivo* and *ex vivo* applications are discussed and previously published results of energy sensitive micro-CT are demonstrated.

Chapter 4 deals with the configuration and operation of Timepix detectors used within the frame of this thesis. It provides basic information on detector configuration needed for its proper function and demonstrates three image correction techniques connected with the use of Timepix detectors as X-ray imaging devices.

Chapter 5 introduces the X-ray imaging apparatus used in the frame of this thesis. The X-ray micro-CT laboratory of Institute of Experimental and Applied Physics operates on two custom built micro-CT systems equipped with large-area photon-counting Timepix detectors. Furthermore, a small animal scanner situated at conjoint laboratory of the Third Medical Faculty of Charles University in Prague, Institute of Experimental and Applied Physics and Faculty of Biomedical Engineering of the Czech Technical University in Prague was used. Construction and capabilities of all three mentioned micro-CT systems are detailed.

Chapter 6 demonstrates the imaging performance of Timepix detectors. Spatial resolution achievable with Timepix detectors is experimentally compared to three different state-of-the-art scintillator-based X-ray imaging detectors. Beside the spatial resolution, the positive influence of dark-current-free photon counting to contrast-to-noise ratio of obtained data is demonstrated.

Chapter 7 explains upgrades done on one of the mentioned micro-CT scanners carried out within frame of this thesis. The performed modifications aimed to improved reliability of remote-control positioning system and also enhanced the achievable spatial resolution. The performed construction changes are described and the improvement of mentioned parameters is evaluated and quantified.

Chapter 8 introduces custom hardware and software tools developed for the purposes of cone-beam micro-CT. High-resolution X-ray imaging of biological samples is a challenging discipline requiring custom-made accessories or sample processing techniques in many cases. A Matlab-based application dedicated for processing of CT projections captured using large-area Timepix detectors is introduced. An own approach for calibration of cone beam CT geometry is described as well. Techniques for improving the data quality by addressing possible inaccuracy of the scanner mechanics have been implemented and their efficiency is demonstrated. Finally, a custom-designed accessory for scanning of delicate and unstable biology samples is shown.

Chapter 9 summarizes the applied results of micro-CT with Timepix detectors. The range of presented applications covers small animal imaging, virtual histology of *ex vivo* soft tissue samples and micro-CT with sub-micrometer resolution of biology samples. Moreover, the chapter opens a topic of *in vivo* imaging using the available equipment. A set of experimental measurements verifying the applicability of available small animal micro-CT scanner for *in vivo* imaging of mice was carried out. Results of the experiment are presented and prospects for practical use are discussed.

Chapter 10 addresses the topic of spectral/multi-bin CT in small animal scale using Timepix detectors. It demonstrates the capability of Timepix to resolve and clearly identify multiple materials within a single CT scan. The chapter starts with a discussion on the suitability of individual operation modes provided by Timepix technology for energy-sensitive X-ray imaging in the case of a large-area detector. Then, a computer model searching for optimal setting of energy bins is presented. Finally, an experimental measurement of a phantom object containing four different materials is presented. The presented data are the first results of multi-bin X-ray micro-CT with large-area Timepix detector combined with basis material decomposition published so far.

1 Principles of transmission X-ray imaging

X-ray imaging is a set of techniques utilizing an X-ray beam to visualize inner structures of investigated objects. One can use term X-ray radiography in the case of 2D projection of the object and computed tomography in the case of 3D imaging. The basic idea of both approaches is the same. An investigated object is placed between a source of radiation and a suitable detection unit. As the beam emitted from the source passes through the object, a certain number of photons undergoes an interaction and is excluded from the beam. The transmitted beam with modulated intensity is then captured by the detector and creates a radiographic projection. The beam attenuation obeys the Lambert-Beer law:

$$I = I_0 \cdot e^{-\mu d} \quad (1)$$

where I is the modulated beam intensity, I_0 is the original beam intensity, μ is the linear attenuation coefficient and d is thickness of the absorber [12]. The linear attenuation coefficient is frequently substituted by a mass attenuation coefficient $\mu_m(\text{cm}^2/\text{g})$ which is given as a ratio of linear attenuation of a material and its density. The equation 1 then transforms to

$$I = I_0 \cdot e^{-\mu_m \cdot \rho \cdot d} \quad (2)$$

The beam attenuation is caused by interactions of individual photons with atoms of the absorbing material. Generally, an X-ray photon can interact with matter in several different processes:

- Photoelectric absorption,
- Compton scattering,
- Rayleigh scattering,
- Thompson scattering,
- Production of electron-positron pairs.

Since X-ray imaging is in most cases performed with photon energies approximately within a range of 10–150 keV, the influence of latter two interactions is negligible. Therefore, only interactions contributing to production of radiographic image will be described in detail.

1.1 Photoelectric absorption

Photoelectric absorption is an interaction of a highly energetic photon with an electron situated in an inner shell of an atom. The photon is absorbed while the electron is emitted from its orbital (figure 1 left). The vacancy in the orbital is filled by an electron from a higher shell and emission of a characteristic X-ray photon occurs (figure 1 right). The ejected electron has kinetic energy equal to the difference of incident photon energy and the binding energy of the electron. Thanks to the provided kinetic energy, the ejected electron can cause secondary ionization. Obviously, the photoelectric absorption is possible only if the incident photon has energy exceeding the binding energy of electrons.

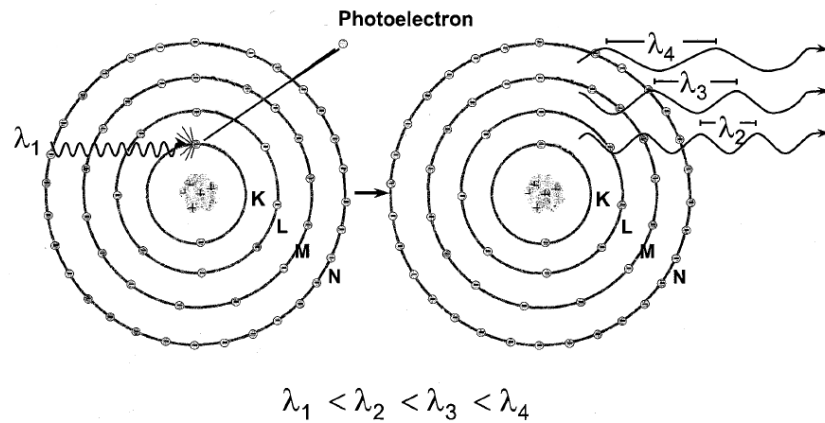


Figure 1: Schematic drawing of photoelectric effect. An incident photon dislodges an electron from an inner shell (left). The energy of a photoelectron is equal to energy difference of incident photon and binding energy of the dislodged electron. The vacancy is immediately filled by an electron from the higher shell and the energy excess is emitted in a form of a characteristic X-ray photon (right). Image modified from [12].

1.2 Compton scattering

Compton effect is an incoherent scattering occurring at loosely bound electrons. The binding energy of the electron is so low compared to the energy of the incident photon that the electron can be considered as a free particle. The incident photon transfers a part of its energy to an electron and is deflected from the original direction (figure 2 left). The energy loss of the electron is proportional to the deflection angle:

$$E_{sc} = \frac{E_0}{1 + \frac{E_0}{m_e c^2} (1 - \cos\theta)} \quad (3)$$

E_{sc} and E_0 are the energy of scattered photon and of the incident photon, respectively. θ is the scattering angle of the photon and $m_e c^2$ is the rest mass energy of an electron. The highest possible energy loss occurs if the photon is deflected backwards (see equation 3). Similarly like in the case of photoelectric effect, the electron provided by kinetic energy leaves its orbital and causes secondary ionization.

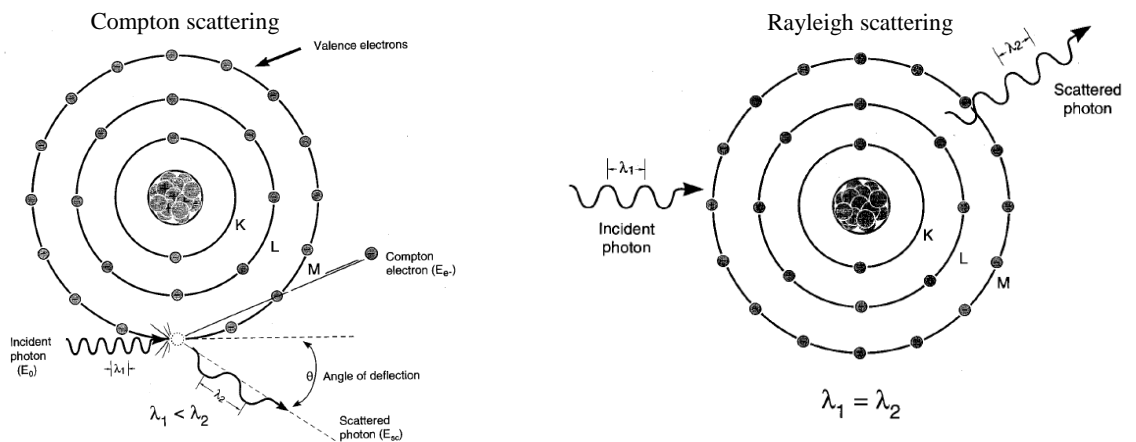


Figure 2: Schematic representation of Compton (left) and Rayleigh scattering (right). While Compton scattering results in ionization of the atom, the Rayleigh scattering is a coherent interaction. The image modified from [12].

1.3 Rayleigh scattering

Unlike the previously described interaction processes the Rayleigh scattering is an interaction of a photon with an entire atom. It is a coherent process as the energies of the incident and the scattered photons are equal and there is no ionization caused to the scattering atom (figure 2 right). An incident photon passes its energy to an atom. All the electrons of the scattering atom oscillate in a phase and immediately emit the whole obtained energy in a form of new photon leaving the atom in different direction than the incident one. The contribution of Rayleigh scattering to X-ray image formation is just minor since it has the highest probability for photons with energies lower than 1 keV.

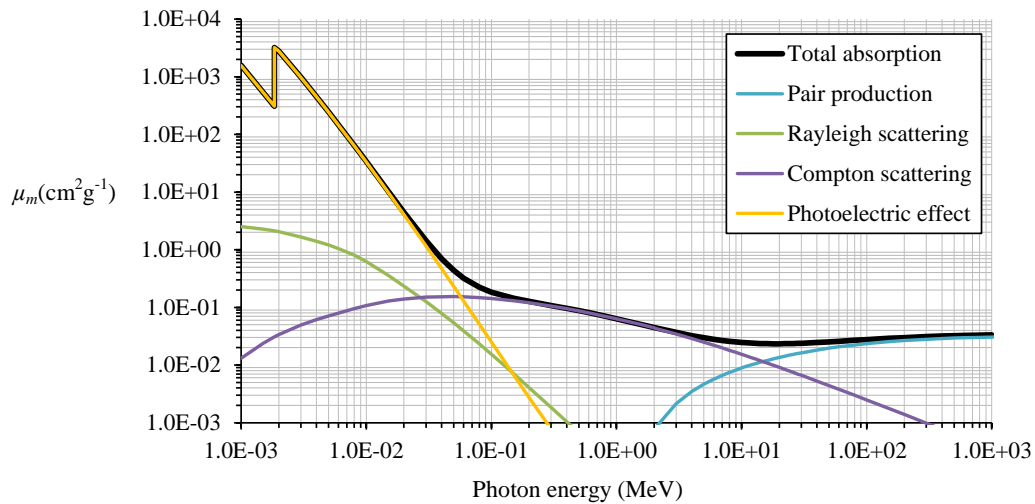


Figure 3: Total mass attenuation coefficient of silicon (black line) and its contributors. The chart was created based on the data from XCOM photon cross sections database [13].

The previously mentioned linear attenuation coefficient μ is a linear combination of contributions originating from individual interaction processes. Generally speaking the attenuation coefficient increases with atomic number Z and decreases with photon energy. An example of energy-dependence of mass attenuation coefficient is shown in figure 3. The figure also demonstrates the influence of individual contributing interaction processes. It is evident, that photoelectric effect is a dominant interaction mechanism for energies below approximately 100 keV, while for higher energies, the most important interaction mechanism becomes the Compton scattering. The probability of both Compton and Rayleigh scattering is significantly lower for energy range useful for small animal imaging (approximately 10 – 50 keV).

1.4 X-ray transmission radiography

X-ray radiography is a basic and the simplest approach of X-ray transmission imaging. Its basic principle is still the same as it was demonstrated by W.C. Roentgen in 1896. An object is put between a radiation source and a suitable detector and its 3D composition is captured into a 2D image called an X-ray projection. The obtained X-ray projection is formed by beam entering the detector after its intensity was modulated by interactions with the exposed object (see schematic drawing in figure 4). The information in each detector pixel is, therefore, result of a sum of all interactions along a ray connecting the pixel with the radiation source.

The contrast of a structure is given by its effective mass attenuation coefficient, density and its thickness in a radiographic projection (see equation 2). It can be generally stated, that X-ray attenuation increases with atomic number. That is the reason why i.e. bones provide higher contrast than soft tissue in clinical X-ray imaging. The simplicity of X-ray radiography is, however, connected with certain limitations in data interpretation. As integration is commutative and associative procedure it is not possible to resolve the order of occurred interaction. Similarly, it is not possible to tell whether the observed signal was formed by one high-contrast object or by several low-contrast overlapping structures. Further, the information on depth of a structure along the ray is missing. Therefore, it is impossible to clearly resolve overlapping structures (symbolized by signal caused by structures 1, 2 and 3 in figure 4). Mentioned shortcomings of 2D radiography have been solved by invention of X-ray computed tomography (CT). Principles of CT are introduced in the next section.

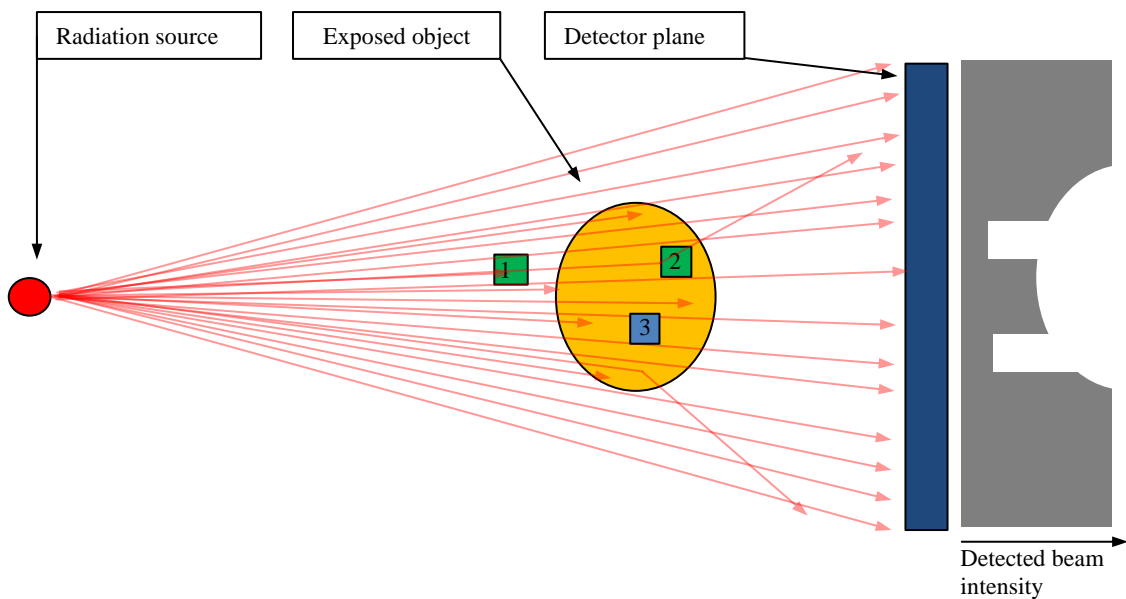


Figure 4: Principle of X-ray transmission radiography. A 3D object is projected into a 2D plane using a beam of X-ray photons. The contrast of a radiographic projection is given by modulation of beam intensity as it passes through the imaged object. The beam intensity is modulated by integration of all photon interactions along a ray.

1.5 Computed tomography

X-ray computed tomography is an advanced X-ray imaging modality noninvasively providing a 3D representation of inner structures of the visualized object. The theoretical base of computed tomography has been proposed in 1917 by Johann Radon [12]. The introduced mathematical approach based on line integrals over planes is nowadays known as Radon transform. Its inverse function is used for CT reconstruction – producing a voxel-based 3D model of the scanned object. As the inverse Radon transform requires significant computational power, it was experimentally applied much later. The first CT scanner was built and tested in 1969 by G. N. Hounsfield. The mathematical reconstruction algorithm was independently implemented and introduced by A. M. Cormack. Ten years later, both of them were awarded by the Nobel Prize in Physiology or Medicine.

A CT scan is based on acquisition of hundreds or thousands 2D X-ray projections of the object acquired under different angles (figure 5A). After obtaining the data and optional pre-processing, the projections are transformed into sinograms (figure 5B). While a projection represents a signal –

detected beam intensity – of each detector pixel in dependence on its position in space, a sinogram represents the signal of a pixel with dependence on the acquisition angle. Sinograms are then used as an input of the CT reconstruction algorithm. The output of CT reconstruction is a set of volume slices (figure 5C). The slices are perpendicular to the object axis of rotation and to projection planes. Each of them represents a radio-density map of the object. The complete set of slices represents a 3D model of the scanned object. Figure 5D shows volume rendering of 3D model of bones extracted from the set of CT slices.

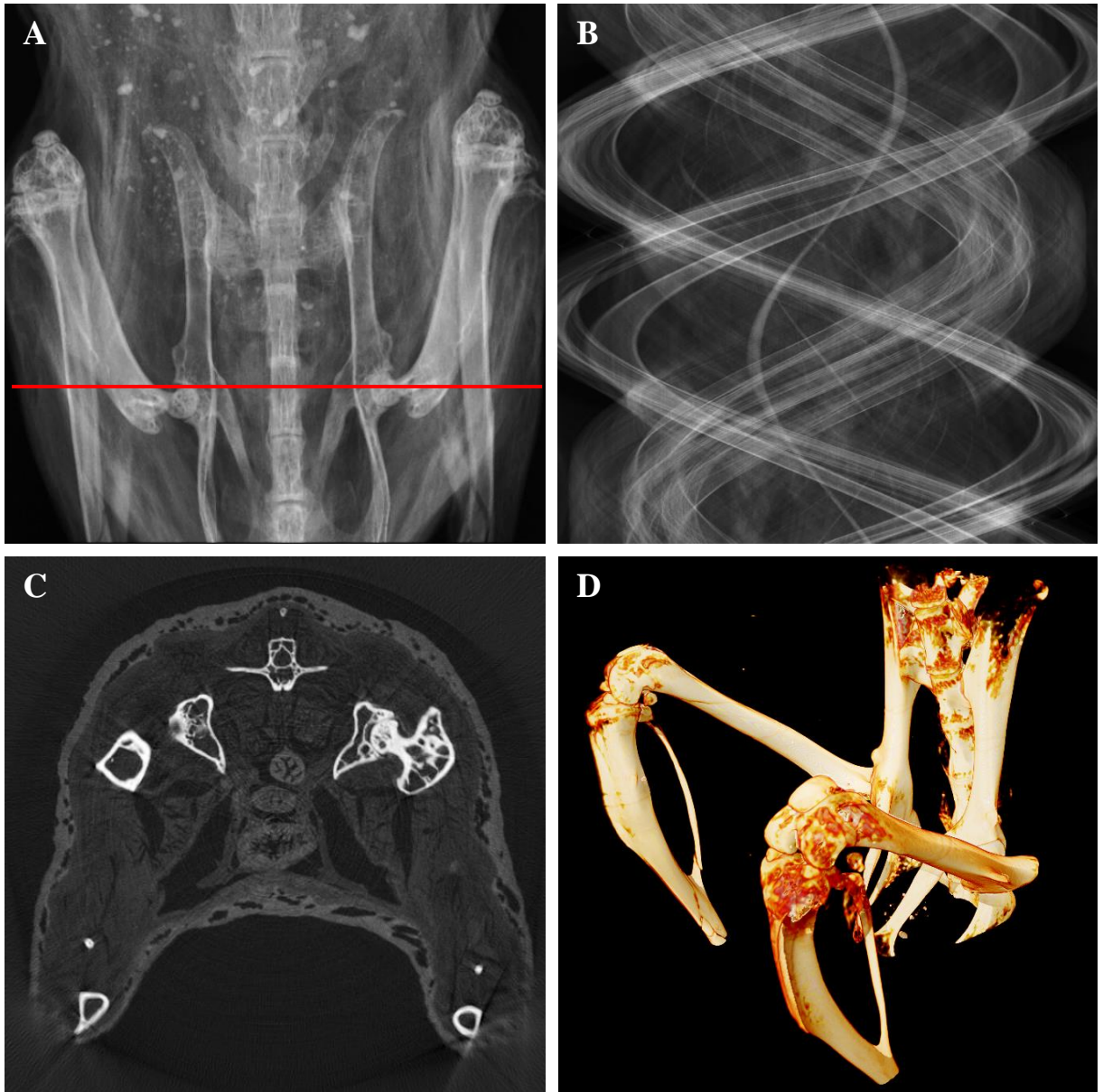


Figure 5: Principle of X-ray computed tomography demonstrated at an example of a mouse. The CT scan is based on collection of hundreds or thousands X-ray projections acquired under different angles (A). Projections are then transformed into sinograms (B). Sinograms are used as an input of the CT reconstruction which produces volume slices (C). A set of volume slices provides a 3D model of the scanned object. (D) shows volume rendering of 3D model of a mouse skeleton created from the set of CT slices. The sinogram (B) and slice (C) originate from the detector line highlighted by a red line.

The 3D representation of the scanned object offers a number of advantages compared to 2D radiography. A CT scan avoids mentioned issues of 2D radiography like i.e. overlapping structures. Moreover it provides huge freedom in visualization of the data. The voxel-based model can be shown

in any demanded angle, it is possible to modify opacity of individual structures, it is possible to use pseudo-color schemes to enhance contrast of certain structures. Virtual sections revealing any demanded plane can be created and visualized. Beside representation of the data in form of slices or planes it is also possible to work with fully 3D data using techniques called volume rendering (figure 5D). And finally, the CT-reconstructed data allows easy and accurate measurements of distances, area and even volumes or it can be i.e. used as an input for advanced computer-based techniques like strain analysis etc.

The grayscale values within CT slices are usually coded by radio-density scale represented by Hounsfield units (HU) in clinical field. HU scale is normalized using radio-density of air and distilled water. A HU value of material x can be calculated using equation:

$$HU_x = 1000 \cdot \frac{\mu_x - \mu_{water}}{\mu_{water} - \mu_{air}} \quad (4)$$

where μ_x is radio-density of the material of interest and μ_{water} and μ_{air} are radio-density values of distilled water and air in the dataset. From equation 4 it is obvious that HU values of water and air are 0 and -1000 , respectively. Radio-density, a quality defining contrast of certain structure within CT slices, can be understood as opacity of a material for X-ray beam. Its level is given by combination of effective atomic number of the material and its density. That is the reason, why cortical bone (effective $Z \approx 12$, density $\approx 1.9 \text{ g}\cdot\text{cm}^3$) provide much higher contrast compared to soft tissue (effective Z approx. ≈ 6 , density $\approx 1 \text{ g}\cdot\text{cm}^3$) [7]. Generally, high radio-density of mineralized structured makes them easy to visualize using X-rays while imaging of soft tissue and especially distinction of different soft tissue types is a highly challenging task. To enhance soft tissue radio-density a number of contrast agents has been introduced [8; 9].

Although the current state-of-the-art micro-CT technology is on a high technology level it still has some known limitations. One of known issues is that a conventional CT system is not capable of clearly identifying or quantification of certain material. It often happens that two different materials or structures within an investigated object have the same radio-density. Under such circumstances, it is not possible to differentiate between those two although it might be highly demanded. Typically, this is a case of bone and an intravenous contrast agent or urinary stones etc. A solution to this issue has been provided by energy-sensitive CT. This approach taking into account the dependence of radio-density values of different materials with respect to energy is discussed in chapters 1.9 and 1.10.

The applications of CT are known mostly from medical field however it has recently became very popular even in industry and it has found its irreplaceable position in scientific research. With the raising popularity the design of CT systems has been modified to fulfill needs of new application fields. The systems used for research in biology and pre-clinical research are usually referred as micro-CT systems as the provided spatial resolution reaches tens of micrometers or even less. The following sub-chapters explain principles of X-ray micro CT and high-resolution X-ray imaging in general. The radiation sources and detection technologies currently used are introduced.

1.6 Principles of high-resolution X-ray imaging

High-resolution X-ray imaging – either micro-radiography in the case of 2D images or micro-CT in the case of 3D imaging – typically rely on so-called cone-beam (CB) imaging geometry. CB geometry means that a sample is imaged using a divergent X-ray beam originated in a point-like source and captured using a 2D detector unit (see figure 6A). The key feature of CB geometry for high resolution imaging is its natural ability to magnify the sample projection. The projection magnification M is denoted as

$$M = \frac{SDD}{SOD} \quad (5)$$

where SDD is the source-detector-distance and SOD is source-object-distance. The geometrical magnification inevitably connected with CB geometry allows acquisition of data with spatial resolution much higher than is the intrinsic resolution of the used detector. The sampling density of the obtained image is given by the detector pixel pitch. Once the magnification factor M is induced, the sampling density is characterized by so-called effective-pixel size EPS . The EPS can be denoted as

$$EPS = \frac{\text{Real pixel size}}{M} \quad (6)$$

Smaller value of EPS brings higher sampling density and, therefore, higher spatial resolution of obtained images (see figure 6B). The achievable spatial resolution is, however, limited. The limit is given by properties of the radiation source, namely by its focal spot size. Once the EPS becomes smaller than focal spot size of the source, the spatial resolution of the image does not further improve due to penumbral blurring caused by the focal spot of the source (see figure 6C).

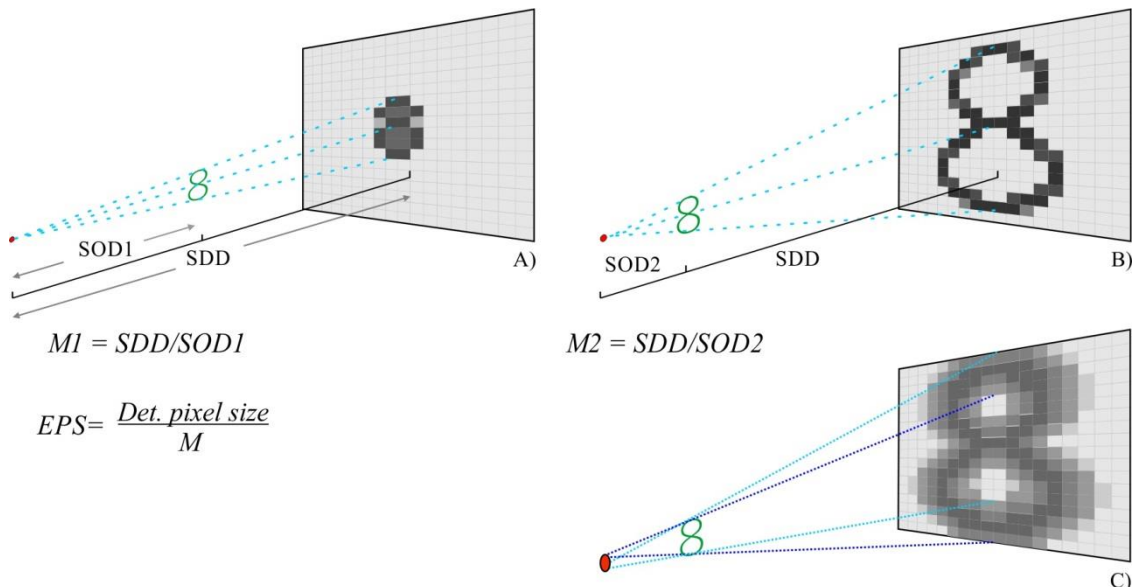


Figure 6: Radiographic imaging in cone-beam geometry. Cone-beam geometry is characterized by a point-like source producing a divergent radiation beam which is captured by a 2D detector (A); further, it allows imaging with spatial resolution higher than intrinsic resolution of the detector due to geometric magnification (B); The maximal achievable resolution is limited by penumbra effect caused by the source focal spot diameter (C).

Therefore, quality of the X-ray tube is of a key importance in the field of micro-radiography and micro-CT. Tubes suitable for such applications are usually marked as mini-focus (spot smaller than approx. 50 μm), micro-focus (spot smaller than approx. 15 μm) or nano-focus (spot smaller than 1 μm). The disadvantage of these tubes is in relatively low output beam intensity.

The exception from described technical approach was developed and introduced by Rigaku company. Their micro-CT system commercially available under brand Rigaku nano3DX utilizes an intensive quazi-parallel beam produced by an X-ray tube with rotating anode together with finely pixelated CCD sensor connected to a scintillator via magnifying optics. In this case the image magnification is performed using the optics at the detector site. Based on information provided by the manufacturer, such construction can provide very fast scanning speed simultaneously with true spatial resolution of 600 nanometers [14].

High quality micro-CT scans are also carried out at synchrotron facilities. Synchrotrons used to be the first source of radiation brilliant enough to provide spatial resolution at micrometer level [15; 16]. Even nowadays, when compact laboratory-scale micro-CT scanners are easily accessible, the synchrotron radiation provides unique features like i.e. enormously high photon flux or imaging with monochromatic beam, which prevents occurrence of some imaging artifacts.

1.7 Construction of a micro-CT imaging systems

The construction of micro-CT systems is usually based on one of two basic approaches [17]:

- The radiation source and detector unit are mounted steadily and a remote-control sample positioning stage is situated between them. The angular positioning is performed by rotation of the sample mounted to a high-precision rotation stage during the scan (see figure 7 left).
- A gantry housing the source and detector rotates around a horizontal axis while a sample is placed steadily in the center of rotation (see figure 7 right).

The first described construction has very adaptable geometry and provides maximal stability and precision as the heavy-weight components are immobile during a measurement. Such construction is typically used in applications where resolution of few micrometers or even less is required.

A sample rotates around a vertical axis on the top of precise rotation stage while it is scanned. Thanks to the variable imaging geometry, the system is capable of scanning samples with large variety in dimensions. The construction is frequently referred as “industrial CT” although it is widely applicable even in natural sciences, biology and even in medicine.

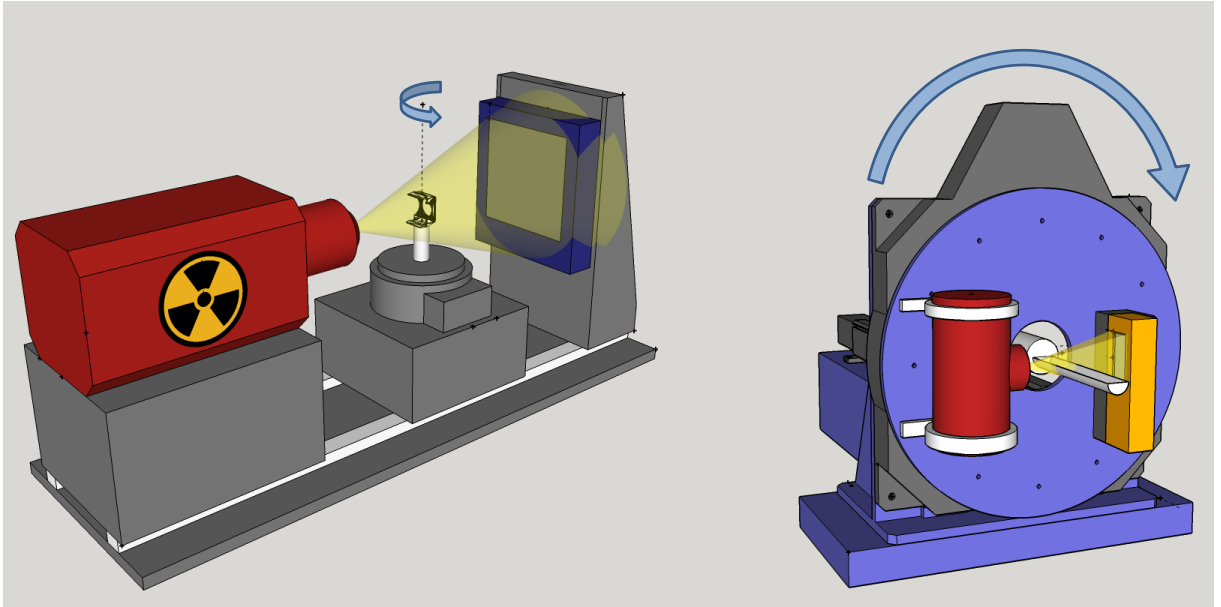


Figure 7: Sketch of an "industrial" micro-CT scanner (left) and a small animal micro-CT scanner (right).

The first construction approach is no longer advantageous in the case of micro-CT of animals. Especially, if *in vivo* imaging is considered. Performing the CT scan via rotating around with a patient is of course unthinkable in the case of human CT. In the case of small animal micro-CT, it is at least impractical. Most of dedicated small-animal-imaging scanners use a construction derived from human-scale medical CT systems, although there has been a successful attempt to scan *in vivo* mice fixed in vertical position during the scan [18]. Micro-CT systems constructed with a rotating gantry generally provide lower resolution but they are irreplaceable since they allow small animals to be scanned in a natural position and maximal stability of the sample is maintained this way.

1.8 X-ray sources

X-ray tubes are the most conventional X-ray sources nowadays used for X-ray radiography and CT. In a very basic approximation, an X-ray tube could be described as two electrodes with different electric potentials encapsulated in a vacuum chamber. The cathode, usually in a form of heated metal wire, behaves as a source of electrons. The thermally emitted electrons are accelerated towards the anode by an electrical field created by a high potential difference applied between cathode and anode (typically within a range from tens to hundreds of kV). Once the stream of electrons reaches the anode, the electrons start interacting with the material of anode. This way they lose the original kinetic energy which is transformed into electromagnetic radiation. The majority of electron energy is transformed into heat and is immediately absorbed in the anode. However, a small fraction (less than 1 %) of the produced radiation consists of highly energetic photons which create the X-ray beam [19]. The X-ray emitted from the tube was produced by two different processes:

- Bremsstrahlung – provides broad and continuous energy spectrum as a consequence of gradual loss of accelerated electron kinetic energy by multiple interaction with electron cloud of anode.
- Characteristic radiation – provides discrete spectrum of one or several characteristic energies. The emission of characteristic radiation occurs if an accelerated electron hits and dislodges an electron bounded on an inner shell. The vacancy is then filled by another electron from a higher shell and the exceeding energy is then emitted in a form of characteristic X-ray photon.

An X-ray tube, therefore, provides a broad continuous spectrum consisting of two superimposed compounds. While the bremsstrahlung depends on anode material just weakly, the characteristic lines are different for each anode material. Further, the characteristic lines occur only in the case, that the kinetic energy of accelerated electrons exceeds the binding energy of electrons at K-shells of anode atoms.

To maximize the X-ray emission it is desirable to manufacture the anode from a material with high electron density. Thus, elements with high atomic number are favorable. The most common material of X-ray tube anode is tungsten; however many tubes are constructed with anodes made of different materials like copper, molybdenum, rhodium, silver and other.

Depending on the intended application, the X-ray tubes are constructed to be operated with accelerating voltage within the range from tens kV up to hundreds kV. The accelerating voltage (usually denoted as kVp, standing for kilovolt peak) defines the maximal photon energy that can occur in the generated X-ray spectrum, however, the mean energy is much lower (see figure 8).

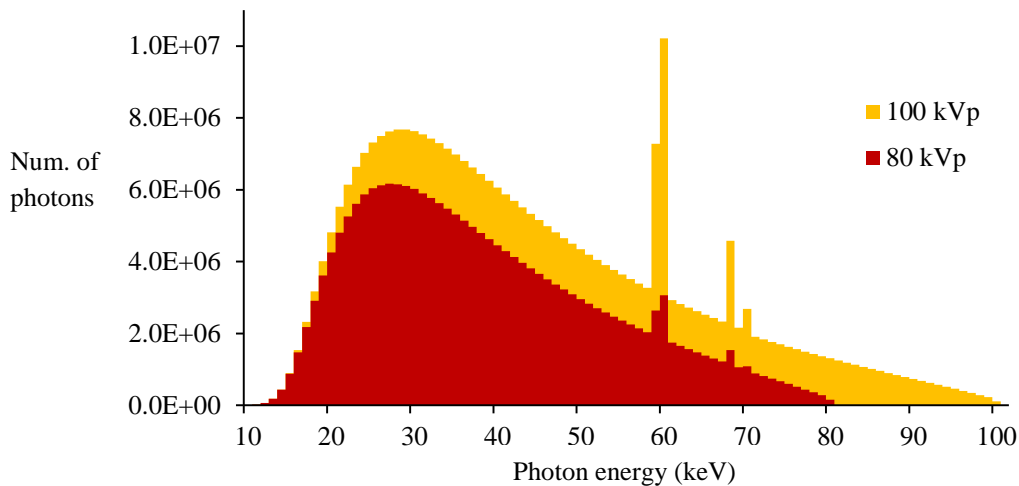


Figure 8: Photon energy distribution provided by an X-ray tube with tungsten anode and accelerating voltage set to 80 kVp (red) or 100 kVp (yellow). The spectra were simulated using the SpekCalc software [20].

1.8.1 X-ray tube construction

As was already mentioned, an X-ray tube consists of a cathode and anode encapsulated in a vacuum chamber. It was also mentioned that the majority of the tube power is transformed into heat and is absorbed by the anode or X-ray tube cover. The high-power tubes usually utilize a massive anode with side emission sealed in a glass bulb. Such X-ray tube is shown in figure 9. The target area is tilted with respect to direction of the electron beam.

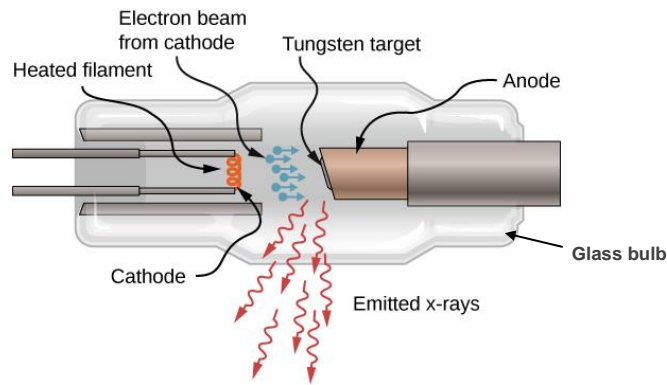


Figure 9: Schematic drawing of an X-ray tube with side emission. The side emission approach is used for high power tubes. Image modified from [21].

The X-ray emission occurs in all directions, however, only those photons facing away from the target surface can reach the exit window of the tube. The rest is again absorbed by the anode material. The X-ray beam direction is, therefore, approximately perpendicular to the electron beam. The whole glass bulb is cooled with oil from the outside to dissipate the produced heat. To further improve the heat dissipation the tube can be equipped with a rotating anode. In such case the anode has a shape of a disc rotating around its axis. This way a certain point of the anode has time to cool down before it will be exposed to electron beam again.

Previously mentioned X-ray tubes are typically used in applications where high beam flux is more important than spatial resolution. In the case of micro-radiography and micro-CT, a different tube construction is typically used. Tubes dedicated for high-resolution usually have a transmission anode. The anode is placed perpendicularly to the electron beam and it is very thin, so the generated X-ray photons are emitted in the same direction as the electron beam (see figure 10).

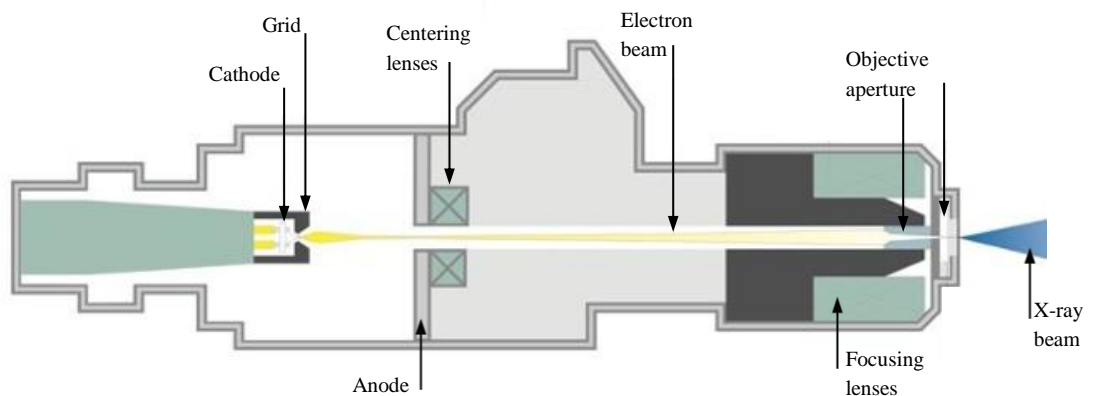


Figure 10: Construction of a micro-focus X-ray tube with a transmission target. Image modified from [22].

Moreover, the electron beam is focused into a very small area via a system of electromagnetic lenses to hit the anode only in an area of several micrometers in diameter. On one hand, such focusing is a key factor for high-resolution use of the tube (will be described in detail in chapter 1.6) on the other hand, it limits the maximal output power of the tube. With a focal area of several square micrometers, the power density can easily reach the level when the anode material would be immediately molten. The maximal output power of a tube with $10\ \mu\text{m}$ focal spot size is $8\ \text{W}$ only considering that the acceptable power density in range of $0.4 - 0.8\ \text{W}/\mu\text{m}^2$ [23].

The issue with heat dissipation in tubes dedicated for high-resolution imaging could be possibly solved by a recently introduced technology of metal-jet anode X-ray tubes (see figure 11). This technology substitutes the solid-state anode by a jet of liquid metal which is continuously regenerated due to its permanent flow [24]. The target material is already molten by its nature and it is renewed by a rate of 100 m/s. Therefore, the power density can be increased up to 3 – 6 W/ μm of focal spot diameter.

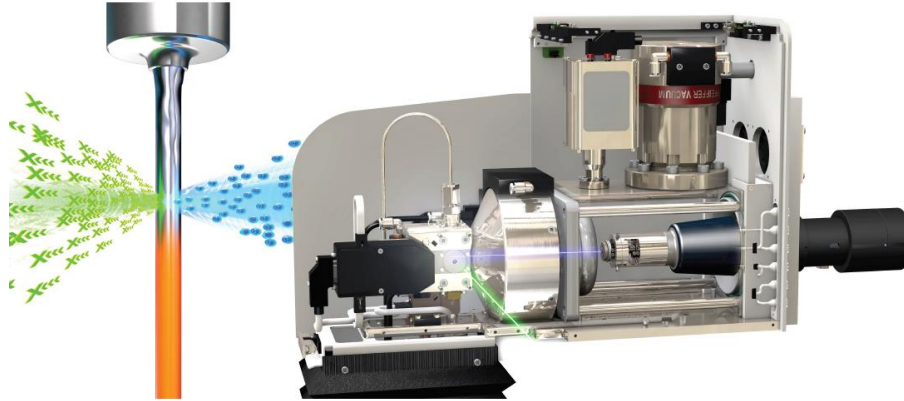


Figure 11: Metal-jet X-ray tube: New technology utilizing a jet of liquid metal instead of solid-state anode. Thanks to enormously high refresh rate of the anode material, a metal-jet tube can provide much higher power density compared to conventional X-ray tubes. Image modified from [24].

1.9 Dual-energy CT

Dual-energy CT (DECT) has been the first implemented approach of energy sensitive X-ray imaging. It can be generally stated that energy-sensitive CT is an X-ray imaging technique considering a fact that the radio-density of a material is a function of energy.

X-ray beam generated by an X-ray tube provide a broad range of different photon energies. A conventional CT system detects just the overall intensity of the beam. A material is, therefore, represented by one radio-density value proportional to the mean energy of used X-ray spectrum. Energy-sensitive approaches, on the other hand, provide at least two radio-density values for each material related to different beam energies. The energy dependence of radio-density can be analyzed and the amount information available for data interpretation can be extended this way.

DECT is the simplest energy-sensitive approach based on use of two energy-dependent measurements. The idea of using two different X-ray energies for tissue characterization was introduced in 1970s. Alvarez and Macovski published a study proposing an algorithm for extraction of material composition of an investigated object using CT scans of two different X-ray spectra [25]. The published study introduced a mathematical apparatus for decomposition of measured linear attenuation coefficients represented in Hounsfield units into contributions given by absorption and scattering. The data obtained by suggested basis material decomposition (BMD), therefore, represented spatial maps of mass density (from absorption) and electron density (from scatter processes).

It took a long time before the proposed technique was empirically verified – i.e. the first dual-source DECT system was introduced in 2006 [26]. Nevertheless, it has found its application area in clinical field very quickly and today it has its stable place in clinical diagnostics. Although DECT is not a concern of this thesis, it is introduced within this chapter since it is a cornerstone of energy sensitive

X-ray imaging. DECT is also a starting point of further development towards spectral CT imaging and lot of data processing approaches known in DECT are applicable for spectral CT as well.

1.9.1 Technical approaches of dual-energy CT

Dual-energy CT (DECT) is an advanced radiographic approach utilizing two exposures of the sample using two X-ray spectra with different mean energies. As the current X-ray detection standard for imaging purposes is based on EID technology, it is not possible to perform the spectral separation on the detector level. Therefore, the X-ray spectrum variation has to be provided by changing the settings of an X-ray source (with exception of a dual-layer detector approach). The typical X-ray source settings are 140/80 kVp (mean photon energy approximately 76 keV and 56 keV, respectively) in the case of clinical DECT [27]. Further spectral separation can be achieved by optional beam filtering by suitable absorption materials.

A dual-energy CT scan (DECT) can be generally performed using any regular CT system. A dedicated device is not necessarily needed. As the only condition is to make two exposures of the sample with different X-ray spectra, a DECT can be carried out as two individual consequent scans with different setting of the X-ray tube. Such approach is also the most frequently used way in the case of dual-energy micro-CT since DE micro-CT is still not widely used and dedicated systems are not available.

Nevertheless, sequential acquisition of DECT data has its shortcomings as a consequence of time delay between both scans. Motion artifacts can easily occur especially in the case of in-vivo imaging. But even in the case of ex-vivo measurements of biology samples, it is necessary to put emphasis to proper sample mounting to avoid misalignment of both datasets. If the sample is stable enough, the sequential DECT provides satisfying results.

Several different technical approaches dedicated for DECT avoiding the mentioned drawbacks have been designed. The following paragraphs briefly introduce available solutions.

Rapid voltage switching

The tube voltage quickly alternates between two accelerating voltage levels. Therefore, in each angular position two exposures with different X-ray spectra are captured. As each of X-ray spectra may provide different photon flux, the exposure time of each projection shall be modified to achieve suitable image statistics. Alternatively, the tube current can be adjusted together with accelerating voltage to provide comparable beam intensity. Rapid voltage switching, obviously, cannot be combined with additional beam filtration and, therefore, both X-ray spectra are significantly overlapping and the spectral separation between high-energy (HE) and low-energy (LE) data is limited (see figure 12A).

Rapid voltage switching is not very convenient for micro-CT field. The control units of mini- and micro-focus X-ray tubes typically need relatively long time – up to several seconds – to switch between tube voltages to prevent tube damage. Switching between the two voltages would be in many cases longer than the data acquisition.

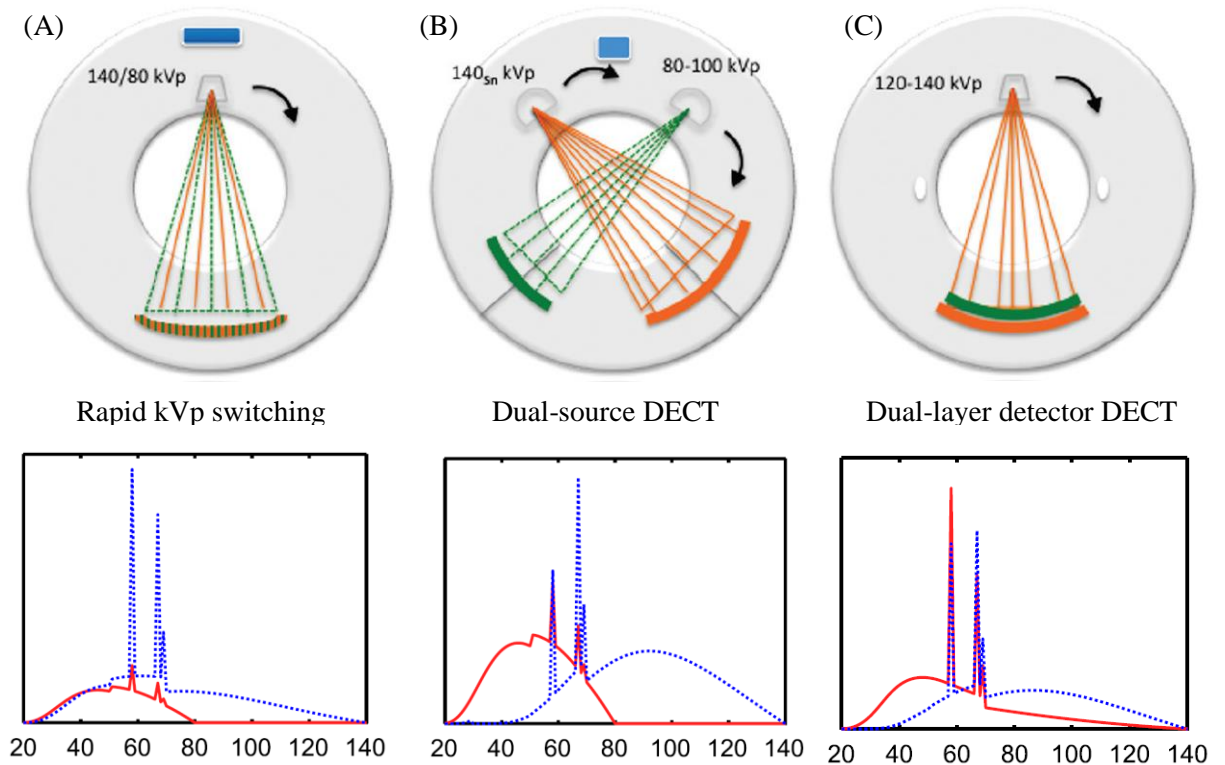


Figure 12: Technological approaches of DECT: Rapid X-ray tube voltage switching (left), dual-source construction (middle) and dual-layer detector (right). The lower row demonstrates LE (red) and HE (blue) spectra of each approach. The best spectral separation is provided by the dual-source approach as the overlap of HE and LE spectra is minimized (lower row). Image modified from [28; 29].

Dual-source CT

Dual-source DECT basically combines two CT scanners into one unit. Two independent X-ray sources irradiating a pair of detectors are mounted in an orthogonal arrangement. As the sources are independent, their voltage, output power and beam filtration can be freely adjusted and the undesirable spectral overlap is minimized. The high- and low-energy data are acquired simultaneously; however, both datasets are angularly misaligned usually by 90 degrees as shown in figure 12B. Therefore, a time delay occurs between angularly matching projections. Considering the high-speed scanning of clinical CT scanners, this delay is negligible, however, in the case of micro-CT scanners it can result in motion artifacts between HE and LE data.

Dual-layer detector

Dual-layer detector is the only approach performing the HE and LE separation on the detector side. But as the detection technology is still based on EID, a direct spectral discrimination is not possible. The detection unit consists of two detectors tightly connected into a stack. The front layer is supposed to capture the LE data and simultaneously works as beam filter, while the back layer is supposed to measure the HE image. Optionally, an additional beam filter can be put in between both detector layers. The tube is operated on high voltage and the separation between HE and LE data is fully dependent on selection of sensor materials (scintillator material, thickness) and, thus, provides rather lower spectral contrast (see figure 12C).

Photon-counting detectors

Photon counting detectors (PCD) are a novel radiation detection technology allowing energy-discriminative imaging by advanced signal processing at the detector level. PCDs provide data with virtually no overlap of HE and LE and optimize the spectral separation this way. Further, the data acquisition does not need to be limited on two energy channels any more. A single imaging unit (source and detector) can provide several energy channels establishing a new branch of X-ray tomography – spectral CT. The drawback of PCD technology preventing its wide applicability in clinical field is the limited photon income rate which can be handled without pile-up effects and resulting in loss of spectral information reliability. Nevertheless, spectral CT with PCD for clinical use is a subject of intensive research and development [30; 31].

1.9.2 Processing and interpretation of DECT data

Retraction of dual-energy information from both HE and LE data requires dedicated data processing techniques. The techniques can be classified as qualitative (identification of a certain substance) or quantitative (estimation of concentration of a target substance). From the other point of view, the data processing techniques can be differentiated as methods applied to projection data and method applied to reconstructed CT slices.

According to [32] the projection-based techniques offer better accuracy in material identification and also allow reduction of beam hardening artifacts. On the other, hand these techniques require perfectly aligned projections in HE and LE datasets to avoid production of motion artifacts. CT-slice-based techniques perform material identification and quantification based on linear combination of HE and LE slices. CT-slice-based techniques provide approximate results but, on the other hand, identification of wider set of material is possible. As the CT-slice-based techniques are nowadays more widely used, the rest of this chapter is focused on brief introduction of several of them

Material subtraction

Material subtraction techniques are known mostly from DE radiography. The approach based on assumption that certain linear combination of HE and LE data can minimize the HE/LE contrast for a specific material while contrast of other material is gained. This simple approach can be easily used i.e. for getting a CT image of soft tissue with bone-connected signal masked or virtually non-contrasted images can be obtained [33].

Weighted average and virtual mono-energy images

Both approaches aim on certain combination of HE and LE data to create a synthetic image representing a virtual CT measurement with certain X-ray spectrum and make the data interpretation easier this way. The weighted average approach is based on blending of HE and LE data to simulate CT data acquired with certain mean X-ray energy. Virtual mono-energy approach uses more complex algorithms and provides CT images representing the radio-densities of the reconstructed object for discrete photon energies and fluently change the observed energy. Both approaches are, besides other applications, used for simulation of a regular CT scan. It was demonstrated that virtual mono-energy images from DECT provide lower noise level and better artifact suppression compared to a standard CT scan in some studies [34].

2D histogram analysis

The radio-density values from HE and LE channels are plotted into a 2D space where the coordinates are given by radio-density values of each voxel. While water-like substances are found on the diagonal of the radio-density map with different distance from the system origin based on its density. Materials with different spectral behavior occupy lines with different slope [27]. An area of the radio-density map enveloped by these two lines can be linked with a mixture of both materials.

Basis material decomposition

The previously presented approaches provide qualitative information only. As opposed to that, the basis material decomposition is capable of providing quantitative information. After prior calibration on a known reference, the basis material decomposition (BMD) is capable of estimating concentration of basis materials in the object or i.e. evaluate volume fraction of a material in a mixture.

BMD is an algebraic technique based on a solution of a set of linear equations [32]. In the case of DECT it offers identification and quantification of two (under certain assumption of three) constituent materials. The task of CT slices decomposition can be characterized by equation

$$\begin{bmatrix} CT_{HE} \\ CT_{LE} \end{bmatrix} = \begin{bmatrix} \mu_{1HE} & \mu_{2HE} \\ \mu_{1LE} & \mu_{2LE} \end{bmatrix} \cdot \begin{bmatrix} X_1 \\ X_2 \end{bmatrix} \quad (7)$$

where CT_{HE} and CT_{LE} are values of a pixel of HE and LE CT slices, μ_{1HE} , μ_{2HE} , μ_{1LE} and μ_{2LE} are linear attenuation coefficients of basis materials and represent the system sensitivity matrix. X_1 and X_2 represent basis materials at the pixel position. The set of equations for each pixel can be solved by sensitivity matrix inversion as

$$\begin{bmatrix} X_1 \\ X_2 \end{bmatrix} = \begin{bmatrix} \mu_{1HE} & \mu_{2HE} \\ \mu_{1LE} & \mu_{2LE} \end{bmatrix}^{-1} \cdot \begin{bmatrix} CT_{HE} \\ CT_{LE} \end{bmatrix} \quad (8)$$

In the original material decomposition approach proposed by Alvarez and Macovski the sensitivity matrix would be formed of cross-sections of photoelectric effect and Compton scattering for two different energy spectra. The basis vectors were actually given by two independent interaction mechanisms rather than by real material. Such way of BMD is widely used in clinical field nowadays. Nevertheless, the BMD can be basically performed into any pair of materials exerting different behavior at used energies. The values of sensitivity matrix are then formed of linear attenuation coefficients or i.e. radio-densities in HU obtained from previous system calibration or manually from a region of interest. Such way is more common in DE micro-CT scans.

As it was already mentioned, the two-basis-material decomposition can be extended for decomposition into three materials [31]. Characterization of the third basis component, however, requires the third equation in the system. The third equation can be formed from assumption of volume conservation:

$$CT_{HE} = f_1 \cdot \mu_{1HE} + f_2 \cdot \mu_{2HE} + f_3 \cdot \mu_{3HE} \quad (9)$$

$$CT_{LE} = f_1 \cdot \mu_{1LE} + f_2 \cdot \mu_{2LE} + f_3 \cdot \mu_{3LE} \quad (10)$$

$$1 = f_1 + f_2 + f_3 \quad (11)$$

Indexes $f_1 - f_3$ denotes material volume fractions within a voxel. The volume conservation (equation 11) expects that sum of volumes of all three basis materials is equal to the volume of a voxel. This way material decomposition into three materials based on only two spectral

measurements is possible. The basis material maps of three constituent materials $X_1 - X_3$ can be obtained by solving the equation:

$$\begin{bmatrix} X_1 \\ X_2 \\ X_3 \end{bmatrix} = \begin{bmatrix} \mu_{1HE} & \mu_{2HE} & \mu_{3HE} \\ \mu_{1LE} & \mu_{2LE} & \mu_{3LE} \\ 1 & 1 & 1 \end{bmatrix}^{-1} \cdot \begin{bmatrix} CT_{HE} \\ CT_{LE} \\ 1 \end{bmatrix} \quad (12)$$

Generally, the number of variables is given by the number of equations. Spectral CT approach – understood here as an energy sensitive CT with more than two energy channels – can offer identification and quantification of larger set of materials contained in the data and, therefore, provide more information from a single scan.

1.10 X-ray spectral radiography and CT

Spectral CT is understood as an X-ray imaging technique based on data collected with more than two energy channels. Several experimental approaches with triple-energy CT based on DECT conventions (spectral separation given by source parameters and filtration) have been published [35]. However, the current research of spectral CT is focused on use of photon-counting detectors (PCD) almost exclusively. PCD technology has capabilities of resolving energy of incoming particles. Therefore, unlike the DECT where the spectral separation is based on working with the source, spectral CT with PCD technology forms the energy bins by signal processing on the read-out chip. Depending on the chip design, it is possible to acquire data with one or several adjustable energy thresholds or perform fully spectroscopic event-by-event processing. It is, therefore, possible to separate the incident X-ray spectrum into a set of freely defined energy bins based on actual needs of certain measurement (figure 13). Parameters and capabilities of available PCD technologies suitable for high-resolution X-ray imaging are discussed in chapter 2.3. The increase in number of energy bins results in more sampling points of an energy-dependent information contained in the investigated object. The attenuation properties of materials can be more accurately observed and consequently the materials can be more precisely differentiated and more individual components can be identified. Alternatively, Spectral CT can take advantage of absorption edges. The absorption edges – abrupt discontinuities of the linear attenuation coefficient at certain energy – are generally an undesirable phenomenon in DECT material decomposition as DECT BMD assumes fluent monotonic behavior of attenuation coefficient with respect to energy [36]. As opposed to that, the PCD-based spectral CT can directly address absorption edges by selection of appropriate energy bins below and above the edge. Such capability allows clear identification and quantification of a specific contrast agent. Or with more such energy bin pairs it becomes possible to differentiate several contrast agents simultaneously in a single scan.

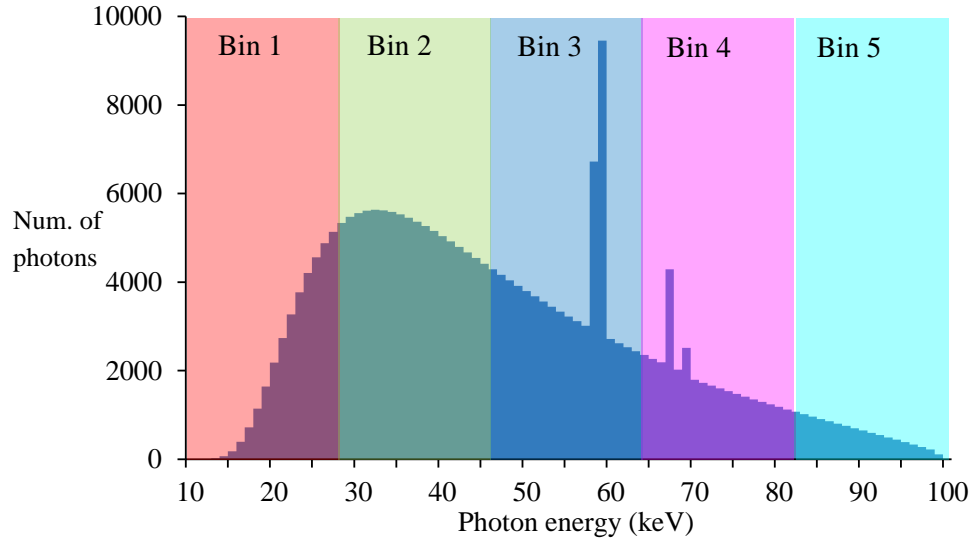


Figure 13: Idea of spectral separation on photon counting-based spectral – a single X-ray spectrum is divided in several adjustable energy bins by dedicated signal processing at the detector level.

The figure 13 shows an ideal case of a spectral CT scan. The X-ray spectrum is divided into a set of sharply separated non-overlapping energy bins. In a real-case scenario the energy resolution of the system is negatively affected by several parameters. PCDs usually provide spectral resolution with standard deviation of several keV. Further, the system energy resolution is limited by charge sharing and pile-up effects. Charge sharing occurs if energy deposited by one photon is divided and read-out simultaneously by two or even more adjacent pixels. This effect results in one high-energy photon interpreted by the detector logic as several low-energy events. Some of PCD technologies try to solve this issue by dedicated signal processing (mentioned in chapter 2.3). The pile-ups, on the other hand, occur when several photons hit a pixel simultaneously or within very short time span. In such case the deposited energy is summed and read-out as a single high-energy event. And finally production of X-ray fluorescence photons in the sensor material can falsely increase the signal for affected energy bin.

Pile-ups are actually the factor currently preventing standard use of PCD in clinical field. While typical PCD detector is capable of handling photon income rate in order of $10^6 - 10^7$ the flux used for clinical imaging is approximately two orders higher [31]. Nevertheless, first prototypes of PCD-based spectral CT scanners applicable for clinical use have been already introduced [37].

Spectral CT has, however, also several negative drawbacks that have to be considered. More energy bins provide more information, on the other hand, it also increases noise level in each energy channel assuming a radiation dose comparable to a standard scan. The probability of a photon beam interactions can be described by Poisson distribution. Standard deviation of Poisson distribution is proportional to a square root of number of events. In the case of X-ray imaging, it basically means that the absolute data variance increases with the number of detected photons but, more importantly, the signal-to-noise ratio raises with the number of detected photons as well.

Assuming an X-ray image formed from 10^4 photons per pixel the signal variance between pixels would be at the level of 1 % based on equation:

$$Variance = \frac{\sqrt{N}}{N} \quad (13)$$

Meaning of N is number of detected photons in the equation. If the whole X-ray spectrum is divided in two same parts, the signal variance increases to 1.4 % approximately. And in the case of five or ten energy bins, the signal variance will be 2.2 and 3.2 %, respectively. Consequently, the signal-to-noise ratio and thus also detail detectability degrades. It is believed that a properly operated PCD can provide 10 – 40 % better contrast compared to an EID [37]. Nevertheless, advanced algorithms for image noise suppression are demanded.

The situation with energy bins selection is moreover complicated by the fact that the energy spectrum generated by an X-ray tube provides non-uniform energy distribution. It can, therefore, easily happen that while low-energy bins are overexposed, the high energy bins suffer from photon starvation. That can be of course overcome by sequential exposures with different acquisition time. However, such solution is very dose-inefficient. To mitigate the non-uniformity of the photon energies distribution, dedicated beam-shaping filters are a subject of research and development [37].

Proper selection of energy bins number, their width and position is a crucial factor significantly affecting the result of the spectral CT scan. Number of studies, both experimental and simulation-based, focusing on optimization of this task has been published [38; 39].

Despite the mentioned issues the spectral CT approach has already proven its viability and is widely considered as very promising imaging modality and huge effort is put in further research of detector technology and data processing techniques. Clinical field requires detectors with high detection efficiency up to 150 keV and improvement of the read-out speed. Therefore, detectors with CdTe or CdZnTe sensors with thickness 1.6 – 3 mm and with pixel pitch varying from 0.2 to 1 mm are tested [40; 41]. In many times, the detector is arranged into 1D array and the data are acquired in fan beam geometry. Some research teams discuss the possibility to prevent pile-ups by making pixels smaller. With more pixels per unit area, the number of incident photons per pixel decreases. On the other hand, such solution increases the charge-sharing between pixels and also the noise level inevitably raises (based on equation 13).

Several attempts focused on spectral CT for pre-clinical use and small animal imaging have been also made. A spectral micro-CT scanner based on photon counting detector technology Medipix has been developed by University of Canterbury, New Zealand, and is currently commercially available as MARS scanner (Medipix All Resolution System) [42]. Further development of the research team aims to build a larger device capable of scanning human-scale samples. The first experimental results of human wrist and ankle scanned with newly developed spectral CT system have been already demonstrated [43]. A part of results presented in this thesis have been obtained using a custom-modified prototype of the MARS scanner (the parameters of the used device are described in detail in chapter 5). Another PCD based micro-CT scanner was introduced as PIXSCAN [44].

2 Digital X-ray imaging detectors for high-resolution X-ray imaging

The origins of X-ray imaging were connected with fluorescent screens and film emulsions. Nowadays, digital detector technologies are in use almost exclusively. In this chapter detector technologies used for X-ray micro-radiography and micro-CT will be introduced with special emphasis on hybrid-pixel photon-counting detectors Medipix and Timepix which play an important role in the experimental part of this thesis.

A digital X-ray detector is usually a 2D array of pixels recording the intensity of incident radiation beam. The detectors can be categorized either based on detection principle or based on the way of signal processing. Digital detectors need the intensity of incident radiation to be transformed into electrical signal. From this point of view the X-ray imaging detectors utilize either principle of scintillation, when certain materials (i.e. CsI, NaI, or Gd_2O_2S) emit visible light after exposure to ionizing radiation, or direct conversion of ionizing radiation into electric signal (typically using semiconductor sensors). The disadvantage of scintillation sensors lays in the fact that the created light flash spreads in all directions evenly. The flash can be, therefore, detected even with pixels relatively far from the original point of interaction which can decrease the detector spatial resolution (see fig. 14 left). This effect has been partially avoided by development of structured scintillation sensors which limit light diffusion to undesirable directions [45]. Such sensors are, however, typically intended for detection of hard X-ray radiation in industrial applications and are not convenient for high-resolution small-animal imaging. Alternatively, the light diffusion can be suppressed by reducing scintillator thickness. Such solution, however, sacrifices the detection efficiency.

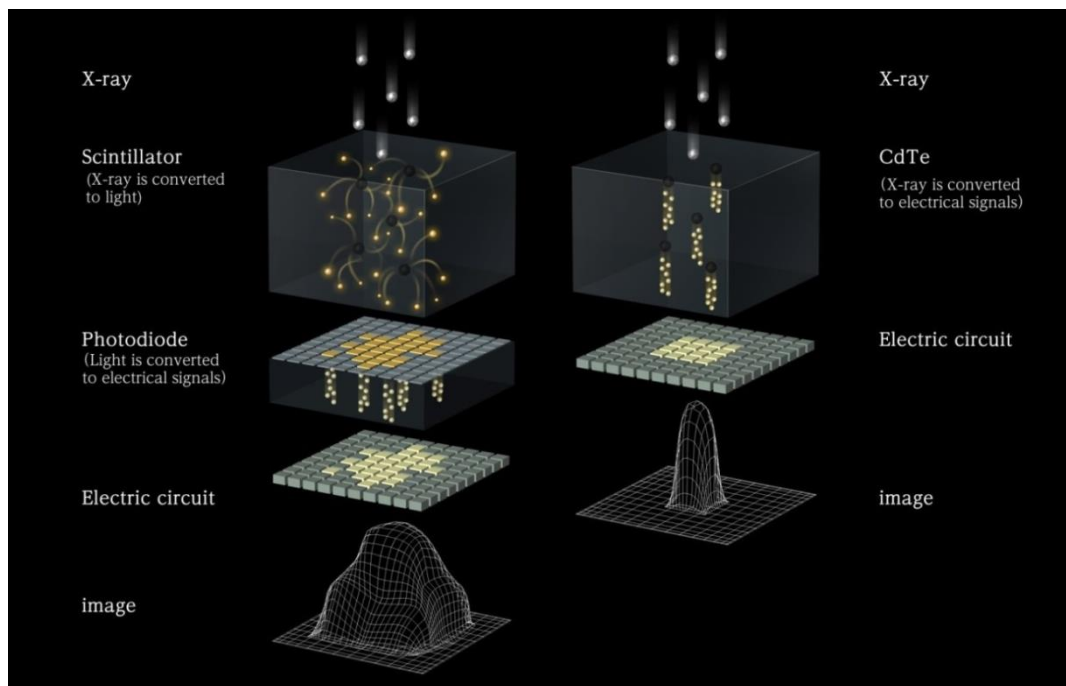


Figure 14: Different principles of conversion of ionizing radiation into electric signal in a scintillator-based detector (left) and in a direct-conversion detector (right) result in different detected signal. The light diffusion in a scintillator caused image blurring while the high bias-voltage in the semiconductor sensor provides very sharp response of the detector. Image modified from [46].

In the case of a direct-conversion detector the semiconductor sensor is operated as a diode biased in closed direction. Once new charge carrier pairs are created in the depleted zone as a consequence of X-ray photon interaction, the electric field in the sensor directs the charge carriers to the closest read-out electrode and minimizes diffusion to undesirable directions (fig. 14 right). Therefore, the direct-conversion detectors are capable of providing sharper response (this fact is demonstrated in chapter 6).

Considering signal processing, a detector can behave either as an energy integrator or as a photon counter. The signal of energy-integrating devices (EID) is created as a sum of deposited energy in each detector pixel. Since a highly energetic photon deposits more energy, its contribution to the detected signal is stronger than contribution of a photon carrying lower energy. An EID is not able to distinguish whether the signal was produced by one or more photons. As a consequence of stronger contribution of high-energy photons to the signal, the EIDs provide decreased contrast considering the fact that linear attenuation coefficient decreases with the photon energy [37]. On the other hand, each detected photon contributes to the overall signal by the same weight regardless to its energy in the case of a photon-counting detector (PCD). PCDs process the signal in a different manner. Thanks to complex electronics integrated in each pixel a PCD processes each detected photon individually. The electronics allows setting a user-adjustable detection threshold which cuts-off the dark current and other sources of noise produced by electronics. PCDs acquire the data with virtually unlimited dynamic range thanks to the dark-current-free quantum-counting operation. Instead of integration of deposited energy, a PCD reports the number of detected photons. Moreover, PCDs are also able to measure the energy deposited by each detected photon besides pure photon counting. Such detector is then capable of measuring not only the overall intensity of the X-ray beam but also resolve its spectral composition. Such capability is a key feature for advanced techniques of energy-sensitive X-ray micro-CT which is one of the key parts of this thesis.

2.1 Energy-integrating detectors

Currently, most of X-ray imaging systems dedicated for high-resolution imaging utilize scintillator-based energy integrating detectors. Depending on the intended application, the scintillator crystals are manufactured from different materials in different thicknesses and are coupled with several types of read-out electronics.

2.1.1 CCD-based detectors

X-ray imaging systems dedicated for imaging of object not larger than several cubic centimeters or when really high resolution is required ($<5\mu\text{m}$) usually combine the scintillator with a CCD-based read-out. The CCD chip is typically connected to the scintillator screen via tapered fiber optics or using a system of mirrors and conventional optical lenses. These detectors usually provide extremely high number of pixels and pixel granularity. The pixel pitch is often smaller than $10\mu\text{m}$. An example of such device is shown in figure 15. To achieve the spatial resolution offered by the CCD chip, it is necessary to use thin scintillator screens to avoid the previously mentioned light diffusion. The scintillator thickness is typically just several tens of micrometers and, therefore, such devices are not very convenient for imaging with hard radiation.



Figure 15: Ximea xiRay16 – a CCD-based X-ray camera for high-resolution X-ray imaging. The detector provides a 22 μm thick Gadox scintillation screen coupled with a 16-megapixel CCD chip (4872×3248 pixels) via fiber optics. The detector provides pixel pitch of 7.4 μm [47].

2.1.2 Flat-panel detectors

The other common X-ray detector type is a flat-panel detector. Flat-panel construction is based on direct connection of the scintillator screen with an array of photodiodes of matching size. Eventually, the direct-conversion sensor is utilized (see both cases in figure 14). Flat-panel detectors usually provide much wider field of view (up to tens of centimeters) and pixel pitch typically in tens or hundreds of micrometers. Read-out speed of the flat-panel detectors is usually very fast since CMOS-based electronics is typically used. Flat-panel detectors are mostly used in industry or medical applications as it provides wide field of view, fast read-out and high quantum efficiency. Nevertheless, small types of flat-panel detectors are also being installed in a range of laboratory micro-CT scanners. An example of a compact flat-panel detector suitable for small animal imaging is shown in figure 16.

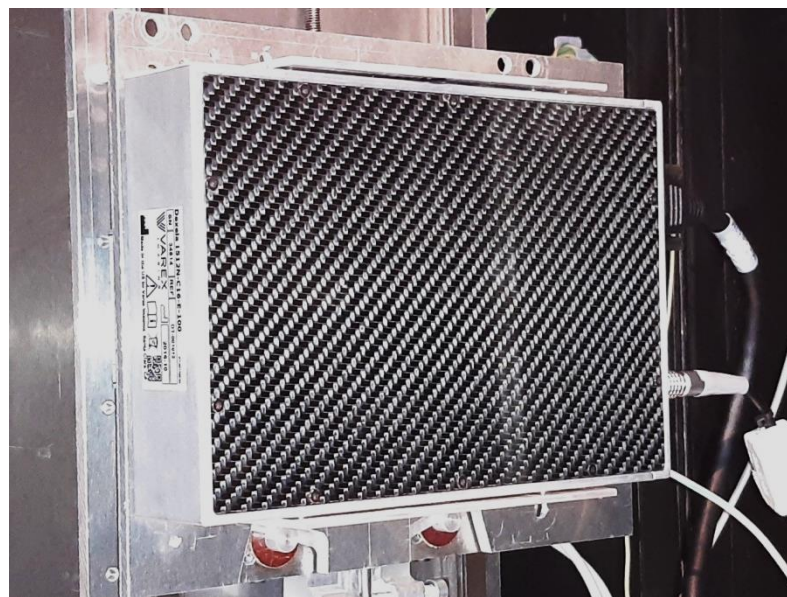


Figure 16: Indirect-conversion flat-panel detector Dexela 1512 installed in the micro-CT laboratory of IEAP. The detector provides field of view of 145×115 mm divided into an array of 1944×1536 pixels with pitch of 75 μm . The scintillator material is 150 μm micro-columnar CsI:Tl [48].

2.2 Photon-counting detectors

PCDs are direct-conversion devices utilizing a semiconductor sensor and a CMOS-based readout with an advanced signal-processing chain integrated in each individual pixel. Each pixel contains pre-amplifier and at least one comparator and counter. The charge deposited by an incident particle is amplified, compared to the user-adjustable threshold and if the threshold value is exceeded, the counter is incremented. As it was already mentioned, thanks to the adjustable threshold value, the intrinsic noise of the ASIC (application-specific circuit) is ignored and the obtained radiographic images do not suffer from dark-current. The availability of one or more custom-adjustable detection thresholds opens new possibilities in form of acquisition X-ray projections in several energy bins. Therefore, the PCDs are a very promising technology for future of advanced techniques of energy-sensitive radiography and CT. Wider use of PCD technology for applied X-ray imaging used to be prevented by small dimensions of the chip and thus the limited FOV. Nevertheless, this limitation has been overcome by several introduced approaches for assembling individual detector modules into larger arrays. This way, PCDs with field of view fully convenient for high-resolution small-animal imaging have become available.

This chapter introduces in detail the technology of photon counting detectors. The PCD anatomy is described and key functionalities are discussed. Eventually, well-established PCD technologies dedicated for high-resolution radiographic imaging are presented.

2.2.1 PCD anatomy

PCDs can be based either on monolithic or hybrid pixel construction. The former integrates the sensor and the read-out logic into a single semiconductor substrate while the latter utilizes separated sensor chip and read-out ASIC connected together via solder micro-balls (bump-bonding). Both detector constructions are shown in figure 17. The monolithic solution can be demanding if i.e. very thin detector unit is required. On the other hand, the monolithic construction has also limitation derived from its nature. Obviously, the only possible sensor material is silicon as the sensor and read-out ASIC are integrated. A representative of monolithic PCDs is the Macropixel detector developed in the MPI Semiconductor laboratory [49].

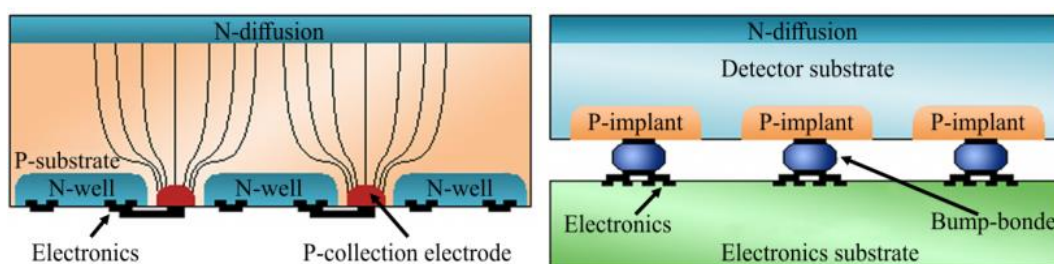


Figure 17: Comparison of construction of a monolithic photon counting detector (left) and a hybrid pixel detector (right). Monolithic construction allows for the construction of extremely thin assemblies; on the other hand, the sensor material is restricted to silicon only. In the case of hybrid pixel construction, a variety of different sensor materials can be used. Image modified from [50].

The hybrid-pixel construction offers more flexibility concerning the used sensor material. Silicon used to be absolutely dominant sensor material for a long time. However, a number of alternative semiconductive or semi-insulating materials have become available (GaAs, CdTe, CdZnTe and other). Properties of individual available sensor materials will be discussed in detail in the following section.

2.2.2 Sensor materials available for hybrid-pixel PCD

The most frequently used sensor material is still silicon. Growing of high-purity silicon crystals and consequent wafer manufacturing is very well managed due to wide application range of silicon as the key building material of electronics components worldwide. Silicon wafers are, therefore, widely and easily available. The disadvantage of silicon as an X-ray sensor material comes from its low atomic number ($Z_{\text{Si}} = 14$). Detection efficiency of silicon sensors in common thicknesses (100 – 1000 μm) is very low above approx. 20 keV (see figure 18). Therefore, silicon sensors are not suitable for imaging of large or dense objects.

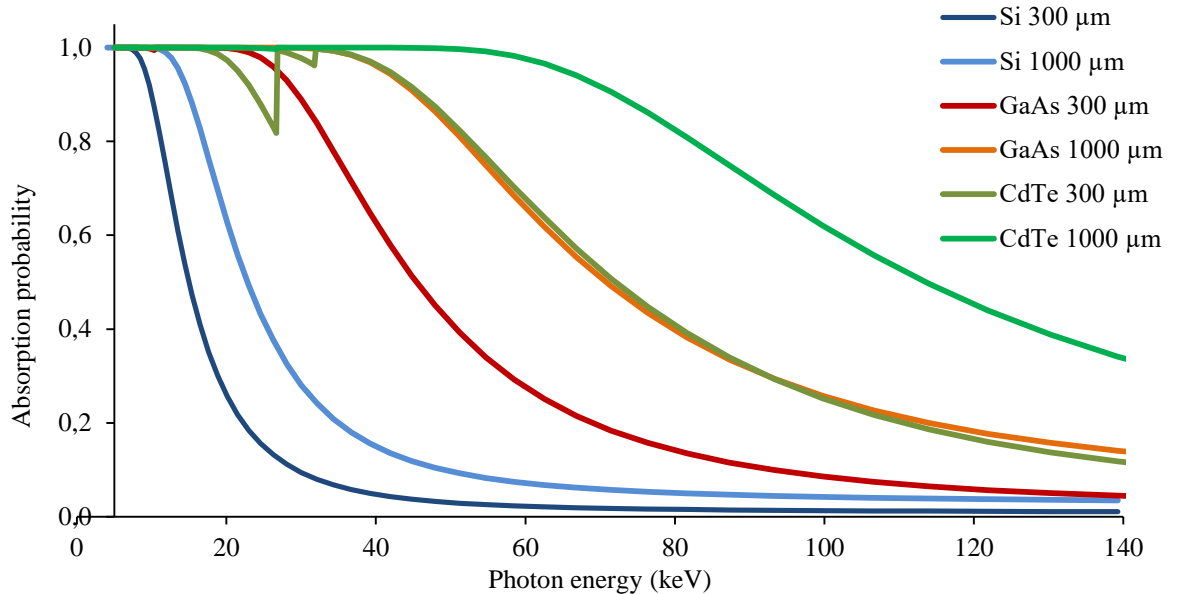


Figure 18: Detection efficiency of various sensor materials available for hybrid-pixel photon counting detectors. The chart was created based on data from National Institute for Standards and Technology [51].

Number of alternative semiconductive or semi-insulating materials addressing this issue is being intensively investigated. Nowadays hybrid PCD with sensors made of GaAs, CdTe or CdZnTe are available. Although the new materials currently cannot compete with silicon by means of response uniformity or temporal and temperature stability, their quality is being constantly improved due to intensive development. The major advantage of newly developed sensor materials compared to silicon is high quantum efficiency due to much higher effective Z of the sensor ($Z_{\text{Zn}}=30$, $Z_{\text{Ga}}=31$, $Z_{\text{As}}=33$, $Z_{\text{Cd}}=48$, $Z_{\text{Te}}=52$). I.e. quantum efficiency of a 1000 μm thick CdTe sensor is approximately 56 % for 100 keV photons as is shown in figure 18 (calculation based on [51]). These sensor materials have opened new application fields for PCDs – mostly in material engineering, industry, but clinical use has been already tested as well [37].

2.3 Hybrid-pixel PCDs convenient for high-resolution X-ray imaging

The hybrid PCD technology has been being developed in a number of independent facilities worldwide. Thus, several well established PCD families are nowadays available. As it was previously mentioned, some manufacturers proposed a solution for assembling large-area devices suitable for imaging applications. This section brings a brief overview on hybrid PCDs suitable for high-resolution X-ray imaging.

2.3.1 Medipix

Medipix is the detector technology used in frame of this thesis. The development has been carried out in the frame of Medipix Collaboration at CERN. Medipix Collaboration is an international partnership associating research facilities including Institute of Experimental and Applied Physics of the Czech Technical University in Prague (IEAP) – at CERN. Medipix technology was introduced in 1997 for the first time. The first generation of Medipix chip consisted of an array of 64×64 pixels with $170 \mu\text{m}$ pixel pitch [52]. Since that time several successive generations have been developed.

The second generation of the chip (Medipix2 and Timepix) consisted of an array of 256×256 pixels with $55 \mu\text{m}$ pitch (overall size of the device was approx. 14 by 14 mm [53; 54]. The later generations have kept the same chip layout. Medipix2 provides a user-adjustable energy threshold and behaves as pure quantum counter. The Timepix can be operated in three different modes:

- **Medipix mode:** particle counting mode; each detected event increases the counter value by one
- **Time-over-threshold mode (ToT):** The counter is used as Wilkinson-type ADC and allows direct measurement of deposited energy; the detector provides fully spectroscopic and position sensitive information
- **Timepix mode:** The counter works as a timer; the detector measures time-of-arrival of incident particles.

The next generation, Medipix3, was designed with two thresholds per pixel and with charge-sharing compensation performed directly on the chip level [55]. Medipix3 can be modified for purpose of spectroscopic imaging. The modification is based on clustering each four pixels into groups called super-pixels. Each super-pixel then offers eight adjustable thresholds, thus, up to eight images created from different X-ray spectra can be obtained at once with spatial resolution of 110 micrometers. The response of the device is, therefore, not truly spectroscopic. Nevertheless, eight energy bins should be fully satisfying for purposes of energy-sensitive X-ray imaging.

The latest generation, Timepix3, provides, similarly as Timepix a fully spectroscopic response. It is able to measure time of arrival, position of an event and deposited energy simultaneously. It was demonstrated that the time-stamp is accurate enough that it is possible to perform 3D reconstruction of a particle passing through the sensor [56]. Furthermore, Timepix3 is operated in a data-driven mode that provides zero dead-time. Properties of Timepix3 detectors – 100% duty cycle, simultaneous information on event position, deposited energy and time stamp – can be potentially extremely useful for gated X-ray imaging of dynamic processes.

Ongoing chip development promises to introduce Timepix4 soon. This generation should come with reduced pixel pitch and more pixels on a chip since TSMC 65 nm technology will be used for the first time. The chips should be also four-side buttable thanks so through-silicon via technology. Therefore, assembling of larger detector arrays will become easier.

As the sensor area of a Medipix chip is only 2 cm^2 it is not very suitable for practical imaging applications. Lot of effort has been put into producing larger detectors. Nowadays Medipix-based devices with continuously sensitive exceeding 10 cm are available at the market. The first steps in increasing the sensor size were so-called Quad, Hexa and LAMBDA detectors (see the first row of figure 19). All mentioned solutions utilized a shared sensor bonded 2×2 , 2×3 or 2×6 chips respectively [57; 58]. The maximal size of such solution is limited by dimensions and mechanical properties of a semiconductor wafer. The only way in production of larger detectors is assembling individual modules into arrays. The first detector of such kind was introduced in frame of RELAXd

project by Nikhef and PANalytical [59]. The detector was modular and consisted of several Quad assemblies aligned into a row. Similarly a row of Hexa modules can be assembled. However, both approaches leave insensitive gaps between individual modules. This undesirable effect was addressed by Canas et al who assembled an array of 11×9 Medipix2 chips [60]. The chips were positioned sparsely with gaps proportional to the chip size. The field of view was huge (24 by 30 cm – a standard in mammography) but each image had to be stitched from four sub-acquisitions taken with different detector positions.



Figure 19: Examples of different types of hybrid pixel photon counting detectors available for high resolution imaging. From top to bottom: Timepix, PILATUS, PiXirad and XPAD . The image taken from an own publication [61].

An important step forward came after introduction of so-called edgeless sensors. Previously a chip was surrounded by a 500 μm wide insensitive guard-ring. Avoiding a guard-ring around a chip allowed tight assembling of individual detector units from three sides (three-sides buttability).

The fourth side is occupied with chip peripheries. The three-sides buttability has been utilized by WidePIX technology developed at IEAP [62]. WidePIX technology builds rows of precisely aligned chips which are then assembled into 2D arrays. Adjacent rows are slightly tilted so sensors of the first row cover peripheries of the second row etc. This way a 2D PCD array with virtually no insensitive gaps is built. The largest detector created this way is WidePIX_{10×10} which is built from 100 individual Timepix assemblies and provides continuous sensitive area of approx. 14 × 14 cm (2560 × 2560 pixels). The WidePIX_{10×10} is shown in the first row of figure 19.

2.3.2 PILATUS, EIGER

PILATUS and EIGER are detector technologies developed at Paul Scherrer Institute, Switzerland, by PSI-SLS group and are currently commercially available [63; 64]. Although the intended application field of these PCDs was at synchrotron facilities, a series of detectors using this technology has been designed for laboratory and industry applications as well. The second row of figure 19 shows the PILATUS detector intended for laboratory use. PILATUS, the older generation, provides pixel pitch of 172 μm the EIGER features 75 μm pixels. An EIGER chip consists of an array of 256 by 256 pixels. A detector module then consists of 8 chips bump-bonded to a common sensor (2 × 4 chips, area approx. 40 × 80 mm). These modules can be used for X-ray imaging due to use of common sensor. Unfortunately, larger EIGER-based detector arrays have significant gaps between individual modules (approximately 6% dead space).

2.3.3 PiXirad

PiXirad is a hybrid PCD technology developed by Pixirad Imaging Counters s.r.l. It offers a unique arrangement of pixels at the chip. The pixels are not square but they are positioned in a hexagonal arrangement [65]. Due to this fact the detector provides almost isotropic resolution in all directions. A single chip consists of an array of 512 × 476 pixels with 60 μm pixel pitch. Each pixel provides two integrated comparators and counters, therefore, the data can be acquired with two adjustable energy thresholds. Two-side buttability of PiXirad chips allows assembling several devices into a row. PiXirad-8 (see the third row of figure 19) built of eight modules provides sensor area of 250 × 25 mm and the insensitive gap width between adjacent chips is proportional to two pixels.

PIXIE, a successor of PiXirad device, uses a regular squared-pixel arrangement (512 × 402 pixels per chip) with 62 μm pixel size and two energy thresholds per pixel. PIXIE, similarly as Medipix3, proposed a solution for undesirable charge sharing within the sensor [66].

2.3.4 XPAD

XPAD is a result of chip development at European Synchrotron Radiation Facility [67; 68]. The XPAD devices are shown in the last row of figure 19. The latest generation, XPAD3, provides a chip consisting of 120 × 80 pixels with 130 μm pixel pitch [69]. Eight chips can be put together into a detector module and up to eight modules can be then assembled. Insensitive gaps between modules are, unfortunately, inevitable. The largest XPAD3-based detector provides sensitive area of 150 by 150 mm. XPAD technology was originally intended directly at European Synchrotron Radiation Facility for diffraction measurements using synchrotron radiation but it has found applications even in laboratory-scale X-ray imaging systems [18; 44].

2.3.5 UFXC32K

UFXC32K is the latest generation of high-speed photon-counting chips developed by AGH University in Krakow designed for measurement with soft X-rays at synchrotron beam lines. The chip consists of an array of 128×256 pixels with $75 \mu\text{m}$ pixel pitch. Each chip contains two independent discriminators and a pair of 14 bit counters [70]. The counters can be operated either independently and measure data in two different energy windows or a high dynamic range mode can be used. The high dynamic mode links both counters together to provide 28 bit dynamic range.

Further development at AGH University in Krakow aims to build a 4-side buttable chips through-silicon via (TSV). First detector modules assembled from two of two UFXC32K chips with TSV technology have been presented [71; 72]. It can be, therefore, expected that detector arrays will be introduced soon.

3 Applications of micro-CT in biology and pre-clinical research

Micro-CT modality has experienced a huge application boom in recent years. The constant development of compact X-ray sources and detection technology has made laboratory-scale micro-CT systems widely available and field of applications in biology constantly increase. Micro-CT techniques are nowadays used either for *in vivo* study of small animals or for 3D characterization of *ex-vivo* samples. This chapter brings a brief overview of applicability of X-ray micro-CT for biology and pre-clinical research.

3.1 *In vivo* small animal imaging

In vivo small animal imaging is currently a highly demanded investigation tool in pre-clinical research. Small animals, typically, rodents, serve as a model of human organism and allow indirect study of processes occurring in human body. Micro-CT data provide valuable information useful for phenotyping, drug development or understanding of mechanics of a disease. Therefore, the target applications of small animal X-ray imaging significantly overlap the clinical CT applications. The key advantage of *in vivo* imaging is a possibility of longitudinal observations. For instance, a carcinoma development in time can be analyzed in a selected specimen. Spatial resolution of *in vivo* micro CT is, however, limited by absorbed dose restrictions. Radiation doses tolerable for rodents are discussed more in detail in chapter 9.4. Published simulations indicate that a radiation dose of 250 mGy is capable of achieving 1% contrast resolution for 135 μm voxel size in the case of a mouse [73]. A post-mortem or *ex vivo* micro-CT scan (discussed in the following section) routinely achieves two orders higher resolution.

The most common *in vivo* application field is imaging of mineralized structures. Micro-CT can be easily applied for bone parameters analysis – volume and surface, cross section, mineral density, trabecular bone density etc. [74; 75]. Micro-CT techniques have been applied in study of bone healing after surgery or stem cell therapy [76; 77]. It was used for analysis of bone loss after bone marrow transplantation and structural changes caused by osteoarthritis [78; 79].

Micro-CT has proved to be a useful tool for lungs imaging as air-filled lung tissue provide reasonable X-ray contrast compared to surrounding tissue. However, the imaging of lung is complicated by a high respiratory rate. Therefore, *in-vivo* micro-CT of rodent lungs usually requires data acquisition with reliable gating [80 – 82].”

A wide application field has been opened with introduction of contrast agents dedicated for *in vivo* micro-CT of small animals. The contrast agents used for clinical applications are usually not convenient for small animal imaging due to much higher renal clearance of rodents compared to humans. The glomerular filtration of a mouse is so fast, that the whole blood pool is filtered within 5 seconds. Therefore, development of dedicated contrast agents with longer stay in the blood pool was needed [6]. Nowadays several suitable blood-pool contrast agents is available and is extensively used for imaging of vasculature, cardiac imaging or cancer development imaging [83 – 85].

3.2 Ex-vivo imaging

Ex-vivo or even post-mortem imaging allows visualization of a sample with much better detail compared to *in vivo* scan. High contrast-to-noise ratio can be achieved as the radiation dose is no longer an issue. In some cases, a certain structure-of-interest i.e. an inner organ, specific bone etc. can be extracted and scanned with much higher spatial resolution compared to *in vivo* scan.

The spatial resolution of the latest state-of-the-art laboratory micro-CT systems almost challenges the conventional optical microscopy [15]. CT scans with true spatial resolution of 600 nm carried-out using laboratory scale equipment have been already reported [14] and an X-ray tube with focal spot smaller than 300 nm is already available [86]. It can be, therefore, expected that with continuous development of compact X-ray sources and X-ray detection technologies, a near future will enable X-ray nano-CT with true spatial resolution comparable or better than optical microscopy methods.

Currently, the spatial resolution routinely achieved for biology samples is typically several micrometers [87]. Such resolution is approximately an order worse than resolution provided by optical microscopy. However, the huge advantage of micro-CT techniques is its non-destructiveness and isotropic resolution within the whole scanned object.

High-resolution of ex-vivo biology samples, especially soft biology tissue, has become known as virtual histology [88 – 91]. Micro CT allows 3D visualization of soft biologic tissue with isotropic resolution of several micrometers or even with sub-micron precision. The intrinsic contrast of soft tissue is generally very low, but number of staining techniques has been introduced. The contrast stains for ex-vivo use is typically a solution with content of a high-Z element. The contrast stains, due to content of high-Z elements, increase the radio-density of soft tissue and consequently improve detail detectability and inner structures differentiation. In case of virtual histology the sample is usually dropped into liquid solution of contrast agent for a certain time. The contrast agent gets inside the sample by simple diffusion along a concentration gradient. The most widely used stains are based on atomic iodine and potassium iodine (I_2KI) dissolved in water or ethanol, phosphotungstic acid (PTA; $H_3PW_{12}O_{40}$), phosphomolybdic acid ($H_3PMo_{12}O_{40}$) or osmium tetroxide (OsO_4) [8; 87]. Figure 20 shows an example of results of virtual histology achievable by means of X-ray micro-CT. The figure demonstrates a comparison of results of an iodine-stained mouse testicle achieved by means of X-ray micro CT (figure 20 A and B) compared to conventional histology processing (figure 20 C).

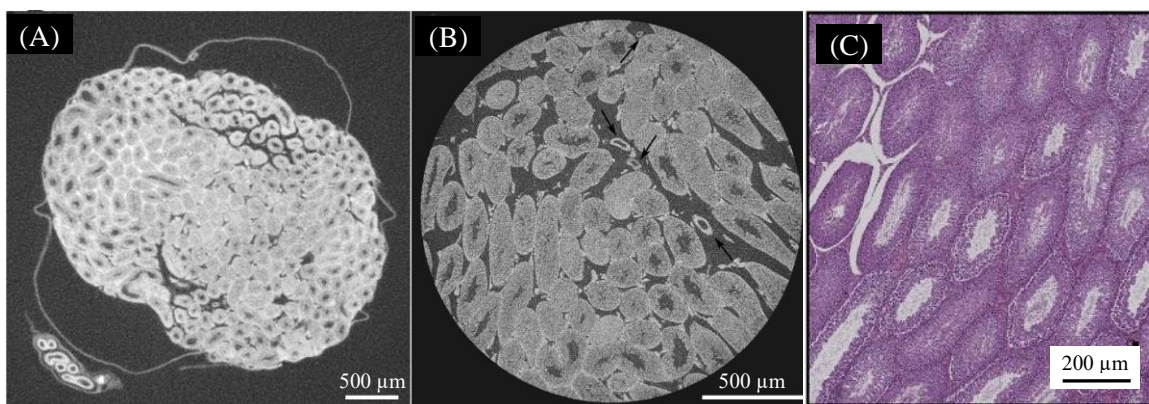


Figure 20: Comparison of a micro-CT virtual histology of an iodine-stained mouse testicle (A, B) and a result of conventional histology processing (C). (A) shows a micro-CT slice of the whole sample scanned with EPS of 7.6 μm while (B) demonstrates a detail detectability in a smaller region of interest scanned with EPS of 1.9 μm . Image modified from [92].

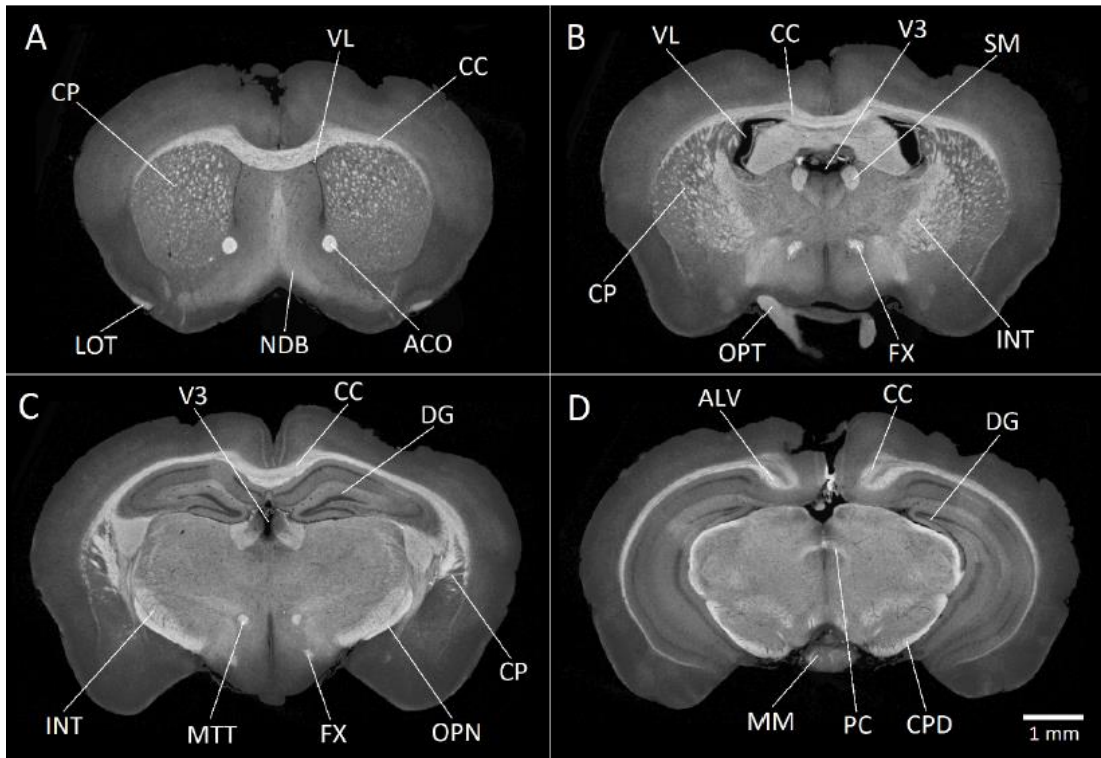


Figure 21: Internal structures of ex-vivo contrast-stained mouse brain visualized using micro-CT. Voxel size of 6.5 μm . Image modified from [93]. An interpretation of visualized anatomical structures denoted by white arrows can be found in the original publication.

X-ray micro-CT of contrast stained soft tissue has provided valuable results in imaging of i.e. muscle or neural tissue but also in high-resolution visualization of whole inner organs like brain, heart, kidneys etc. [92 – 97]. Figure 21 demonstrates interesting results of micro-CT scan of a contrast-stained mouse brain (EPS of 6.5 μm). The interpretation of all successfully resolved anatomic structures denoted by white arrows can be found in the original publication [93].

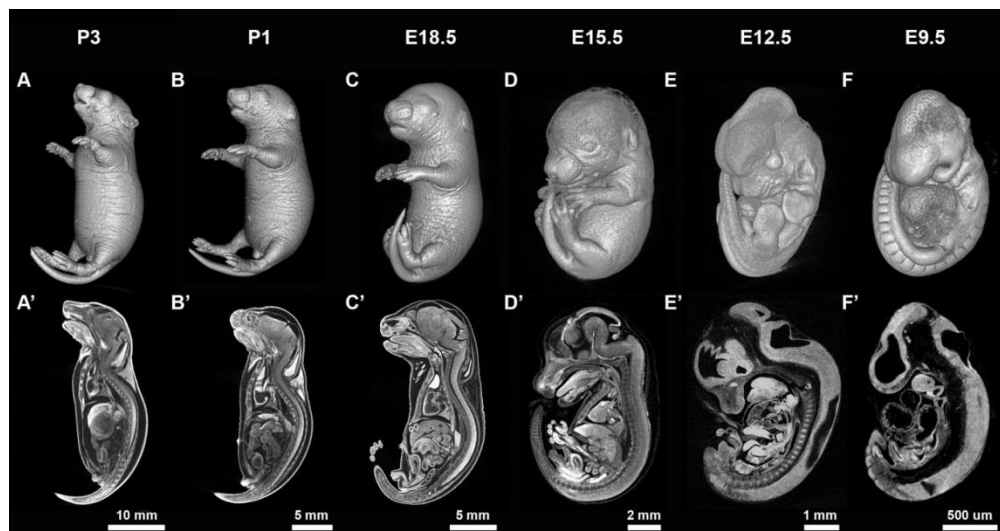


Figure 22: Mouse embryo development from early post-natal to early post-implant stage (from A to F) visualized using micro-CT. samples were contrast-stained by iodine. Voxel size of the data was within range from 3 to 11 μm in dependence on sample size. The first row shows a surface rendering of samples while the second row demonstrates a sagittal slice revealing development of inner organs. Image modified from [98].

Further, micro-CT found a wide application field in developmental biology [87; 89; 98; 99]. It has been reported as a valuable tool for nondestructive phenotyping and evaluation of development models. Figure shows development of a mouse from early embryonic to post-natal state captured using micro-CT. A set of iodine-stained samples was scanned with voxel size within range 3 – 11 μm depending on sample size.

3.3 Energy-sensitive micro-CT

Energy sensitive micro-CT of small animals has been demonstrated both for *in vivo* and *ex vivo* applications. Similarly like in clinical field, the majority of published results is based on dual-energy CT. Experimental use of triple-energy CT has been reported as well, however, this approach has not been widely used [100]. Spectral CT using PCD technology for use in biology and pre-clinical research is a highly demanded imaging modality and, therefore, it is an intensively investigated.

DE and triple-energy micro-CT is usually carried out as a sequence of individual scans in the case of micro-CT. Therefore, it is possible to perform such scan with basically any micro-CT scanner. On the other hand, spectral micro-CT requires dedicated setup equipped with an energy resolving detector. One PCD-based small-animal micro-CT scanner has been already introduced to the market. It was designed and developed by University of Canterbury, New Zealand, and it is available as MARS CT [42]. MARS CT is nowadays equipped with Medipix3 detector technology and is capable of acquiring up to 8 energy bins simultaneously. Another PCD-based micro-CT prototype was introduced as PIXSCAN [44]. PIXSCAN utilizes XPAD3 detector technology and was successfully used for monitoring of lung cancer development in mice.

Imaging of rodent lungs is also one of the most common applications of DE [101]. DE micro-CT was successfully used i.e. for analysis of pulmonary ways obstruction [100; 102], for imaging of for lung cancer in mice [103; 104]. Further, applications for vascular system imaging have been reported [105]. DE micro-CT was also used for atherosclerotic plaque imaging in mice [106] and for number of other applications.

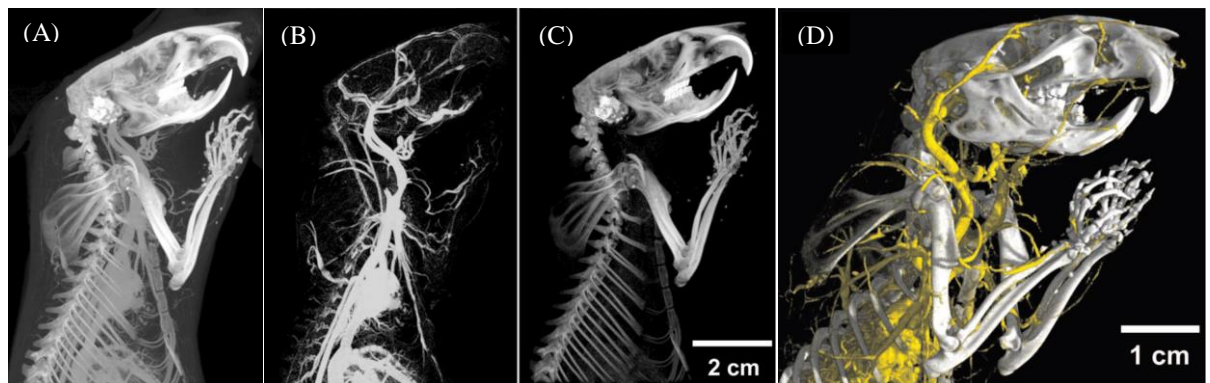


Figure 23: DE micro-CT of a mouse with an intravenous contrast agent Microfil injected. Maximum-intensity projection of the reconstructed volume for LE channel shows that resolving the contrast agent from bone-signal is difficult using a standard CT (A); The signal from Microfil (B) and cortical bone (C) is, however, clearly separated after basis material decomposition; Simultaneous volume rendering of Microfil-only data and bone-only data (D). Image modified from [100].

Impressive results of DE micro-CT applied for imaging of *ex vivo* biology samples have been published by Handschuh et al [107]. The mentioned work extended the conventional virtual histology and tested possibilities of double staining of soft biology tissue – two different contrast stains were

used for one sample simultaneously. Spatial distribution of each of them was then resolved using basis material decomposition (see figure 24).

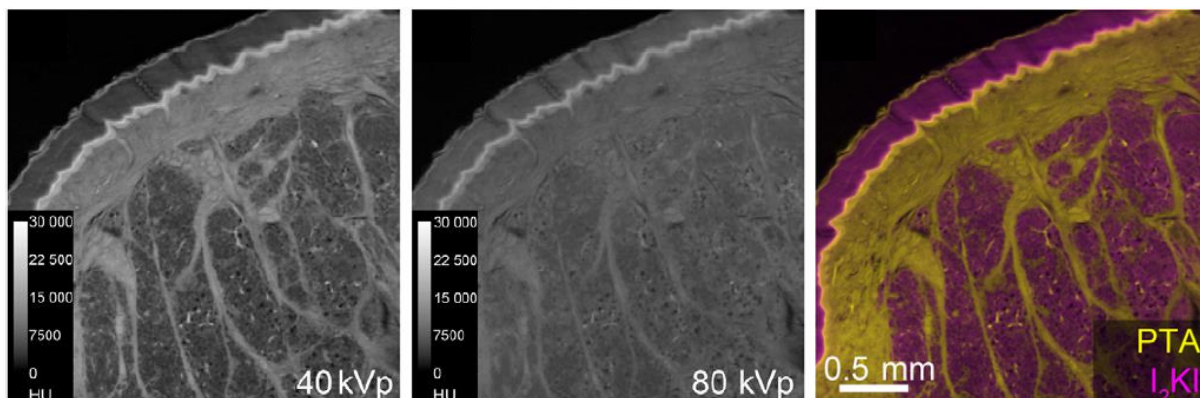


Figure 24: DE micro-CT of skin and subcutaneous fat of a cat digital pad scanned with EPS of 2.88 μm . (A) shows a CT slice resulting from 40 kVp spectrum, (B) shows the same slice scanned with 80 kVp spectrum and (C) shows a color-coded slice created by overlay maps of tungsten and iodine distribution maps obtained from basis material decomposition. Image modified from [107].

Ongoing development of spectral CT techniques, however, already demonstrated that more than two target materials can be addressed in micro-CT [108 – 110]. Figure 25 shows volume rendering of a spectral micro-CT of a post-mortem mouse injected with three different contrast agents. The individual colors denote spatial distribution of five different target materials (denoted in the image).

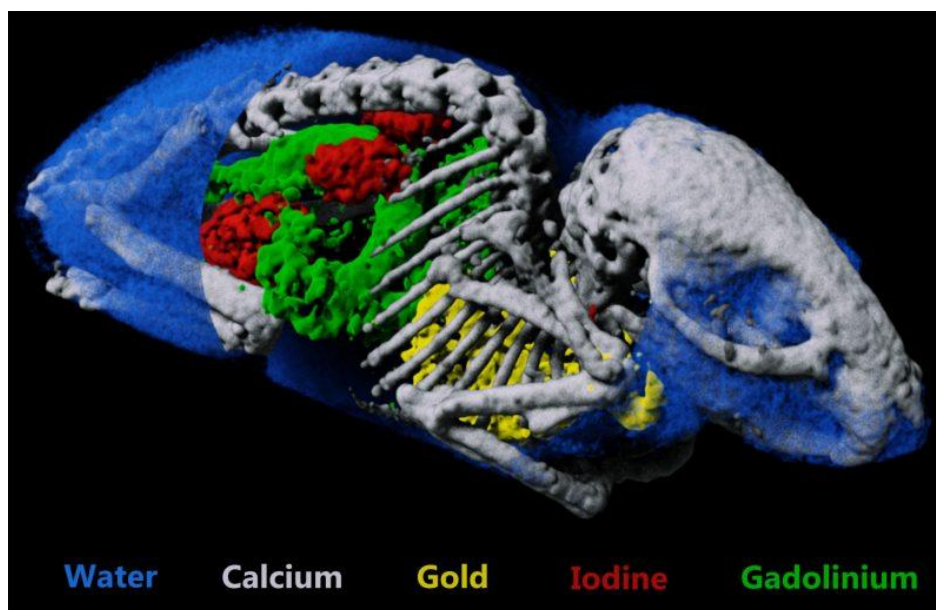


Figure 25: Spectral micro-CT scan of a post-mortem mouse using MARS CT scanner resolved five different materials in a single scan. It can be observed that golden nanoparticles were localized mostly in lungs while iodine could be found in bladder and kidneys and gadolinium was concentrated in stomach and intestines. Image modified from [111].

4 Operation of Timepix detectors

Timepix detectors are provided with a set of dedicated software tools for detector configuration, data acquisition and basic data processing. Depending on the particular detector type and manufacturing date, it can be controlled by Pixelman or Pixet software [112]. Both software packages provide basically the same functionality. This chapter provides a brief introduction to detector configuration, calibration of the spectral response and application of data corrections necessary for X-ray imaging.

4.1 Detector configuration

This section describes detector basic configuration procedures needed for proper function of the device during data acquisition. A proper threshold equalization is an important detector configuration step considering dark-current free quantum counting. Energy calibration of the ToT mode and threshold calibration ensures reliability of spectral information provided by a device.

4.1.1 Threshold equalization

Each Medipix2/Timepix chip consists of 65536 pixels behaving as independent counters. As it was already mentioned, each pixel contains integrated electronic circuits providing an adjustable energy threshold which supposed to be set above the level of dark and leakage currents during the detector operation. The THL level of all pixels within one chip has a Gaussian distribution with typical spread of 450 – 600 e⁻ rms since gain of each preamplifier slightly differs [113]. The aim of THL equalization is to find the noise edge and to make the response of the detector matrix as uniform as possible.

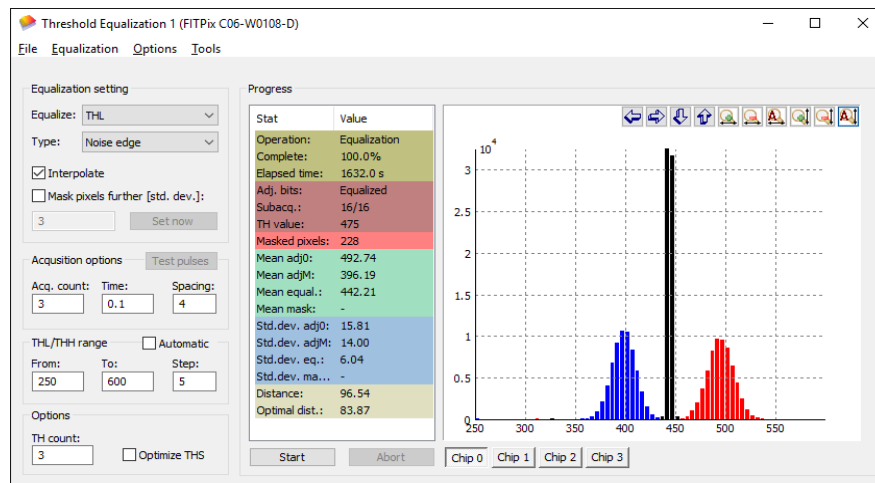


Figure 26: User interface of the Threshold equalization plugin of the Pixelman software package. Red and blue histograms show distribution of threshold values equal to noise level for the lowest and highest value of THL adjustment bits, respectively. The narrow black peak indicates the THL distribution of the equalized detector matrix.

Figure 26 shows the user interface of a dedicated plugin of the Pixelman software. The threshold (THL) value is set globally to the whole chip but each pixel is provided with 4bit THL adjustment. The THL equalization procedure scans a user-specified threshold-range while the adjustment bits are set either at the lowest or the highest value searching for THL value, where a pixel becomes noisy (noise edge), in two subsequent runs create THL distributions for both measurements (blue and red

distributions in fig. 26). The equalized THL value of noise edge for each pixel is determined as the closest THL value to the midpoint between measured distributions.

4.1.2 Energy calibration of Timepix detector

A Timepix device operated in so called time-over-threshold mode provides fully spectroscopic and position sensitive information about the detected events. An interacting particle creates a charge proportional to its energy in the sensor. The amount of deposited charge is measured as a time needed to compensate the produced charge with a constant current. The counter, in this case, works as a reference clock signal.

To provide reliable information on measured charge/deposited energy, it is necessary to perform a dedicated calibration procedure. The function describing the dependence of ToT on deposited energy can be expressed as

$$ToT(E) = a \cdot E + b - \frac{c}{E - t} \quad (14)$$

where a , b , c and t are parameters to be estimated during the calibration and E is the deposited energy per pixel. The functional dependence has a strongly nonlinear characteristics close to the detector threshold and becomes linear for higher energies (see figure 27). The calibration is based on measurement of at least four radiation sources of known discrete energies (radionuclide sources or X-ray fluorescence photons). The typical standard deviation of a Timepix detector spectral resolution after proper calibration is approximately 3 keV at 60 keV [114].

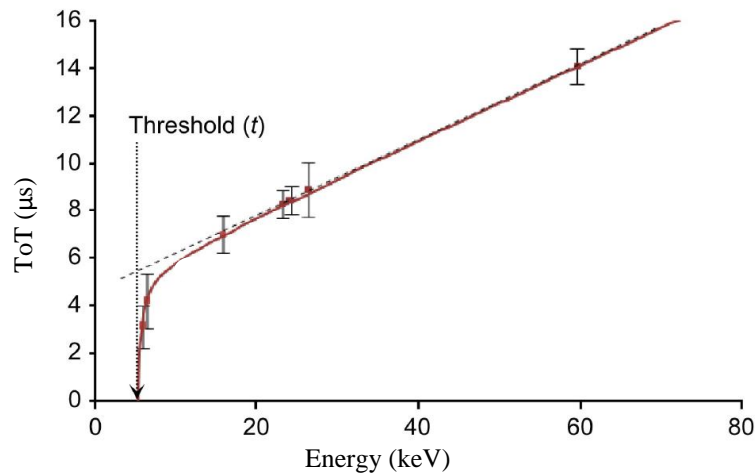


Figure 27: Functional dependence of ToT on deposited energy in a single pixel of Timepix device. The energy resolution has a standard deviation of approximately 2 keV at 60 keV. Image modified from [115].

4.1.3 Detector threshold calibration

Spectroscopic measurements can be carried out even with Timepix device operated in Medipix mode or with Medipix2 device. Utilizing the adjustable threshold, a set of measurements produced

by polychromatic photon spectrum with different minimal energy can be carried out. Subtraction of individual frames provides data originating from different energy bins.

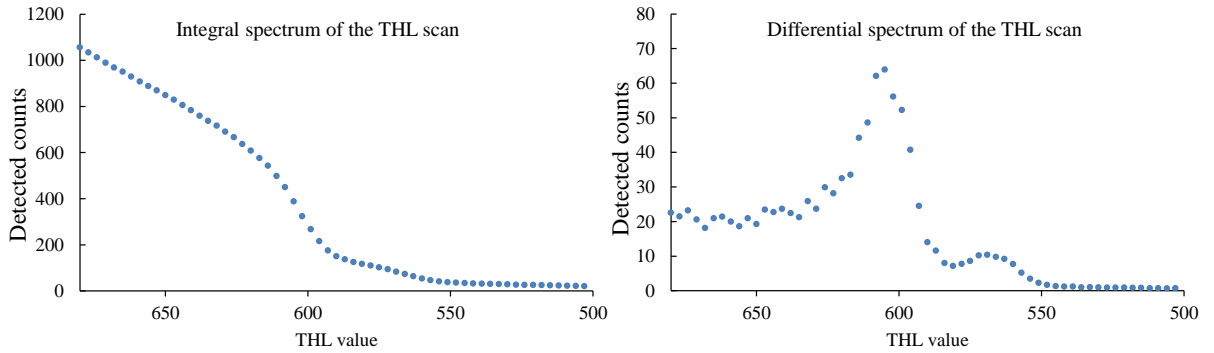


Figure 28: Integral (left) and differential (right) THL scan of X-ray fluorescence signal emitted from Indium foil. Both $k\alpha$ and $k\beta$ lines (24.2 and 27.3 keV, respectively) are visible in the differential spectrum. The curves represent an average response of all pixels in a chip.

Generally, the THL level after threshold equalization of a Medipix2/Timepix device is approximately 3.5 – 4 keV. To shift the THL level by 1 keV, approximately 12 steps of THL DAC are taken. Nevertheless, to be able to set the THL level precisely to specified energy a threshold calibration is needed. Moreover, in the case of large area detectors, the THL energy dependency differs between chips. Therefore, each chip has to be calibrated independently.

Similarly like in the case of ToT calibration, monochromatic X-ray radiation is used. Since the dependency on actual threshold level on THL value is linear, two calibration points are needed. Figure 28 presents a THL scan of X-ray fluorescence photons emitted from an indium foil. The THL scan measured within the range of THL values 680 – 500 with THL step of 3 reveals, after the differentiation, both $k\alpha$ and $k\beta$ lines (24.1 and 27.3 keV, respectively).

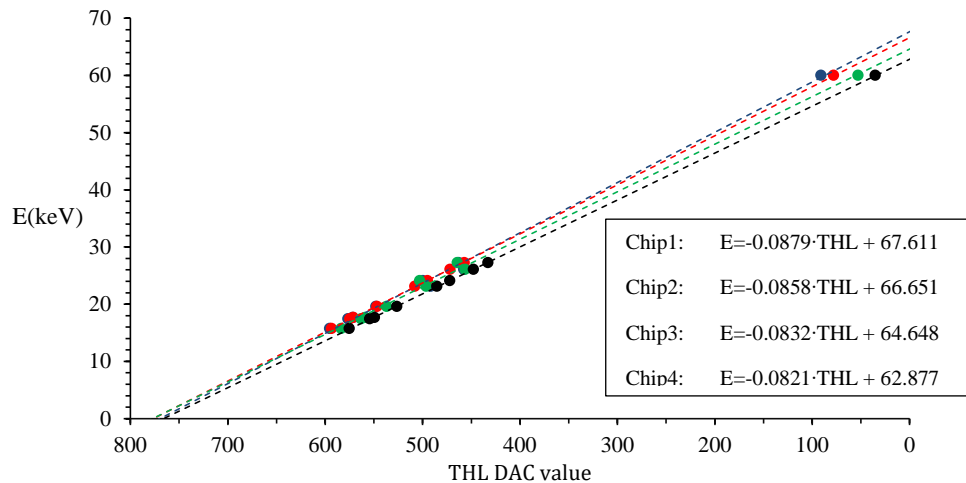


Figure 29: Dependency of detector threshold energy with respect to the DAC value at example of four chips. The chips were calibrated using X-ray fluorescence photons of Zr ($k\alpha$ 15.7 keV, $k\beta$ 17.7 keV), Mo ($k\alpha$ 17.4 keV, $k\beta$ 19.6 keV), Cd ($k\alpha$ 23.1 keV, $k\beta$ 26.1 keV), In ($k\alpha$ 24.1 keV, $k\beta$ 27.3 keV) and 241Am radioisotope source (60 keV). While the THL value is linear with the threshold energy, the slope of the line is slightly different for individual chips.

The exact position of each peak in the differential spectrum is then determined from the mean value of its Gaussian fit. The calibration function for each chip is then obtained as a linear approximation of measured calibration points. Figure 29 shows calibrated THL responses of four Timepix chips based on THL scan of X-ray fluorescence photons of Zr ($k\alpha$ 15.7 keV, $k\beta$ 17.7 keV), Mo ($k\alpha$ 17.4 keV, $k\beta$ 19.6 keV), Cd ($k\alpha$ 23.1 keV, $k\beta$ 26.1 keV), In ($k\alpha$ 24.1 keV, $k\beta$ 27.3 keV) and ^{241}Am radioisotope source (59.5 keV) [116]. Higher number of calibration points was measured in this case to demonstrate the linear behavior of the THL DAC.

4.2 Detector operation

In this section, basic image corrections optionally applicable to the radiographic data are briefly introduced. The first two introduced techniques improve the uniformity of detector response, improve the achievable signal to noise ratio and allow detection of malfunctioning pixels. Both of them are useful for any radiographic detector in general. The third one deals with radiographic image geometry and is dedicated for use with large area photon counting detectors WidePIX.

4.2.1 Flat field correction

Flat field (FF) is a basic correction widely used in radiographic imaging. It suppresses systematic patterns in the radiographic images. Such pattern can have many sources like variations of efficiency of individual pixels, inhomogeneity of the sensor or dust on its surface etc. FF correction is based on normalization of the radiographic image by previously acquired open beam (OB) image [117]. Generally, the FF correction is calculated as

$$FFI = \frac{RI - DI}{OB - DI} \quad (15)$$

where FFI is flat-field-corrected image, RI is a raw image and DI is a dark image. The dark image is acquired while the X-ray source is off to measure any fixed pattern caused by either dark or leakage currents of the detector. Since PCDs do not suffer from these effects, the formula for FF correction of a photon counting detector reduces to:

$$FFI = \frac{RI}{OB} \quad (16)$$

Figure 30 illustrates how the FF correction improves the quality of radiographic data by means of removing fixed patterns and improving the detector response uniformity for certain X-ray spectrum. The presented data were acquired using Timepix Quad detector. The bright central cross in the image is caused by larger effective area of pixels at borders of the chips. It is not fully compensated behind the phantom due to effect of beam hardening which is discussed in the following section.

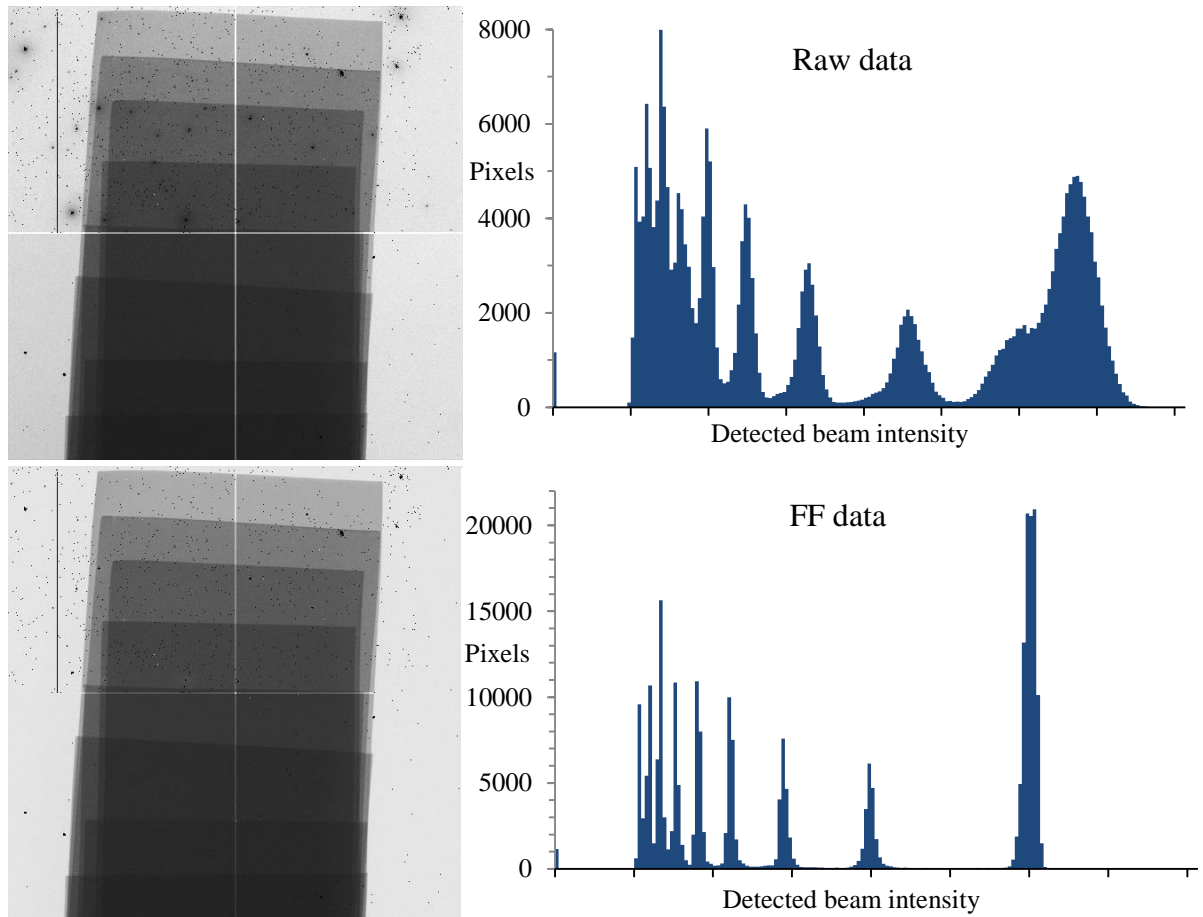


Figure 30: Comparison of a raw X-ray image (upper row) and FF-corrected image (lower row) of a phantom object. The phantom consisted of eight aluminum foils (70 μm in thickness each) arranged into step-like structure. FF correction improves uniformity of the detector response by compensation of slightly different efficiency of individual pixels. The bright central cross of the detector cannot be fully compensated by FF correction as it is caused by beam hardening effect.

4.2.2 Beam hardening correction

Beam hardening is an effect inevitably connected with use of polychromatic X-ray spectra for imaging purposes. The Lambert-Beer law (equation 1) is completely valid for a monochromatic beam only. The attenuation of a polychromatic beam can be approximated as a linear combination of attenuation of its individual spectral components. As the low-energy photons have higher probability of an interaction (energy dependence of mass attenuation coefficient was shown in figure 3) the mean energy of the transmitted X-ray spectrum becomes higher than the mean energy of the incident spectrum – the beam becomes harder [12]. Therefore, depending on sample thickness and variations of its density, each detector pixel is irradiated by a beam with different mean energy. Since detection efficiency of individual pixels is energy-dependent and unique the previously introduced FF correction is not fully sufficient.

IEAP introduced so-called beam hardening correction (BHC) based on empirical evaluation of the detector response to an X-ray beam being attenuated by a set of well-defined absorbers [118; 119]. Typically, the set of absorbers consists of several plastic or metal sheets of different known thicknesses. The dependence of the count rate on the absorber thickness is recorded for each detector

pixel and creates a set of calibration points. The areas between measured calibration points are then interpolated by locally exponential fit function to provide a continuous empirical BHC function for each individual pixel.

The application of the BHC function to the data has several consequences:

- **Signal to equivalent thickness calibration:** The raw data representing recorded beam intensity (open beam is bright, dense or thick sample areas are dark) is transformed into an equivalent thickness of the calibration material (open beam becomes dark as it is equivalent to zero thickness, the object becomes bright) using the inverse of BHC function (see figure 31 left).
- **Data linearization:** The raw data have approximately exponential dependence derived from Lamber-Beer law. The BHC data are linear as the information is coded as a thickness of an absorber. This feature is very useful for CT reconstruction, since linear data are required at its input (see figure 31 right).
- **Detection of faulty pixels:** Since response to the attenuated radiation is analyzed for all pixels individually it is possible to find pixels with unexpected behavior (see figure 32). The information from such pixel can be then avoided and its value interpolated from neighborhood.

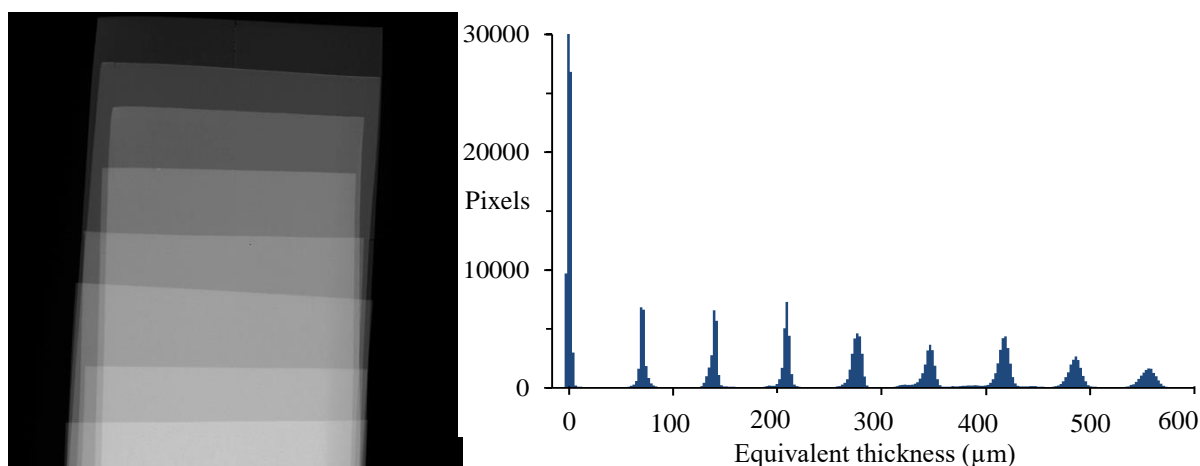


Figure 31: Radiographic image of a phantom object after performing the BH correction. The phantom consisted of eight aluminum foils ($70 \mu\text{m}$ in thickness each) arranged into step-like structure. As the BHC transforms the signal from beam intensity to equivalent thickness, the background of the image becomes dark while the thickest parts of the object are bright. Moreover, the data represented in equivalent thickness of the calibration material are linear.

The described correction can be easily performed using a dedicated plugin of both Pixelman and Pixet software. Figure 32 shows user interface of the BHC plugin in Pixelman (left) and examples of responses of a standard pixel (upper right) and of a faulty pixel (lower right).

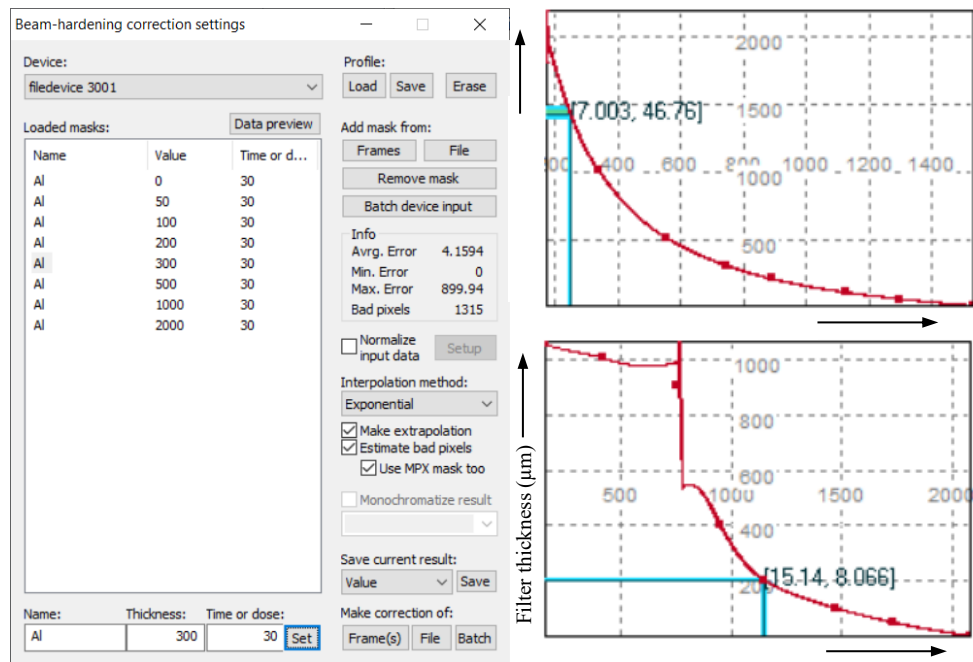


Figure 32: GUI of the BHC plugin in the Pixelman software allows loading of previously acquired set of filters, adjusting their exposition parameters and performing BHC on radiographic data (left). Examples of counts-thickness dependence of a standard pixel (upper right) and a faulty pixel (lower right).

4.2.3 WidePIX detector geometry correction

The WidePIX technology is currently the only technological approach that is able to assemble PCD chips into large arrays with virtually no gaps between individual chip assemblies. Nevertheless, the radiographic data are affected by geometric distortions that have to be compensated. The image distortions (see fig. 33) come partially from chip design and partially from the way how the WidePIX detectors are assembled.

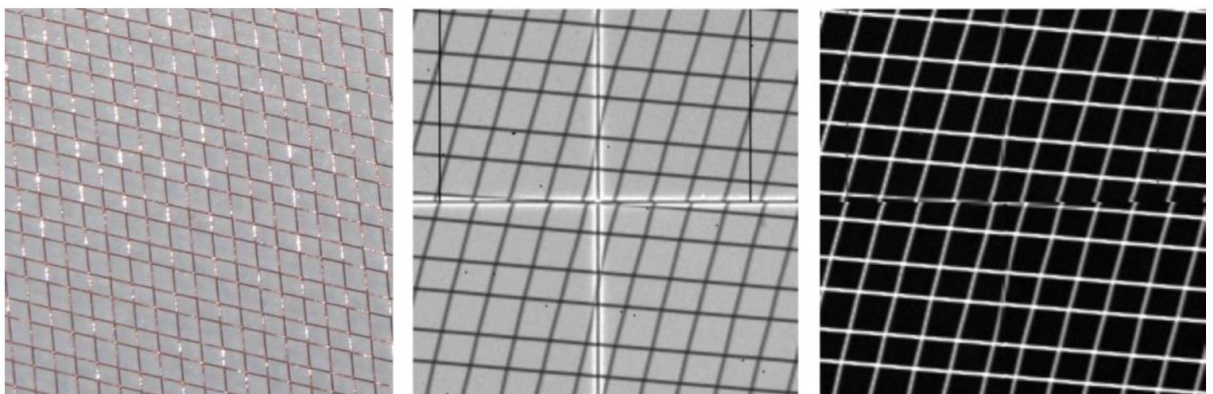


Figure 33: A photography of a copper-wire mesh used for demonstration of WidePIX detectors geometry distortions (left); Raw radiographic image of the mesh acquired on four chips (middle); The same image after applying BHC (right). BHC effectively compensates the brightness offset of edge-pixels. Geometry-distortions caused by WidePIX detector array assembly has to be corrected separately. The image was taken from an own publication [120].

The brightness offset on edges of each chip is caused by the fact that the border pixels are larger than in the rest of the matrix and that the electric field within the sensor is deformed near its edge [121].

The size of border pixels is $140.5 \mu\text{m}$. The different brightness can be corrected either by FF or BHC. However, as the sampling density is different at the chip edge, it induces geometric artifacts to the image matrix (see a schematic drawing shown in figure 34 left and middle). The geometry artifact can be avoided by creating a new pixel grid into which the individual chips are inserted with a three-pixels gap between neighbors. The values missing in the gaps are interpolated from the surrounding pixels (see figure 34 right). The spatial resolution of the images is locally reduced due to interpolation. On the other hand, the proposed approach efficiently suppresses the geometry distortions in the radiographic projections and consequently avoids geometry artifact in the CT reconstructions.

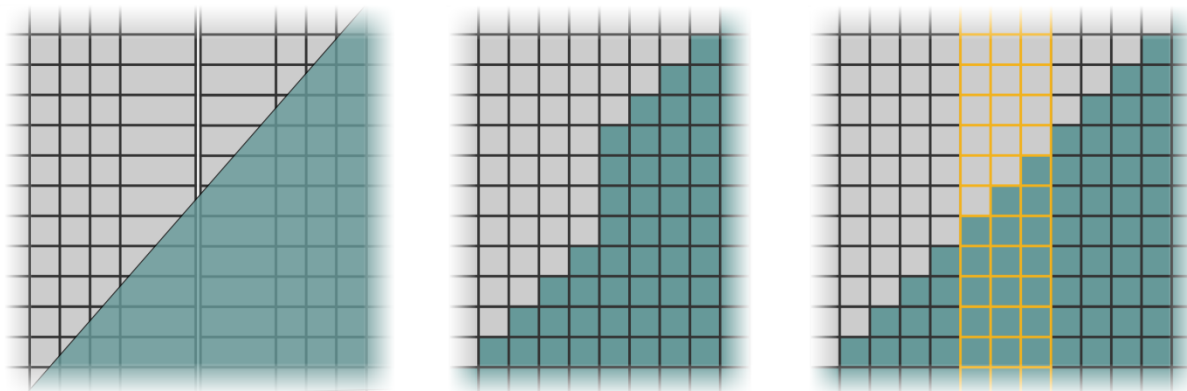


Figure 34: Scheme of a border of two chips irradiated over a slanted edge (left) and its digital image representation showing a distortion as a consequence of larger pitch of edge pixels (middle). The geometry artifact can be compensated by insertion of three virtual pixels (highlighted by orange color) between each two chips and interpolate their values from neighbors (right).

The other source of geometric distortions comes from the way how WidePIX detectors are assembled (see figure 35 A). The chips are tightly assembled into rows. Then the rows are assembled together in such way that sensors of the first row overlap chip peripheries of the second row etc. During the data acquisition in the CB geometry, the detector is positioned in such way that the LAD sensor plane is perpendicular to the beam direction (figure 35 B). That, however, means that the plane of each chip row is slightly tilted with respect to the global plane of the LAD. As a consequence the upper and lower edge of each row has different SDD and thus it captures data with slightly different magnification factor.

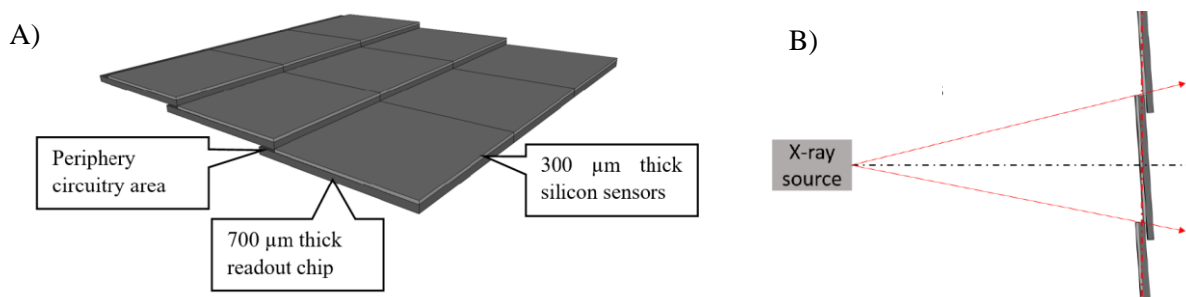


Figure 35: Assembling architecture of WidePIX detector (A). Individual chips are tightly assembled into rows. The rows are then put together in such way that sensors of the first row overlap chip peripheries of the second row etc. During the data acquisition individual chip rows are slightly tilted with respect to the beam direction (B). Therefore, the image magnification factor changes between upper and lower edge each row as a consequence of different SDD. The image was taken from an own publication [120].

The gradually changing magnification factor within a row causes the deformity of X-ray projection into a trapezoidal shape (see the higher row of figure 36). Such image distortion is known as keystone effect. An approach of keystone effect correction based on projective transformation using a Matlab function “imtransform” was successfully tested within this thesis. The results of the correction are shown in the lower row of figure 36.

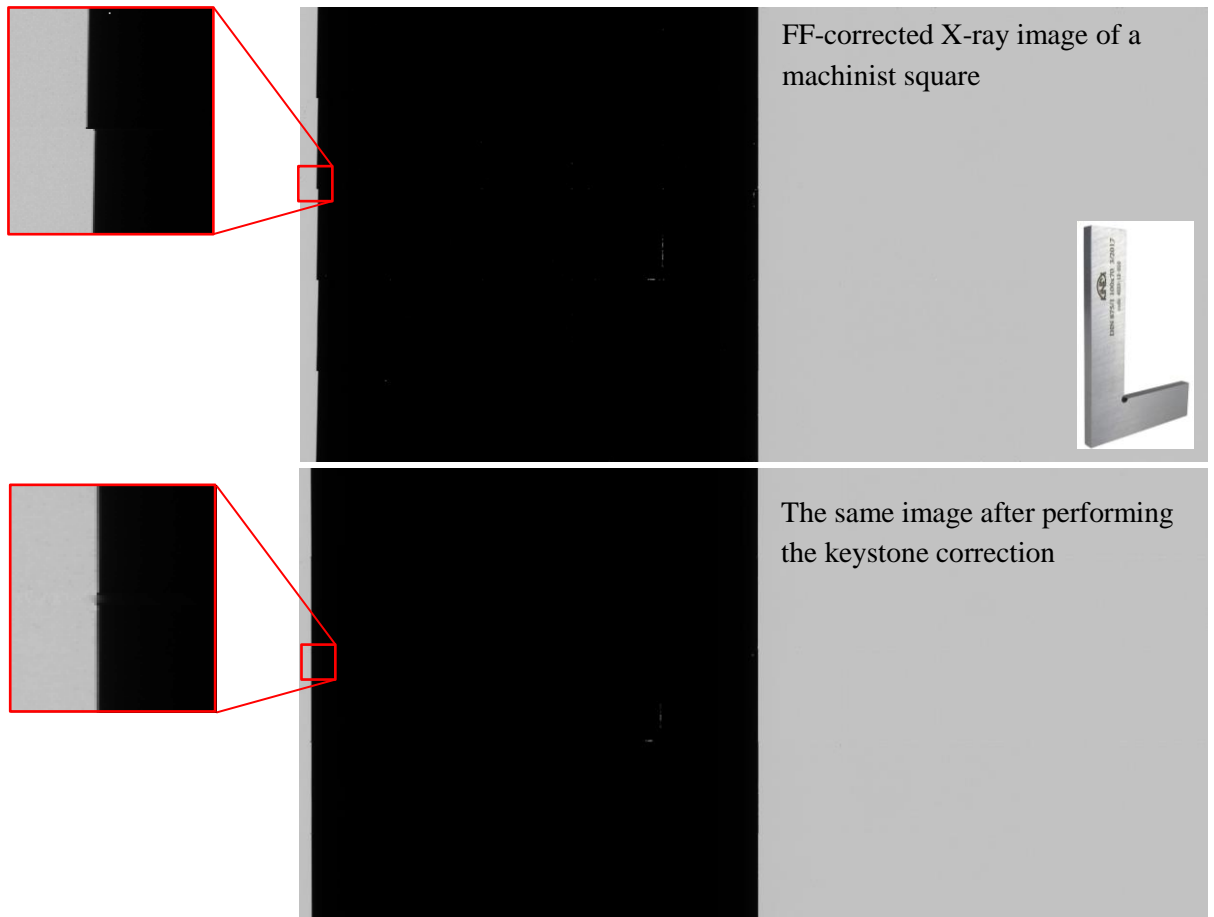


Figure 36: Machinist square acquired with WidePIX_{5×10}. The right edge of the square is aligned with detector center and indicates possible shift between rows. The left edge of the square is used for evaluation of the keystone effect. The first row shows the data after FF correction while the second row shows the same data after the keystone correction was carried out.

The other possible solution is based on complex modelling of the WidePIX sensor geometry and overall CB geometry of the system. Then, the measured data can be re-projected into a new plane and creating a new pixel grid with inverse bilinear interpolation [120]. Interpolation techniques are employed in both mentioned approaches and, therefore, could lead to certain loss of resolution of the data. However, the proper data geometry is of key importance for artifact-free CT reconstruction and other imaging approaches based on ray-tracing.

5 The micro-CT apparatus used in the thesis

The experimental part of the thesis was carried out at micro-CT laboratory of IEAP and at the Joint Laboratory for Experimental Imaging (JLEI) situated at the Third Faculty of Medicine, Charles University (3FM). The JLEI is a conjoint workplace of 3FM, IEAP and Faculty of Biomedical Engineering of the Czech Technical University in Prague (FBME).

The micro-CT laboratory of IEAP offers two custom-built micro-CT scanners. Both of them are table-top devices designed in the manner of industrial scanners – X-ray tube and detector are stable during the scan while the sample rotates on the top of a high precision multi-axial positioning stage. The imaging geometry of both systems is very flexible as even the remaining components (detector and source) can be freely positioned using remote-controlled stepper motors. Therefore, high magnification factors can be achieved thanks to the cone beam geometry. Consequently, very high scan resolution can be achieved.

The first available setup is equipped with X-ray source Hamamatsu L8601-01 (5 μm focal spot, accelerating voltage up to 90 kV, 10 W output power). Figure 37 shows the system with detector WidePIX_{5 \times 10} installed and ready for measurement.

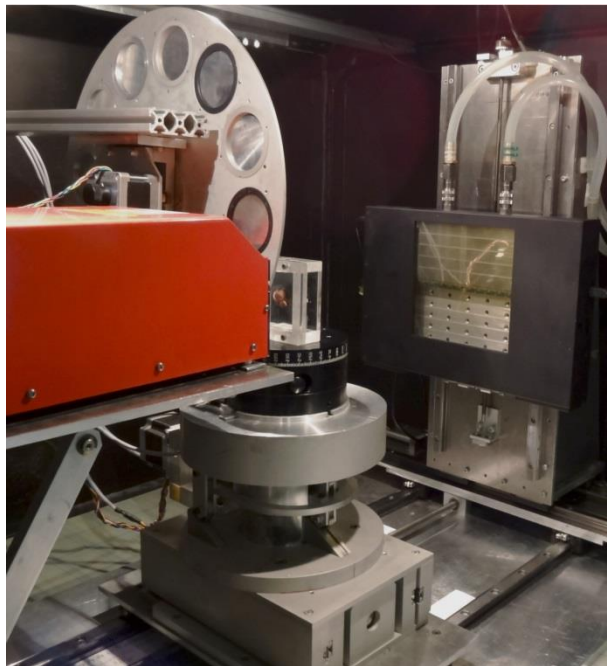


Figure 37: Micro-CT scanner equipped with X-ray tube Hamamatsu L8601-01 (5 μm focal spot) and WidePIX_{5 \times 10}.

The other setup is equipped with a nano-focus X-ray tube FeinFocus FXE-160.51 (figure 38). The maximal acceleration voltage is 160 kV and maximal output power 10W in this case. The positioning system of the setup allows to acquire data with magnification factor higher than 200 (EPS approx. 270 nm). Nevertheless, the maximal true spatial resolution achievable by the system is, due to the tube parameters, approximately one micrometer.



Figure 38: The nano-focus X-ray setup situated at IEAP micro-CT laboratory. Thanks to spacious shielded cabinet and nano-focus X-ray tube FeinFocus FXE-160.51, it is possible to acquire data with extremely high magnification factor (left); a detailed view into the setup with main components depicted (right).

As IEAP is one of research facilities contributing to development of Medipix detector technology, its micro-CT laboratory utilizes a variety of different Medipix-based detectors. The devices most widely used for X-ray imaging are WidePIX_{4×5} (silicon sensor 1024 × 1280 pixels, FOV approx. 5.6 × 7 cm) and WidePIX_{5×10} (silicon sensor, 1280 × 2560 pixels, FOV approx. 7 × 14 cm). Further, WidePIX_{2×5} with CdTe sensor is available. The detectors are installed into the introduced micro-CT systems based on actual need.

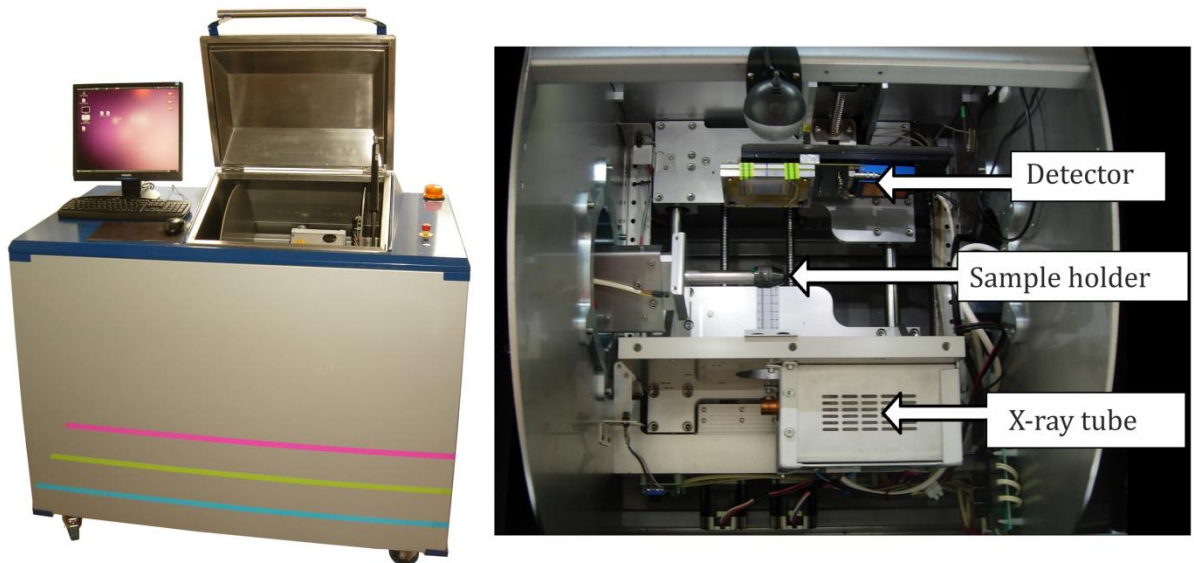


Figure 39: The MARS CT scanner operated at Joint Laboratory of Experimental Imaging (left); detailed view to the scanner gantry showing its arrangement (right). The image was taken from an own publication [122].

The JLEI has been equipped with a modified micro-CT scanner MARS (Medipix All Resolution System) dedicated for small animal imaging (see fig. 39 left). The device was originally designed by University of Canterbury, New Zealand [42], however, after installation in JLEI it underwent several major changes in the construction to improve its imaging performance. These upgrades have been one of the goals of this thesis and are further described in chapter 7. Both X-ray source and detector unit were replaced and a new user interface was developed. Further, a set of accessories and software tools for data acquisition and processing has been developed and successfully tested.

As the discussed micro-CT scanner had been designed for small animal imaging, its construction was derived from clinical CT scanners. It utilizes a rotating gantry holding the X-ray source and the detector while the sample is placed steadily on a horizontal sample bed. The used X-ray tube, KEVEX-PXS11 8012 is characterized with 30 μm focal spot and can be operated with acquisition voltage up to 75 keV and with 11 W output power. The X-ray projections are captured using Timepix Quad detector with silicon sensor (512×512 pixels). The detailed view into the gantry is shown in the right part of figure 39. The gantry allows fluent change of magnification factor and thus to perform scans with EPS within the range of 28 – 44 μm (FOV 14.5 – 22.5 mm).

Recently, the equipment of JLEI was extended by purchasing a commercially available micro-CT scanner. Therefore, nowadays JLEI offers a Timepix-based small animal scanner and Bruker SkyScan 1275 equipped with 100 kVp X-ray tube and 3megapixel indirect CMOS-based flat-panel detector. The newly purchased micro-CT system was used as a reference for evaluation of performance of LAD Timepix detectors. Further, several reference measurements were carried out using Bruker SkyScan 1172 scanner [123]. The access to the device was a courtesy of the National Museum in Prague.

6 Imaging performance of Timepix detectors compared to EID technology

In this chapter, imaging performance of an LAD Timepix device by means of spatial resolution, image noise and connected detail detectability is tested compared to state-of-the art scintillator based EIDs. Although the PCD technology has recently become competitive by means of field of view with conventionally used X-ray imaging detectors, it is still being used mostly in experimental apparatus and it is not easy to reach it.

It was already mentioned that the most widely used detection technology for purposes of micro-radiography and micro-CT are nowadays scintillator-based energy-integrating X-ray detectors. These devices have number of advantages. Especially CCD-based detectors provide huge pixelated arrays (often more than 10 megapixels) with extremely fine pixel granularity. The chip can be also connected to variety of different sensor sizes as the connection is usually performed via tapered fiber optics or conventional objective lenses. Flat-panel detectors are radiation-hard and usually provide very fast read-out. Both technologies are widely available at the market for a reasonable cost.

On the other hand, EID technology suffers from dark and leakage currents and their spatial resolution is limited by the used scintillator. To minimize the integration of the dark current, it is demanded to acquire the x-ray projection as fast as possible. Therefore, high beam intensity is needed. Unfortunately, the micro- and nano-focus X-ray sources provide limited photon flux due to power density restrictions (discussed in chapter 1.8.1). According to [118], EID technology provides better results than PCD if the photon income rate is larger than 10^6 incident photons per pixel per second. The beam intensity delivered by micro-CT systems is generally much lower.

The true spatial resolution of a scintillator-based EID is usually defined more by the sensor thickness than by the pixel size. In many cases the EPS of a radiographic image of micro-CT scan is mistakenly interpreted as the spatial resolution of the scan. However, the true spatial resolution is usually worse due to wide point-spread function of the detector. In the case of a PCD, the PSF is very steep thanks to the bias voltage applied to the sensor. The sharp response of PCD was previously demonstrated in a work comparing contrast and modulation transfer function (MTF) of a Medipix2 chip and an X-ray CCD camera CRYCAM [124]. The study demonstrated that although the pixel pitch of Medipix2 detector is more than 6times larger than in the case of the CRYCAM device (55 vs. 9 μm) the spatial resolution of Medipix2 and CRYCAM at 0.05 MTF is 10.69 lp/mm and 13.44 lp/mm respectively. Furthermore, approaches leading to achieving sub-pixel resolution with Timepix detectors were published [125].

Within the frame of this thesis, the imaging performance of WidePIX devices was compared to a flat-panel detector Dexela1512 (CsI:Tl structured scintillator screen, pixel pitch 74.8 μm , array of 1944×1536 pixels) and micro-CT systems SkyScan 1172 (CCD-based detector; 9 μm pixel pitch, array of 4000×2664 pixels, X-ray tube with $<5 \mu\text{m}$ focal spot) and SkyScan 1275 (flat-panel detector, 75 μm pixel pitch, array of 1944×1536 pixels, X-ray tube with $< 5 \mu\text{m}$ focal spot) [47; 48].

The intrinsic spatial resolution of all available detectors was evaluated using the slanted edge test. Fine steel edge was placed as close to the sensor surface as possible and an X-ray projection was captured. Under such geometry the influence of the source penumbra blur to the result is minimized. Figure 40 shows that while the Timepix device provides almost ideal response to the edge, the data from

the CCD X-ray camera are blurred over approximately eight pixels. The obtained data was evaluated using SE MTF2xNyquist plugin of ImageJ software [126].

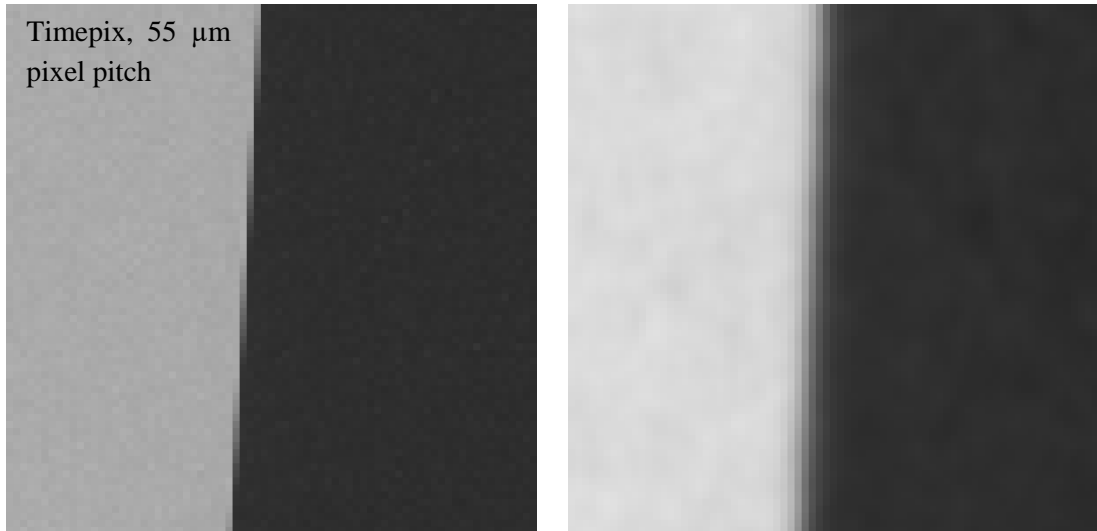


Figure 40: ROI (75×75 pixels) of radiographic image of a sharp steel edge acquired in contact geometry with a Timepix detector with 300 μm silicon sensor (left) and CCD X-ray camera with 9 μm pixels (right). Comparison demonstrates that thanks to the steep PSF, photon counting detectors provide almost ideal edge response. The image was taken from an own publication [127].

The results of the slanted edge test are plotted in figure 41. The figure shows the PSF of the Timepix detector and the CCD X-ray camera operated in three different modes (full resolution and binning of 2 × 2 or 4 × 4 pixels). The left part of the figure 41 demonstrates that Timepix technology provides extremely steep PSF with respect to the pixel dimensions. Plotted in micrometer scale (figure 41 right) the PSF of the Timepix device provide comparable FWHM (full-width at half-maximum) to the CCD detector operated in 2 × 2 binning mode. Evaluation of MTF showed that the spatial resolution at 0.3 MTF level is 8.7, 14.7, 10.9 and 7.6 lp/mm for Timepix, CCD in full resolution, 2 × 2 and 4 × 4 binning. The results indicate that with given imaging geometry, the Timepix detector can provide comparable resolution as a state-of-the art CCD X-ray camera with 2 – 3 times smaller pixels.

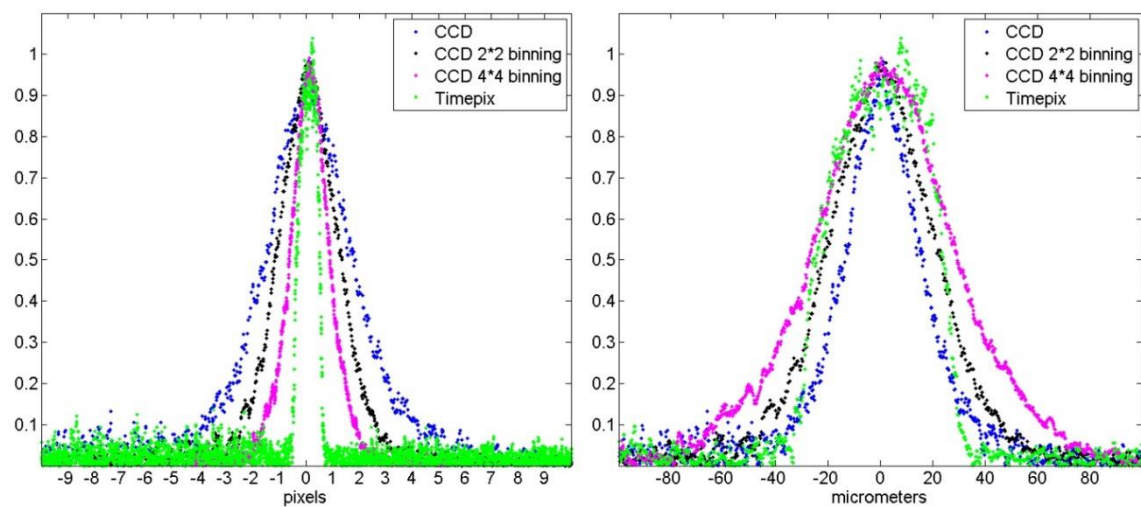


Figure 41: Comparison of PSF between a Timepix detector (55 μm pixel pitch) and a CCD camera (9 μm pixel pitch) with full resolution and two pixel binning modes (2 × 2, 4 × 4 pixels). With respect to pixel size, Timepix detectors provide extremely steep PSF (left). Despite relatively large pixel size (55 μm) of the Timepix detector, its PSF at FWHM is comparable to EIDs with 2 – 3 times smaller pixels (right). The image was taken from an own publication [127].

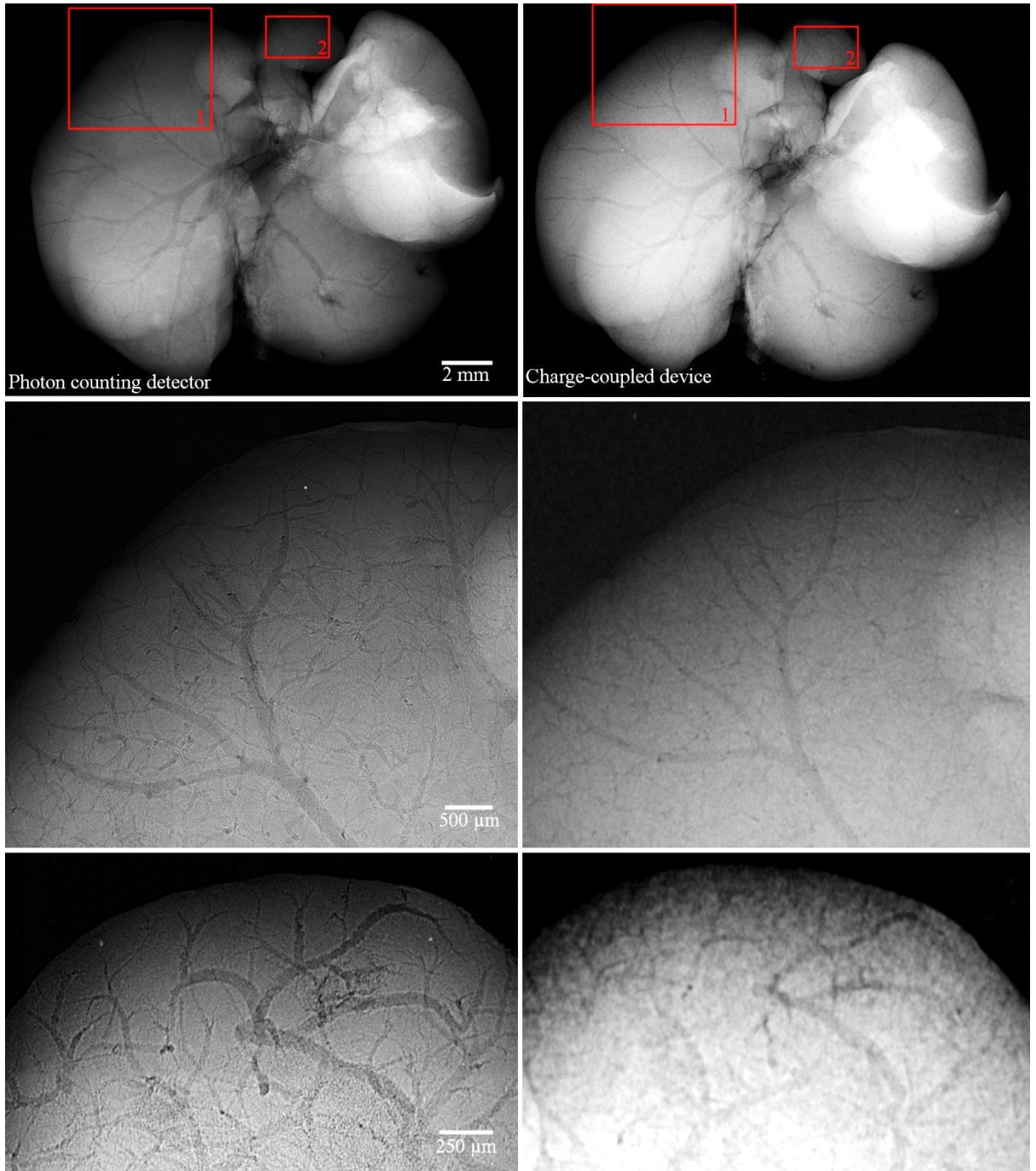


Figure 42: Comparison of X-ray micro-radiography of the ethanol-preserved mouse liver acquired using the Timepix detector (left column) and CCD (right column). The pixel resolution of both setups was set to $4.3\ \mu\text{m}$. Acquisition time of each imaging system was set individually to provide comparable detected intensity of the open beam. While globally both images look very similar when observing a small region of interest (lower rows) the Timepix reveals finer structures thanks to much higher CNR. While the Timepix detector clearly visualizes venules smaller than $15\ \mu\text{m}$, in the case of the CCD detector only structures larger than $60\ \mu\text{m}$ are visible. The image was taken from an own publication [128].

From the other point of view it is possible to say, that with given EPS a Timepix detector will provide data with higher spatial resolution and thus better detail detectability. This capability is demonstrated in figure 42. The figure shows comparison of X-ray micro-radiographic images of ex-vivo murine liver stabilized in ethanol. The sample was scanned twice under comparable conditions at IEAP micro-CT laboratory using detector WidePIX_{10x5} and Hamamatsu L8601-01 and at National Museum

in Prague using SkyScan 1172. The EPS was set to $4.3 \mu\text{m}$ in both cases and the exposure times were individually adjusted to achieve the same signal intensity in the obtained data. While globally both X-ray projections look comparable the selected regions of interest demonstrate that data provided by the Timepix device is sharper and less noisy. Thank to combination of these facts it provides much better detail detectability – clearly visible in the lowest row of figure 42. The finest venules captured using Timepix device have approx. $15 \mu\text{m}$ in diameter while The CCD camera was able to visualize only structures larger than ca. $60 \mu\text{m}$

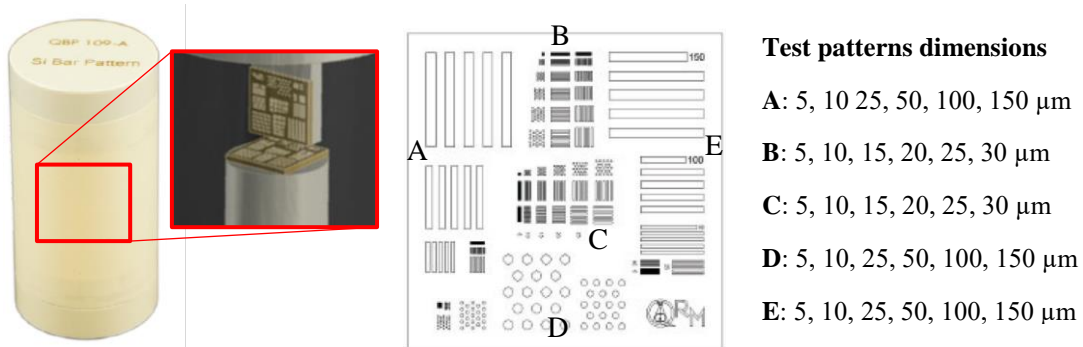


Figure 43: QRM MicroCT Bar Pattern Phantom. The phantom consists of two silicon chips with test structures for evaluation of micro-CT scan resolution. Image modified from [129].

The detail detectability is similarly affected by the PSF of a detector unit even in the case of micro-CT data. The comparison was carried out using a QRM Micro-CT-Bar-Pattern phantom [129]. The phantom (see figure 43) consists of two silicon chips 5 mm in size placed in perpendicular arrangement in a plastic container. Each chip contains a set of test pattern structures 5 – $150 \mu\text{m}$ in size to directly indicate the spatial resolution achieved during micro-CT scan.

The phantom was scanned at IEAP laboratory using WidePIX_{4x5} detector and using the SkyScan 1275 for comparison. Unfortunately, it was not possible to set the same imaging geometry for both scanners. The EPS of the data is 5.7 and $8.5 \mu\text{m}$ for data from WidePIX and SkyScan 1275 respectively. Therefore, it is not possible to compare the data directly. However, it is possible to analyze the data relatively to the EPS. The SkyScan data is obviously smoother (see figure 44) on the other hand, WidePIX data provide higher contrast of imaged structures. The plot in figure 44 shows that while WidePIX detector provide approximately 50 % contrast transfer for $10 \mu\text{m}$ bar pattern (proportional to 1.8 EPS) and 100 % contrast transfer for larger patterns, the SkyScan data provide approx. 16 % contrast for $20 \mu\text{m}$ structures (proportional to 2.4 EPS) and 40 % contrast transfer for $30 \mu\text{m}$ structures (3.5 EPS) only. The comparison indicates that photon counting detectors provide better detectability of small and low-contrast detail in the micro-CT data.

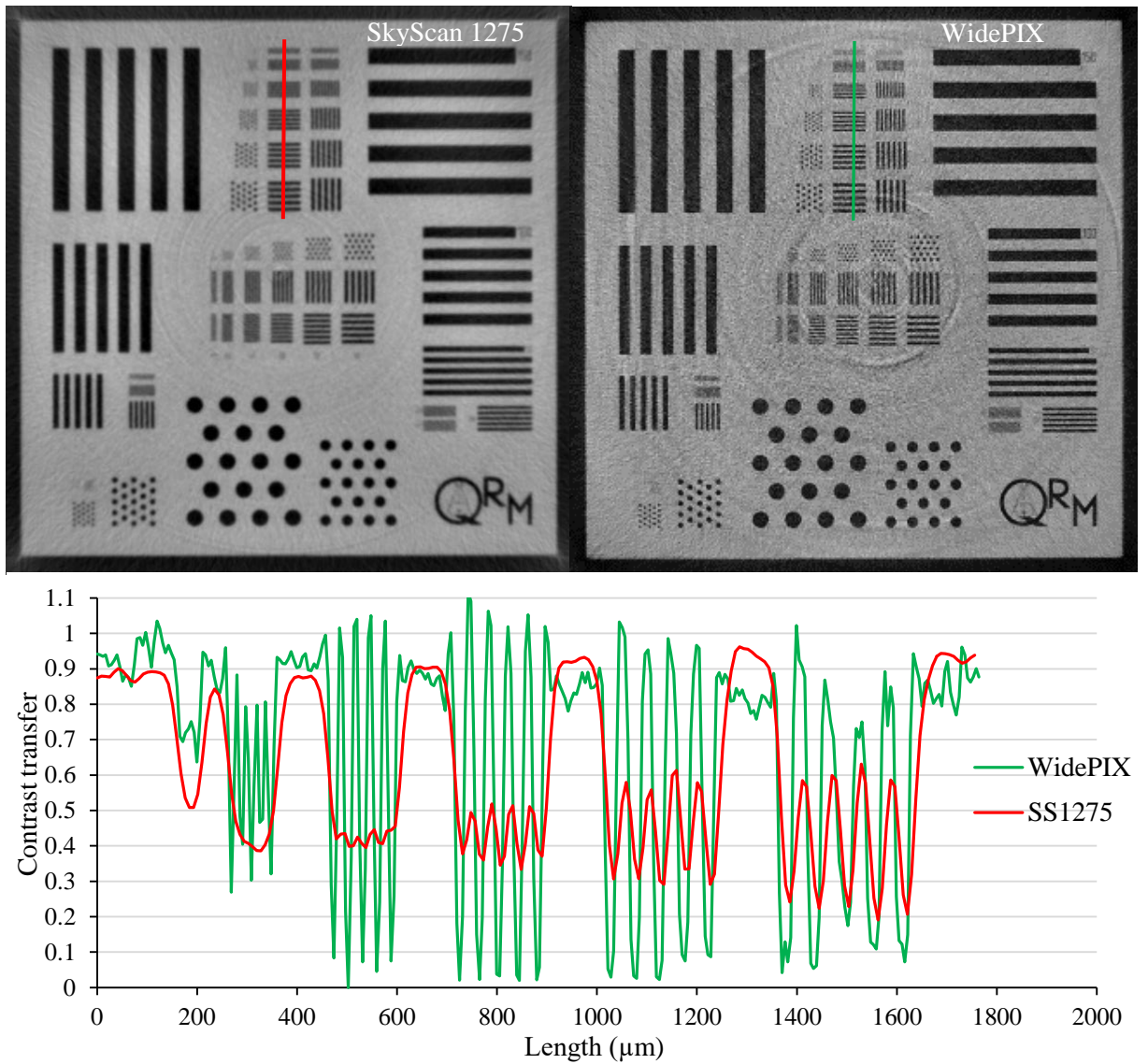


Figure 44: Imaging performance of SkyScan1275 (left, EPS of $8.5 \mu\text{m}$) and WidePIX_{4x5} (right, EPS of $5.7 \mu\text{m}$). The plot below shows the contrast transfer of both datasets on bar patterns of different sizes ($5 - 30 \mu\text{m}$). WidePIX detector provide approximately 50 % contrast transfer for $10 \mu\text{m}$ bar pattern (proportional to 1.8 EPS) and 100 % contrast transfer for larger patterns the SkyScan data provide approx. 16 % contrast for $20 \mu\text{m}$ structures (proportional to 2.4 EPS) and 40 % contrast transfer for $30 \mu\text{m}$ structures (3.5 EPS) only.

7 Upgrades of the MARS micro-CT Scanner

As mentioned earlier in chapter 5, the small animal micro-CT scanner operated at JLEI underwent custom modifications compared to the original design. This chapter introduces a brief description on how the device was constructed, as well as a detailed overview of the hardware and software modifications carried out which contributed to the improvement of imaging performance.

The gantry was designed as a cage made of two steel plates interconnected by four steel rods. Each endplate has a circular opening of 106 mm in diameter with cylindrical flanges mounted to them. The flanges are in a contact with a set of ball bearings which keeps the gantry in place and allow its free rotation during the scan. The gantry is fitted to bearings by its own weight only. Rotation of the gantry is controlled using a rubber timing belt connecting the gantry to a stepper motor. The rotation range is 370 degrees [130]

Both X-ray source and detector mounted to gantry are provided with linear rails allowing adjustment of magnification factor and scanning large samples in several sub-acquisitions with different detector positions. The sample stage provides 200 mm positioning range along the rotation axis of the gantry.

The scanner was originally equipped with a Medipix3 Quad detector and a Source Ray SB-120-350 X-ray tube. It underwent a series of tests after it had been purchased. Unfortunately, the tests yielded unsatisfactory results. The focal spot of the source was considerably larger than the manufacturer declared it to be. Moreover the shape of the spot was highly anisotropic. More importantly, the gantry movement precision was very low. Therefore, the quality of the obtained CT scans was inadequate.

Both aforementioned issues were caused by the x-ray source. The low spatial resolution was consequence of large and elliptical shape of the focal spot. The mass of the installed tube (approx. 12 kg) was a source of gantry movement inaccuracy. The weight localized on one side of the gantry caused its strong imbalance. The angular increment was shorter than a set value if the X-ray tube was moving up and longer if the tube was descending during the rotation. Further the trajectory of the gantry contained lot of undesirable discontinuities and significant discrepancy between the start and end positions of the gantry rotation which should be identical.

Therefore, the X-ray source was replaced by a new one – KEVEX PXS-11 8012 characterized with focal spot of 30 μm and with approximately 4 kg of weight. Simultaneously, the Medipix3 detector was replaced with a Timepix Quad since there was much wider experience with operating Timepix detectors and a set of dedicated software tools available at IEAP.

7.1 Evaluation of the gantry movement precision

Assuming the CB geometry, a set of projections of random point, being rotated around a certain axis, produces an elliptic trajectory on the detector plane (see figure 45). This known fact is a starting point of many CBCT (cone-beam computed tomography) calibration procedures. Deviations of the trajectory from its supposed shape can then be used for evaluation of positioning system precision.

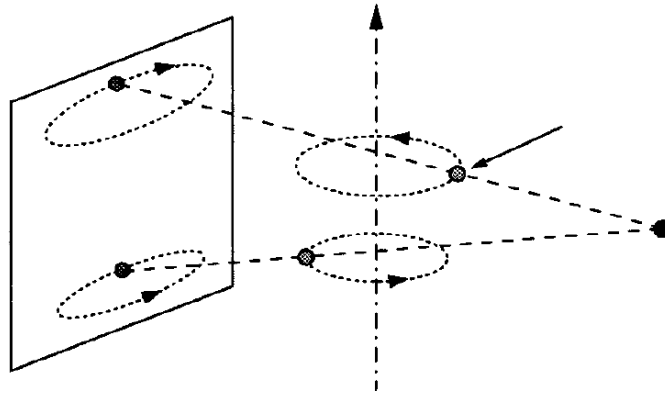


Figure 45: A set of projections of a random point rotating around a certain axis will be projected to an elliptic trajectory in the CB geometry. Such fact can be used for geometry calibration of the imaging system. Image modified from [131].

The accuracy of gantry positioning was evaluated based on data obtained from scanning of a steel ball acquired under a set of angles within the range of 0 – 360 degrees. The projection data were segmented and the ball center of gravity was estimated in each angular position. This way the trajectory of the ball projection with respect to the gantry angle was tracked.

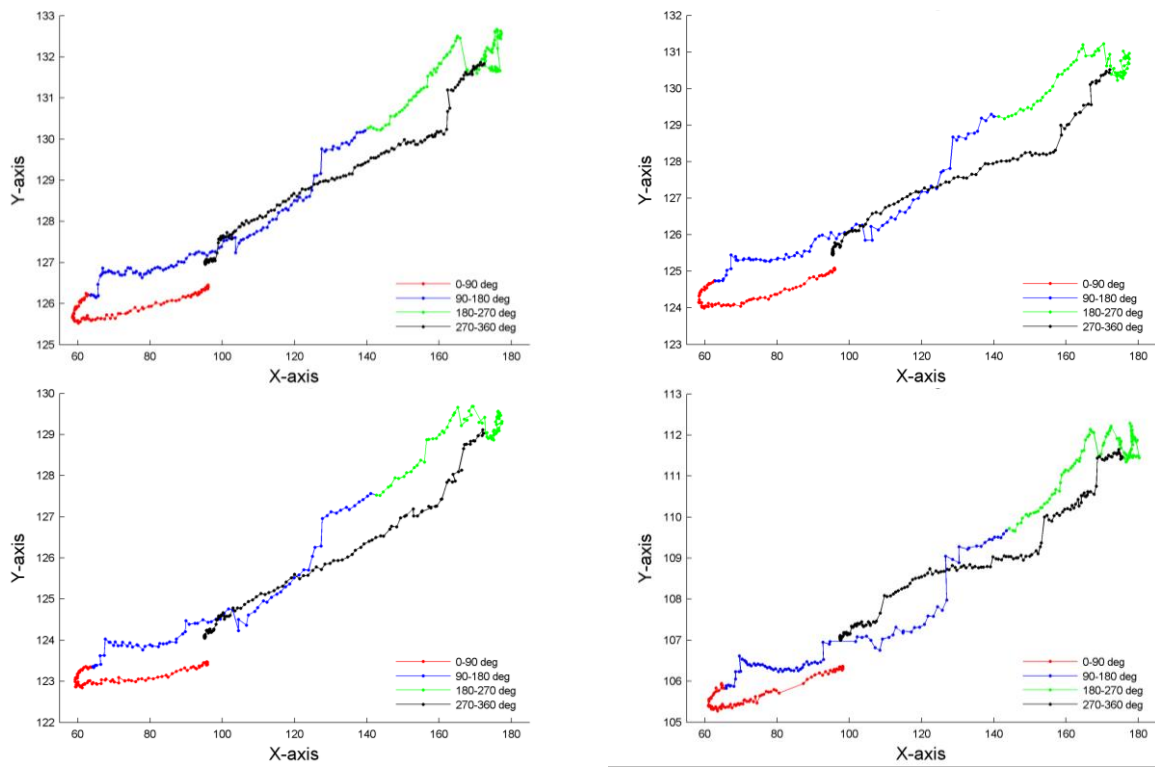


Figure 46: Trajectories of a steel ball tracked over 360 degree rotation range using the original setup. Four runs of total number of 50 are presented. The trajectories are erratic and unpredictable. The start and final points are not matching.

Figures 46 and 47 show the results of the mentioned scans. The Y-axis in the charts is parallel to the rotation axis of the gantry, while the X-axis is perpendicular to it in all charts. Figure 46 demonstrates examples of four individual trajectories selected from total number of fifty performed measurements. Each curve is color-coded to divide the whole scan range into four parts (0 – 90° in red, 90 – 180° in blue, 180 – 270° in green and 270 – 360° in black). The trajectories were erratic with a lot of

unpredictable discontinuities along the angular range. The most problematic regions were correlated with those angular positions where the X-ray source position was close to very top or bottom of its trajectory. Furthermore, the first and last angular positions (0 and 360 degree, respectively) were not matching. The discrepancy between the start and end point of the scan was approximately 1 detector pixel in average.

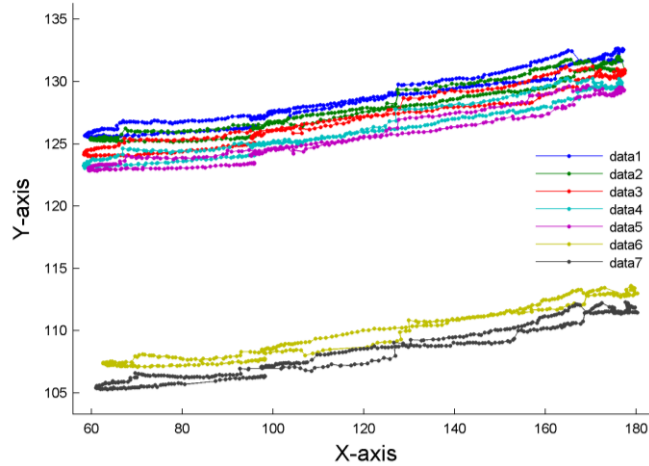


Figure 47: Axial shift of the ball trajectory between individual runs. The projected position of the ball position gradually moves along the rotation axis. Switching the machine off and on again results in a significant skip of the projected position as can be seen between data5 and data6.

Figure 47 demonstrates an axial shift between individual scans that was observed. The sample projection position gradually moved along the rotation axis between consequent scans (fig. 47 data1 – data5) and exerted sudden skips if the system was powered off and initialized again (the skip between data5 and data6). The average displacement of subsequent scans was 0.9 pixels along the rotation axis and 2.55 pixels in the direction perpendicular to rotation axis. After the re-initialization of the system the displacement was more than 15 pixels.

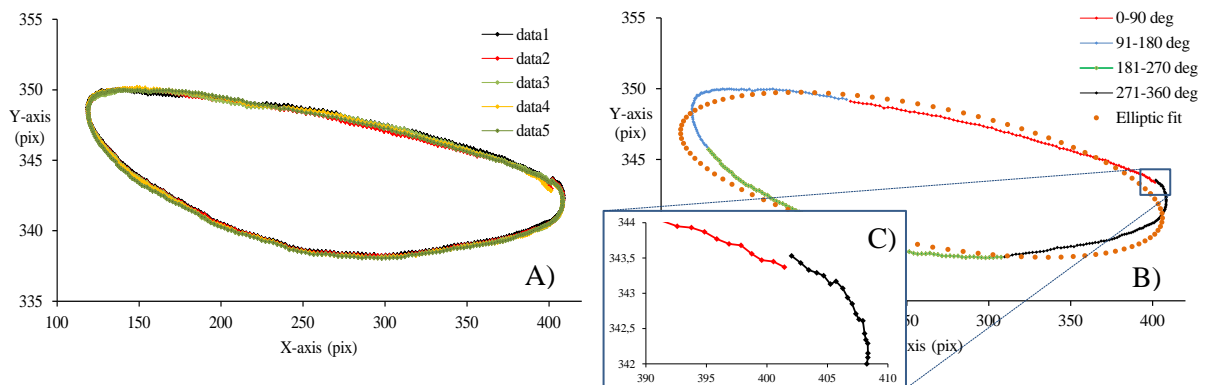


Figure 48: Stability of the gantry rotation after installation of the new X-ray source: A) tracking of a steel ball projection of five subsequent measurements; B) average trajectory calculated from a set of performed measurements and an elliptic fit of the data; C) The average discrepancy between the first and the last projection was reduced to 0.2 pixels.

The situation significantly improved with installation of the new tube (see figure 48). The results of individual measurements are in a good agreement and individual trajectories are overlapping (figure 48A). The axial shift of the gantry between consequent measurements disappeared. Figure 48B

shows an average trajectory of the steel ball projection and an elliptic fit of the measured data. The trajectory still deviates from the ideal path, nevertheless, as it has become more stable and repeatable. Therefore, it is possible to correct the deviation during data pre-processing. The efficiency of the implemented correction is described and demonstrated in chapter 8.2. The discrepancy between the first and the last angular positions of the trajectory was reduced to 0.2 pixels together with considerable suppression of its erraticness (see figure 48C)..

7.2 Improvement of the spatial resolution

The newly installed X-ray tube also increased the achievable spatial resolution, beside improvement of the gantry stability. Figure 49 shows the sharpness of X-ray projections acquired using the original tube (left) and using the newly installed tube Kevex PXS-11 8012 (right). Both projections were acquired with the same magnification factor of 1.96. From the left part of figure 49 it is obvious that the focal spot of the original source was too large for imaging in magnifying geometry and that its dimensions were significantly asymmetric as the blur is different in X and Y directions.

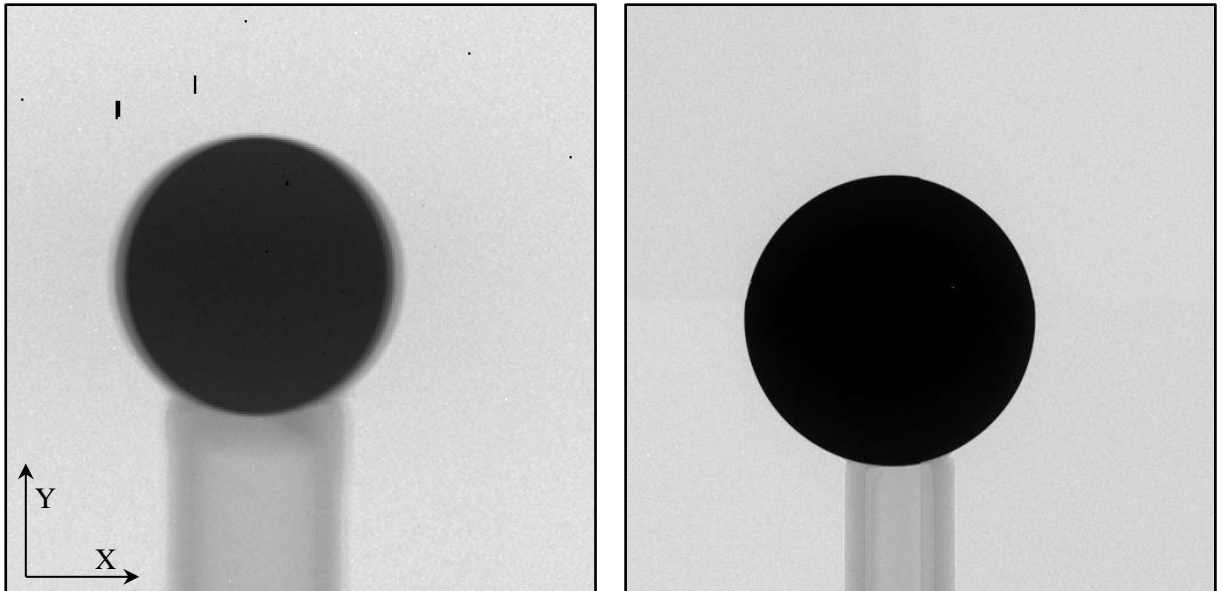


Figure 49: Sharpness of X-ray projections achievable with the originally provided X-ray source, Source Ray SB-120-350, (left) and with the newly installed tube Kevex PXS-11 8012 (right). Both projections were acquired with magnification factor of 1.96. While the projections provided by Source Ray SB-120-350 suffer from anisotropic blur, the projections provided by Kevex PXS-11 are perfectly sharp in the used imaging geometry.

The achievable spatial resolution was evaluated using slanted edge test. A fine steel edge was imaged by both tubes. Evaluation of the data provided the edge-spread-function, which was then used for calculation of the point-spread-function (PSF) which can be easily used for interpretation of provided spatial resolution. The results of the evaluation are summarized in table 1.

Table 1: Comparison of spatial resolution achievable with Source Ray SB-120-350 and Kevex PXS-11 8012. The results are based on slanted edge test experimentally carried out using X-ray projections of a fine steel edge.

X-ray source	Declared spot size	Magnification factor	PSF FWHM X (μm)	PSF FWHM Y (μm)
Source Ray SB-120-350	75 μm	1.96	204	53
Kevex PXS-11 8012	30 μm	1.96	28	28

8 SW and HW tools developed for high-resolution X-ray imaging with large area Timepix detectors

8.1 Calibration CBCT geometry

The CB imaging geometry is very flexible as it was already mentioned in chapter 1.6. Especially in experimental CBCT systems, where it is possible to freely change the magnification factor to accommodate a wide range of object sizes into the detector field of view. The used geometry strongly influences the quality of obtained result. At least knowledge of EPS is required in the case of 2D radiography. In the case of a CBCT scan, properly adjusting the imaging geometry is of key importance. To be able to perform an artifact-free CT reconstruction, it is not enough to know SDD and SOD . A precise knowledge of complex geometry is a necessity. A CBCT reconstruction algorithm usually works with several assumptions:

- SDD and SOD are known
- The detector pixel pitch is known
- An imaginary line connecting the radiation source and detector center is perpendicular to detector plane.
- The origin of the beam, sample rotation axis and detector center are aligned.
- Sample rotation axis is parallel to detector plane and parallel with pixel columns or rows

Some of the reconstruction algorithms are flexible and do not rely on keeping all these basic assumptions. In specific cases, some of the stated rules can be broken intentionally. Nevertheless, it is necessary to know exactly how the actual imaging geometry deviates from the ideal case. By then, the actual geometry can be used as an input of a CT reconstruction algorithm.

Number of calibration techniques dedicated for cone beam CT has been introduced [131 – 135]. Most of the published approaches rely on a CT scan of a dedicated high-contrast phantom object – usually a set high-contrast objects (typically steel balls) arranged in precisely known positions. The imaging geometry can be then evaluated either from projection data by tracking and evaluation of individual steel balls trajectories or from reconstructed CT slices by iterative tuning of the reconstruction parameters. It was demonstrated that 7 geometry parameters (combination of linear shifts and tilts) can be estimated.

In frame of this thesis a simple CBCT geometry calibration procedure suitable for most of micro-CT scanners was developed. Unlike the previously mentioned techniques, the proposed approach does not rely on sample rotation but on controlled change of the image magnification factor. It is based on image-processing-based tracking of two X-ray projections of a steel ball acquired with two different SOD or SDD while the distance between used two positions ΔSOD or ΔSDD , respectively, is known. The proposed technique estimates four geometry parameters – SDD , SOD , central-horizontal plane (CHP) and central-vertical plane (CVP). CHP is an imaginary horizontal plane perpendicular to the detector plane and intersecting the beam origin. CVP is an analogous case for a vertical plane. Detector tilt angles can be measured directly at the available micro-CT systems and easily compensated.

The assumptions for successful geometry calibration using the proposed technique are:

- The diameter of the tracked ball is known.
- The radiographic system allows changing the image magnification factor either by changing of SOD or SDD.
- The rotation axis is parallel to the detector plane and to the detector rows.
- The tracked ball is fully in the FOV in both projections.

The two obtained projections undergo flat-field correction followed by keystone correction for LAD devices if necessary (both introduced in chapter 4.2). Then the projections are segmented using a data-driven threshold to identify the steel ball in each of them. The segmented data can be used for calculation of imaging system geometry.

Magnification factor of each projection as ratio of real ball dimensions and diameter of its respective X-ray projections can be calculated using formula:

$$M = \frac{\sqrt{\frac{4 \cdot S}{\pi}}}{d} \quad (17)$$

where S is the area of the ball projection and d is the real diameter of the used steel ball. With magnification factors $M1$ and $M2$ known, it becomes possible to calculate SDD as:

$$SDD = \frac{M_2 \cdot \Delta SOD}{1 - \frac{M_2}{M_1}} \quad (18)$$

where ΔSOD is the distance between both measured sample positions in the case of constant SDD . Alternatively, in the case of constant SOD and variable SOD, it can be estimated as:

$$SDD_1 = \frac{M_1 \cdot \Delta SDD}{M_1 - M_2}; SDD_2 = \frac{M_2 \cdot \Delta SDD}{M_1 - M_2} \quad (19)$$

The complete imaging system geometry is estimated from tracking the center of gravity of both acquired radiographic projections. The system is aligned in two plains – horizontal and vertical. The alignment in each plane can be calculated independently since these two are linearly independent. The calculation will be demonstrated at an example of central horizontal plane (CHP). The case of central vertical plane is analogous. The CHP of a radiographic imaging system is calculated as

$$CHP = COG_1 + \frac{COG_1 - COG_2}{M_2 - M_1} \cdot M_1 \quad (20)$$

where CHP is central-horizontal-plane of the imaging system, and COG_1 and COG_2 are coordinates of center-of-gravity of the segmented steel ball projections in both measured projections. Once the actual CHP is known, the detector can be aligned with it. Usually, the desired geometry is achieved after 2 – 3 iterations of previously described algorithm.

The described calibration procedure is simple to perform and the calculations easy to implement. The suggested procedure does not require scanning and processing of full CT dataset; unlike most of the previously established procedures for CBCT system geometry calibration. The calibration is, therefore, quick and convenient both for CBCT and CB radiographic systems. Furthermore, the algorithm is not dependent on the use of any dedicated, precise and expensive calibration phantom.

Unfortunately, it was not possible to compare the results and verify the accuracy with any widely recognized CBCT calibration procedure due to unavailability of any dedicated phantom objects in the laboratory. On the other hands, tens of geometry-artifact-free CBCT scans carried out in frame of this thesis clearly prove the viability of the proposed calibration procedure.

The proposed algorithm can further be used for evaluation of mechanical stability of a CBCT scanner. Especially in the case of gantry-based CBCT scanners in which the gantry can deviate from its ideal path during the rotation. Thus, the imaging geometry can dynamically change in dependence on actual gantry angle. If the deviation is repetitive, it is possible to evaluate it using the proposed algorithm and then compensate prior or during the CT reconstruction. An improvement of data quality after such correction is demonstrated in chapter 8.2.1.

8.2 Sample projection trajectory drift compensation.

The basic idea of a CT scan is that a sample is exposed by an X-ray beam from a set of previously defined angles. Rotation around a certain axis is, therefore, the only desired motion during the scan. Any other unexpected movement of the setup negatively affects the imaging geometry and induces geometry and motion artifacts to the reconstructed CT slices. Consequently, the spatial resolution of the data together with detail detectability is compromised.

Micro-CT systems usually utilize high-precision remote-control positioning systems. Nevertheless, it is not possible to construct a perfectly rigid and stable device. The rigidity and temporal stability of the construction parts are not perfect; the accuracy and repeatability of positioning apparatus is limited. Thus, micro-CT scan can suffer from undesirable parasitic movements superimposed to sample projection trajectory originated from pure rotation. Compensation of sample projection drift (SPD) is a subject of this section. SPD can be either systematic or random. An independent compensation technique for each of them was implemented within the frame of this thesis and their efficiency is demonstrated.

Both of introduced techniques are based on empiric evaluation of SPD that create a functional dependence of SPD on acquisition angle for compensation of the effect. The obtained curve is then applied to the data and each projection of the dataset is individually shifted with sub-pixel precision to its estimated optimal position. It should be noted, that shifting the projection data is not a correct approach in compensation of the SPD effect. SPD is not caused by sample movement but by slight distortions of imaging geometry during the scan. Therefore, the proper way would be to estimate these changes and utilize them during CT reconstruction. Unfortunately, the CT reconstruction algorithms used in this thesis are not flexible enough to work with imaging geometry variable in time.

On the other hand, the proposed correction techniques are easy to implement and the achieved results prove the efficiency for geometry artifacts suppression.

8.2.1 Systematic SPD

Systematic SPD can be described as an undesirable effect negatively affecting imaging geometry which is repeatable and stable in time. Such behavior was observed in the case of small animal scanner introduced in chapter 5. Despite the hardware changes (detailed in chapter 7.1) that improved the gantry movement precision, the obtained micro-CT reconstruction suffered from motion artifacts anyway.

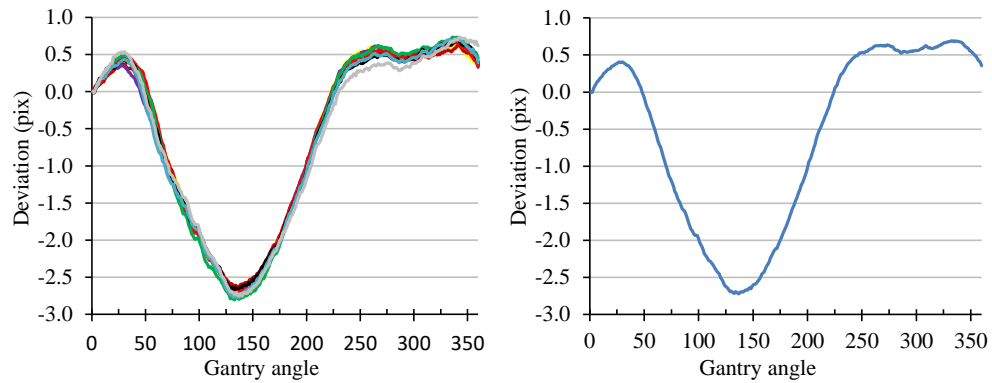


Figure 50: Ten curves evaluating the sample projection drift along the rotation axis exert very good repeatability (left). Their average can be, therefore, applied for compensation of the effect (right).

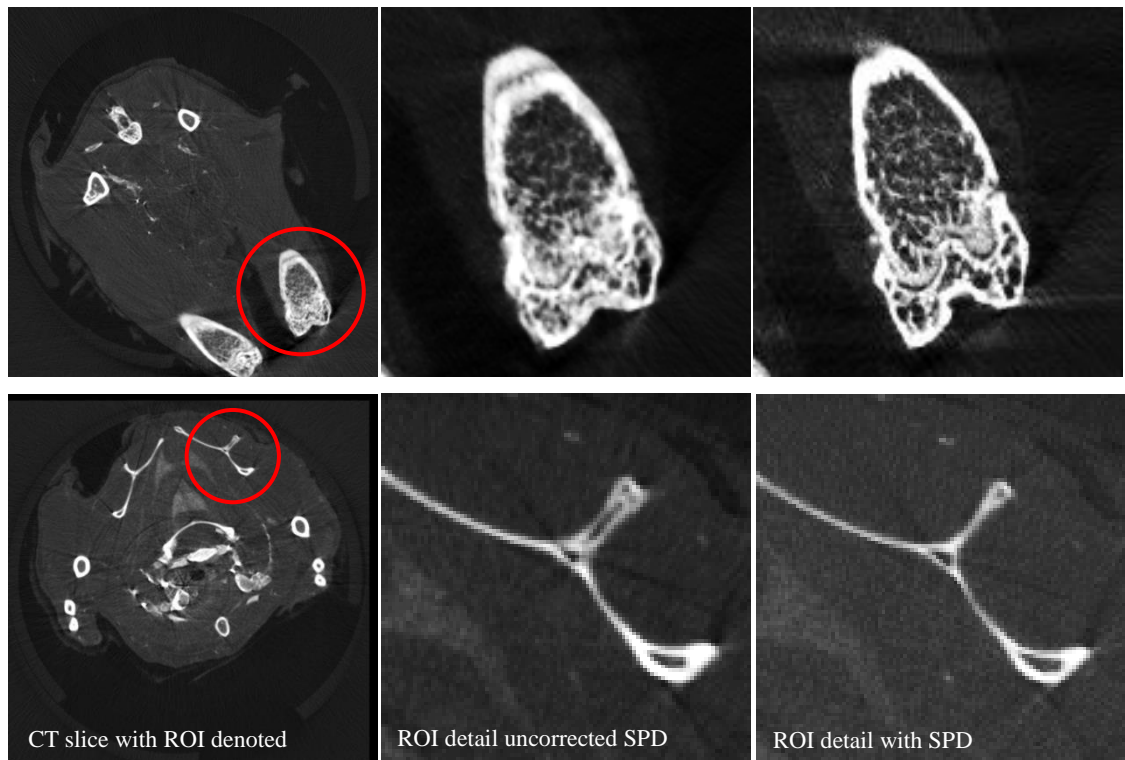


Figure 51: Demonstration of the systematic SPD compensation efficiency. The red circles denote regions of interest – mouse knee joint and scapula (left). The middle and the right row show differences between the uncorrected and corrected data.

The gantry movement accuracy was evaluated from radiographic projections of a steel ball acquired under a set of different angles. Further processing of the data presented in figure 48 quantified the deviation of gantry trajectory from its ideal path. The sample drift achieves magnitude of approximately 4 pixels along the rotation axis while it is negligible in direction perpendicular to the axis. The left part of figure 50 shows an estimated drift along the rotation axis of ten different measurements. It is clearly visible, that individual trajectories are in a good match. The right part of figure 50 presents the average trajectory of the drift. The estimated average path can be then used for correction of projection images position in dependence on acquisition angle. Figure 51 demonstrates the geometry artifact suppression and connected improvement of detail detectability as a consequence of systematic SPD correction. It is shown at an example of two different micro-CT slices of a mouse.

8.2.2 Random SPD

Random SPD is typically an issue of micro-CT scans with extremely high resolution connected with long scan time. Under such circumstances, effects such as rotation stage mechanical inaccuracy, X-ray source spot drift or thermal dilatation of setup components can contribute to data quality degradation. The occurrence of the latter two is more probable to appear in the case of long-lasting scans. These effects are hardly predictable, therefore, the compensation has to be adjusted specifically for each individual scan.

The stated processes can induce severe motion artifacts in the case of long-lasting (> 2 hours) scans with sub-micron EPS. The sample projection drift (SPD) – a deviation from ideal trajectory – has reached even tens of pixels in extreme cases (see figure 52). In such case, it is not possible to reconstruct the data at all without implementation of a convenient correction.

Selection of proper construction materials and hardware can suppress these undesirable effects, however, it cannot be avoided completely. Several studies addressing this issue have been published [136 – 141]. Experimental results published in [136] indicate that under given X-ray system settings (source kVp and current, overall scan time) is repeatable and a previously created calibration can be used for correction of later acquired datasets. Nevertheless, other studies provide contradictory conclusions [137]. Therefore, the most generally reliable techniques seem to be empiric approaches using a static reference object placed into the detector field of view sideways a sample [138 – 140] or using a sparsely-sampled reference dataset [141].

A compensation method of random SPD based on image cross-correlation of the projection data with a sparsely-sampled reference dataset was implemented and tested within the frame of this thesis. The idea of the correction is illustrated in figure 53. The method is based on an assumption that sources of SPD develop slowly in time. Immediately after the standard micro-CT scan, a reference dataset is captured. The reference data are acquired with an angular step of 30 degrees and therefore, the reference data scan time is typically less than two minutes and the influence of SPD to it is negligible. During the data pre-processing the matching projections of both datasets are cross-correlated to evaluate the SPD effect during the scan. Cross-correlation provides a set of calibration points. The measured points are then fit by a polynomial curve to provide a SPD correction coefficient for each angular projection of the dataset. Using affine transformation each projection is shifted with sub-pixel precision to match the reference dataset.

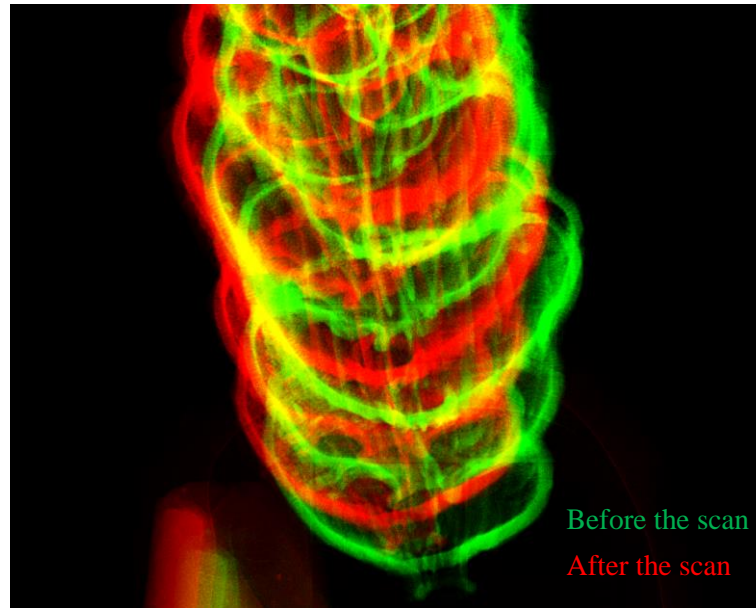


Figure 52: Demonstration of the undesirable sample projection drift –the first (green) and the last (red) projection of the CT dataset are misaligned by tens of pixels. The projection drift is probably caused by thermal dilatation of sample stage or movement of the source spot during the time-consuming scan. CT reconstruction without severe motion artifacts is not possible without a convenient correction.

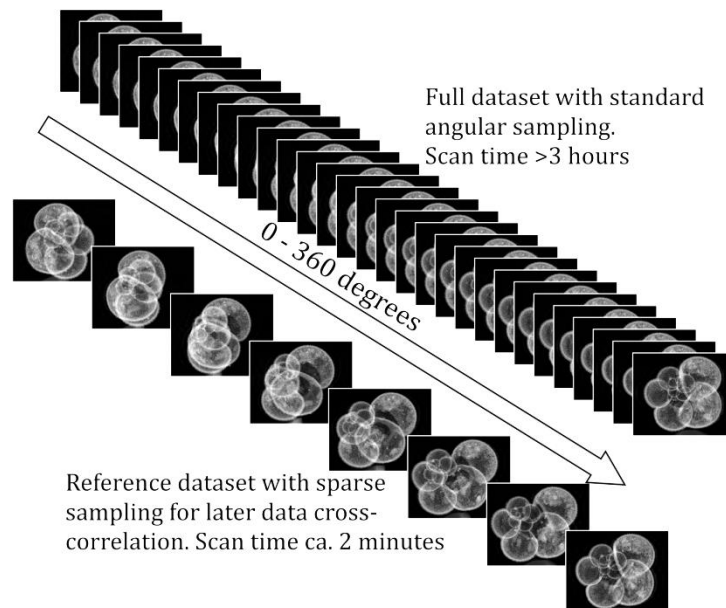


Figure 53: The idea of SPD correction using a sparsely-sampled reference dataset. Immediately after the micro-CT scan the sample is scanned again with coarse angular sampling. As the second dataset is acquired quickly it is not affected by SPD effect. Matching projections of both datasets are cross-correlated to estimate the SPD effect during the performed micro-CT scan and for its compensation.

The correction curves in horizontal (X) and vertical (Y) directions of 10 samples are plotted in figure 54. While the SPD trajectory is almost linear in the vertical direction, the trajectory in horizontal direction is more complicated and unpredictable. The magnitude changes significantly, although several trends in SPD trajectory shape can be observed (indicated by shades of red, green and blue) indicating a certain level of repeatability. It is, therefore, not possible to use general values for SPD correction and it has to be evaluated for each individual scan. Nevertheless, the presented

approach significantly suppresses motion artifacts of high-resolution CT data and improves detail detectability (see figure 55).

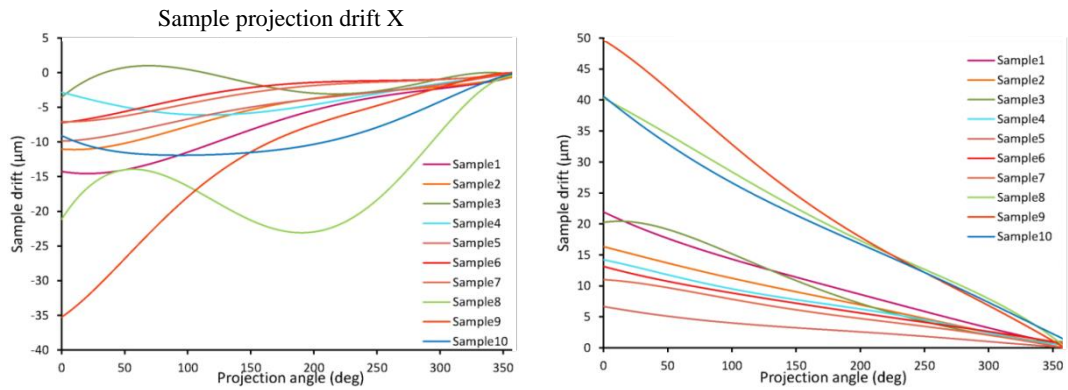


Figure 54: Correction curves dedicated for compensation of SPD in horizontal (X) and vertical (Y) directions obtained from cross-correlation of appropriate dataset projections with reference frames. While the vertical shift is almost linear, the horizontal drift can be better approximated by a polynomial curve. The SPD in X exerts a certain level of repeatability of trajectory shape (shades of green, blue and red) but the magnitude changes significantly.

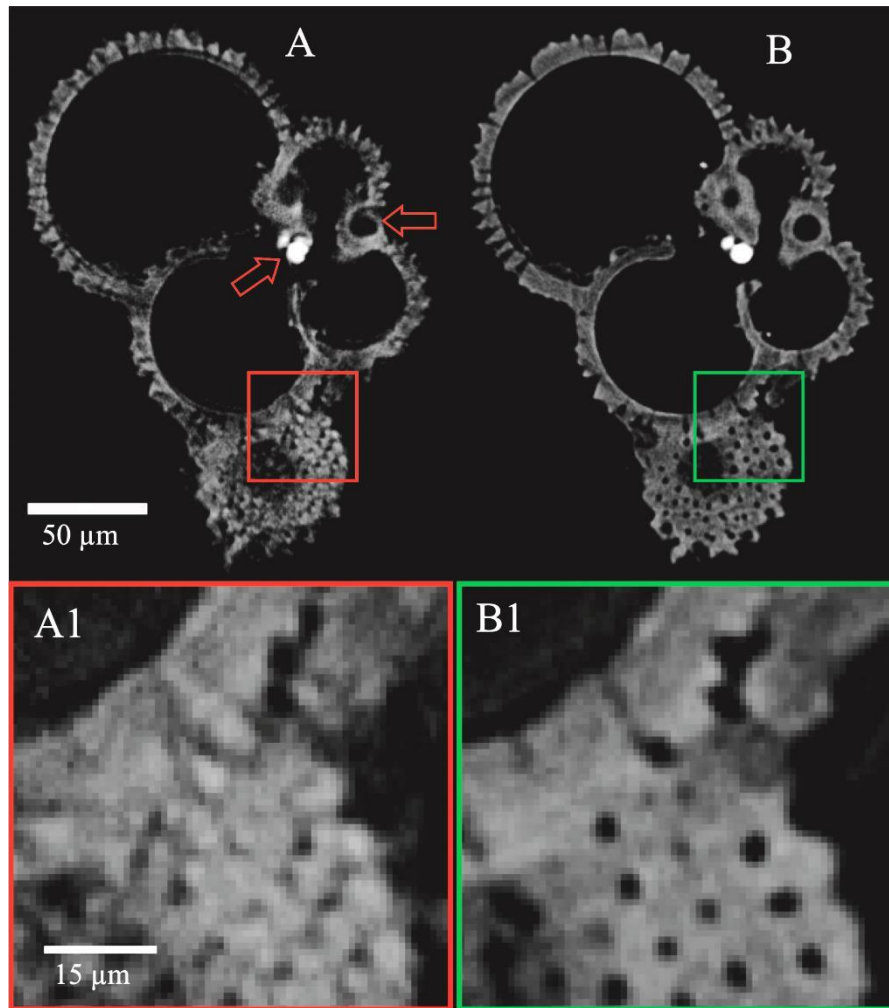


Figure 55: SPD correction suppresses motion artifacts and improves detail detectability within the reconstructed CT slices. While the uncorrected data (A) suffer from occurrence of several artifacts (denoted by red arrows) the SPD corrected data (B) are artifact free. The magnified regions of interest (A1) and (B1) demonstrate the improvement of fine detail visibility. The image was taken from an own publication [142]

8.3 Adapter system for soft tissue sample stabilization during micro-CT scan

Collection of micro-CT data can vary from several minutes up to several hours. Typically, using Timepix detectors, the data acquisition time is in the order of tens of minutes. In some cases, typically if an ex-vivo soft tissue sample is scanned it is a highly complicated task to keep the sample stable during the scan. The soft tissue samples are very delicate, given that the soft tissue has a high content of water, it dries out very quickly once it is extracted. The loss of water causes structural changes within the sample and consequently produces motion artifacts in the micro-CT slices [143].

The water evaporation can be stopped i.e. by embedding the sample into agarose gel which simultaneously provides mechanical support for the sample. Such solution is merely convenient for contrast-stained samples only due to comparable radio-density of native soft tissue and the gel.

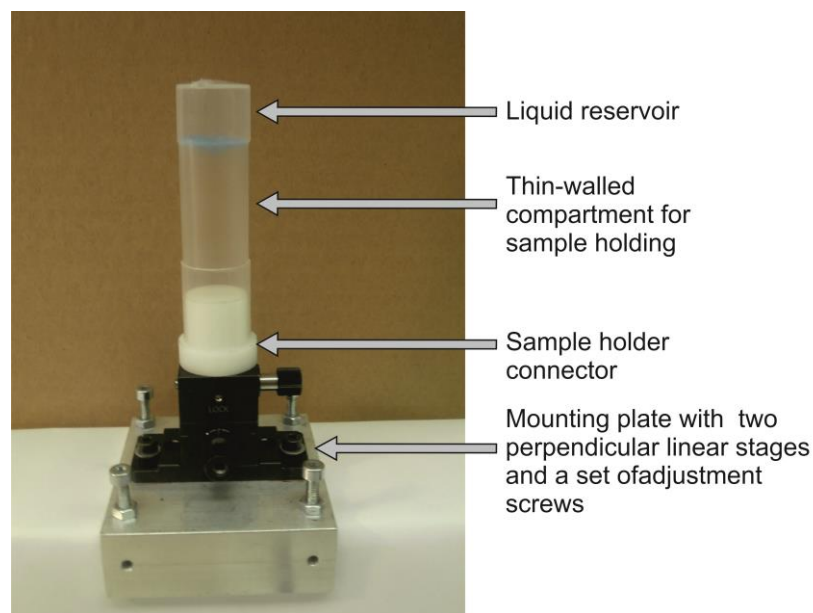


Figure 56: Adapter system for soft tissue sample stabilization during micro-CT scan. The adapter consists of a mounting plate, cross-table for precise sample positioning in the scanner and from a set of double-compartment sample containers (2 – 50 ml in volume) with compatible connectors.

Therefore, a sample holder dedicated for suppression of undesirable drying-out of ex-vivo soft tissue samples undergoing precise micro-CT measurements was designed (see figure 56). The sample adapter system consists of a mounting plate, a set of cylindrical double-compartment containers (2 – 50 ml of volume) for holding samples and a set of cylindrical reductions for connecting a selected container to the mounting plate. The mounting plate is equipped with a pair of mutually perpendicular linear translation stages and four adjustment screws for precise centering of the sample into the gantry axis and compensation of the holder tilt with respect to the rotation axis.

Each sample container has two semi-separated compartments – a larger one for holding the sample and a smaller one serving as a liquid reservoir. The liquid in the smaller compartment creates a saturated atmosphere of gases inside the container and prevents undesirable structural changes of soft tissue samples during long lasting scans. Figure 57 shows the improvement of sample stability using the double-compartment sample adapter. Figure 58 then demonstrates how the improved sample stability avoids occurrence of motion artifacts visible in CT slices.

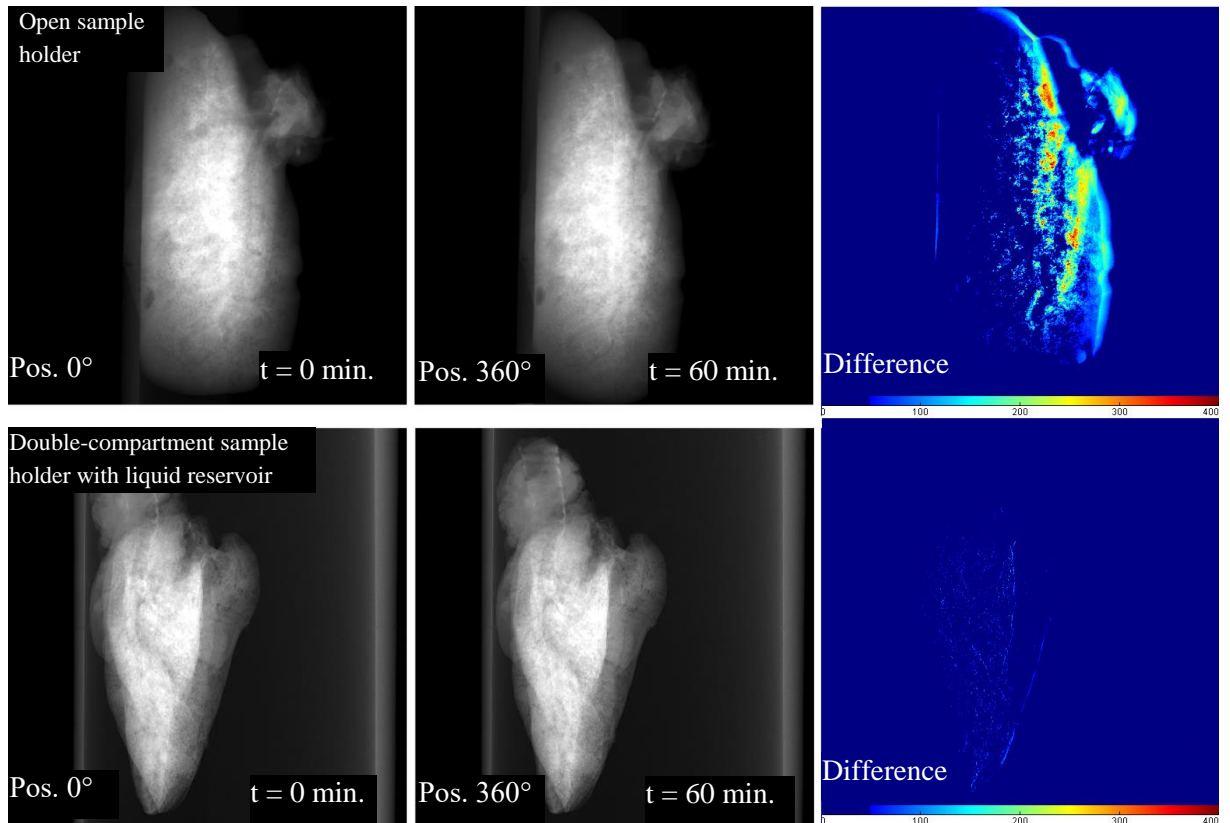


Figure 57: Ex-vivo mouse lungs scanned with an open sample holder (top row) and with a proposed double-compartment holder with a liquid reservoir (lower row). Subtraction of projections acquired under matching angle before and after the micro-CT scan demonstrates that sample stability in time is significantly improved with the double-compartment sample container. The image was taken from an own publication [143].

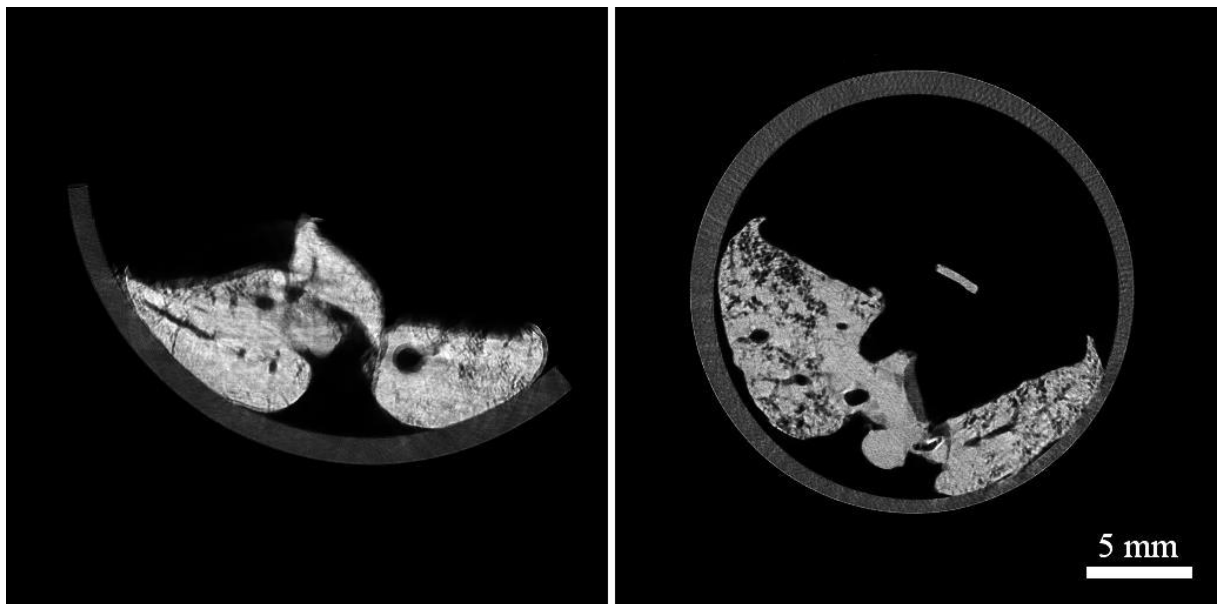


Figure 58: The improved sample stability positively affects the resulting micro-CT slices. While the data from open-holder suffer from motion artifacts (left), the data originated from sample scanned in the double-compartment container provide much sharper result with better detail detectability (right). The image was taken from an own publication [143].

8.4 Matlab-based application for micro-CT projections pre-processing

Processing of radiographic projections obtained from large area Timepix detectors consists of several subsequent steps before it can be used for CT reconstruction. Raw data are processed using the BHC (detailed in chapter 4.2.2). BHC improves the uniformity of detector response, identifies malfunctioning pixels and most-importantly, it transforms the projections from intensity domain into equivalent material thickness coding. Subsequently, the geometry distortion originating from WidePIX array assembly has to be corrected (explained in chapter 4.2.3). Furthermore, optional steps like SPD correction or ring artifact reduction can be employed in the projection data processing chain. Finally, the native format of Timepix frames – ASCII matrix – has to be converted into a data format acceptable for CT reconstruction software tool. Typically, the demanded data formats are RAW, TIFF or PNG.

A Matlab-based application with simple graphical user interface was implemented within the frame of this thesis to simplify and improve efficiency of the projection data processing. Performing each mentioned data processing step was ineffective due to protracted data loading and saving the modified data back to hard drive in each step. Furthermore, enormous hard drive space was needed for the case of sequential data processing.

The application loads and writes data only once. All the subsequent operations are applied on the data stored in RAM. Therefore, sufficient RAM capacity is necessary. Figure 59 shows the user interface of the implemented application with its main components denoted. The application accepts data after BHC in ASCII format together with a log-file containing necessary information for data processing (number of files, sensor size, imaging geometry, etc.). Currently the application is capable of loading and process data from six different detector layouts (Quad detector, WidePIX 2×5, 3×3, 4×4, 4×5 and 5×10).

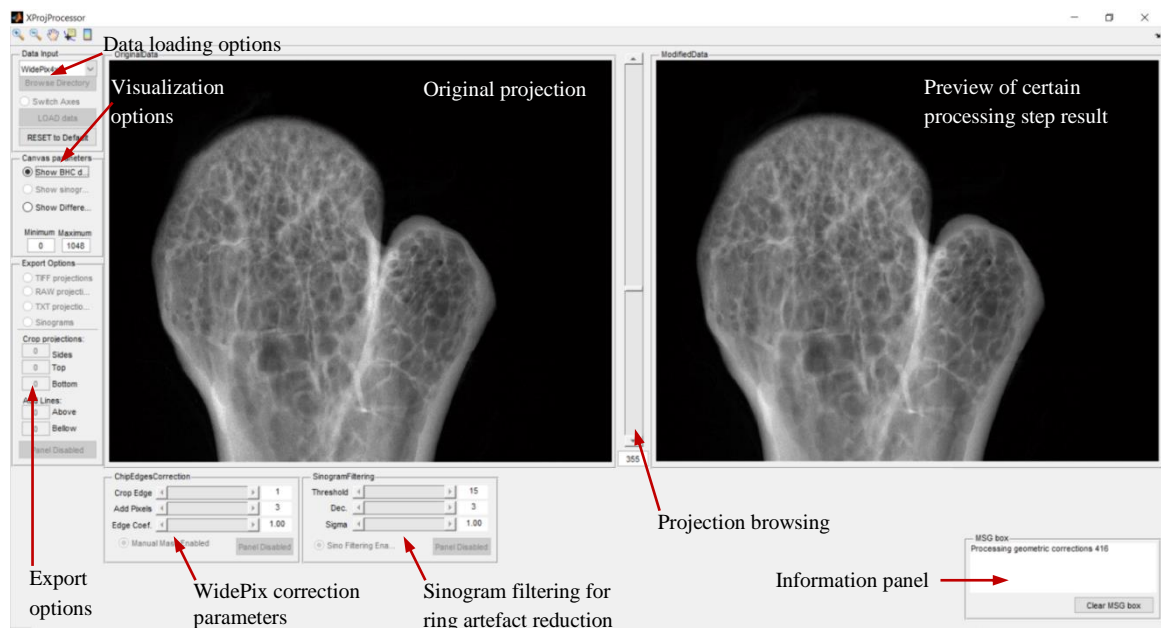


Figure 59: User interface of the implemented Matlab-based application for X-ray projection data processing with main components denoted.

During projection, loading it automatically checks the presence of defective pixels that were not interpolated during BHC. If needed, a manually created defect-pixel mask can be loaded and used. Figure 60 shows the results of the automatic defective pixel identification and masking. Once the data are loaded, the WidePIX-geometry correction is applied. Correction parameters for each supported detector type are stored in a configuration file and can be modified for optimal performance of the correction. Ring artifact reduction can be applied optionally after the WidePIX-geometry correction. The projections are transformed into sinograms for the purposes of ring artifact reduction. The undesirable rings frequently affecting the CT slices appear in the form of stripes in a sinogram domain. Therefore, the task to suppress circular structures is transformed into detection and compensation of stripes in sinogram-based filtration. The sinogram filtering is based on a combination of several different published approaches [144 – 147].

The user can select several output formats (ASCII, 32 bit RAW, 16 bit TIFF) and crop the projections if the sample does not fill the whole FOV before the final data export. All the used parameters are written into the log-file simultaneously with export of processed data. The parameters of data processing are, therefore, stored can be verified and the data processing with same parameters can be easily repeated.

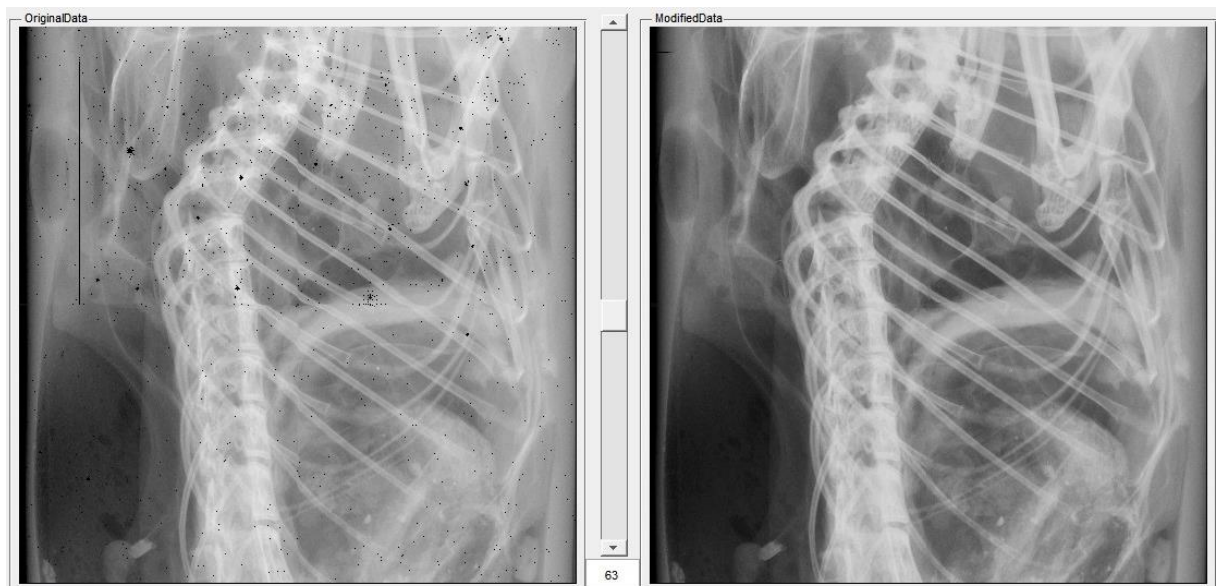


Figure 60: The application automatically detects and masks defective pixels that were not identified during the beam hardening correction.

8.5 Automated acquisition of BHC data for the MARS scanner

Beam hardening correction is an empirical procedure utilizing X-ray projections of a set of filters of well-defined thickness to calibrate the detector response to X-ray spectrum of different mean energies. Typically, 6 – 12 filters of different thicknesses are used. Changing the filters by hand is ineffective and can compromise the BHC performance as the X-ray tube has to be repeatedly switched off and on in a short period of time.

The micro-CT systems situated in IEAP laboratory are equipped with revolving carousels holding a set of filters (visible in figures 37 and 38). The data for BHC can be, thanks to the complex positioning apparatus of discussed systems, acquired automatically in the frame of a micro-CT scan without a necessity to switch-off the tube and manually remove the sample from the beam. Unfortunately,

the carousels are too large and heavy to be installed into gantry of the available small animal scanner. Therefore a dedicated BHC filter holder was designed and made specifically for the scanner (see figure 61). The holder houses fifteen aluminum filters with thickness range from 0.05 mm up to 10 mm. It was designed to be compatible with the scanner sample-mounting system and utilizes the fact that the sample stage is capable of traveling along the rotation axis in range of 175 mm. The automatic BHC data acquisition procedure controlled by dedicated user interface (see figure 62) combines positioning of the sample stage with gantry rotation to expose the required filters to the beam and saves the data to hard drive.



Figure 61: The BHC filter holder designed for use with the available small animal scanner. The holder is compatible with the sample-mounting system of the scanner and holds fifteen aluminum filters with thickness range from 0.05 mm up to 10 mm.

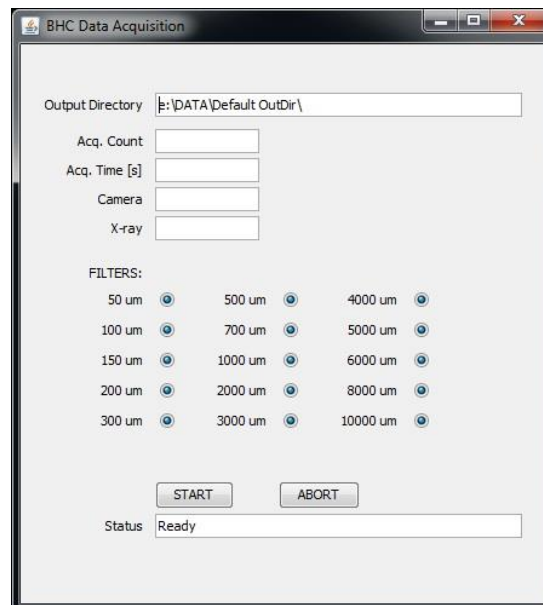


Figure 62: User interface of the Python-based tool for BHC data acquisition compatible with Pixelman software. The interface allows the user to easily set acquisition parameters and select range of filters suitable for a specific sample.

The designed BHC filter holder has to be put into the gantry instead of a sample for BHC data acquisition. This solution, unfortunately, does not provide the opportunity to incorporate the BHC data acquisition into the sample scanning procedure. Nevertheless, it provides significant improvement in user comfort compared to manually-changed filters and provides better results as all the data are acquired without a need to repeatedly switch off and on the source.

9 High-resolution X-ray imaging using Timepix detectors in biology and medicine

This chapter summarizes the applied results achieved within frame of this thesis. The presented results have been achieved in cooperation with the Third Faculty of Medicine, Charles University in Prague (3FM) and Faculty of Science, Charles University in Prague, and National Radiation Protection Institute (NRPI). The use of laboratory mice was approved by ethical committee of the Third Faculty of Medicine, Charles University in Prague. The animals were treated with accordance to guidelines defined by Ethical Committee in decisions no. 246/1992 and no. 419/2012.

9.1 Sub-micron resolution micro-CT

X-ray imaging with spatial resolution reaching 1 micrometer has been enabled in laboratory conditions with progress in technology of compact X-ray sources. Nano-focus tubes – X-ray tubes with focal spot size smaller than 1 μm – have become available. With such sources X-ray imaging in CB geometry can be carried out with extremely high magnification factors with minimal penumbra blur. The latest generation of nano-focus X-ray tubes is capable of producing images with true spatial resolution of 150 nm [86].

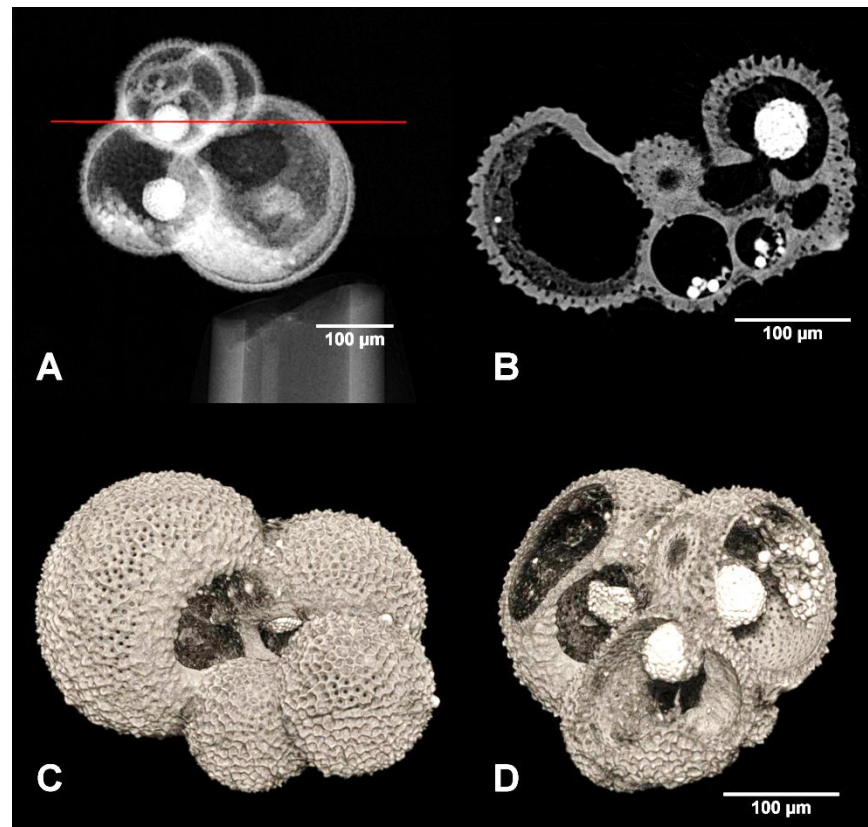


Figure 63: A fossil foraminifera sample scanned with EPS of 830 nm. (A) shows one of acquired projections; (B) demonstrates a selected CT slice; (C) is volume rendering of the sample and (D) reveals inner structures of the sample including developing pyrite crystals. The sample was kindly provided by doc. RNDr. Katarína Holcová, CSc, Faculty of Science, Charles University.

The beam intensity provided by nano-focus X-ray tubes is much lower compared to micro- and mini-focus sources due to limitations of power density at the X-ray tube target. The low photon income rate inevitably prolongs exposure time of each projection and the total scan time as well. The exposition needed for sufficient photon statistics is usually several seconds but can reach even tens of seconds or even minutes in some cases [4; 5]. EIDs suffer in such conditions due to integration of dark current. Dark-current-free operation of PCDs is, therefore, extremely useful feature in this case. The exposure time can be freely extended without compromising of the data signal-to-noise ratio.

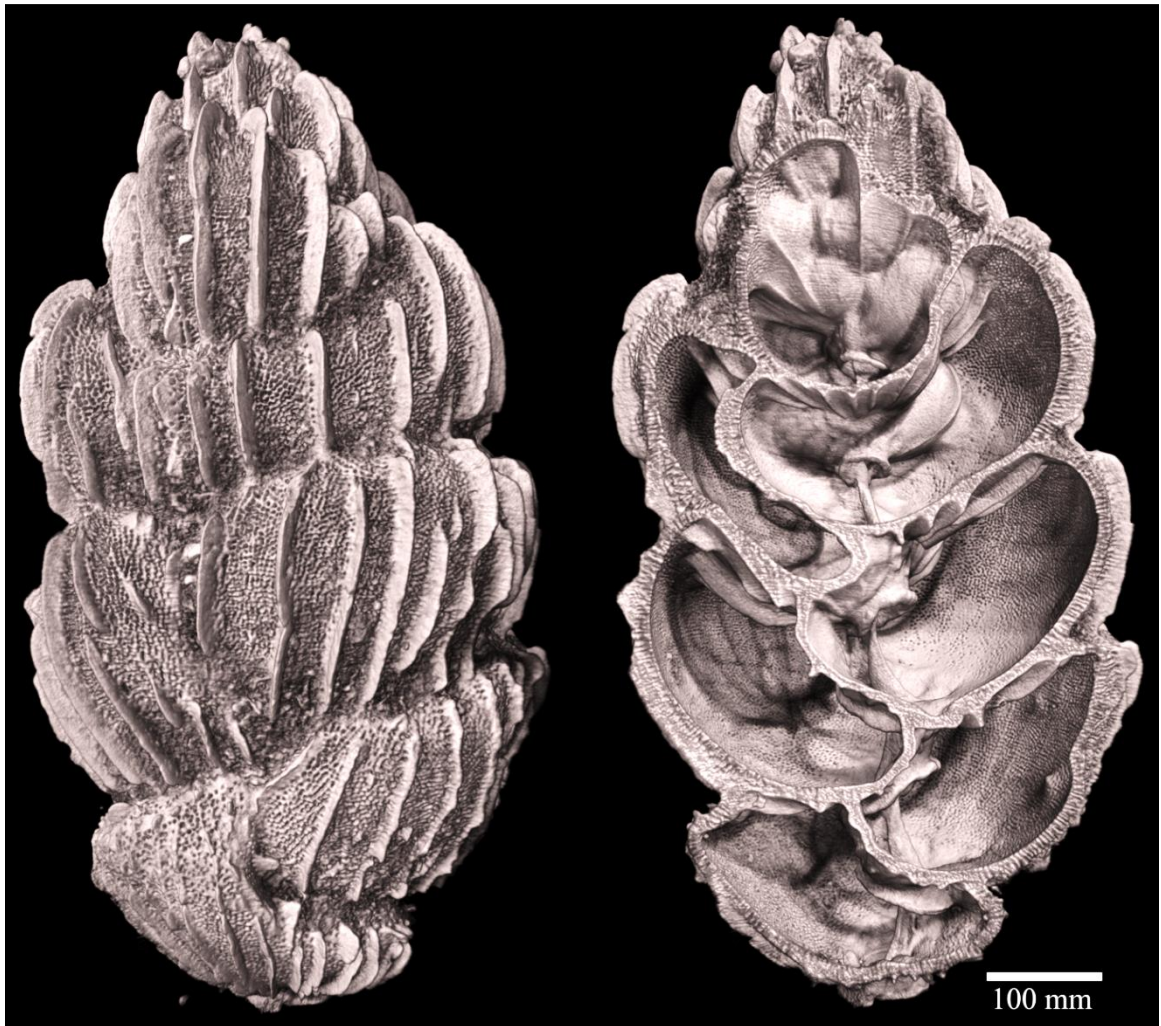


Figure 64: Volume rendering of another foraminifera species. The Micro-CT scan was carried out using WidePIX_{4x5} detector and with EPS of 690 nm. The sample had to be scanned in two individual datasets as it exceeded detector field in the selected imaging geometry. Both parts were merged together to produce a complete 3D model of the sample. The sample was kindly provided by doc. RNDr. Katarína Holcová, CSc, Faculty of Science, Charles University.

The micro-CT with Timepix detectors and sub-micron EPS has found great application field in biology focusing on research of foraminifera in cooperation with Faculty of Science, Charles University in Prague. Foraminifera are single-cell organisms living mostly in the seafloor sediment or in plankton. Although the largest species can reach up to several centimeters in size, they are smaller than 1 mm in most cases. Foraminifera build an external shell of chitin, CaCO₃ or agglutinated sediment particles. The shell is penetrated by a high number of fine openings. The openings are used for streaming the ectoplasm outside and catching food. The conventional research approaches is based on use of either optical or electron microscopy. As both mentioned methods allow visualization

of outer surfaces only application of micro-CT has provided new possibilities in nondestructive research of these fascinating creatures. Micro-CT still cannot compete with microscopy by means of resolution, but as it provides 3D model of the investigated sample a number of new parameters can be observed. Micro-CT measurements allow analysis of the shell growth distortions – number of individual chambers, their volume, shape etc. An example of a micro-CT scan of a fossil foraminifera sample scanned with EPS of 830 nm is presented in figure 63. It shows one of the acquired projections (A), a selected CT slice (B) and volume rendering of the sample 3D model revealing the outer shell (C) and its inner structures (D). The overall dimensions of the sample were smaller than 300 μm .

The maximal achievable spatial resolution is a function of the sample size. Therefore, it is not possible to perform a scan with spatial resolution at micrometer level for all samples. The sample must be fully visible in the detector FOV in all angular positions. Such factor defines the suitable sample dimensions for imaging with certain resolution. I.e. detectors WidePIX_{4x5} (1024 \times 1280 pixels) or WidePIX_{5x10} (1280 \times 2560 pixels) provide FOV of 1.28 or 2.56 mm wide respectively considering a CB imaging geometry scan with EPS of 1 micrometer. The detector FOV can be, further, virtually extended – if the detector is mounted on a precise positioning stage it can travel between several positions in each angular projection. A set of partially overlapping sample projections is created this way. The projections are then merged together during data pre-processing using image-registration techniques. Obviously the total scan time will be several times longer compared to a regular scan, advanced data processing is required and it also needs enormous space for data storage. Results of a micro-CT scan carried out as two subsequent scans due to sample dimensions exceeding the detector FOV is shown in figure 64. The sample presented in figure 64 was scanned with EPS of 690 nm. The smallest structures detected at foraminifera samples were openings of the shell with diameter of approx. 2 μm . It is questionable whether this was given by spatial resolution limit of the system or by absence of smaller shell openings.

Micro-CT in biology research can be easily combined with other modern technologies. I.e. combination of high-resolution CT data with 3D printing can create reliable macroscopic models of barely visible samples as shown in figure 65.

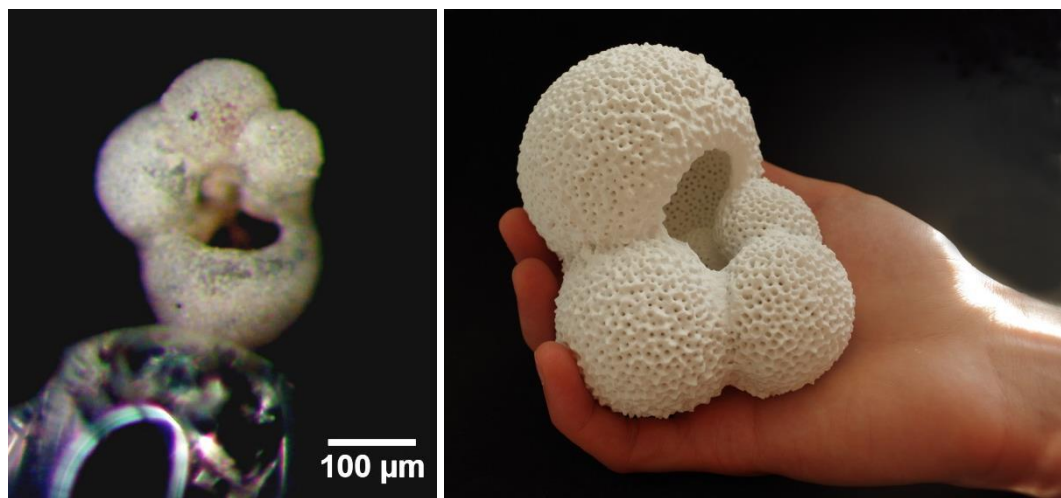


Figure 65: A microscope photo of a foraminifera and its 3D printed model based on a micro-CT scan. The 3D print was created in cooperation with RNDr. Luděk Míka, Ph.D., Faculty of Science, Charles University.

9.2 Small-animal imaging

Routine imaging of whole small animals with Timepix detectors has been enabled with introduction of WidePIX technology. The FOV of WidePIX detectors can easily accommodate small animal like mice, lizards etc. The detectors WidePIX_{10×N} are capable of scanning whole mice in one exposure with spatial resolution below 30 μm . An example of such measurement is demonstrated in figure 66. The figure shows frontal and sagittal slices of a PlastiMouseTM phantom scanned with detector WidePIX_{5×10}. PlastiMouse as a member of PlastiCreature products is a perfectly reliable mouse anatomy phantom since it was made by a plastination procedure from a real animal [148]. It is an extremely useful tool for methodology development and testing as it avoids the necessity to use real animals for this purpose. The reconstructed data with voxel size of 20 μm reveals a number of important anatomic structures. Some of them are denoted by red arrows in the figure 66.

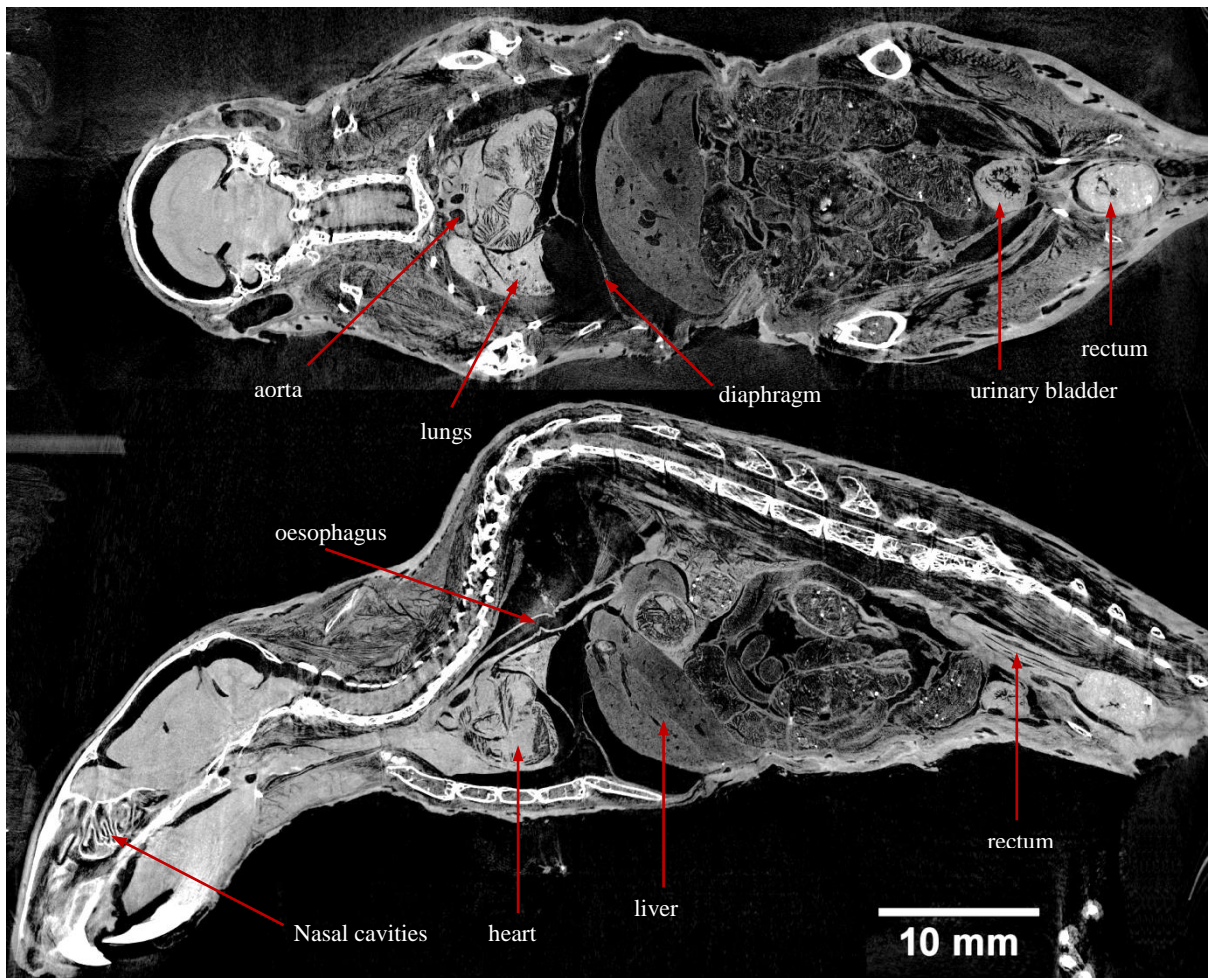


Figure 66: Results of a micro-CT scan of a PlastiMouseTM phantom carried out using WidePIX_{5×10} detector. Tube operated at 70 kVp, 720 projections acquired, voxel size 20 μm . Some of successfully visualized anatomical structures are denoted by red arrows. The image was taken from an own publication [61]

An animal can be scanned in several subsequent scans that are later co-registered and merged into one dataset. Such way is obviously much more time consuming, however, it can provide much higher spatial resolution. Alternatively, spiral scanning strategy can be used for samples exceeding the detector FOV in length. An example of results obtained from a cone-beam spiral scan using WidePIX_{4×5} detector is shown in figure 67. The image shows three selected micro-CT slices of mouse newborn stained in aqueous IKI solution (iodine concentration 2.9 mg/ml) for 5 days. The sample was

scanned with EPS of 12.5 μm , angular step 1.55 degree and total of 2905 projections with table feed of 2 mm/360° was acquired. Iodine staining significantly enhances the radio-density of soft tissue and also improves differentiation of diverse tissue types based on different iodine affinity.

Figure 68 then shows volume rendering of a mouse injected with intravenous contrast agen. The presented micro-CT scan was carried out *post mortem* using the modified MARS CT scanner. As the scanner is equipped with Timepix Quad detector, scanning the mouse's whole-body required sequential acquisition of four individual datasets. Each dataset consisted of 720 projections with EPS of 44 μm . The blood pool contrast was enhanced using Aurovist™ contrast agent [9]. Aurovist™ is one of the contrast agents that have been developed specifically for small animal X-ray imaging. The contrast enhancement is given by content of gold nano-particles of relatively large diameter that prevent fast clearance from the blood pool by kidneys.



Figure 67: Micro-CT scan of a post-mortem iodine-stained mouse newborn scanned using WidePIX_{4x5} detector in spiral geometry. The tube was operated at 60 kVp, total number of 2905 projections with 1.55 degree angle step and table feed 2 mm per 360 degree. Voxel size 12.5 μm . A number of important anatomical structures was revealed due to contrast enhancements induced by iodine-based staining.

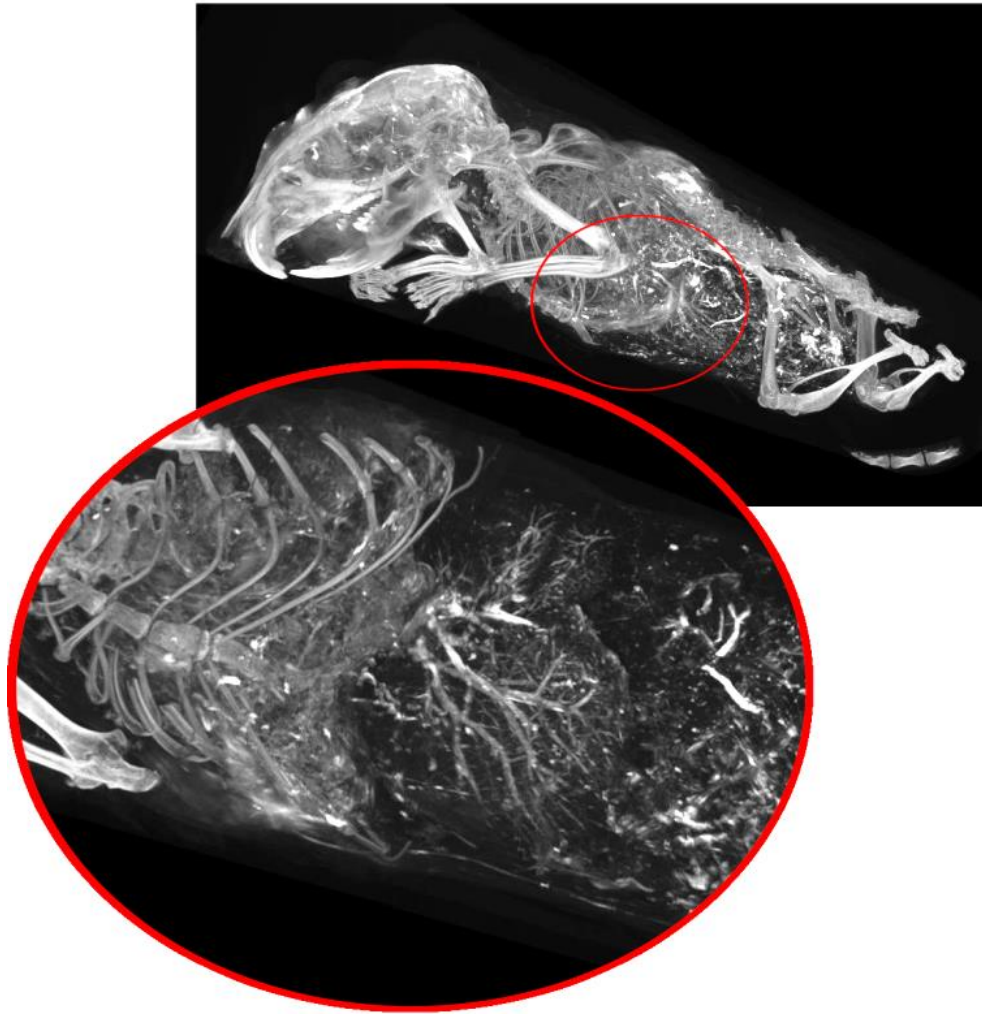


Figure 68: Post-mortem micro-CT scan of a mouse with nanoparticle-based contrast agent Aurovist injected into the blood pool. The contrast agent enhanced radio-density of liver and kidney vascular system. The scan was carried out using the modified MARS small animal scanner. The sample was scanned in four individual datasets which were later co-registered and merged together. Voxel size of the CT reconstruction is $44\ \mu\text{m}$

9.3 Ex-vivo soft tissue imaging

Visualization of both microscopic and macroscopic structures of soft biologic tissue provides crucial information needed for both medical diagnostics and research. The conventional way to study microscopic structures of ex-vivo biologic samples, i.e. tissue biopsies, rely on histology techniques. The traditional histology is unfortunately based on elaborate, time consuming and destructive sample preparation protocols. The histology sample processing consists of several stages of sample dehydration, chemical fixation, staining and embedding into resin. The resin block is then sliced using dedicated microtome knife. The individual slices are mounted on glass slides for analysis using a microscope. The slides used to be stored in depositories in the past. Nowadays it is more common that the images of slides are digitalized and stored electronically. The histology also provides a kind of 3D information on the sample as it is sliced into a set of slides. However, the spatial resolution is highly anisotropic. While the spatial resolution within a slice is limited only by wavelength of the used light it is much worse from slide to slide due to its thickness (typically from tens to hundreds of micrometers). Assembling a 3D volume from histology slides is, moreover, complicated due to possible deformities of individual slides, the procedure is prone to various geometry artifacts and is very time consuming.

The true volumetric information based on histology processing is achievable from high resolution episcopic 3D microscopy or surface imaging microscopy. Both techniques are capable of providing the volumetric information with isotropic spatial resolution at level of 500 nm due to different slicing technique. The microscope scans the whole resin block while extremely thin slices that are cut from the sample surface are disposed. The obvious drawback of these techniques is that the sample is completely destroyed during the scan.

Chapter 3 concisely introduced the term virtual histology – an application of high-resolution X-ray imaging techniques for imaging of ex-vivo soft tissue samples. The spatial resolution achievable by X-ray micro- and nano-CT system nowadays still cannot compete with the resolution provided by optical microscopy. The unique advantage of X-ray imaging is in its non-destructivity.

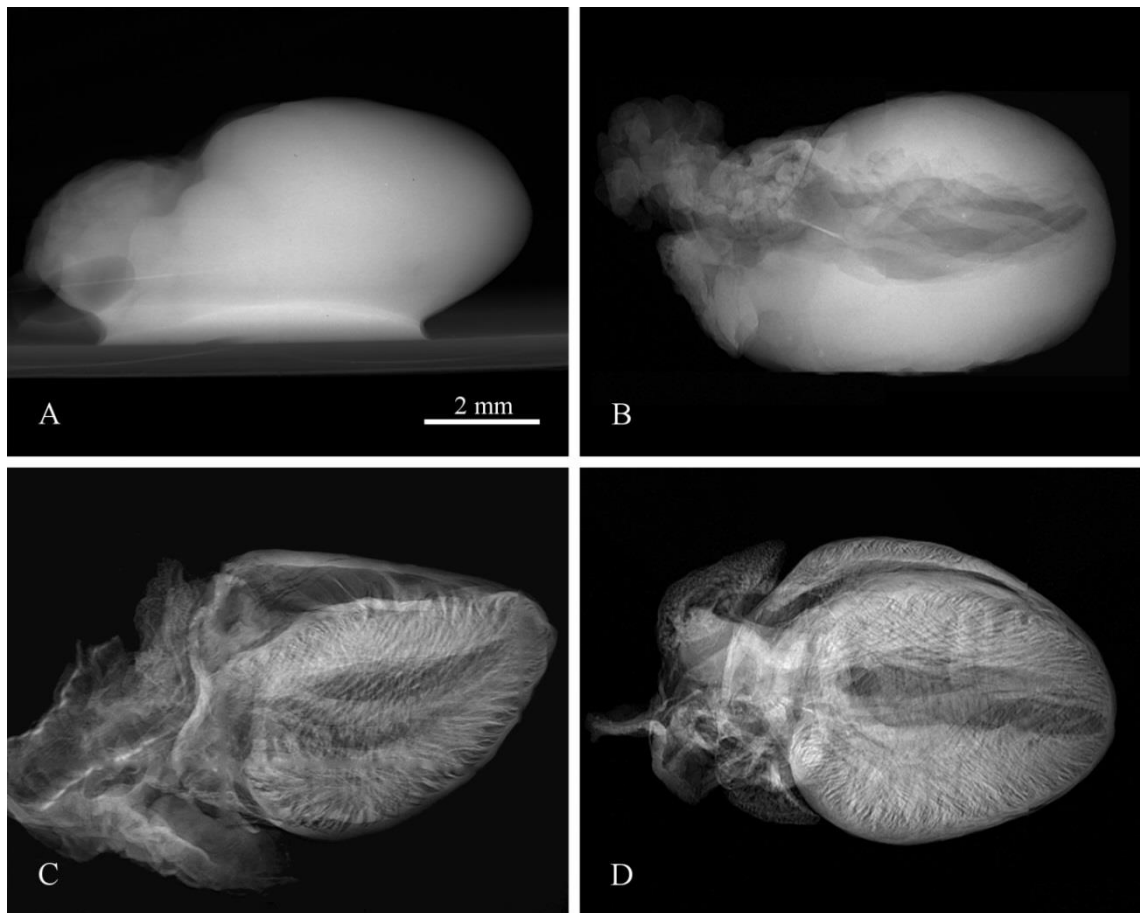


Figure 69: Demonstration of the contrast improvement in X-ray micro-radiography between a native sample and ethanol preserved samples. X-ray radiography of a native mouse heart (A) and samples preserved in 50% ethanol solution (B), 100% ethanol solution (C) and the ethanol series of increasing concentrations (D). Acquisition parameters: Tube voltage 60 kV, current 120 μ A, acquisition time 40 s. The image was taken from an own publication [128].

Virtual histology techniques typically rely on sample staining using various contrast agents to increase the intrinsic radio-density of soft tissue. In the case of Timepix detectors it was, nevertheless, demonstrated that a detectable improvement of tissue contrast is achieved by simple ethanol-induced dehydration of the tissue. The effect of ex-vivo tissue contrast enhancement was previously reported in studies dealing with phase-contrast X-ray imaging [149 – 152]. Concerning absorption-contrast X-ray imaging the use of ethanol has been known a tissue fixative prior the contrast staining was performed. Timepix detector, due to enhanced CNR as a consequence of dark-current-free photon

counting, is capable of visualizing fine inner structures of ethanol-preserved soft tissue samples even without further contrast staining. The advantage of such approach is that it preserves the samples unchanged for standard imaging techniques. As ethanol preservation belongs to standard steps in histology, it would be possible to incorporate the micro-CT scan in a standard processing chain of histology samples. This would not be possible with contrast-stained samples as the staining is in many cases irreversible.

The ethanol preservation causes denaturation and dehydration of the tissue. It also stiffens the tissue the samples to become more stable to easily withstand a CT scan without undesirable structural changes. The ethanol-induced contrast compared to a native sample is demonstrated at an example of mouse heart in figure 69. Microradiography of the native heart kept in saline (figure 69A) provides minimal contrast of inner structures as ventricles and veins are still filled by blood or by a saline solution that almost has the same attenuation properties as the surrounding heart muscle tissue. On the other hand, in the case of ethanol preserved hearts (figure 69B – D) the microradiography reveals numerous details of sample inner structures. The gained contrast developed during first days of fixation, as ethanol penetrated the tissue in all tested samples. However, the contrast becomes stable without further changes after 7 days in ethanol solution. All samples presented in this work were preserved for at least 7 days. The best results were achieved if a sample was preserved in a series of ethanol baths with gradually increasing concentrations.

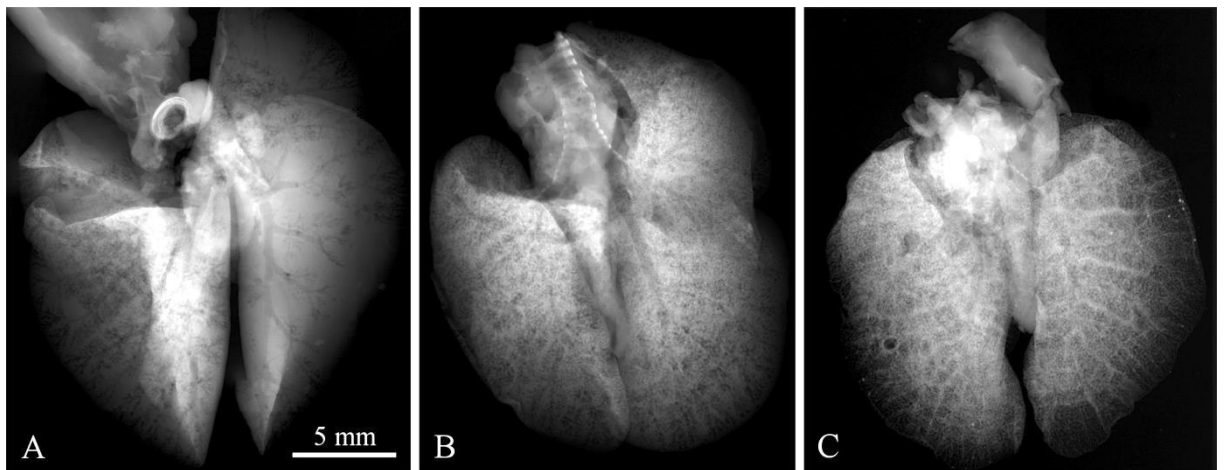


Figure 70: Contrast development in X-ray micro-radiography of ethanol-preserved mouse lungs as a function of resting time. Three different samples scanned after 10, 20 and 40 minutes of relaxation, respectively, are shown. Short resting time makes the trachea and bronchial tree being visible (A), while longer resting time leads to discernment of the alveolar structures of lungs. In (B) a superposition of bronchial and alveolar structures are visible, in (C) the alveolar structures hinder the visibility of the trachea and bronchial tree. Acquisition parameters: Tube voltage 60 kVp, current 120 μ A, acquisition time 40 s. The image was taken from an own publication [128].

The samples are scanned outside the fixative, to gain the contrast. As ethanol evaporates much faster than water, it quickly leaves all kind of cavities as ventricles, vessels, bronchi etc. Structures that are normally filled by liquid become hollow and produce detectable absorption contrast. It was observed that the detectable contrast developed as a function of resting time (the time delay between removing the sample from the ethanol solution and the measurement). The contrast development is demonstrated in figure 70 at example of mouse lungs. Different lung samples A, B and C were extracted from the ethanol solution and rested on paper towel in air for varying time periods. The sample A mostly shows the trachea and its bifurcations since rested for just 10 minutes. At longer rest time, finer structures start appearing (see fig. 2 B). Finally, the contrast of the trachea and bronchial tree is almost

completely shadowed by pronounced alveolar structure (see fig. 2 C). The resting time is of key importance, especially for CT scans, as it is expected that the sample would be stable during the scan. Resting time of 40 – 60 minutes was sufficient in most cases.

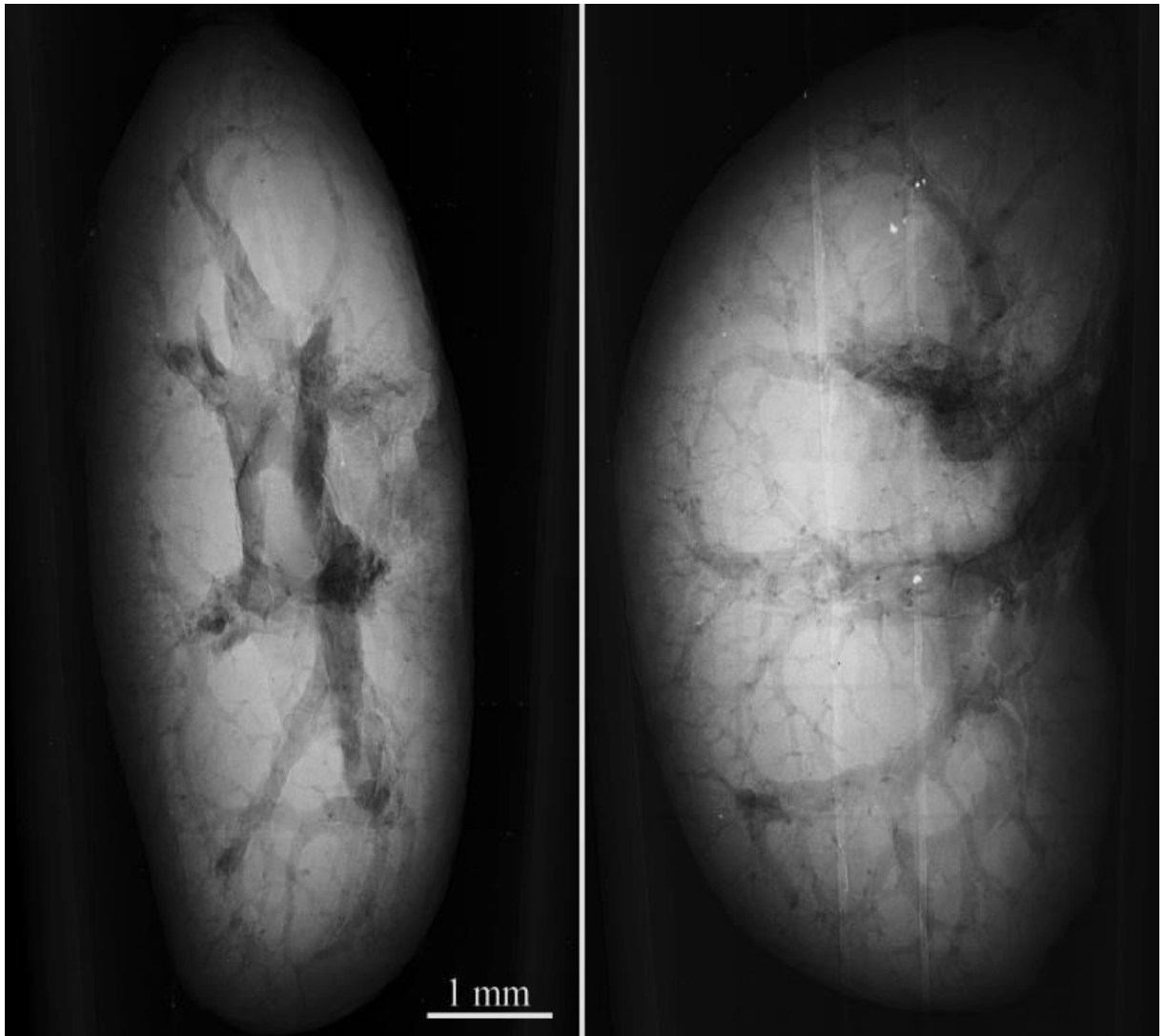


Figure 71: X-ray projections of ethanol preserved mouse kidney acquired with EPS of 2.5 μm . The projections reveal the vasculature of the kidney with great detail. Acquisition parameters: Accelerating voltage 60 kV, current 90 μA , acquisition time 10 s.

Ethanol preservation induced a contrast improvement in all tested inner organs. The best results were obtained in the case of kidneys, heart, liver and brain. Figure 71 shows two different radiographic projections of mouse kidney acquired with EPS of 2.5 micrometers revealing its vasculature. The finest visualized vasculature structures were approximately 8 micrometers in diameter. Such dimensions are proportional to the smallest venules (diameter 7 – 1000 μm) or capillaries (diameter 5 – 10 μm) – the finest structures of the blood pool system.

Micro-CT scans of mouse heart samples revealed not only the arrangement of ventricles and atria, but it also clearly showed the heart vortex – helical composition of muscle wall of ventricles. Figure 72 shows a virtual section through volume rendering of one of scanned heart samples and for selected axial slices with visible muscle-fiber structure. Furthermore, the heart valves were

successfully visualized (mitral valve denoted by the red arrow in figure 72). Finally, chordae tendineae – fine tendons keeping heart valves under tension – were visualized (see figure 72). 3D visualization of mouse heart with such detail has been previously reported only using phase-contrast CT at synchrotron facilities [128].

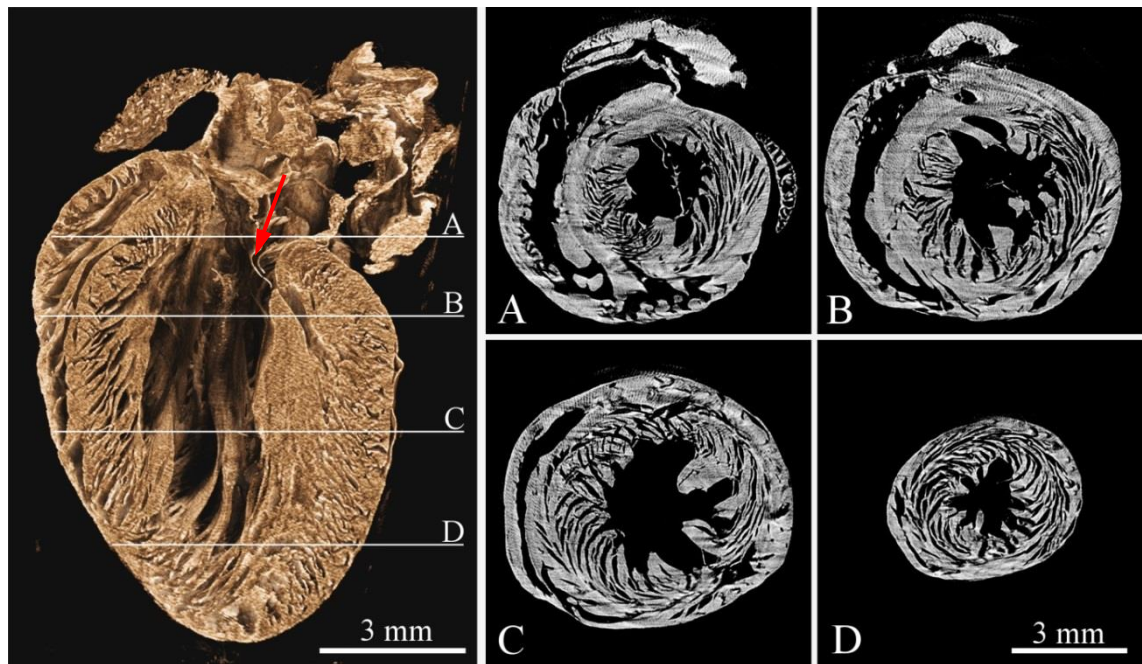


Figure 72: Tomographic reconstruction of an ethanol-preserved mouse heart. The left image shows the volume rendering of reconstructed dataset visualized using the false-color system. The red arrow points to successfully visualized mitral valve. The right part of the figure shows four different transversal slices (see labels A – D) across the reconstructed volume demonstrating the heart vortex – helical structure of the muscle. Acquisition parameters: Tube voltage 70 kV, current 100 μ A, 720 projections, acquisition time 5 s per projection. Spatial resolution 7.2 μ m. The image was taken from an own publication [128].

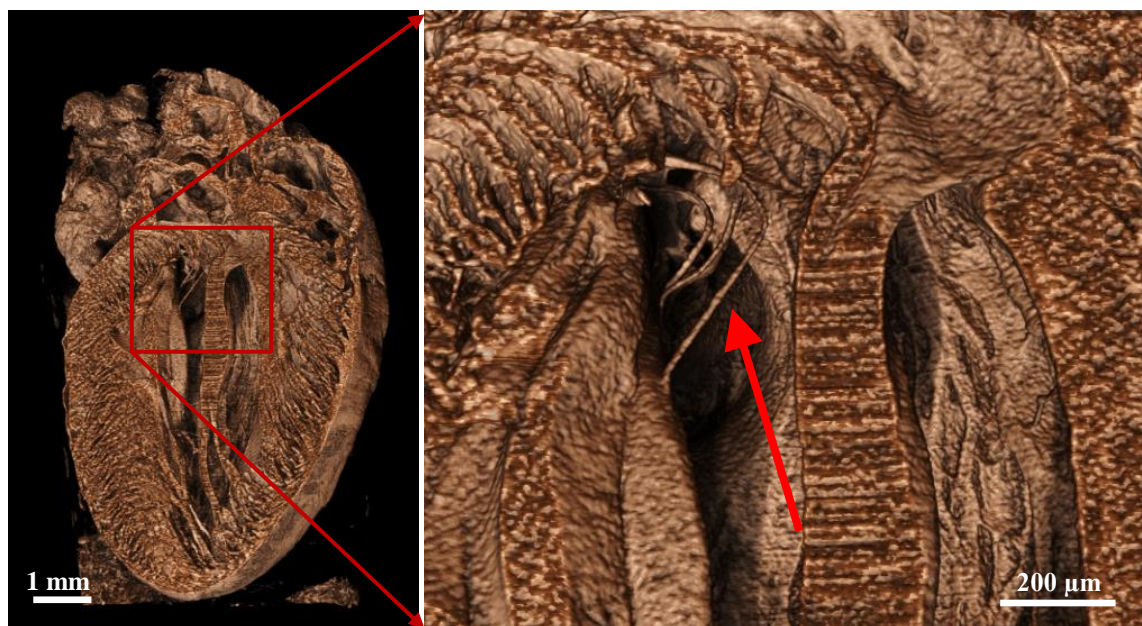


Figure 73: Micro-CT scan of a mouse heart sample reveals chordae tendineae – fine tendons keeping tension on heart valves.

The results of brain micro-CT (see figure 74) were compared with Allen Mouse Atlas Library [153]. The comparison resulted in identification of 42 white matter and 53 gray matter brain structures. The achieved scan resolution ($< 5 \mu\text{m}$) significantly exceeded the spatial resolution of available 3D mouse brain atlases. The highest resolution was approximately $32 \mu\text{m}$ as these are usually based on nuclear magnetic resonance imaging [154]. Similar results have been obtained by micro-CT techniques earlier but using high-Z contrast agents in all cases or using phase-contrast imaging. An example of results of a micro-CT scan of a contrast-stained mouse brain was shown in chapter 3.2 figure 21. The micro-CT slices presented in figure 74 provide comparable result without a need to use a high-Z contrast agent.



Figure 74: Micro-CT scan of an ethanol-preserved mouse brain reveals a number of clinically relevant anatomic structures. Acquisition parameters: Tube voltage 60 kV, current $100 \mu\text{A}$, 848 projections, acquisition time 3.6 s. per projection. Voxel size $4.4 \mu\text{m}$. The image was modified from an own publication. The data interpretation performed by skilled neuroanatomists is detailed in the published study [155].

While the previously presented data were all based on physiologic samples the figure 75 demonstrates a result of micro-CT scan of mouse liver infected with parasitic tapeworm larvae. Although in this case the used resolution was approximately 20 μm only it was fully sufficient to clearly detect the presence of pathologic cysts created by a certain developmental stage of tapeworms. Thanks to the provided data, it is extremely easy to evaluate the number of cysts or their dimensions without cutting the sample apart.

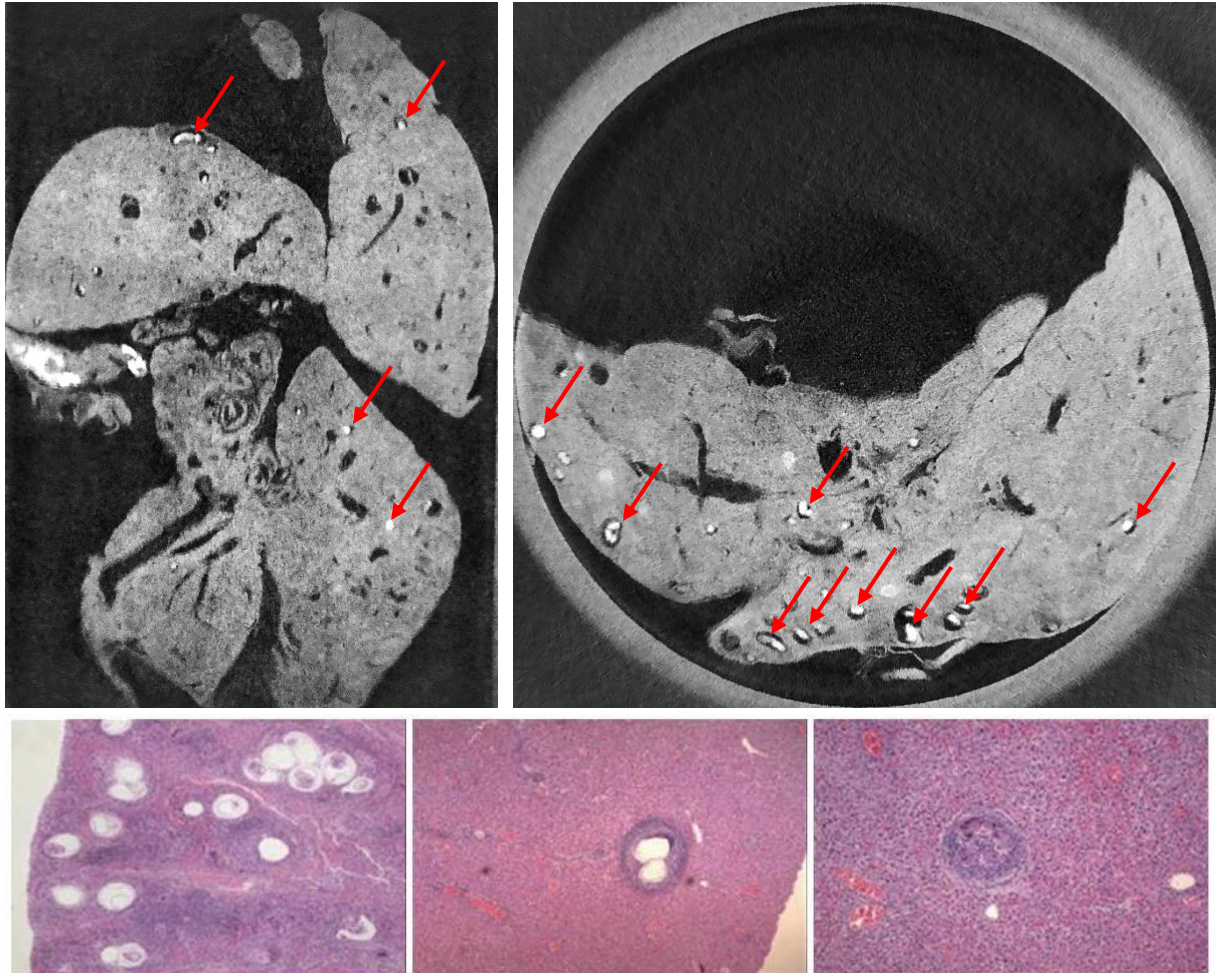


Figure 75: Micro-CT scan of ethanol-preserved mouse liver infected with parasitic worm *mesocostoides corti* (top row) and an example of histology analysis of the same pathology (lower row). The cavities visible within the tissue in CT slices are partially the liver vasculature and partially a pathologic hydatid cysts created by the worms development. The cysts are very well visible – denoted by red arrows. The sample was kindly provided by RNDr. Jana Bulantová, Ph.D., Charles University in Prague. The histology images were taken from [156].

9.4 Considerations towards in-vivo imaging with available devices

A set of simulations and experiments verifying the applicability of the available small-animal scanner (introduced in chapter 5) was carried out in cooperation of IEAP and National Radiation Protection Institute (NRPI). The X-ray spectrum of the installed X-ray tube was modelled using SpekCalc software [20] and convenient beam filtration was suggested. Considering the quantum efficiency of the currently installed detector (Timepix Quad, 300 μm silicon sensor) it was decided to use 250 μm aluminum filter. Figure 76 shows the simulated spectrum of KEVEX PXS11-8012 operated at 70 kVp, 150 μA with previously mentioned aluminum filter.

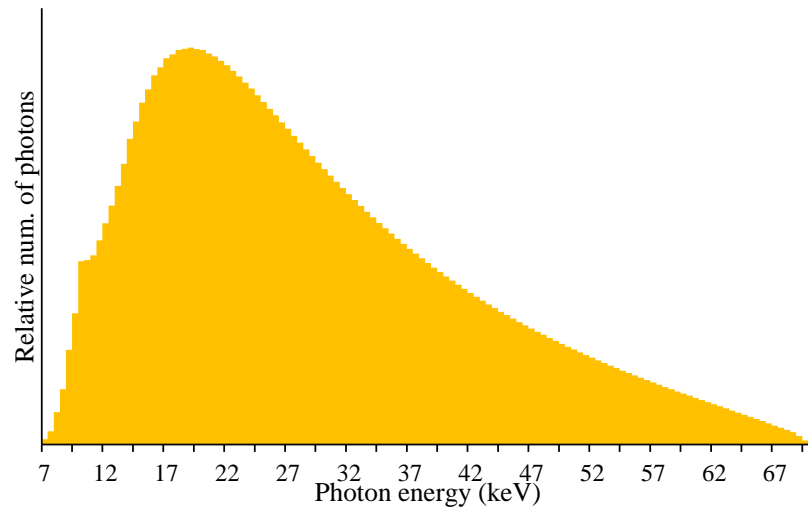


Figure 76: Simulated X-ray spectrum of the Kevex PXS11-8012 operated at 70 kVp, 150 μ A with 250 μ m aluminum filtration. The spectrum was simulated using SpekCalc software [20]. Courtesy of RNDr. Libor Judas, Ph.D., NRPI.

A polyethylene phantom with dimensions appropriate to a laboratory mouse was created. The phantom contained a cavity dedicated for insertion of a thermo-luminescent dosimeter. The measurements with the thermo-luminescent dosimeters placed inside the phantom showed that the dose rate was 2.1 mGy per second at the sample position in the case of 44 μ m EPS and the spectrum shown in figure 76.

9.4.1 Acceptable radiation dose for micro-CT of rodents

Previously published studies focused on X-ray irradiation of rodents concludes that a lethal radiation dose for a laboratory mouse is generally in range of 7 – 11 Gy [157] depending on the age and specie of the specimen. Such radiation dose causes complete myeloablation. The referred level LD50/30 (a dose causing death of 50% of irradiated specimens within 30 days) is 5 – 7.6 Gy [158]. Such a dose level is obviously way too high for practical micro-CT measurements. It was also reported that immunosuppression was observed in case of doses exceeding 500 mGy [157]. Rodents are capable of recovering from a dose of 250 – 500 mGy within a day according to [159]. A standard radiation dose of an *in vivo* micro-CT scan of a mouse seems to be 100 – 300 mGy, although scans with dose as low as 16 mGy have been reported [158; 160; 161]. Such dose is non-lethal, however, it can already induce deterministic effects.

An acceptable scan time for an *in vivo* mouse scan using the available micro-CT scanner can be easily calculated based on the mentioned dose limits, taking into consideration the experimentally measured dose rate. The total scan time should be within the time range of approximately 50 – 250 seconds for achieving dose of 100 – 500 mGy.

The dose is also closely connected with the achievable spatial and contrast resolution. A dose of 250 mGy should be capable of providing 1% contrast resolution for 135 μ m voxels based on published simulations [73]. The dose proliferates to 5 Gy for 65 μ m if the same contrast resolution is required. The published results are in an agreement with the calculations performed by NRPI in frame of experimental verification of the available small animal scanner dose rate. Considering 50 μ m voxel size, the dose required for contrast resolution of 5 or 2 % is 100 mGy or 640 mGy, respectively based on the NRPI calculations (courtesy of RNDr. Libor Judas, Ph.D., NRPI).

9.4.2 Parameters of the available small animal scanner

The total scan time – the time contributing to the delivered radiation dose – can be easily estimated as a product of time needed for capturing a single projection and total number of projections in the dataset. The projection capture time can be further divided into three components:

- Data acquisition time – active time of data collection while the detector shutter is open
- Data read-out time – data processing and saving to hard drive while the detector shutter is off.
- Sample positioning – setting a desired angle of projection

The latter two are generally undesirable since they do not contribute formation of the data while they increase the delivered radiation dose. Terms of total scan time (TST – overall time the sample spends in the scanner) and total acquisition time (TAT – sum of acquisition time of all captured projections) will be used in further text. Ratio of TAT and TST would be equal to one in an ideal case. In the case of a real scanner, the value of the ratio gets smaller depending on the detector read-out time and angular positioning speed.

Both mentioned parameters have fixed values and can be hardly optimized in the case of available small animal scanner. The detector read-out is approximately 200 ms, and changing the gantry angular position takes 600 – 900 ms, depending on the angular step between adjacent projections. That unfortunately means that approximately 260 seconds is needed just for the movement of the gantry considering a 360-degree scan with 1 degree angle step. Figure 77 shows a slice of micro-CT reconstruction of a mouse phantom scanned into a dataset consisting of 195 projections with an angular step of 1 degree and 250 ms acquisition time. The TST was 238 seconds, therefore, the dose absorbed by the sample was approximately 500 mGy. The TAT/TST ratio of the scan was approximately 0.2 only, meaning that 80 % of the absorbed dose was accumulated uselessly. It implies that the direct use of the available scanner is possible but very limited.

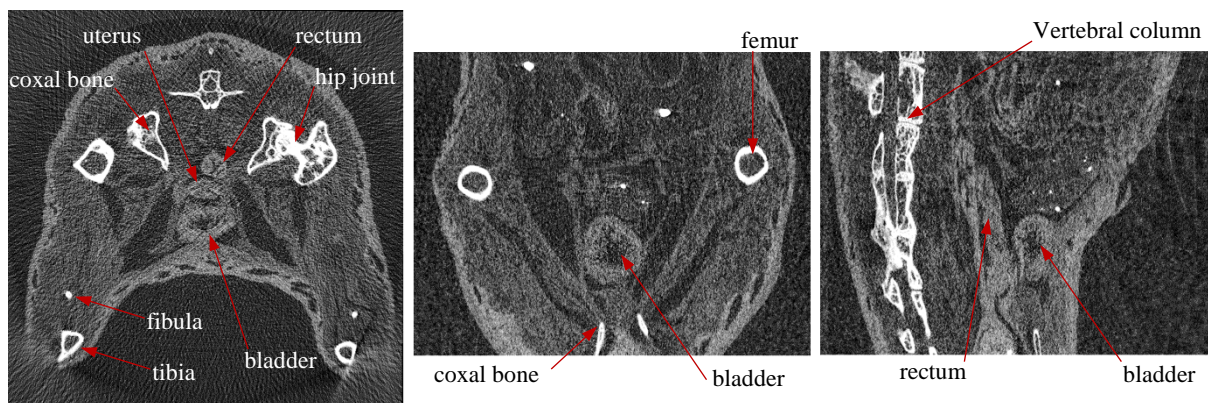


Figure 77: Results of micro-CT scan with of pelvic area of PlastiMouse™ phantom acquired with EPS of 44 micrometers. The TST was 238 seconds and, therefore, the absorbed dose was proportional to 500 mGy. Unfortunately, 80 % of the dose was accumulated uselessly due to low TAT/TST ratio.

A reduction of the TET/TST ratio is not feasible, since it is not possible to speed up the gantry movement without compromising the positioning accuracy and the read-out speed of the installed detector is given. The possible solution which is being explored now is based on reduction of dose rate while the detector shutter is off. Switching the tube periodically off is not possible due to the slow rise-up of the source output power. Suitable solution might be an implementation of a fast mechanic shutter to shield the beam during data read-out and gantry positioning.

9.4.3 Experimental evaluation of achievable data quality with respect to radiation dose and data sampling strategy

This section introduces an experimental phantom study on the micro-CT data quality in dependence on absorbed dose and data sampling strategy. The maximal data quality achievable by the current setup with absorbed dose less than 500 mGy is demonstrated in Figure 77. Higher absorbed dose induces immunosuppression in rodents as it was already mentioned. An adaptation of the CT scanner by installation of a fast mechanic shutter for shielding the beam while the data are being read-out and the mechanics are moving is, therefore, a necessity for practical *in vivo* use. The conclusions made in this section are based on an assumption of an ideally working beam shutter.

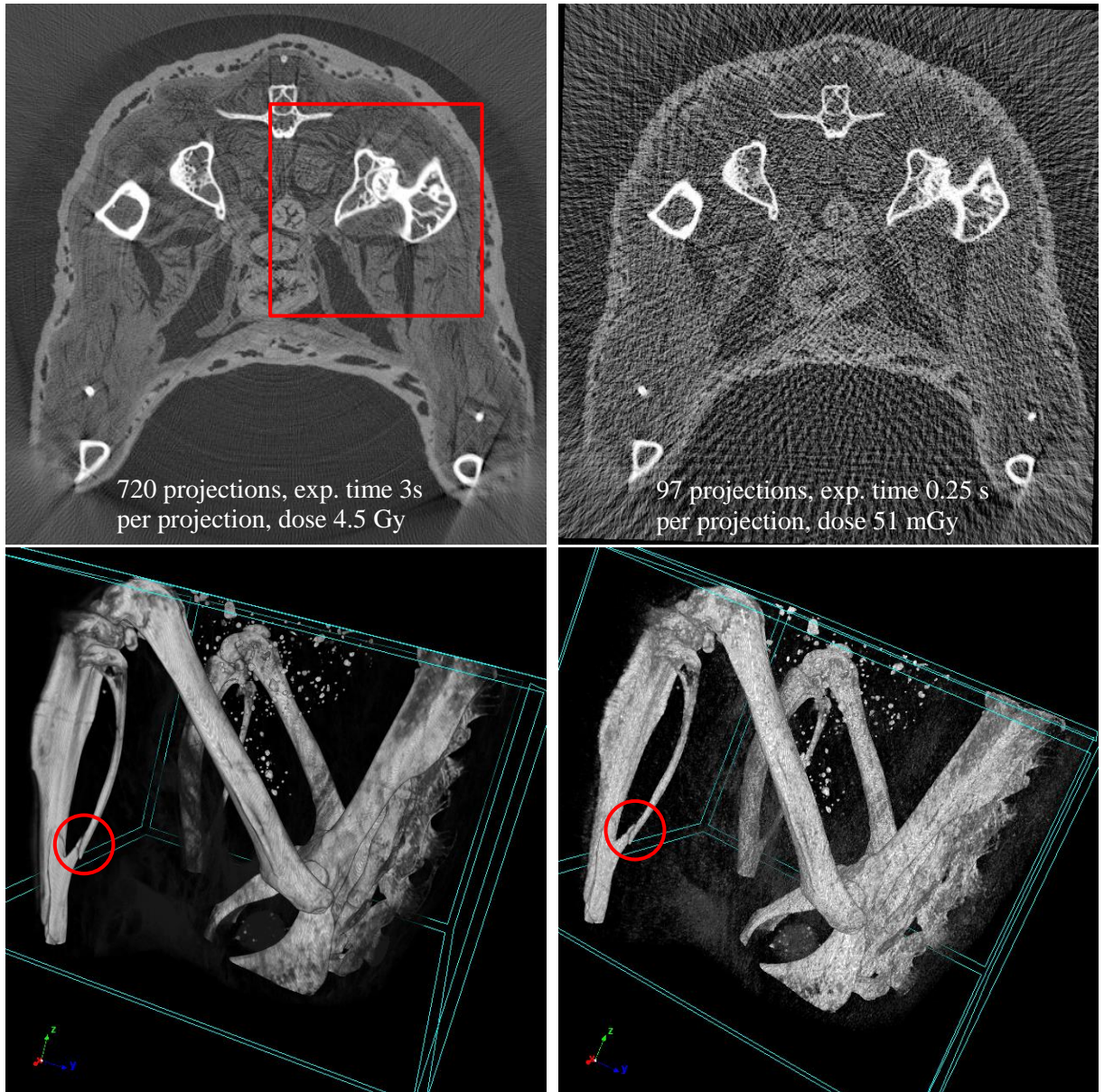
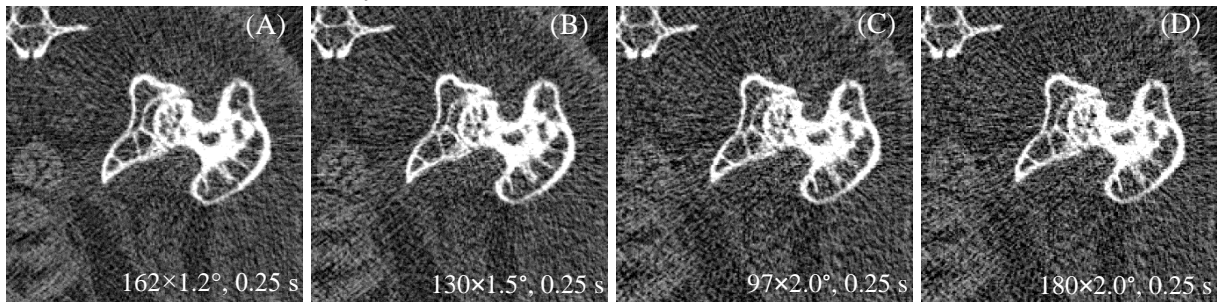


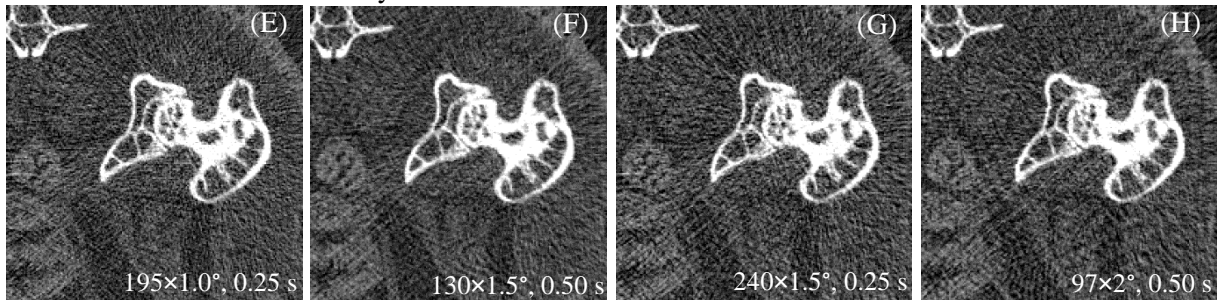
Figure 78: Comparison of the same slice (top row) and volume rendering of the skeleton (lower row) of the PlastiMouseTM phantom scanned with total acquisition time of 2160 seconds (left) and 24.5 seconds (right). It is clearly visible that the low-dose data suffer from high noise level and angular sampling artifacts but it is fully sufficient i.e. for visualization of bone fractures (denoted by red circles). The red square denotes a region of interest used for further analysis of the data shown in figures 79 and 80.

A set of measurements was carried out to experimentally verify the data quality provided by the scanner, if the mentioned dose restrictions are considered. PlastiMouseTM phantom was used instead of a living mouse for the measurement. The phantom was scanned multiple times with different values of angular step and exposure time per projection. A total number of 112 micro-CT datasets was created, combining angular sampling from 0.5° to 2° with exposure time within range from 0.25 to 3 s per projection. All measurements were carried out using a Timepix Quad detector with 300 μm thick silicon sensor. Figure 78 shows a comparison between the same dataset created with the highest dose (720 projections, acquisition time 3 s per projection, absorbed dose 4.5 Gy) and with the lowest tested dose (98 projections, acquisition time 250 ms per projection, absorbed dose 51 mGy). The low-dose image obviously suffers from high image noise and presence of angular sampling artifacts that degrade the contrast resolution, especially in soft tissue. On the other hand, it is still capable of clear visualization i.e. bone fractures (lower row of figure 78).

Absorbed dose 51 – 100 mGy:



Absorbed dose 101 – 150 mGy:



Absorbed dose 151 – 200 mGy:

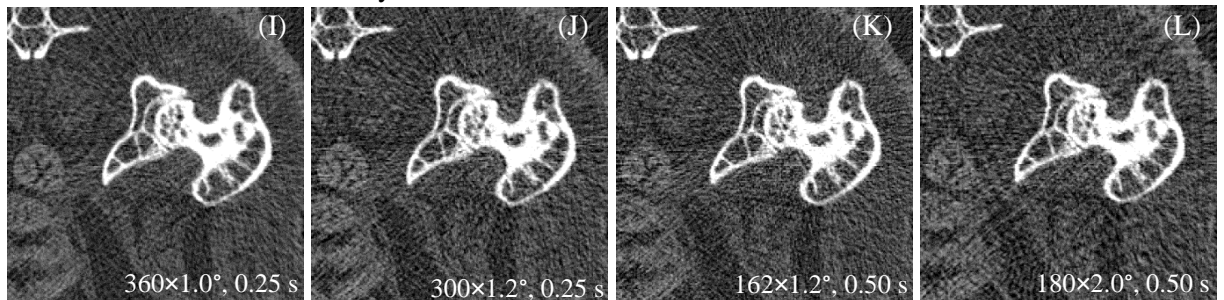
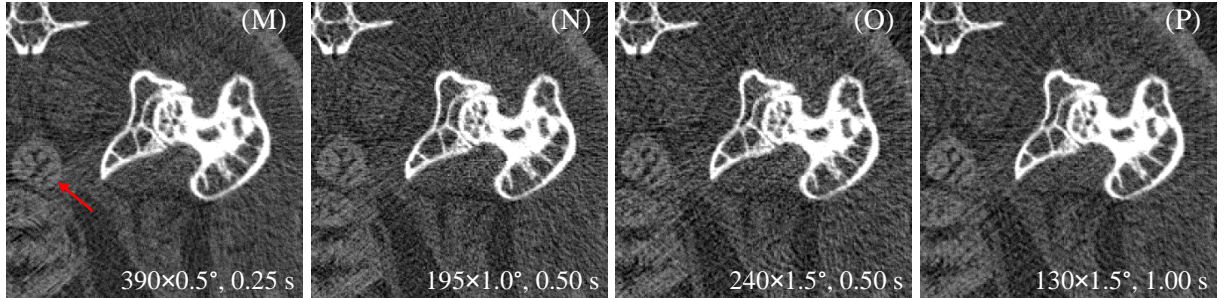


Figure 79: ROI of a set of CT reconstructions acquired with absorbed dose within an interval of 51 – 200 mGy. The note at each image denotes “number of projections × angular step, acquisition time per projection”. The noise level decreases with dose increase as can be expected. On top of that, the detail detectability within a “dose category” improves with reduction of angle step.

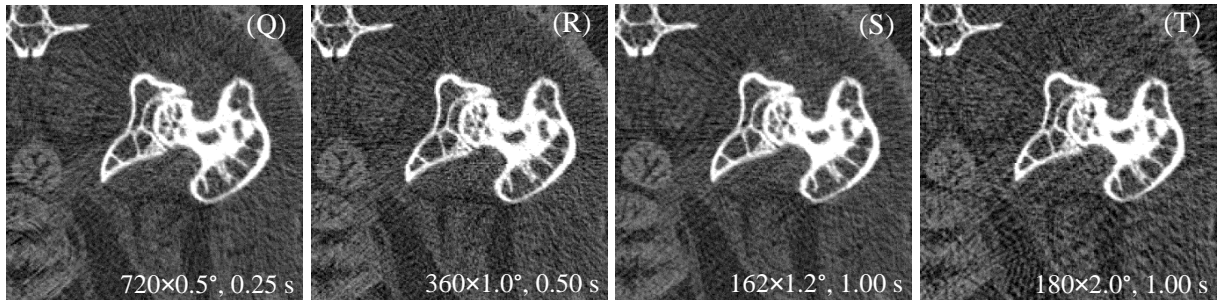
Figures 79 and 80 show a region of interest containing bone and several different soft tissue structures (skin, muscle, rectum, bladder and uterus) acquired with absorbed dose between 51 mGy and 500 mGy, and with different angular sampling. The absorbed dose grows from top row to bottom row

while the angle step increases from the left to the right. Actual acquisition parameters of each of presented datasets are denoted at the image in the form of “*number of projections × angular step, acquisition time per projection*”. It can be observed that the noise level is indirectly proportional to the absorbed dose. It can be also noted that the detail detectability is generally better in the case of finer angular sampling. I. e. the fine structure of rectum is visualized with similar detail in figure 80 (M), (W) and (X) although the latter two were formed from data with reasonably higher absorbed dose.

Absorbed dose 201 – 300 mGy:



Absorbed dose 301 – 400 mGy:



Absorbed dose 401 – 500 mGy:

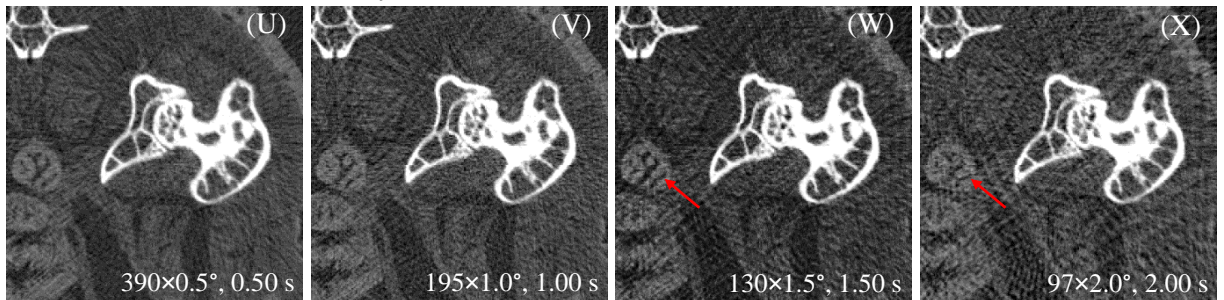


Figure 80: ROI of a set of CT reconstructions acquired with absorbed dose within an interval of 201 – 500 mGy. The note at each image denotes “*number of projections × angular step, acquisition time per projection*”. The noise level decreases with dose increase as can be expected. On top of that, the detail detectability within a “dose category” improves with reduction of angle step.

A further objective evaluation of the presented data is shown in figure 81. It shows contrast-to-noise ratio between two different soft tissue types (skin and muscle) and contrast-to-noise ratio of bone with respect to muscle. The data are plotted in dependence on absorbed dose and projection angle step. Both plots confirm the previously stated observations regarding the improved detail detectability for finer angular sampling.

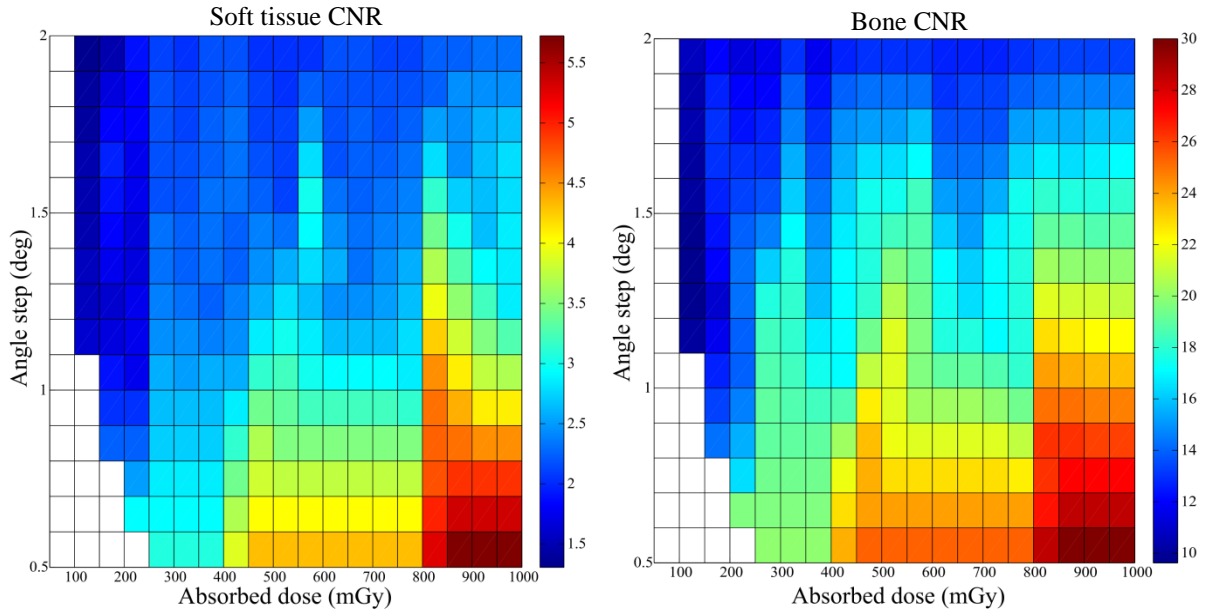


Figure 81: Contrast-to-noise ratio of soft tissue (left) and bone (right) with respect to absorbed dose and projection angle step.

9.4.4 *In vivo* considerations summary

It should be stressed again that the presented conclusions are valid under an assumption of an ideally functioning fast beam shutter. The CNR of bone fulfills the Rose criterion ($CNR > 5$; [162]) even for the lowest values of absorbed dose. Soft tissue requires a dose of more than 800 mGy to cross the criterion level. Therefore, it can be assumed that different types of soft tissue would not be resolvable using the tested detector. A detector with 300 μm thick silicon sensor was used for acquisition of the presented data. Therefore, a significant part of the beam is omitted due to quantum efficiency of silicon. The detection efficiency of the sensor is 22 % for given spectrum only. Utilization of a different detector with higher sensor efficiency would further improve the imaging performance. A CdTe sensor of 1 mm thickness would provide quantum efficiency exceeding 99 % for the given spectrum. The comparable data quality, as presented in figures 79 and 80, could be obtained using 4times lower absorbed dose under such circumstances. Alternatively, the CNR could be improved while the dose would be conserved. Soft tissue CNR could fulfill the Rose criterion at dose level of 200 mGy.

10 Spectral micro-CT using large area Timepix detectors

Since Timepix technology belongs to PCD family, it works in energy-resolving mode and thus, it is applicable for energy-sensitive radiography and CT. As it was stated earlier, spectral radiography and CT is understood as imaging approaches using more than two individual energy channels for characterization of the scanned object.

In the case of DECT, it is usually possible to identify one exogenous contrast agent. Typically iodine-based contrast is differentiated from bone signal. Spectral CT provides a capability to resolve more substances from a single CT scan. Considering clinical applications, it will be possible i.e. to visualize the vascular system, digestive system and pulmonary ways in one scan if three convenient contrast agents would be used. The aim of this chapter is to demonstrate capabilities of large area Timepix detectors for simultaneous imaging of several contrast agents in small-animal scale, and their identifications using addressing absorption edges in their linear attenuation coefficient.

Absorption edge is an abrupt increase of attenuation coefficient at an energy close to the binding energy of an inner electron shell of an atom – typically a K-shell. As the edge position is characteristic for each element, it is possible to use it for identifying a certain material based on the content of the concerned element. K-edges are provided by elements with Z higher than approximately 40 (zirconium, K-edge 18 keV) in energy range relevant for X-ray imaging. The upper limit cannot be clearly defined. However, addressing an absorption edge with energy significantly higher than 50 keV would be difficult, considering that small animal scanners typically utilize tubes with an accelerating voltage up to 70 keV or 90 keV. Iodine, barium and gadolinium (absorption edges 33.2, 37.4 and 50.2 keV, respectively) can be named as representatives of contrast agents suitable for K-edge identification for purposes of small animal imaging.

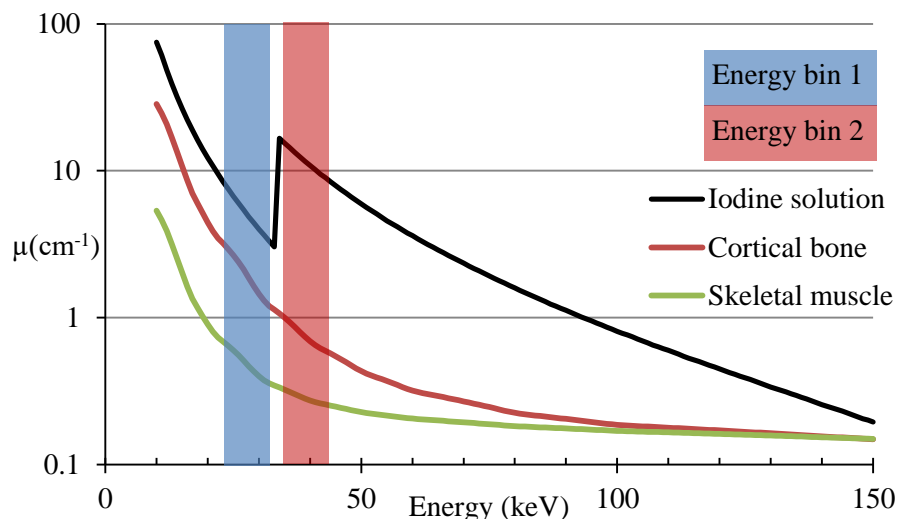


Figure 82: Linear attenuation coefficients of cortical bone, skeletal muscle and iodine contrast solution. While in the case of bone and muscle the linear attenuation coefficients decrease between energy bin 1 and 2, it raised for iodine as a consequence of absorption edge between both energy bins. The chart was created based on data from National Institute for Standards and Technology [51].

The idea of K-edge identification is based on taking an X-ray image with mean-energy below and another image with mean energy above the edge energy (see figure 82). Generally, the value of linear-attenuation coefficient decreases with energy. It can be, therefore, expected that radio-density of a certain material in CT slices will decrease with energy. This is the case of i.e. bone and muscle (red and green lines in figure 82). However, an absorption edge causes radio-density increase of certain materials for photon energies above the edge.

The arrangement of energy bins by means of their width and distance from the edge has key importance for edge detectability. The search for an ideal arrangement of energy bins for K-edge identification is a goal of many published studies. Depending on the specific conditions of each study, the conclusions are quite inconsistent as some publications suggest optimal energy bin 4 – 6 keV while others propose as ideal bin width of more than 30 keV [163; 164].

This chapter addressed the question of optimal energy bin parameters, specifically for Timepix detectors using a computer-based model. Furthermore, the capability of large-area Timepix detector with silicon sensor to differentiate four different materials within one CT scan on a phantom object is demonstrated.

10.1 ToT vs. threshold scan

Any Timepix device can be operated in three different modes (detailed in chapter 2.3.1). Two of them are applicable for imaging purposes – Time-over-threshold and Medipix mode. The device in ToT mode behaves as a fully spectroscopic detector and reports the energy deposited by each detected photon in form of a cluster-log. The Medipix mode, or so-called counting mode, collects information on number of photons that exceeded a user-adjustable energy threshold. While the Medipix mode provides directly radiographic projections, the cluster-log obtained from ToT mode is a list of event coordinates and deposited energies that has to be processed first to produce a radiographic projection. A radiographic projection based on any demanded energy range can be created from the cluster-log. Therefore the ToT mode provides a virtually unlimited flexibility in data post-processing. The Medipix mode requires a different approach if an X-ray image based on a discrete energy bin is required. An energy bin is created as a subtraction of two frames acquired with different energy thresholds. In such case, the position and width of the bin has to be decided before the data acquisition. The ToT mode, therefore, seems to be much more versatile and flexible. Unfortunately, practical reasons prevent the ToT mode to be used in routine X-ray imaging with large area Timepix detectors. The following paragraphs discuss the practical usability of both ToT and Medipix mode for high-resolution spectral-CT with LAD Timepix.

Data acquisition using Timepix detectors is frame-based. The device opens its shutter for a defined time and collects the incoming events. After the shutter is closed, the whole frame is read-out and analyzed. As the detector spectral resolution suffers from pile-up effects, it is necessary to acquire sparsely occupied frames to avoid pile-ups. Approximately 2000 events per frame on one chip are conventionally desired. Considering a pixel array of 256×256 pixels, the average occupancy is approximately 0.03 events per pixel. Now assuming that 1% contrast resolution would be demanded in the data, it is necessary to collect at least 10^4 photons per pixel (based on eq. 13). To integrate such image statistics, approximately 330 000 frames would be needed. Currently the LAD devices are capable of reading out no more than 10 frames per second (depending on the actual number of assembled chips). The conclusion based on stated facts unfortunately is that acquisition of a single X-ray projection in ToT mode would take more than 9 hours. Fully spectral radiography allowing

differentiation of different types of soft tissue was demonstrated [114]. The mentioned experiment proved viability and performance of the fully spectral approach; however, it was merely demonstrated on one X-ray projection of a phantom object using a single Timepix chip. Spectral CT with Timepix detector operated in ToT mode has not been demonstrated so far. A proof-of-concept experiment would be theoretically possible with a Timepix chip equipped with a parallel readout. Such device is capable of reading out several hundred frames per seconds [165]. In such case, the acquisition time for one projection could be reduced to several minutes. Such a CT scan would still be enormously time consuming but probably feasible.

The situation gets better with the new chip generation – Timepix3. Timepix3 supports event-driven read-out instead of frame-based. During the operation the shutter is constantly open and the events are read-out individually as soon as they occur [166]. The Timepix3 read-out should be capable of reading out up to 40 million of events per second [167]. Such read-out speed would collect 10^4 photons per pixel in less than 20 seconds. The maximal FOV of these devices is nowadays however still limited to size of a single chip (14 mm).

The detector in Medipix mode is capable of collecting 10^4 photons per pixel in less than 500 ms using a conventional micro-focus X-ray tube. Two frames need to be read-out and integrated due to the saturation level of the counter. Several consequent acquisitions with different thresholds are needed to be able to form demanded energy bins. Nevertheless, the exposure time per angular projection is still in the order of several seconds and thus, it is incomparably shorter to ToT mode. However, the threshold-based approach has also two drawbacks. The first drawback was already mentioned – the arrangement of energy bins has to be decided before the measurement is started and cannot be changed later. The other drawback comes from the fact that part of the incident spectrum is omitted due to the selected threshold. With higher threshold values, it can easily happen that waste majority of photons is ignored. It contributes to the dose deposited to the sample but does not contribute to the data. This fact has to be considered, especially in the case of potential in-vivo applications. This weakness can be solved by use of a detector that provides more thresholds per pixel – i.e. Medipix3 detector provides up to eight thresholds per pixel.

On the other hand, the sequential exposure of data with different thresholds has also advantages. The photon-energy distribution in a spectrum produced by an X-ray tube is highly non-uniform. Therefore, it can easily happen that while the low-energy bins are being saturated, the high-energy bins can suffer from the lack of photons in the case of fixed acquisition time. Sequential scanning allows individual adjustment of time for each threshold to achieve optimal image statistic and consequently improve contrast-to-noise ratio in high-energy channels this way.

10.2 Simulation of X-ray transmission near an absorption edge

A simple computer model was created to estimate the optimal parameters for energy bins, as the aim of this chapter is to demonstrate the capabilities of large-area Timepix detectors for simultaneous identification of several contrast agents within one volume by means of K-edge spectral CT. The model focuses on the relationship between energy bin width and its mean energy, with respect to the data CNR and detectable radio-density difference below and above the edge.

10.2.1 Modelling of X-ray beam and detector response

The computer model simulates the transmission of an X-ray beam through a layer of an absorber containing an element with absorption edge, and then compares it with the absorption in a layer of

water of the same thickness. The transmitted signal is linearized using a negative logarithm and the data values are normalized to HU units. The radio-density changes of the targeted material can be, therefore, directly compared between different energy bins.

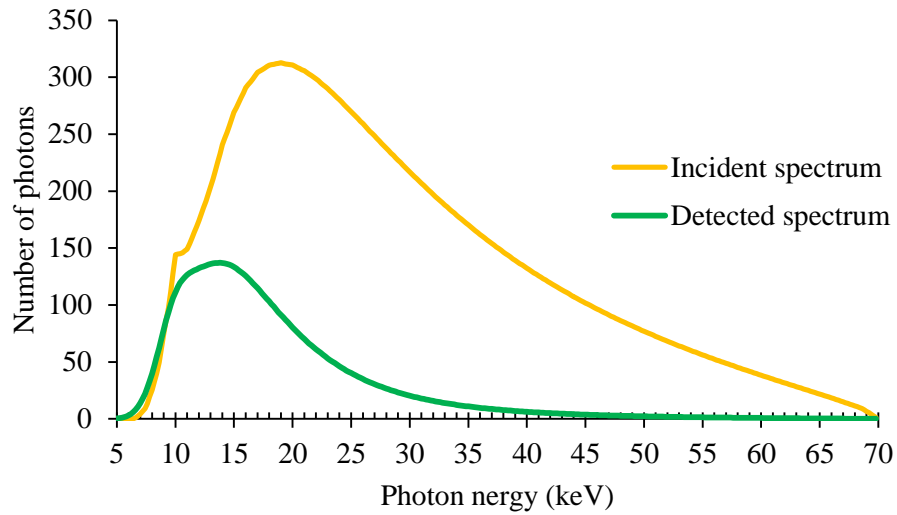


Figure 83: The simulated X-ray spectrum sampled in 0.2 keV steps used in the designed model. The yellow line demonstrates the spectrum produced by the X-ray source while the green line shows energy distribution detected by 300 μm silicon sensor. The photon distribution was normalized to achieve the value of integral under the red curve equal to 10^4 photons.

The model simulates the conditions of the available small animal scanner (introduced in chapter 5). The model assumes 70 kVp tungsten spectrum with 250 μm aluminum filtration (as shown in figure 76). Furthermore, it assumes the quantum efficiency of 300 μm thick silicon sensor and standard deviation of the detector energy resolution of 2 keV. Figure 83 shows the simulated incident X-ray spectrum produced by the X-ray tube (orange) and distribution of the detected spectrum (green line).

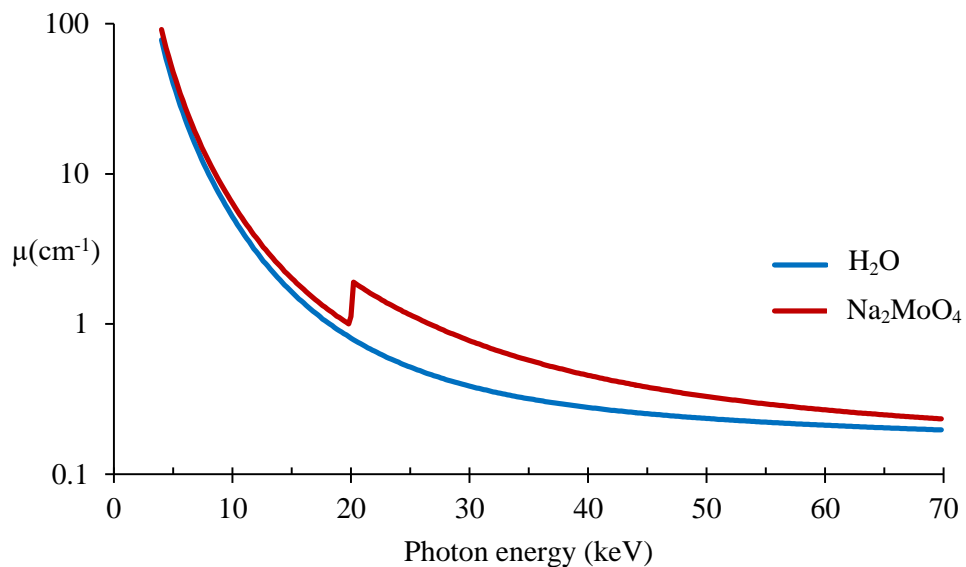


Figure 84: Linear attenuation coefficients of water (blue) and 5% aqueous solution of Na_2MoO_4 (red). The absorption edge at 20 keV is caused by presence of molybdenum. The chart was created based on data from National Institute for Standards and Technology [51].

The simulated spectrum irradiates an object consisting of 10 mm layer of water and the same layer of aqueous solution of Na_2MoO_4 . Five different concentrations from 1 % to 25 % were modelled. Figure 84 shows linear attenuation coefficients of both substances. The absorption edge at energy of 20 keV is caused by the presence of molybdenum. Figure 85 demonstrates the distribution of photon energies after it passes the mentioned absorbers. The beam transmitted through the molybdenum solution exerts a distinct discontinuity.

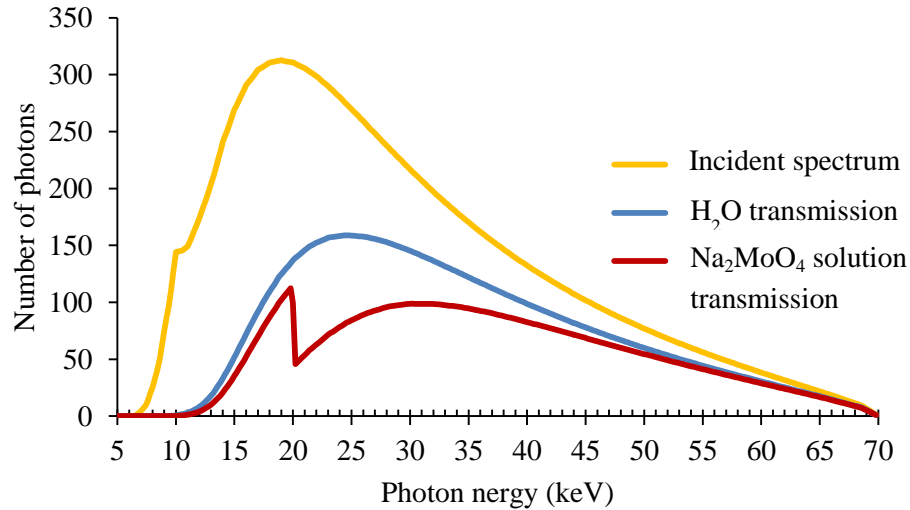


Figure 85: Energy distribution of the incident X-ray beam (orange) and the beam modified by attenuation in water and Na_2MoO_4 solution (blue and red).

Figure 86 then shows the same situation interpreted by the used detector. Unfortunately, the quantum efficiency of silicon sensor, together with energy resolution makes the K-edge discontinuity of molybdenum much less apparent. The energy distributions plotted in figure 86 are, nevertheless, proportional to the real behavior of the silicon sensor and, hence, were used for further calculations.

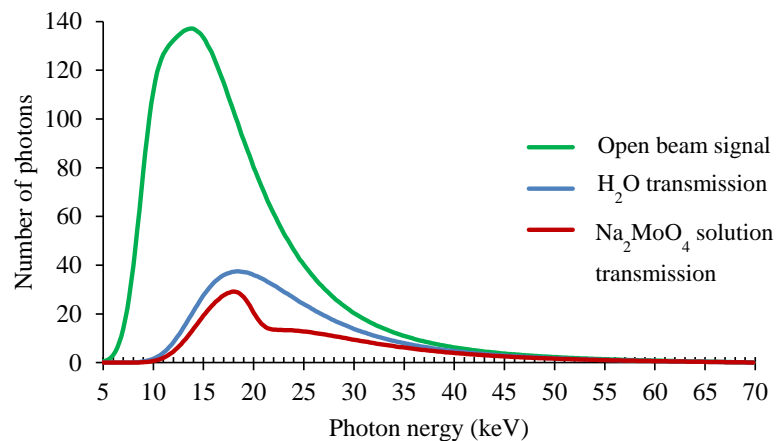


Figure 86: A response of 300 μm Si sensor with 2 keV standard deviation of the energy resolution to the X-ray spectra showed in figure 85.

10.2.2 Occupancy of energy bins with respect to its width and mean energy

Number of photons occupying an energy bin of certain width and mean energy were one of the studied parameters in the frame of this model. The simulated X-ray spectrum was normalized to provide the value of integral under the curve equal to 10^4 photons. A standard X-ray projection formed from such

number of photons provides a contrast resolution at a level of 1 % and is commonly used for micro-CT scans with PCDs. Figure 87 shows the results of the analysis. The chart clearly shows, that practical applicability of narrow energy bins is limited by photon starvation, although

that although narrow energy bins could potentially provide the best K-edge identification the practical applicability is limited by photon starvation. Considering an absorption edge with energy of 30 keV or higher, the number of photons per bin is just in the order of tens, which is insufficient. Of course the number of counts can be increased by higher beam intensity. In reality, it usually means prolongation of the exposure time. However, in this case the exposure time would need to be prolonged by an order or more to get sufficient photon statistic. As a reasonable tradeoff between the bin width and statistics seem to be lines representing bin widths from 4 – 10 keV. Under these conditions a bin with mean energy of 30 keV can achieve photon statistics within the range of approximately 500 – 1100 counts per pixel. Such X-ray projections can be successfully used for CT reconstruction although the result will exert increased noise level. Consequently, the bin width also defines the smallest distance between two absorption edges that can be differentiated from each other.

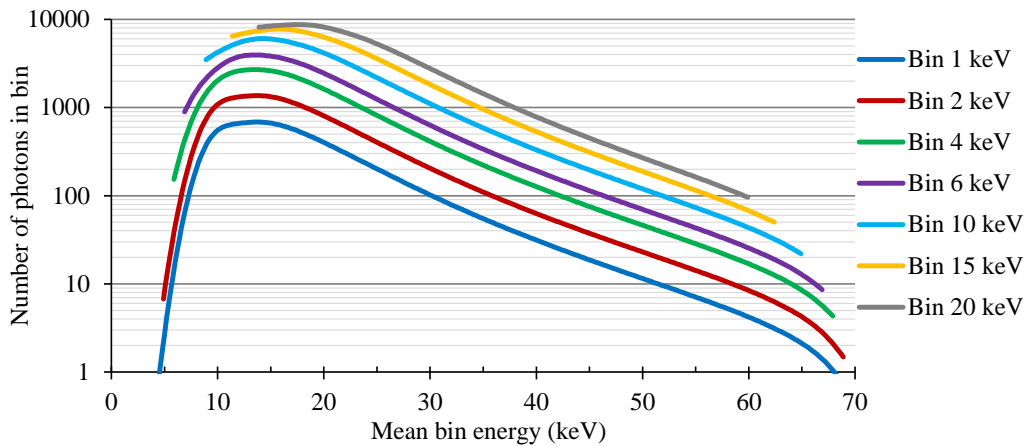


Figure 87: Number of photons occupying an energy bin of width in range of 1 – 20 keV in dependence on the bin mean energy. The curves assume the total number of photons in the X-ray spectrum to be 10^4 per pixel.

10.2.3 Radio-density increase above the absorption edge

The simulated data normalized to HU allow direct comparison of the radio-density below and above an absorption edge. The three plots presented in figure 88 show the dependence of radio-density on mean energy of the bin and its width for three different concentration of molybdenum. In a theory, assuming ideal response of the detector and infinitely narrow energy bins, the locally minimal radio-density would be expected directly under the absorption edge energy (20 keV) followed by abrupt increase. The parameters of the model – energy resolution, quantum efficiency and width of the energy bin – smears the discrete radio-density skip into a continuous rise-up with a round local maximum followed by slow decrease. A local minimum that might be expected below the absorption edge is not visible in the simulated energy range as a consequence of HU conversion. Considering the energy dependence of both molybdenum and water below the absorption edge (shown in figure 84) and principle of HU conversion (equation 4) the HU values of molybdenum solution gets smaller with decreasing photon energy. It can be therefore concluded that proper setting of the energy bin above the absorption edge (HE) is more important than parameters of the bin below the edge (LE). The LE bin can be much wider than HE bin without compromising the edge identification. The limiting factor

might be a proximity of an absorption edge of another element in the case of simultaneous imaging of multiple substances.

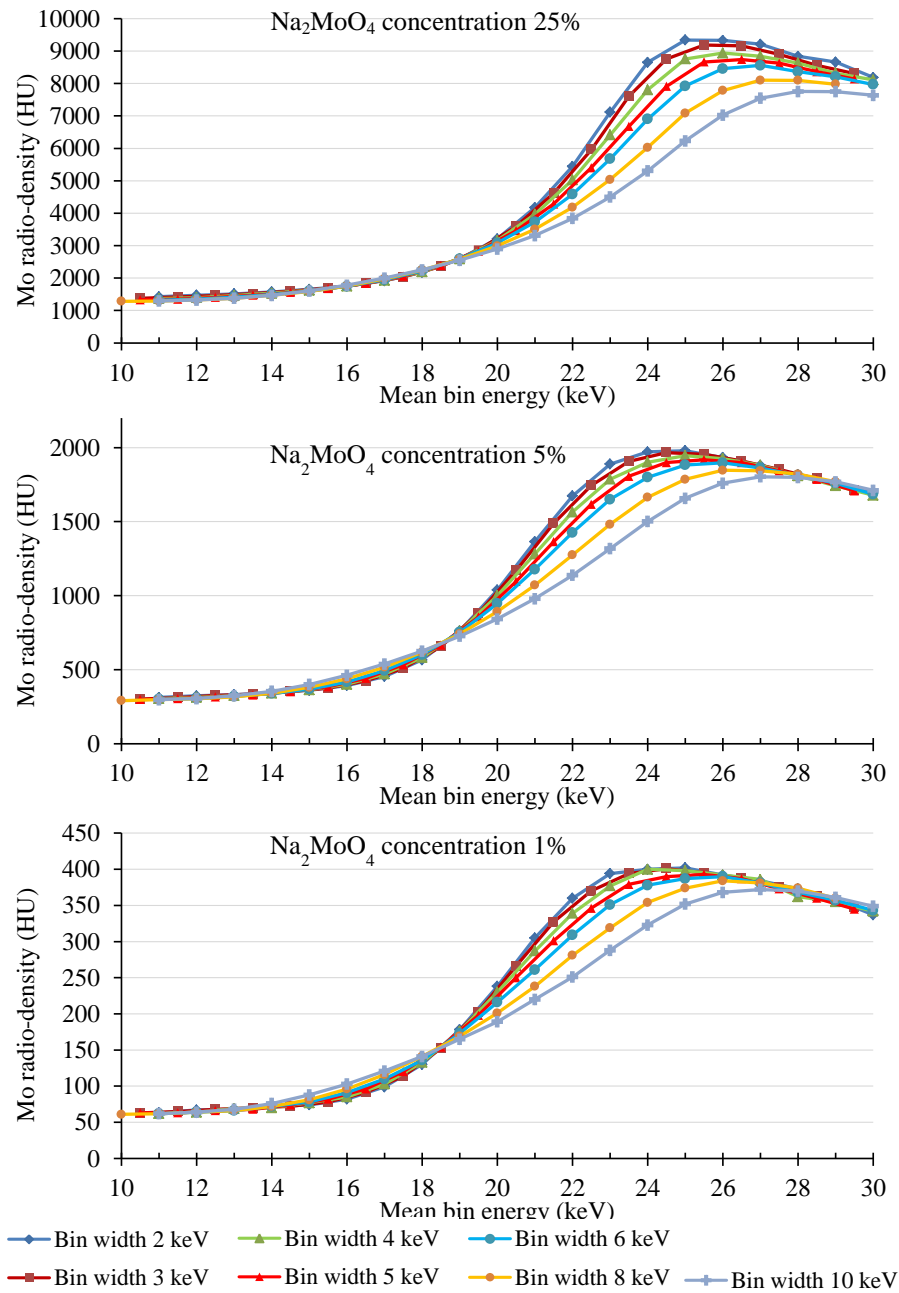


Figure 88: Simulated dependence of molybdenum radio-density near the absorption edge on the mean bin energy with respect to width of the bin demonstrated for three different concentrations of Na_2MoO_4 solution.

A detailed view to the charts in figure 88 shows that narrow energy bins represent the same substance by higher HU values. Further, it can be observed that the maximum of the curve is closer to the absorption edge energy for narrow bins. It can be also seen that the ratio of radio-density below and above the edge is not significantly dependent on molybdenum concentration, while the absolute radio-density values, off course, are concentration dependent. Plotting the radio-density values

of different molybdenum concentration into 2D space given by HU units of LE an HE bin can be approximated by a line trend. The more the line slope deviates from the diagonal of the space – which represents the water-like substances – the easier the absorption edge identification is.

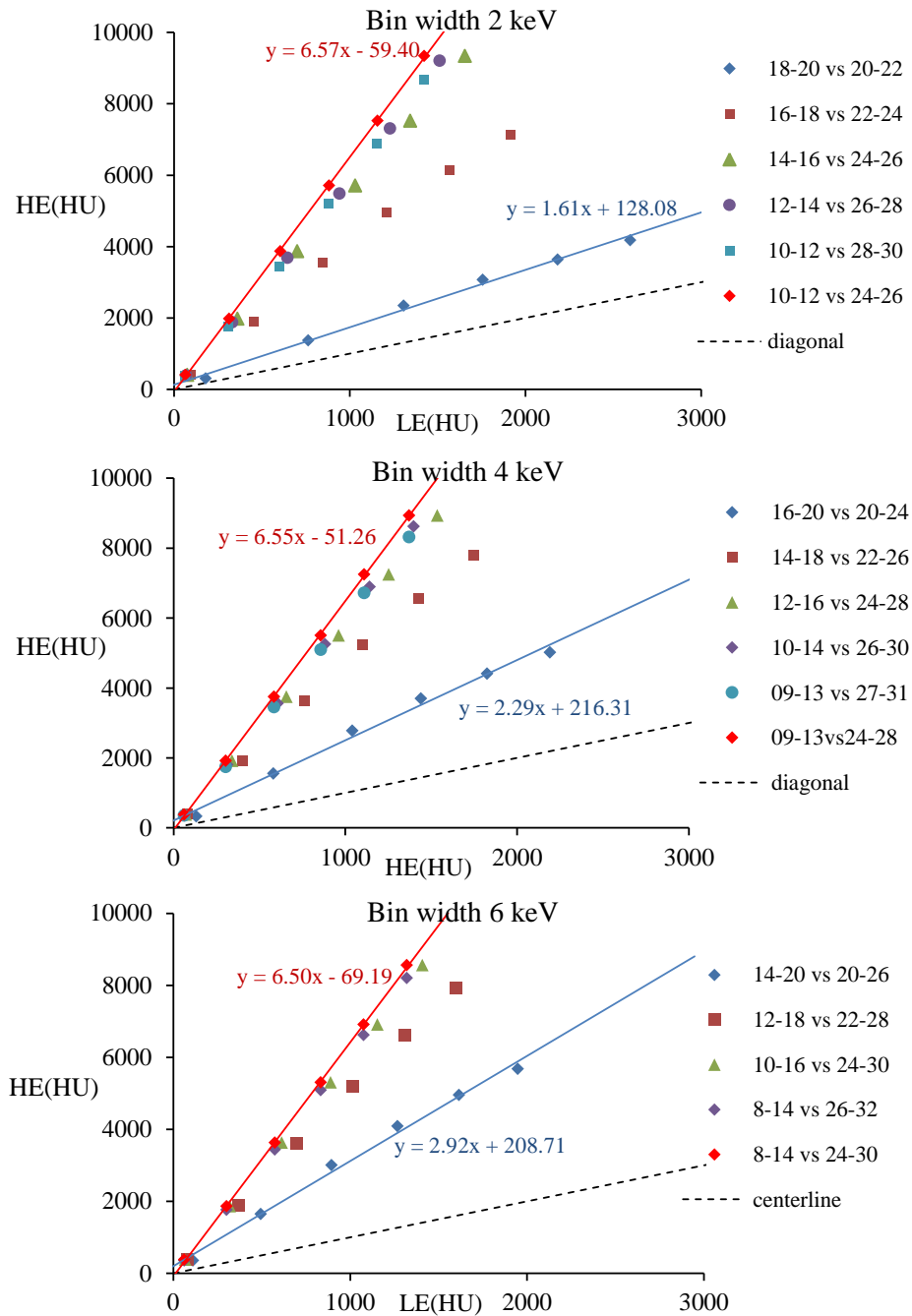


Figure 89: Different simulated concentrations of molybdenum solution plotted in space defined by LE and HE radio-density values for three energy bin widths. The data can be approximated by a line trend. The more the line slope deviates from the system diagonal, the easier the absorption edge identification is. The legend describes energy bin boundaries in keV.

Figure 89 shows three such charts for energy bin width 2, 4 and 6 keV. In agreement with expectations, the highest slope is provided by the narrowest bin. Nevertheless, the slope value decreases just faintly with broadening the bin. The 10 keV wide energy bin (the widest tested bin; not shown in the plot) provides line slope of 6.0 which is less than 10 % lower than the highest achieved value. On the other hand the slope is very sensitive to mean energy of the bin. This fact is most

apparently visible in the case of 2 keV bin width. Based on figure it can be expected that the highest slope can be expected for mean bin energy 4 – 9 keV above the absorption edge energy.

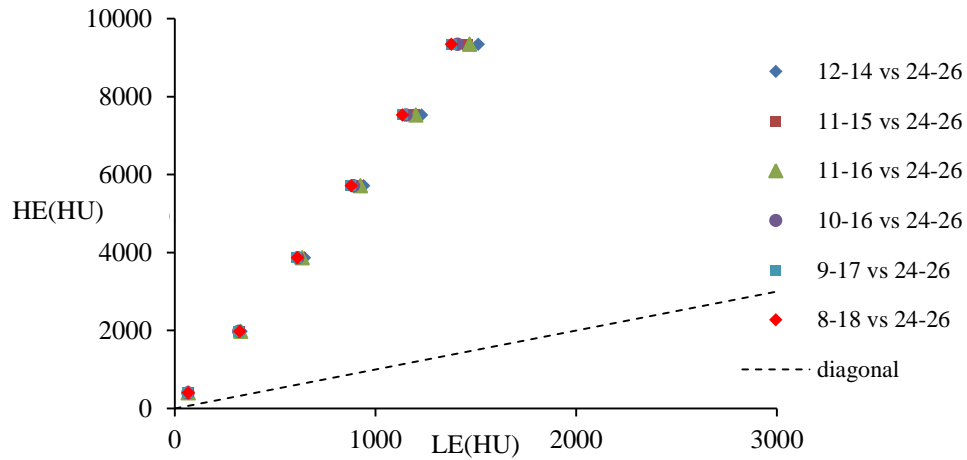


Figure 90: The width of LE bin contributes to the variations in the slope of the line just weakly. The legend describes energy bin boundaries in keV.

10.2.4 Contrast-to-noise ratio of the data

Analysis of the contrast-to-noise ratio provides additional information to the previously presented simulated results of radio-density value with respect to energy bin width and the mean energy of the bin. Contrast-to-noise ratio (CNR) is a metric defining detectability of a structure based on combination of its contrast and noise. Generally it is defined as

$$CNR = \frac{|I_1 - I_2|}{\sigma} \quad (21)$$

where I_1 and I_2 are intensities of signal in two different regions of interest while σ represents pure image noise. Some sources, moreover, connects use more complex CNR evaluation considering also the size of the ROI [168]. For purposes of the model it was calculated using formula suggested in [169] as it considers the signal variance in both regions of interest. The CNR was calculated as:

$$CNR = \frac{|HU_1 - HU_2|}{\sqrt{HU_1 + HU_2}} \quad (22)$$

HU_1 and HU_2 represent the radio-density values of two regions of interest. The denominator in equation 22 represents the geometric addition of quantum noise in both regions of interest derived from Poisson distribution (introduced in equation 13). Based on Rose criterion, a region of interest is visible if its CNR exceeds value of 5 [162]. Figure 91 shows the relationship of CNR with respect to concentration of the Na_2MoO_4 solution for different mean energies of an energy bin, and for different widths of a bin. Based on the simulation, the highest CNR is achieved with the widest energy bins. This conclusion contradicts the results of radio-density evaluation presented in previous sub-

chapter. It indicates that the ROI detectability is more dependent on the noise level than on the absolute contrast.

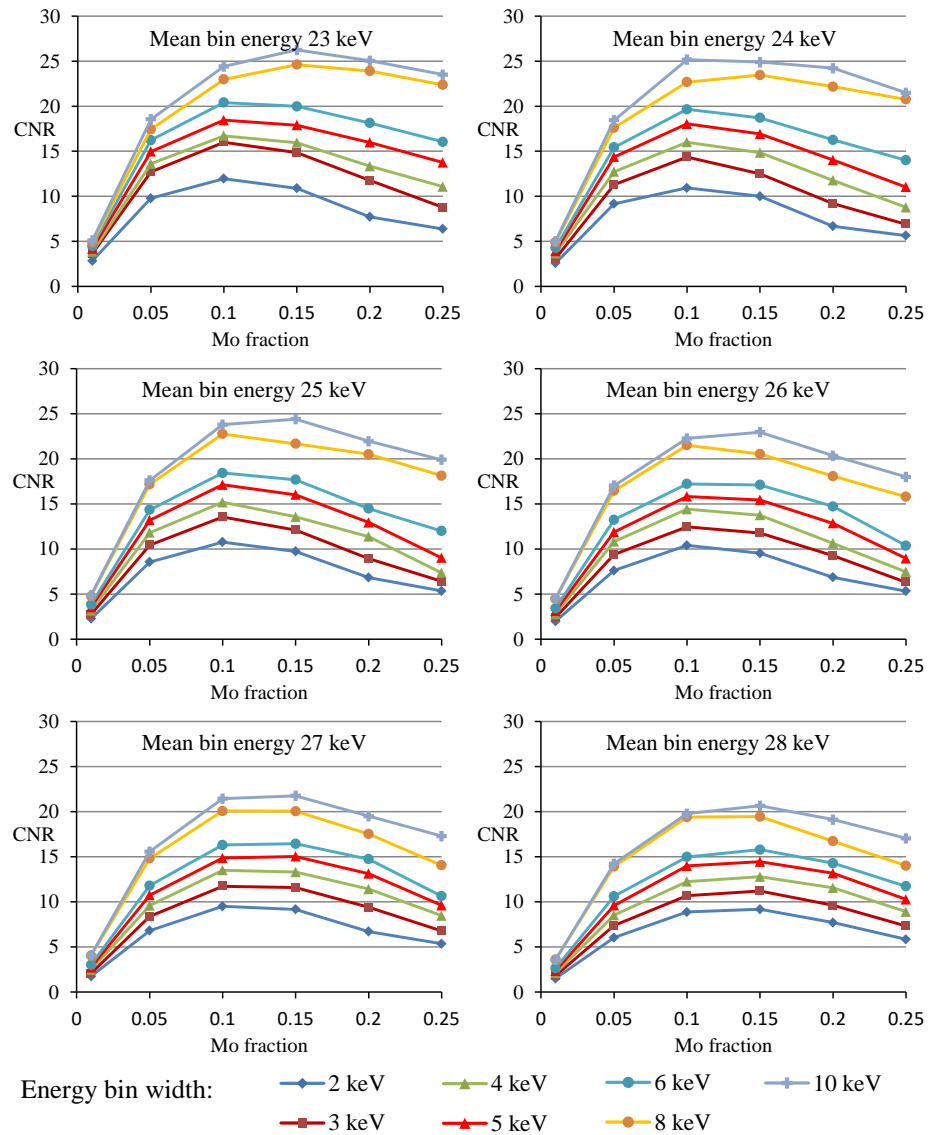


Figure 91: Modelled contrast-to-noise ratio of molybdenum solution with respect to its concentration for different mean energies of an energy bin, and for different bin widths. The highest CNR is achieved by the widest energy bins. Surprisingly, the CNR values do not increase monotonically with molybdenum concentration but culminates at concentration of 0.15 and then its values decrease.

It can be also seen from figures 89 and 91 that narrow bins raise the radio-density values above the edge just weakly compared to widest bins. On the other hand the dependence of CNR on the bin width is much stronger. It is also interesting to notice that the modelled CNR values do not monotonically grow with contrast agent concentration. The CNR values increase from the lowest concentrations to volume fraction of 0.15 and then decrease again for higher concentrations. This trend is most likely caused by low transmission through highly attenuating structures connected with high Poisson noise.

10.2.5 Simulation summary

The presented analysis of modelled transmission of an X-ray beam showed several key points important for experimental measurements. The points are briefly summarized in following indents:

- Absorption edge – and abrupt increase of linear attenuation coefficient at certain energy – is smeared over several keV by the limited detector energy resolution.
- The highest radio-density in HE bin was observed if its mean energy was 4 – 9 keV above the absorption edge energy.
- Due to principle of HU conversion, the setting of LE bin is of minor importance
- Achievable CNR, thus the detail detectability, depends strongly on energy bin width. Therefore, narrow energy bins are not very advantageous based on the model evaluation.

10.3 Spectral CT of multi-material phantom object

This chapter demonstrates the capability of a large area Timepix detector to perform simultaneous scan of three different contrast agents and their resolving by means of spectral CT. A phantom object consisting of six polyethylene (PE) chambers with inner diameter of 5 mm was designed for this purpose (see figure 92 left). The first container was filled with water while the remaining five were filled with aqueous solutions of Na_2MoO_4 and I+KI (atomic iodine and potassium iodine) and suspension of BaSO_4 in agarose gel. All the mentioned compounds contain an element with K-edge in a relevant energy range. The absorption edges energies are 20.0, 33.2 and 37.4 keV for molybdenum, iodine and barium, respectively [116]. Water-filled chamber served as a reference for HU normalization after the CT reconstruction. The layout of the phantom object and information on used relative concentrations are denoted in right part of figure 92. The concentrations of individual substances were adjusted to be undistinguishable in a standard CT with 5 keV threshold and 70 kVp X-ray spectrum.

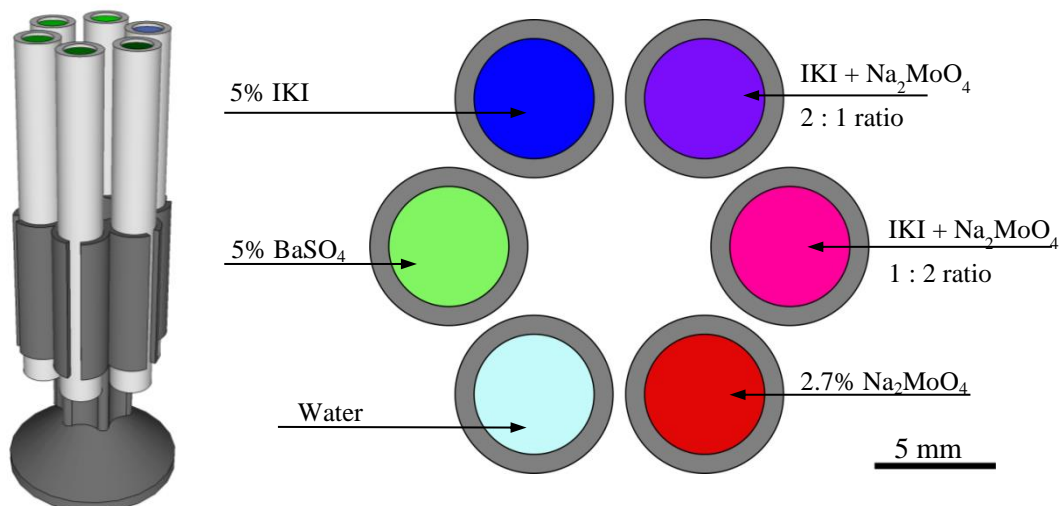


Figure 92: A 3D model of the multi-material phantom object (left) and description of its content (right). The first chamber is filled with water while the remaining five were used for three different substances and their mixtures. The used substances represent three contrast agents visualized simultaneously within a single micro-CT scan.

The phantom object was scanned using a microfocus X-ray tube operated at 70 kVp with additional 500 μm aluminum filtration and WidePIX_{4x5} detector with silicon sensor.

The sample was scanned with 4 different threshold values in each angular position. The lowest threshold value was set to 5 keV, the remaining three addressed absorption edges of molybdenum, iodine and barium. Therefore, the thresholds were set to 20.0, 33.2 and 37.4 keV. Total number of 748 projections was taken for each energy threshold. The exposure time of projections was adjusted to obtain approximately 10^4 detected photons per pixel. The datasets with appropriate thresholds were subtracted to create energy bins. Projections belonging to each of formed energy bins underwent BHC and WidePIX-geometry correction. Both mentioned corrections are detailed in chapter 4.2. The CT reconstruction was carried out using a dedicated module of Volume Graphics Studio 3.2 using filtered back-projection algorithm and the radio-density within the obtained slices were converted to HU.

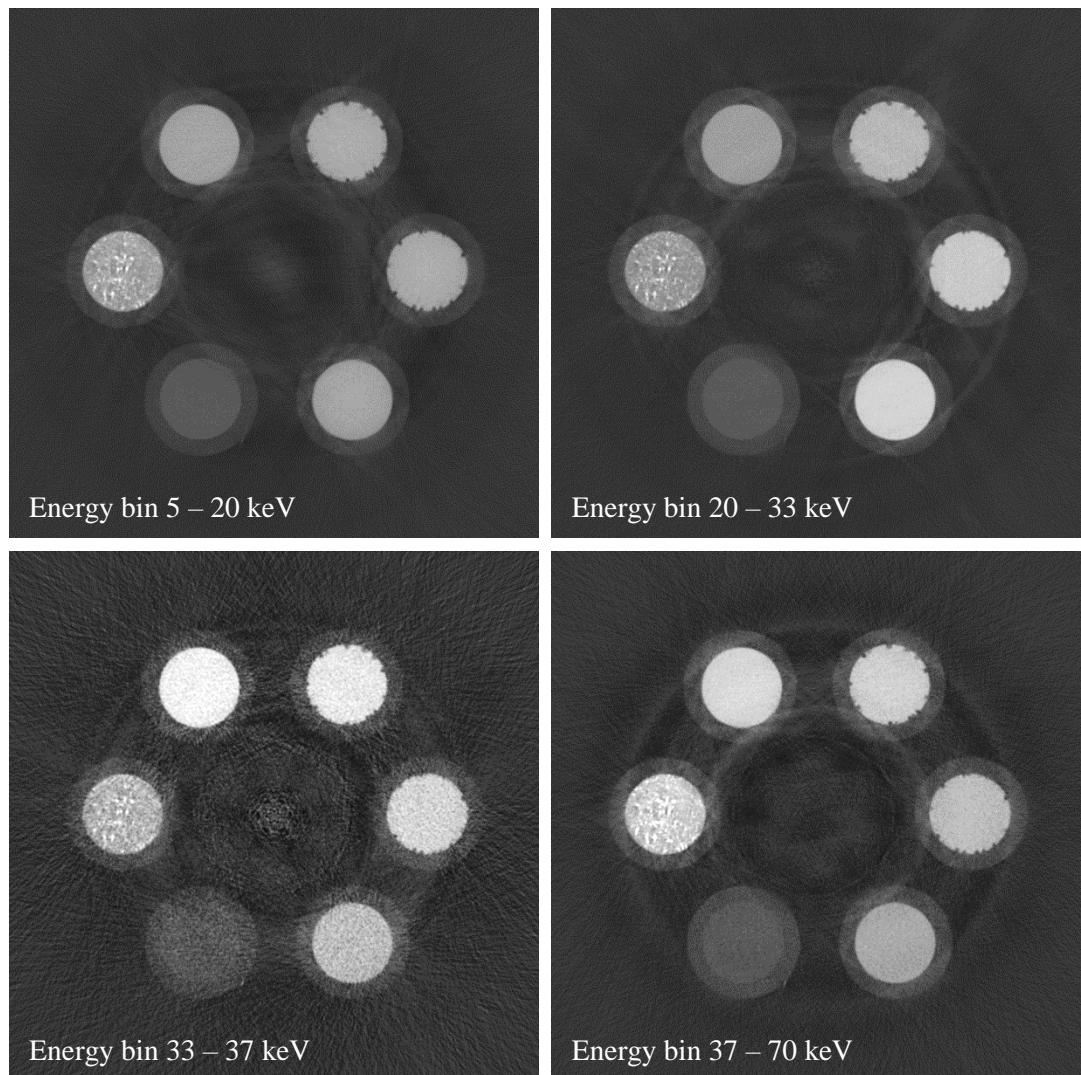


Figure 93: The same CT slice of the phantom object formed from four different energy bins.

Figure 93 shows reconstructed CT slices originated from four used energy bins. Figure 94 then demonstrates radio-densities of selected ROIs within the data with respect to the mean energy of the bin. It clearly shows that the contrast agents have very similar radio-density in the area below the absorption edges and would be undistinguishable in a standard CT scan. On the other hand, the plot in figure 94 shows clear and characteristic energy-dependent behavior of radio-density

function of each used substance. Such behavior allows identification of individual elements within the data by means of multi-channel basis material decomposition. A slight trend can be observed even between water and PE walls of the phantom chambers. The bright speckles in the barium chamber are caused by larger BaSO₄ grains captured in the agarose gel.

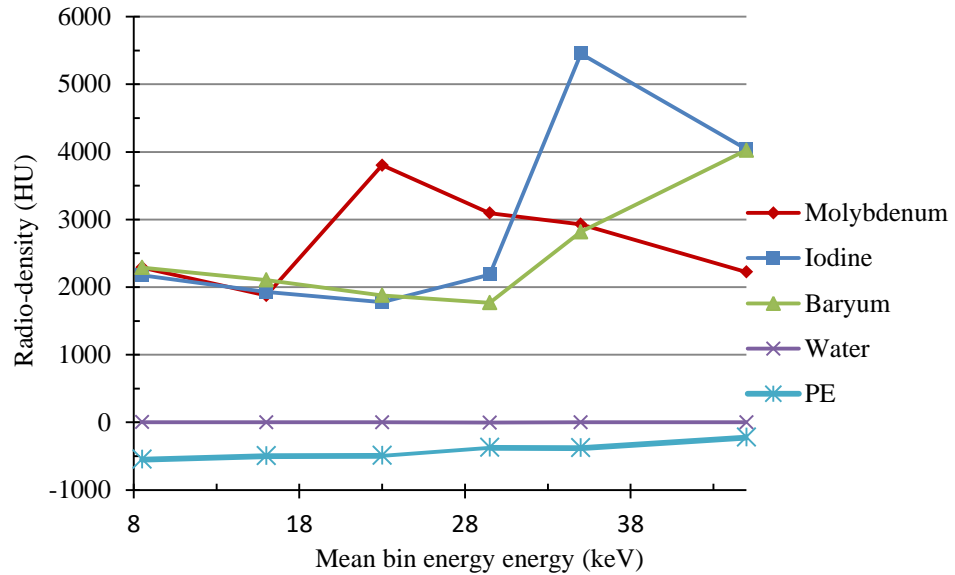


Figure 94: Radio-density of phantom materials with respect to the mean bin energy.

10.3.1 Material decomposition

The basis material decomposition described in chapter 1.9.2 was adapted for purposes of multi-bin spectral CT. The two-material decomposition approach was extended into four channels in this case:

$$\begin{bmatrix} X_1 \\ \vdots \\ X_4 \end{bmatrix} = \begin{bmatrix} \mu_{1E_1} & \mu_{2E_1} & \cdots \\ \vdots & \ddots & \\ \mu_{1E_4} & \cdots & \mu_{4E_4} \end{bmatrix}^{-1} \cdot \begin{bmatrix} CT_{E_1} \\ \vdots \\ CT_{E_4} \end{bmatrix} \quad (23)$$

X_m represents a fraction of basis material in certain position, μ_{mn} is radio-density of m -th basis material and n -th energy bin, and CT_n represents radio-density value of a pixel in the data. Solving the set of equations provide four maps representing spatial distribution of basis materials. Generally, the number of energy bins can be further increased as long as the sensitivity matrix of the system remains regular.

Figure 95 shows result of BMD of the multi-material phantom. The four channels represent distribution of water-like materials, molybdenum, iodine and barium. Different intensity levels can be observed in the case of molybdenum and iodine since these two solutions were mixed together. Figure 96 then shows a color CT slice formed from molybdenum, iodine and barium maps obtained from BMD. The red, green and blue shades indicate presence of molybdenum, barium and iodine, respectively. The shades of purple are formed from mixture of molybdenum (red) and iodine (blue). The color slice clearly demonstrates the additional information provided by spectral micro-CT with a Timepix detector. The spectral micro-CT clearly resolves the composition of all phantom chambers while they are undistinguishable for a regular CT scan (Figure 96 right).

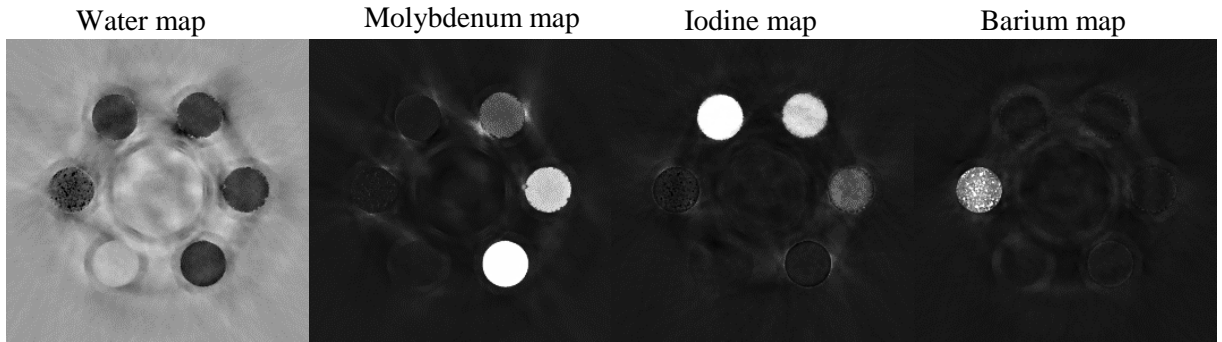


Figure 95: Material maps obtained from basis material decomposition.

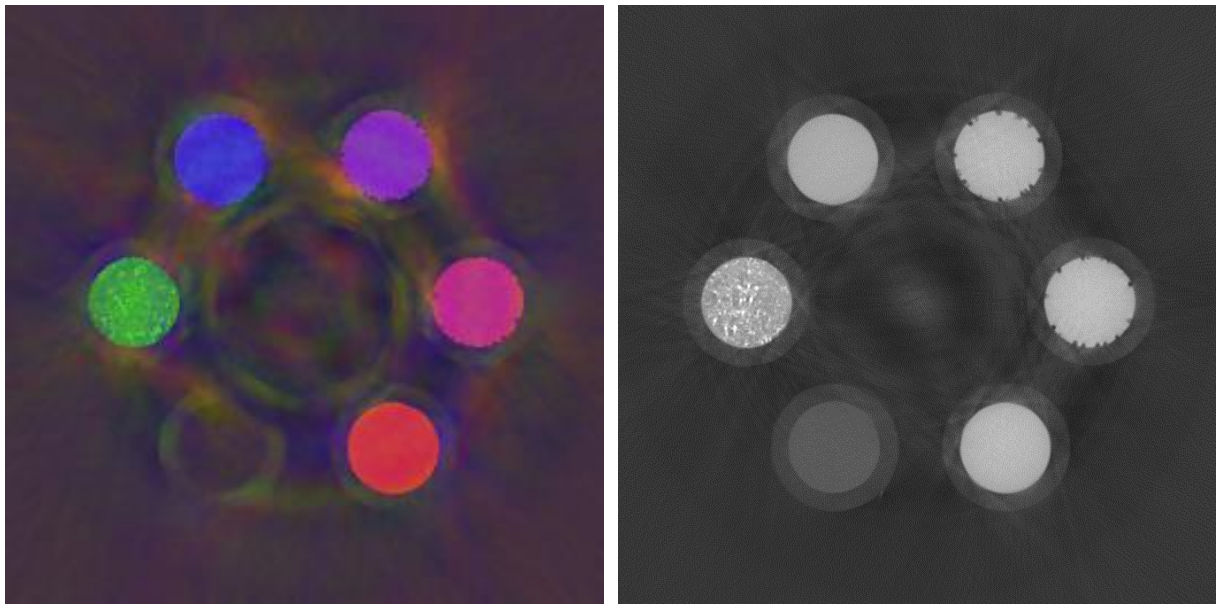


Figure 96: RGB CT slice formed from molybdenum, barium and iodine maps (left) compared to a standard CT slice (right). Spectral CT successfully resolves substances that are undistinguishable in a standard CT scan. The red, green and blue shades indicates presence of molybdenum, barium and iodine, respectively. Mixture of molybdenum (red) and iodine (blue) produces shades of purple.

10.4 Spectral micro-CT with WidePIX 3D detector

WidePIX 3D is a compact Timepix-based particle tracking detector with 3D position sensitivity [170]. The device consists of four Timepix chips with $300\ \mu\text{m}$ silicon sensors tightly stacked together. The sensor volume is, therefore, divided into a 3D array of $256 \times 256 \times 4$ voxels (see figure 97). Dual-energy X-ray imaging with sandwich detector is already known as single-shot dual-energy X-ray radiography utilizing a two-layer detector (discussed in chapter 1.9). In the case of WidePIX 3D, the detector can provide up to four sample images produced by different photon spectra from a single exposure. Furthermore, the detection threshold of each layer can be individually adjusted to optimize the resolving performance for elements expected within the scanned sample.

The FOV of WidePIX 3D device is obviously very limited, nevertheless, it was successfully tested for multi-channel energy-sensitive micro-CT of a phantom object. The phantom object was designed

to fit the detector FOV. It consisted of four plastic tubes (6 mm diameter) filled with water (as a reference material) and solutions of silver, molybdenum and iodine compounds. The materials were selected since each of them has an absorption edge in energy range detectable with silicon sensors (Ag \sim 19.99 keV, Mo \sim 25.55 keV, I \sim 33.17 keV). The concentration of all the solutions was adjusted in such way that their contrast with respect to water was approximately the same for 45 kVp X-ray spectrum and detection threshold of 4 keV.

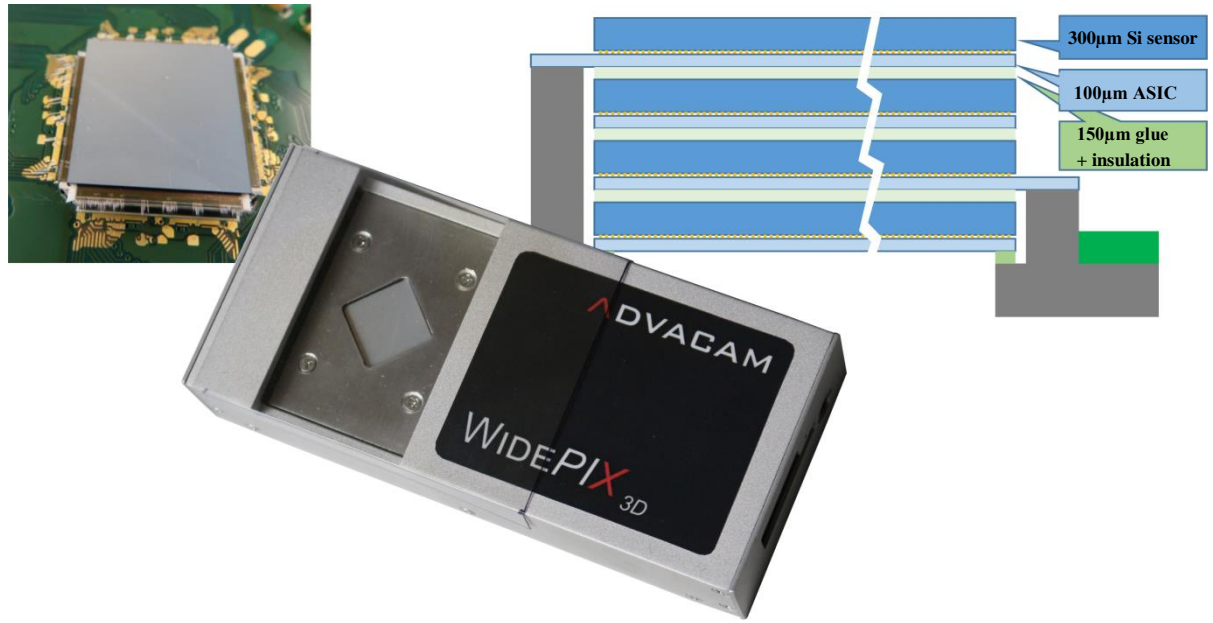


Figure 97: WidePIX 3D - a compact wide-field-of-view particle tracker (left). It is built of four tightly stacked Timepix assemblies with 300 μ m silicon sensors and read-out chips thinned-down to 100 μ m. The sensor volume is, therefore, divided into a 3D array of $256 \times 256 \times 4$ voxels, $55 \times 55 \times 300$ μ m each. Each chip is turned 90 degrees with respect to its neighbors, so the peripheries can be easily connected to the chip carrier board (right).

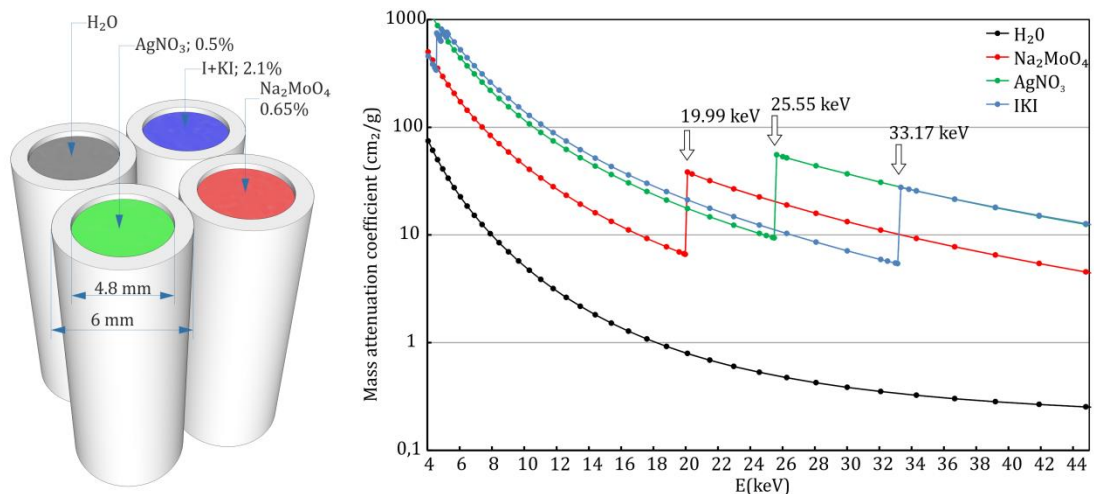


Figure 98: The phantom object consisted of four cylindrical compartments filled with solutions of molybdenum, silver, iodine and water (left). All the selected elements have an absorption edge within the range approx. 20–34 keV, while water served as a reference (right). The concentration of solutions was adjusted to provide comparable radio-density for 45 kVp tungsten spectrum and threshold of 4 keV [170].

As the detector consists of four layers, the CT scan was carried out in four energy channels with different threshold values. The THL values for layers L1 – L4 were set to energies 4.0, 19.9, 25.5 and 33.1 keV, respectively. The 4keV thresholds represents the detector setting for a standard scan while the remaining three channels address absorption edges of targeted materials. The X-ray tube was operated at 45 kVp and with 18 W of output power.

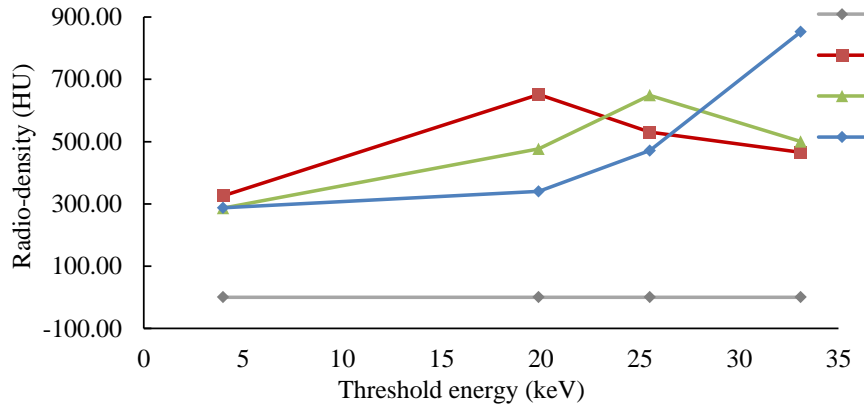


Figure 99: Radio-density values of solutions used in the phantom within the reconstructed data with respect to different thresholds. While the relative radio-density of observed compounds was the same (difference smaller than 5 %) with the 4 keV threshold it changed significantly at each energy threshold matching a K-edge of one of observed elements.

Each energy channel was processed individually by BH correction and ring artifact reduction. Then, image registration was carried out to align perfectly the data in individual layers. The projection processing and CT reconstruction was the same as described in the previous section. Figure 99 shows that while at the 4 keV threshold it is not possible to distinguish the observed solutions as their relative densities are comparable. However, the remaining energy channels – THL 19.9, 25.5 and 33.1 keV – exert detectable variations of relative densities. The maximal radio-density is achieved with the substance containing the element with its absorption edge close to the detection threshold. The increase of the relative density is at least 10 % in all cases.

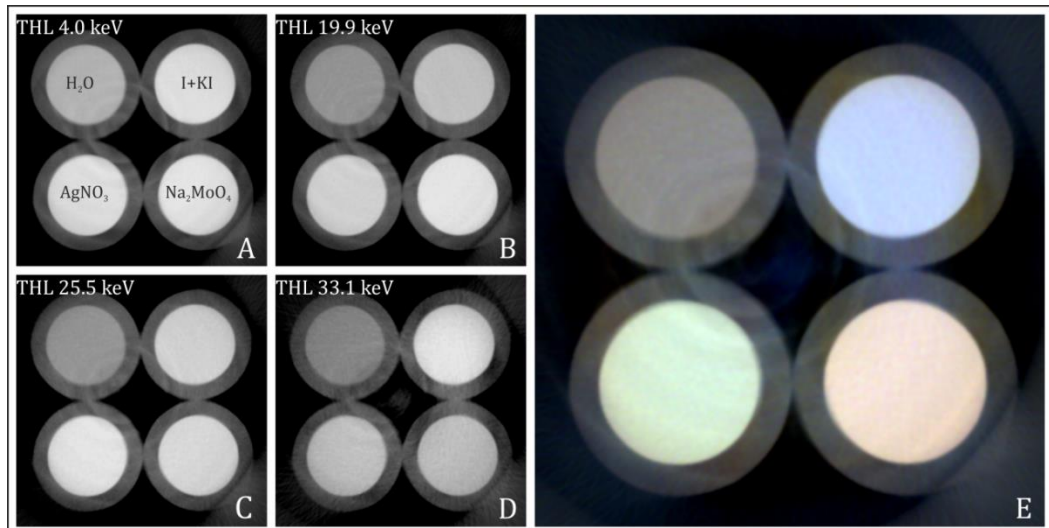


Figure 100: CT reconstruction of the same slice of the phantom object using data acquired with different energy thresholds (A–D) and an energy-sensitive color CT slice (E) created as an RGB combination of B, C and D with thresholds of 19.9, 25.5 and 33.1 keV respectively. The grayscale values of all energy channels were normalized to achieve constant contrast of water with respect to the air.

Figure 100 shows examples of reconstructed slices from L1 – L4 (A – D) and an RGB slice (E) from slices addressing absorption edges of molybdenum (B), silver (C) and iodine (D) used as individual color channels of the image. Therefore, the color hues indicate presence of observed elements – red for molybdenum, green for silver and blue for iodine. The water remains gray as its values are in all channels due to prior data normalization.

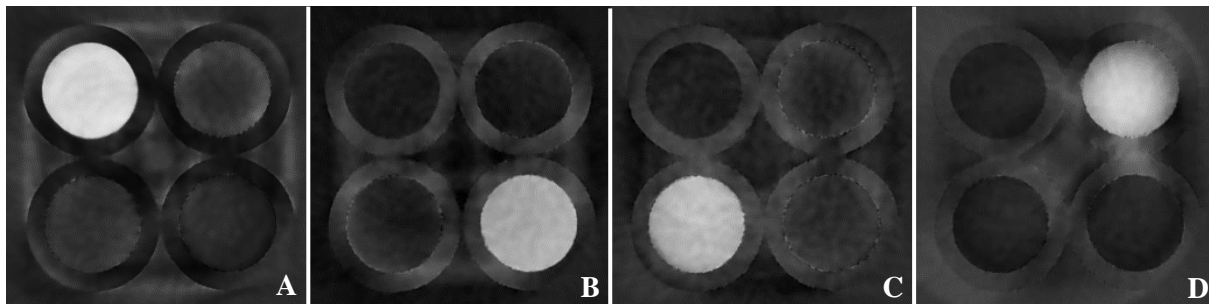


Figure 101: Material maps based on 4-channel material decomposition: Water (A), molybdenum (B), silver (C) and iodine (D).

To further improve the ability to identify the occurrence of individual observed materials within the CT slices, the material decomposition can be applied. The results of 4-channel material decomposition are shown in figure 101.

Conclusions

The thesis addresses high resolution and energy-sensitive X-ray imaging with photon counting detectors Timepix. The first part explains the physics background of radiographic imaging. Furthermore, it summarizes different known technical approaches of X-ray computed tomography and connected data processing techniques and it provides an overview of the state-of-the-art technologies. Finally, the applications of X-ray micro-CT in biology and pre-clinical research are discussed. The majority of the thesis is dedicated to the evaluation of performance of photon-counting detectors Timepix and to demonstration of applied results of X-ray imaging of biological samples achieved using this novel detector technology.

The practical use of Timepix detectors for high-resolution X-ray imaging used to be limited in the past due to small dimensions of the chip. The applicability was significantly extended by the invention of WidePIX technology introduced by IEAP in 2014. Large-area Timepix detectors (LAD) based on WidePIX technology provide field of view up to 143 mm. It was shown in this thesis that the LAD Timepix can be efficiently used for micro-CT of whole adult mice with resolution of approximately 20 μm . Resolution of 12 μm was demonstrated at an example of contrast-stained newborn mouse. If demanded, spatial resolution better than 5 μm is achievable for such sample. Number of important anatomical structures was successfully visualized in both cases.

Possible *in vivo* applications of Timepix detectors were addressed. A set of experimental measurements demonstrated that the available equipment is potentially suitable for *in vivo* measurements in mice. The current state of available small animal micro-CT scanner is capable of performing a scan with a dose of approximately 500 mGy. A construction upgrade of the scanner, that will substantially reduce the absorbed dose of the scanned object, has been suggested and is now under development. It is expected, that after implementation of the suggested construction changes and considering the use of a highly-efficient detector with CdTe sensor, the scanner will be capable of *in vivo* scanning with absorbed dose lower than 50 mGy. Once such dose level of a standard micro-CT scan is achieved, *in vivo* spectral CT can be further considered.

As mentioned previously, PCD technology provides enhanced CNR, thanks to the dark-current free photon counting. This fact was demonstrated in a direct comparison of LAD Timepix and a state-of-the-art scintillator-based CCD X-ray camera within the thesis. The Timepix detector revealed four times finer details with a given effective pixel size (EPS) and comparable detected beam intensity in the same sample. The enhanced CNR was utilized for micro-CT scanning of *ex vivo* murine organs. X-ray imaging of *ex vivo* soft biology tissue has become generally known as virtual histology. Typically, it relies on the application of a high-Z contrast agent to enhance the soft tissue radio-density and improve the differentiation of various tissue types.

The results presented in this thesis demonstrate that Timepix technology is capable of resolving fine structures within ethanol-preserved soft biology tissue, even without further contrast staining. Micro-CT scans of brain, liver, heart and kidneys are presented. EPS down to 3 μm was achieved for these samples. Fine venules with diameter of only 8 micrometers were detectable in the case of kidneys. Heart vortex, valves and chordae tendineae were visualized in the sample of a mouse heart. Micro-CT of ethanol-preserved brain with EPS of 4.4 μm revealed comparable anatomical structures as previously published studies utilizing iodine staining. Furthermore, the achieved resolution is an order better than available mouse-anatomy atlases based on magnetic resonance imaging.

Dehydration of tissue using ethanol is one of the standard steps of histology sample preparation. Virtual histology of ethanol-preserved samples with Timepix detectors could be, therefore, easily incorporated into a standard sample processing chain used in tissue histology and could be used for non-destructive 3D visualization of tissue biopsies. Consequently, micro-CT could contribute to early detection of tumors or other pathologies in the human body.

The thesis further demonstrates micro-CT measurements with sub-micrometer EPS. It was applied to visualization of shells of foraminifera – single-cell organisms living in seafloor sediment or as a constituent part of plankton. The finest EPS used for these measurements was 550 nm. A scan with such parameters crosses the bounds of standard micro-CT imaging and a term nano-CT could be considered. The latest state-of-the-art nano-focus X-ray sources are capable of providing true spatial resolution better than 200 nm. Therefore, advanced X-ray imaging techniques nowadays challenge the spatial resolution of optical microscopy and moreover are capable of providing 3D information with isotropic resolution.

X-ray imaging with sub-micrometer precision puts enormous requirements, not only to the radiation source and the detector, but on the whole setup. Long-lasting scans require extreme accuracy and stability of the system mechanics. Effects like rotation stage wobble, drift of the focal spot or thermal expansion of system components can induce severe geometry artifacts to the data and can compromise the quality of the results. These sources of error have been addressed within the thesis. As these effects cannot be fully avoided a set of correction techniques has been developed and implemented. The principles of these corrections are described and their efficiency is demonstrated.

The thesis further presents unique results of multi-bin energy-sensitive micro-CT. Spectral CT resulting in multi-material decomposition using large-area photon counting detectors WidePIX have not been published so far. The work was focused on resolving specific target elements within the scanned object based on identification of absorption edges. Such approach opens new possibilities for micro-CT with contrast agents. It makes possible to carry out scans with several contrast agents being simultaneously applied. Spectral CT is then capable of clearly identifying the individual contrast substances, separating them and even providing quantitative information on their concentrations.

The question of optimal parameters of energy bins used for efficient identification of an absorption edge is addressed by a computer model. The model simulates the transmission of an X-ray beam through an absorber containing an element with absorption edge in its linear attenuation coefficient. Experimental measurements have been carried out using a custom-made phantom object. The data presented in the thesis demonstrate the results achieved with the phantom containing water, three different solutions with content of an element with absorption edge within a range from 20 to 37 keV and also their mixtures. Successful basis material decomposition is demonstrated, although the distance of absorption edges was just 4 keV in one case. Moreover, the composition of the mixtures was resolved, which clearly indicates the suitability of Timepix technology for quantitative spectral micro-CT imaging.

Future work will be focused on further development of multi-bin CT methodology, associated software and accessories dedicated for small animal imaging towards potential *in vivo* applications. Simultaneously with suggested upgrades of the available small-animal scanner, a new micro-CT system of own design dedicated for small animal imaging is under development. The construction design was made in 2018. All the required construction parts should be available before the end

of 2019. The scanner was designed to be used with WidePIX_{2x5} detector. Therefore, it should be fully capable of scanning not only mice, but also rats.

Further plans are also connected with use of the latest generation of detectors developed in frame of the Medipix Collaboration. The functionalities newly offered by the Timepix3 chip – zero dead time, simultaneous information on position of an event, the deposited energy and the time-stamp – enable new options for use of these detectors in imaging applications. Concerning the use in biology research, the combination of mentioned features is very promising for *in vivo* gated imaging of dynamic processes or for fully spectroscopic X-ray imaging.

Author's publications

The information on author's published results including number of citations and H-index value are based on data available at the Web of Science on September 23rd 2019.

H-index:	4
Total number of citations:	53
Without self-citations:	35

Publications related to the topic of the thesis

Book chapter

- [1] **J. Dudak**, "Applications of hybrid pixel detectors for high resolution table-top X-ray imaging", in *Semiconductor Radiation Detectors: Technology and Applications*, 1st ed., Boca Raton: CRC Press, 2017, pp. 183-208, ISBN: 9781138710344.

Articles Published in Impacted Journals

As the main author

- [2] **J. Dudak**, J. Karch, J. Jakubek, M. Jakubek, and J. Zemlicka, "Compact four-layer Timepix-based particle tracker WidePIX 3D: the first applications in X-ray CT imaging", *Journal of Instrumentation*, vol. 13, no. 12, pp. C12001-C12001, Dec. 2018, DOI: 10.1088/1748-0221/13/12/C12001.

Journal IF (2018): 1.366
Times cited = 1

- [3] **J. Dudak**, J. Zemlicka, J. Karch, Z. Hermanova, J. Kvacek, and F. Krejci, "Microtomography with photon counting detectors: improving the quality of tomographic reconstruction by voxel-space oversampling", *Journal of Instrumentation*, vol. 12, no. 01, pp. C01060-C01060, Jan. 2017, DOI: 10.1088/1748-0221/12/01/C01060.

Journal IF (2018): 1.366
Times cited = 3

- [4] **J. Dudak**, J. Karch, K. Holcova, and J. Zemlicka, "X-ray imaging with sub-micron resolution using large-area photon counting detectors Timepix", *Journal of Instrumentation*, vol. 12, no. 12, pp. C12024-C12024, Dec. 2017, DOI: 10.1088/1748-0221/12/12/C12024.

Journal IF (2018): 1.366
Times cited = 1

- [5] **J. Dudak, J. Zemlicka, J. Karch, M. Patzelt, J. Mrzilkova, P. Zach, Z. Hermanova, J. Kvacek, and F. Krejci**, “High-contrast X-ray micro-radiography and micro-CT of ex-vivo soft tissue murine organs utilizing ethanol fixation and large area photon-counting detector”, *Scientific Reports*, vol. 6, no. -, p. 30385, Jul. 2016, DOI: 10.1038/srep30385.

Journal IF (2018): 4.525

Times cited = 17

- [6] **J. Dudak, J. Zemlicka, F. Krejci, J. Karch, M. Patzelt, P. Zach, V. Sykora, and J. Mrzilkova**, “Evaluation of sample holders designed for long-lasting X-ray micro-tomographic scans of ex-vivo soft tissue samples”, *Journal of Instrumentation*, vol. 11, no. 03, pp. C03005-C03005, Mar. 2016, 10.1088/1748-0221/11/03/C03005.

Journal IF (2018): 1.366

Times cited = 3

- [7] **J. Dudak, J. Zemlicka, F. Krejci, S. Polansky, J. Jakubek, J. Mrzilkova, M. Patzelt, and J. Trnka**, “X-ray micro-CT scanner for small animal imaging based on Timepix detector technology”, *Nuclear Instruments and Methods in Physics Research Section A: Accelerators, Spectrometers, Detectors and Associated Equipment*, vol. 773, pp. 81-86, 2015, DOI: 10.1016/j.nima.2014.10.076.

Journal IF (2018): 1.433

Times cited = 10

As a co-author

- [8] J. Mrzilková, M. Patzelt, P. Gallina, Z. Wurst, M. Šeremeta, **J. Dudák**, F. Krejčí, J. Žemlička, V. Musil, J. Karch, J. Rosina, and P. Zach, “Imaging of Mouse Brain Fixated in Ethanol in Micro-CT”, *BioMed Research International*, vol. 2019, pp. 1-7, Jul. 2019, DOI: 10.1155/2019/2054262.

Journal IF (2017): 2.583

Times cited = 0

- [9] M. Patzelt, J. Mrzilkova, **J. Dudak**, F. Krejci, J. Zemlicka, J. Karch, V. Musil, J. Rosina, V. Sykora, B. Horehledova, and P. Zach, “Ethanol fixation method for heart and lung imaging in micro-CT”, *Japanese Journal of Radiology*, vol. 37, no. 6, pp. 500-510, 2019, DOI: 10.1007/s11604-019-00830-6.

Journal IF: 1.5

Times cited = 0

- [10] J. Zemlicka, **J. Dudak**, J. Karch, and F. Krejci, “Geometric correction methods for Timepix based large area detectors”, *Journal of Instrumentation*, vol. 12, no. 01, pp. C01021-C01021, Jan. 2017, 10.1088/1748-0221/12/01/C01021.

Journal IF (2018): 1.366

Times cited = 5

- [11] P. Frýdlová, V. Nutilová, **J. Dudák**, J. Žemlička, P. Němec, P. Velenský, T. Jirásek, and D. Frynta, “Patterns of growth in monitor lizards (Varanidae) as revealed by computed tomography of femoral growth plates”, *Zoomorphology*, vol. 136, no. 1, pp. 95-106, 2017, DOI: 10.1007/s00435-016-0338-3.

Journal IF (2018): 1.143

Times cited = 2

Publications in impacted journals not related to the thesis

- [12] J. Zemlicka, **J. Dudak**, D. Kubanda, and F. Krejci, “Single absorption grating based X-ray phase contrast CT using Timepix detector”, *Journal of Instrumentation*, vol. 14, no. 05, pp. C05007-C05007, May 2019, 10.1088/1748-0221/14/05/C05007.

Journal IF (2018): 1.366

Times cited = 0

- [13] D. Kubanda, B. Zařko, A. řagátová, J. řemlička, Z. Zápřařný, P. Boháček, **J. Dudák**, E. Kováčová, and V. Nečas, “Performance of bulk semi-insulating GaAs-based sensor and its comparison to Si-based sensor for Timepix radiation camera”, *Journal of Instrumentation*, vol. 14, no. 01, pp. C01023-C01023, Jan. 2019, DOI: 10.1088/1748-0221/14/01/C01023.

Journal IF (2018): 1.366

Times cited = 0

- [14] J. Kvaček, E. Barrón, Z. Heřmanová, M. M. Mendes, J. Karch, J. řemlička, **J. Dudák**, and L. Seyfullah, “Araucarian conifer from late Albian amber of northern Spain”, *Papers in Palaeontology*, vol. 4, no. 4, pp. 643-656, 2018, DOI: 10.1002/spp2.1223.

Journal IF (2018): 2.056

Times cited = 4

- [15] B. Zařko, D. Kubanda, J. řemlička, A. řagátová, Z. Zápřařný, P. Boháček, V. Nečas, Y. Mora, M. Pichotka, and **J. Dudák**, “First tests of Timepix detectors based on semi-insulating GaAs matrix of different pixel size”, *Journal of Instrumentation*, vol. 13, no. 02, pp. C02013-C02013, Feb. 2018, DOI: 10.1088/1748-0221/13/02/C02013.

Journal IF (2018): 2.056

Times cited = 3

- [16] J. Karch, **J. Dudák**, J. řemlička, D. Vavřík, I. Kumpová, J. Kvaček, Z. Heřmanová, J. řoltés, L. Viererbl, M. Morgano, A. Kaestner, and P. Trtík, “X-ray micro-CT and neutron CT as complementary imaging tools for non-destructive 3D imaging of rare silicified fossil plants”, *Journal of Instrumentation*, vol. 12, no. 12, pp. C12004-C12004, Dec. 2017, DOI: 10.1088/1748-0221/12/12/C12004.

Journal IF (2018): 1.366

Times cited = 1

- [17] F. Krejci, J. Zemlicka, J. Jakubek, **J. Dudak**, D. Vavrik, U. Köster, D. Atkins, A. Kaestner, J. Soltes, L. Viererbl, J. Vacik, and I. Tomandl, “Development and characterization of high-resolution neutron pixel detectors based on Timepix read-out chips”, *Journal of Instrumentation*, vol. 11, no. 12, pp. C12026-C12026, Dec. 2016, DOI: 10.1088/1748-0221/11/12/C12026.

Journal IF (2018): 1.366

Times cited = 4

- [18] J. Karch, B. Bartl, **J. Dudak**, J. Zemlicka, and F. Krejci, “Non-destructive imaging of fragments of historical beeswax seals using high-contrast X-ray micro-radiography and micro-tomography with large area photon-counting detector array”, *Micron*, vol. 91, pp. 22-28, 2016, DOI: 10.1016/j.micron.2016.09.006.

Journal IF (2017): 1.728

Times cited = 1

- [19] J. Karch, F. Krejci, B. Bartl, **J. Dudak**, J. Kuba, J. Kvacek, and J. Zemlicka, “High-contrast X-ray micro-tomography of low attenuation samples using large area hybrid semiconductor pixel detector array of 10×5 Timepix chips”, *Journal of Instrumentation*, vol. 11, no. 01, pp. C01073-C01073, Jan. 2016, DOI: 10.1088/1748-0221/11/01/C01073.

Journal IF (2018): 1.366

Times cited = 1

Other publications

- [20] J. Zemlicka, J. Jakubek, **J. Dudak**, J. Hradilova, and O. Trmalova, “X-ray Radiography of paintings with High Resolution I. Testing and Measurements with Large Area Pixel Detector”, in *Acta Artis Academica 2014: Interpretation of Fine Art's Analyses in Diverse Contexts*, 2014, pp. 51 - 61.

List of References

- [1] E. Watson, "The Discovery of X-Rays", *American Journal of Physics*, vol. 13, no. 5, pp. 281-291, 1945.
- [2] K. Sansare, V. Khanna and F. Karjodkar, "Early victims of X-rays: a tribute and current perception", *Dentomaxillofacial Radiology*, vol. 40, no. 2, pp. 123-125, 2011.
- [3] F. Knutsson, "Röntgen and the Nobel Prize", *Acta Radiologica. Diagnosis*, vol. 15, no. 5, pp. 465-473, 2016.
- [4] F. Nachtrab, T. Ebersperger, B. Schummer, F. Sukowski and R. Hanke, "Laboratory X-ray microscopy with a nano-focus X-ray source", *Journal of Instrumentation*, vol. 6, no. 11, p. C11017, 2011.
- [5] F. Nachtrab, T. Hofmann, C. Speier, J. Lučić, M. Firsching, N. Uhlmann, P. Takman, C. Heinzl, A. Holmberg, M. Krumm and C. Sauerwein, "Development of a Timepix based detector for the NanoXCT project", *Journal of Instrumentation*, vol. 10, no. 11, p. C11009, 2015.
- [6] J. Ashton, J. West and C. Badea, "In vivo small animal micro-CT using nanoparticle contrast agents", *Frontiers in Pharmacology*, vol. 6, 2015.
- [7] N. Yang, P. Lechner and W. Hawkins, "Effective atomic numbers for low-energy total photon interactions in human tissues", *Medical Physics*, vol. 14, no. 5, pp. 759-766, 1987.
- [8] E. Pauwels, D. Van Loo, P. Cornillie, L. Brabant and L. Van Hoorebeke, "An exploratory study of contrast agents for soft tissue visualization by means of high resolution X-ray computed tomography imaging", *Journal of Microscopy*, vol. 250, no. 1, pp. 21-31, 2013.
- [9] H. Lusic and M. Grinstaff, "X-ray-Computed Tomography Contrast Agents", *Chemical Reviews*, vol. 113, no. 3, pp. 1641-1666, 2013.
- [10] M. Willeminck, M. Persson, A. Pourmorteza, N. Pelc and D. Fleischmann, "Photon-counting CT: Technical Principles and Clinical Prospects", *Radiology*, vol. 289, no. 2, pp. 293-312, 2018.
- [11] "Medipix website: A family of pixel detector read-out chips for particle imaging and detection developed by the Medipix Collaborations". [Online]. Available: <https://medipix.web.cern.ch/>. [Accessed: 2019-09-08].
- [12] J. Bushberg, *The essential physics of medical imaging*, 2nd ed. Philadelphia, 2002.
- [13] M. Berger, J. Hubbel, S. Seltzer, J. Chang, J. Coursey, R. Sukumar, D. Zucker and K. Olsen, "XCOM: Photon Cross Sections Database", *National Institute of Standards and Technology*. Gaithersburg.
- [14] "X-ray microscope: Microtomography of large samples at high resolution", *Rigaku*. [Online]. Available: <https://www2.rigaku.com/products/xrm/nano3dx>. [Accessed: 30-Aug.-2019].

- [15] P. Withers, "X-ray nanotomography", *Materials Today*, vol. 10, no. 12, pp. 26-34, 2007.
- [16] R. Zehbe, A. Haibel, H. Rieseemeier, U. Gross, C. Kirkpatrick, H. Schubert and C. Brochhausen, "Going beyond histology. Synchrotron micro-computed tomography as a methodology for biological tissue characterization: from tissue morphology to individual cells", *Journal of The Royal Society Interface*, vol. 7, no. 42, pp. 49-59, 2009.
- [17] H. Li, H. Zhang, Z. Tang and G. Hu, "Micro-computed tomography for small animal imaging: Technological details", *Progress in Natural Science*, vol. 18, no. 5, pp. 513-521, 2008.
- [18] F. Debarbieux, A. Bonissent, P. Breugnon, F. Cassol Brunner, P. Delpierre, C. Hemmer, J. Clemens, B. Dinkespiler, J. Luchino, F. Mann, C. Meessen, E. Vigeolas, G. Rougon and C. Morel, "Repeated Imaging of Lung Cancer Development Using PIXSCAN, a Low Dose Micro-CT Scanner Based on XPAD Hybrid Pixel Detectors", *IEEE Transactions on Nuclear Science*, vol. 57, no. 1, pp. 242-245, 2010.
- [19] P. Weeks, "A Determination of the Efficiency of Production of X-Rays", *Physical Review*, vol. 10, no. 5, pp. 564-574, 1917.
- [20] G. Poludniowski, G. Landry, F. DeBlois, P. Evans and F. Verhaegen, "SpekCalc: a program to calculate photon spectra from tungsten anode x-ray tubes", *Physics in Medicine and Biology*, vol. 54, no. 19, pp. N433-N438, 2009.
- [21] "Atomic spectra and X-rays", *Physics Library*. [Online]. Available: [https://phys.libretexts.org/Bookshelves/University_Physics/Book%3A_University_Physics_\(OpenStax\)/Map%3A_University_Physics_III_-_Optics_and_Modern_Physics_\(OpenStax\)/8%3A_Atomic_Structure/8.5%3A_Atomic_Spectra_and_X-rays](https://phys.libretexts.org/Bookshelves/University_Physics/Book%3A_University_Physics_(OpenStax)/Map%3A_University_Physics_III_-_Optics_and_Modern_Physics_(OpenStax)/8%3A_Atomic_Structure/8.5%3A_Atomic_Spectra_and_X-rays). . [Accessed: 02-Sep.-2019].
- [22] F. Maur, "Advances in X-ray Inspection for Electronics: Part 1: Tubes", in *YXLON*. [Online]. Available: [https://www.yxlon.com/blog/march-2016-\(1\)/advances-in-x-ray-inspection-for-electronics,-part](https://www.yxlon.com/blog/march-2016-(1)/advances-in-x-ray-inspection-for-electronics,-part). [Accessed: 09-Feb.-2019]
- [23] D. Grider, A. Wright and P. Ausburn, "Electron beam melting in microfocus X-ray tubes", *Journal of Physics D: Applied Physics*, vol. 19, no. 12, pp. 2281-2292, 1986.
- [24] "MetalJet X-Ray Source Technology", Excillum: Redefining the X-ray tube. [Online]. Available: <https://www.excillum.com/technology/>. [Accessed: 02-Sep.-2019].
- [25] R. Alvarez and A. Macovski, "Energy-selective reconstructions in X-ray computerised tomography", *Physics in Medicine and Biology*, vol. 21, no. 5, pp. 733-744.
- [26] A. Primak, J. Giraldo, C. Eusemann, B. Schmidt, B. Kantor, J. Fletcher and C. McCollough, "Dual-Source Dual-Energy CT With Additional Tin Filtration: Dose and Image Quality Evaluation in Phantoms and In Vivo", *American Journal of Roentgenology*, vol. 195, no. 5, pp. 1164-1174, 2010.
- [27] T. Johnson, "Dual-Energy CT: General Principles", *American Journal of Roentgenology*, vol. 199, no. 5, pp. S3-S8, 2012.

- [28] M. Patino, A. Prochowski, M. Agrawal, F. Simeone, R. Gupta, P. Hahn and D. Sahani, "Material Separation Using Dual-Energy CT: Current and Emerging Applications", *RadioGraphics*, vol. 36, no. 4, pp. 1087-1105, 2016.
- [29] E. Fredenberg, "Spectral and dual-energy X-ray imaging for medical applications", *Nuclear Instruments and Methods in Physics Research Section A: Accelerators, Spectrometers, Detectors and Associated Equipment*, vol. 878, pp. 74-87, 2018.
- [30] E. Roessl and R. Proksa, "K-edge imaging in x-ray computed tomography using multi-bin photon counting detectors", *Physics in Medicine and Biology*, vol. 52, no. 15, pp. 4679-4696, 2007.
- [31] C. McCollough, S. Leng, L. Yu and J. Fletcher, "Dual- and Multi-Energy CT: Principles, Technical Approaches, and Clinical Applications", *Radiology*, vol. 276, no. 3, pp. 637-653, 2015.
- [32] Y. Xu, B. Yan, J. Zhang, J. Chen, L. Zeng and L. Wang, "Image Decomposition Algorithm for Dual-Energy Computed Tomography via Fully Convolutional Network", *Computational and Mathematical Methods in Medicine*, vol. 2018, pp. 1-9, 2018.
- [33] N. Takahashi, R. Hartman, T. Vrtiska, A. Kawashima, A. Primak, O. Dzyubak, J. Mandrekar, J. Fletcher and C. McCollough, "Dual-Energy CT Iodine-Subtraction Virtual Unenhanced Technique to Detect Urinary Stones in an Iodine-Filled Collecting System: A Phantom Study", *American Journal of Roentgenology*, vol. 190, no. 5, pp. 1169-1173, 2008.
- [34] R. Forghani, B. De Man and R. Gupta, "Dual-Energy Computed Tomography", *Neuroimaging Clinics of North America*, vol. 27, no. 3, pp. 371-384, 2017.
- [35] W. Zhao, D. Vernekohl, F. Han, B. Han, H. Peng, Y. Yang, L. Xing and J. Min, "A unified material decomposition framework for quantitative dual- and triple-energy CT imaging", *Medical Physics*, vol. 45, no. 7, pp. 2964-2977, 2018.
- [36] T. Zhao, L. Li and Z. Chen, "K-edge eliminated material decomposition method for dual-energy X-ray CT", *Applied Radiation and Isotopes*, vol. 127, pp. 231-236, 2017.
- [37] K. Taguchi, "Energy-sensitive photon counting detector-based X-ray computed tomography", *Radiological Physics and Technology*, vol. 10, no. 1, pp. 8-22, 2017.
- [38] A. Wang, E. Samei, J. Hsieh and N. Pelc, "Optimal energy thresholds and weights for separating materials using photon counting x-ray detectors with energy discriminating capabilities", pp. 725821-.
- [39] A. Wang and N. Pelc, "Sufficient Statistics as a Generalization of Binning in Spectral X-ray Imaging", *IEEE Transactions on Medical Imaging*, vol. 30, no. 1, pp. 84-93, 2011.
- [40] X. Wang, D. Meier, S. Mikkelsen, G. Maehlum, D. Wagenaar, B. Tsui, B. Patt and E. Frey, "MicroCT with energy-resolved photon-counting detectors", *Physics in Medicine and Biology*, vol. 56, no. 9, pp. 2791-2816, 2011.
- [41] J. Schlomka, E. Roessl, R. Dorscheid, S. Dill, G. Martens, T. Istel, C. Bäumer, C. Herrmann, R. Steadman, G. Zeitler, A. Livne and R. Proksa, "Experimental feasibility of multi-energy

- photon-counting K-edge imaging in pre-clinical computed tomography", *Physics in Medicine and Biology*, vol. 53, no. 15, pp. 4031-4047, 2008.
- [42] M. Walsh, A. Opie, J. Ronaldson, R. Doesburg, S. Nik, J. Mohr, R. Ballabriga, A. Butler and P. Butler, "First CT using Medipix3 and the MARS-CT-3 spectral scanner", *Journal of Instrumentation*, vol. 6, no. 01, p. C01095, 2011.
- [43] E. Baumgaertner, "3-D Color X-Rays Could Help Spot Deadly Disease Without Surgery", in *The New York Times*. [Online]. Available: <https://www.nytimes.com/2018/07/17/health/3d-color-xrays-cern.html>. [Accessed: 2019-09-08].
- [44] P. Delpierre, F. Debarbieux, S. Basolo, J. Berar, A. Bonissent, N. Boudet, P. Breugnon, B. Caillot, F. Cassol Brunner, B. Chantepie, J. Clemens, B. Dinkespiler, R. Khouri, I. Koudobine, V. Mararazzo, C. Meessen, M. Menouni, C. Morel, C. Mouget, P. Pangaud, F. Peyrin, G. Rougon, D. Sappey-Marinier, S. Valton and E. Vigeolas, "PIXSCAN: Pixel detector CT-scanner for small animal imaging", *Nuclear Instruments and Methods in Physics Research Section A: Accelerators, Spectrometers, Detectors and Associated Equipment*, vol. 571, no. 1-2, pp. 425-428, 2007.
- [45] S. M. Yun, E. Samei, J. Hsieh, C. H. Lim, T. W. Kim, and H. K. Kim, "Pixel-structured scintillators for digital x-ray imaging: The International Society for Optical Engineering 7258", in *Proceedings of SPIE*, p. 72583N, 2009.
- [46] M. Funaki, Y. Ando, R. Jinnai, A. Tachibana, and R. Ohno, "Development of CdTe detectors in Acrorad", *Acrorad Co., Ltd*, 2007.
- [47] "XiRay: NEW X-Ray cameras with 11 Mpix and 16 Mpix", XIMEA. [Online]. Available: <https://www.ximea.com/en/products-news/new-xray-camera-xiray11>. [Accessed: 03-Sep.-2019].
- [48] "Medical Flat Panel Imaging Detectors", *Varex Imaging*. [Online]. Available: <https://www.vareximaging.com/products/medical/medical-flat-panel-detectors>. [Accessed: 05-Sep.-2019].
- [49] C. Zhang, P. Lechner, G. Lutz, J. Treis, S. Wölfel, L. Strüder and S. Nan Zhang, "Development of X-type DEPFET Macropixel detectors", *Nuclear Instruments and Methods in Physics Research Section A: Accelerators, Spectrometers, Detectors and Associated Equipment*, vol. 588, no. 03, pp. 389-396, 2008.
- [50] M. Platkevic, "Signal Processing and data Read-out from Position Sensitive Pixel Detectors", Ph.D. Thesis, Czech Technical University in Prague, 2014.
- [51] C. Chantler, K. Olsen, R. Dragoset, J. Chang, A. Kishore, S. Kotochigova and D. Zucker, "X-Ray Form Factor, Attenuation, and Scattering Tables", *National Institute for Standards and Technology*. Gaithersburg.
- [52] M. Bisogni, M. Campbell, M. Conti, P. Delogu, M. Fantacci, E. Heijne, P. Maestro, G. Magistrati, V. Marzulli, G. Meddeler, B. Mikulec, E. Pernigotti, V. Rosso, C. Schwarz, W. Snoeys, S. Stumbo, J. Watt, O. Siegmund and M. Gummin, "Performance of a 4096-pixel photon counting chip", *Proc. SPIE*, vol. 3445, pp. 298-304, 1998.

- [53] X. Llopart, M. Campbell, R. Dinapoli, D. San Segundo and E. Pernigotti, "Medipix2: A 64-k pixel readout chip with 55- μm square elements working in single photon counting mode", *IEEE Transactions on Nuclear Science*, vol. 49, no. 5, pp. 2279-2283, 2002.
- [54] X. Llopart, R. Ballabriga, M. Campbell, L. Tlustos and W. Wong, "Timepix, a 65k programmable pixel readout chip for arrival time, energy and/or photon counting measurements", *Nuclear Instruments and Methods in Physics Research Section A: Accelerators, Spectrometers, Detectors and Associated Equipment*, vol. 581, no. 1-2, pp. 485-494, 2007.
- [55] E. Gimenez, R. Ballabriga, M. Campbell, I. Horswell, X. Llopart, J. Marchal, K. Sawhney, N. Tartoni and D. Turecek, "Study of charge-sharing in MEDIPIX3 using a micro-focused synchrotron beam", *Journal of Instrumentation*, vol. 6, no. 1, p. C01031, 2011.
- [56] B. Bergmann, M. Pichotka, S. Pospisil, J. Vycpalek, P. Burian, P. Broulim and J. Jakubek, "3D track reconstruction capability of a silicon hybrid active pixel detector", *The European Physical Journal C*, vol. 77, no. 6, 2017.
- [57] M. Zuber, T. Koenig, E. Hamann, A. Cecilia, M. Fiederle and T. Baumbach, "Characterization of a 2x3 Timepix assembly with a 500 μm thick silicon sensor", *Journal of Instrumentation*, vol. 9, no. 05, p. C05037, 2014.
- [58] D. Pennicard, S. Lange, S. Smoljanin, J. Becker, H. Hirsemann, M. Epple and H. Graafsma, "Development of LAMBDA: Large Area Medipix-Based Detector Array", *Journal of Instrumentation*, vol. 6, no. 11, p. C11009, 2011.
- [59] Z. Vykydal, J. Visschers, D. Tezcan, K. De Munck, T. Borgers, W. Ruythooren and P. De Moor, "The RELAXd project: Development of four-side tilable photon-counting imagers", *Nuclear Instruments and Methods in Physics Research Section A: Accelerators, Spectrometers, Detectors and Associated Equipment*, vol. 591, no. 1, pp. 241-244, 2008.
- [60] A. Canas, M. Chmeissani, R. Coll, D. Glass, M. Kolstein, R. Martinez, C. Puigdengoles, C. Sanchez and A. Sancho, "Large area detector with the Medipix2 chip", *2011 IEEE Nuclear Science Symposium Conference Record*, pp. 4501-4505, 2011.
- [61] J. Dudak, "Applications of hybrid pixel detectors for high resolution table-top X-ray imaging", in *Semiconductor Radiation Detectors: Technology and Applications*, 1 ed., Boca Raton: CRC Press, 2017, pp. 183-208.
- [62] J. Jakubek, M. Jakubek, M. Platkevic, P. Soukup, D. Turecek, V. Sykora and D. Vavrik, "Large area pixel detector WIDEPIX with full area sensitivity composed of 100 Timepix assemblies with edgeless sensors", *Journal of Instrumentation*, vol. 9, no. 04, p. C04018, 2014.
- [63] B. Henrich, A. Bergamaschi, C. Broennimann, R. Dinapoli, E. Eikenberry, I. Johnson, M. Kobas, P. Kraft, A. Mozzanica and B. Schmitt, "PILATUS: A single photon counting pixel detector for X-ray applications", *Nuclear Instruments and Methods in Physics Research Section A: Accelerators, Spectrometers, Detectors and Associated Equipment*, vol. 607, no. 1, pp. 247-249, 2009.
- [64] I. Johnson, A. Bergamaschi, H. Billich, S. Cartier, R. Dinapoli, D. Greiffenberg, M. Guizar-

- Sicairos, B. Henrich, J. Jungmann, D. Mezza, A. Mozzanica, B. Schmitt, X. Shi and G. Tinti, "Eiger: a single-photon counting x-ray detector", *Journal of Instrumentation*, vol. 9, no. 05, pp. C05032-C05032, 2014.
- [65] P. Delogu, P. Oliva, R. Bellazzini, A. Brez, P. de Ruvo, M. Minuti, M. Pinchera, G. Spandre and A. Vincenzi, "Characterization of Pixirad-1 photon counting detector for X-ray imaging", *Journal of Instrumentation*, vol. 11, no. 01, p. P01015, 2016.
- [66] R. Bellazzini, A. Brez, G. Spandre, M. Minuti, M. Pinchera, P. Delogu, P. de Ruvo and A. Vincenzi, "PIXIE III: a very large area photon-counting CMOS pixel ASIC for sharp X-ray spectral imaging", *Journal of Instrumentation*, vol. 10, no. 01, p. C01032, 2015.
- [67] S. Basolo, J. Berar, N. Boudet, P. Breugnon, B. Caillot, J. Clemens, P. Delpierre, B. Dinkespiller, I. Koudobine, C. Meessen, M. Menouni, C. Mouget, P. Pangaud, R. Potheau and E. Vigeolas, "XPAD: pixel detector for material sciences", *IEEE Transactions on Nuclear Science*, vol. 52, no. 5, pp. 1994-1998, 2005.
- [68] P. Delpierre, S. Basolo, J. Berar, M. Bordesoule, N. Boudet, P. Breugnon, B. Caillot, B. Chantepie, J. Clemens, B. Dinkespiller, S. Hustache-Ottini, C. Meessen, M. Menouni, C. Morel, C. Mouget, P. Pangaud, R. Potheau and E. Vigeolas, "XPAD: A photons counting pixel detector for material sciences and small-animal imaging", *Nuclear Instruments and Methods in Physics Research Section A: Accelerators, Spectrometers, Detectors and Associated Equipment*, vol. 572, no. 1, pp. 250-253, 2007.
- [69] J. Berar, N. Boudet, P. Breugnon, B. Caillot, B. Chantepie, J. Clemens, P. Delpierre, B. Dinkespiller, S. Godiot, C. Meessen, M. Menouni, C. Morel, P. Pangaud, E. Vigeolas, S. Hustache and K. Medjoubi, "XPAD3 hybrid pixel detector applications", *Nuclear Instruments and Methods in Physics Research Section A: Accelerators, Spectrometers, Detectors and Associated Equipment*, vol. 607, no. 1, pp. 233-235, 2009.
- [70] A. Koziol, M. Bordessoule, A. Ciavardini, A. Dawiec, P. Da Silva, K. Desjardins, P. Grybos, B. Kanoute, C. Laulhe, P. Maj, C. Meneglier, P. Mercere, F. Orsini and R. Szczygiel, "Evaluation of the UFXC32k photon-counting detector for pump–probe experiments using synchrotron radiation", *Journal of Synchrotron Radiation*, vol. 25, no. 2, pp. 413-418, 2018.
- [71] K. Kasinski, P. Grybos, P. Kmon, P. Maj, R. Szczygiel and K. Zoschke, "Development of a 4-side Buttable X-ray Detection Module with Low Dead Area Using the UFXC32k Chips with TSVs", *IEEE Transactions on Nuclear Science*, pp. 1-1.
- [72] M. Zoladz, P. Maj, R. Szczygiel, P. Kaczmarczyk and P. Grybos, "UFXC32k based camera module with a custom soft processor and USB 3.0 for large area detectors", *Journal of Instrumentation*, vol. 13, no. 01, pp. P01017-P01017, 2018.
- [73] N. Ford, M. Thornton and D. Holdsworth, "Fundamental image quality limits for microcomputed tomography in small animals", *Medical Physics*, vol. 30, no. 11, pp. 2869-2877, 2003.
- [74] M. Bouxsein, S. Boyd, B. Christiansen, R. Guldberg, K. Jepsen and R. Müller, "Guidelines for assessment of bone microstructure in rodents using micro-computed tomography", *Journal of*

- Bone and Mineral Research*, vol. 25, no. 7, pp. 1468-1486, 2010.
- [75] J. Hsu, Y. Chen, J. Ho, H. Huang, S. Wang, F. Cheng, J. Wu, M. Tsai and L. Malaval, "A Comparison of Micro-CT and Dental CT in Assessing Cortical Bone Morphology and Trabecular Bone Microarchitecture", *PLoS ONE*, vol. 9, no. 9, 2014.
- [76] R. Li, D. Stewart, H. von Schroeder, E. Mackinnon and E. Schemitsch, "Effect of cell-based VEGF gene therapy on healing of a segmental bone defect", *Journal of Orthopaedic Research*, vol. 27, no. 1, pp. 8-14, 2009.
- [77] N. Sagar, A. Pandey, D. Gurbani, K. Khan, D. Singh, B. Chaudhari, V. Soni, N. Chattopadhyay, A. Dhawan, J. Bellare and R. Roeder, "In-Vivo Efficacy of Compliant 3D Nano-Composite in Critical-Size Bone Defect Repair: a Six Month Preclinical Study in Rabbit", *PLoS ONE*, vol. 8, no. 10, 2013.
- [78] D. McErlain, C. Appleton, R. Litchfield, V. Pitelka, J. Henry, S. Bernier, F. Beier and D. Holdsworth, "Study of subchondral bone adaptations in a rodent surgical model of OA using in vivo micro-computed tomography", *Osteoarthritis and Cartilage*, vol. 16, no. 4, pp. 458-469, 2008.
- [79] A. Dumas, M. Brigitte, M. Moreau, F. Chrétien, M. Baslé and D. Chappard, "Bone mass and microarchitecture of irradiated and bone marrow-transplanted mice: influences of the donor strain", *Osteoporosis International*, vol. 20, no. 3, pp. 435-443, 2009.
- [80] E. Namati, D. Chon, J. Thiesse, E. Hoffman, J. Ryk, A. Ross and G. McLennan, "In vivo micro-CT lung imaging via a computer-controlled intermittent iso-pressure breath hold (IIBH) technique", *Physics in Medicine and Biology*, vol. 51, no. 23, pp. 6061-6075, 2006.
- [81] C. Badea, L. Hedlund and G. Johnson, "Micro-CT with respiratory and cardiac gating", *Medical Physics*, vol. 31, no. 12, pp. 3324-3329, 2004.
- [82] N. Ford, A. Wheatley, D. Holdsworth and M. Drangova, "Optimization of a retrospective technique for respiratory-gated high speed micro-CT of free-breathing rodents", *Physics in Medicine and Biology*, vol. 52, no. 19, pp. 5749-5769, 2007.
- [83] A. Sheikh, K. van der Bogt, T. Doyle, M. Sheikh, K. Ransohoff, Z. Ali, O. Palmer, R. Robbins, M. Fischbein and J. Wu, "Micro-CT for Characterization of Murine CV Disease Models", *JACC: Cardiovascular Imaging*, vol. 3, no. 7, pp. 783-785, 2010.
- [84] K. Ghaghada, C. Badea, L. Karumbaiah, N. Fettig, R. Bellamkonda, G. Johnson and A. Annapragada, "Evaluation of Tumor Microenvironment in an Animal Model using a Nanoparticle Contrast Agent in Computed Tomography Imaging", *Academic Radiology*, vol. 18, no. 1, pp. 20-30, 2011.
- [85] B. Vandeghinste, B. Trachet, M. Renard, C. Casteleyn, S. Staelens, B. Loeys, P. Segers and S. Vandenberghe, "Replacing Vascular Corrosion Casting by In Vivo Micro-CT Imaging for Building 3D Cardiovascular Models in Mice", *Molecular Imaging and Biology*, vol. 13, no. 1, pp. 78-86, 2011.
- [86] "NanoTube has uncompromising Nano Performance", *Excillum: Redefining the X-ray tube*.

- [Online]. Available: <https://www.excillum.com/products/nanotube-n1-60-kv/>. [Accessed: 30-Aug.-2019].
- [87] B. Metscher, "MicroCT for developmental biology: A versatile tool for high-contrast 3D imaging at histological resolutions", *Developmental Dynamics*, vol. 238, no. 3, pp. 632-640, 2009.
- [88] V. Cnudde, B. Masschaele, H. De Cock, K. Olstad, L. Vlamincx, J. Vlassenbroeck, M. Dierick, Y. Witte, L. Van Hoorebeke and P. Jacobs, "Virtual histology by means of high-resolution X-ray CT", *Journal of Microscopy*, vol. 232, no. 3, pp. 476-485, 2008.
- [89] J. Johnson, M. Hansen, I. Wu, L. Healy, C. Johnson, G. Jones, M. Capecchi and C. Keller, "Virtual Histology of Transgenic Mouse Embryos for High-Throughput Phenotyping", *PLoS Genetics*, vol. 2, no. 4, pp. 06-PLGE-RA-0014R1, 2006.
- [90] H. Martinez, S. Prajapati, C. Estrada, F. Jimenez, M. Quinones, I. Wu, A. Bahadur, A. Sanderson, C. Johnson, M. Shim, C. Keller and S. Ahuja, "Microscopic Computed Tomography-Based Virtual Histology for Visualization and Morphometry of Atherosclerosis in Diabetic Apolipoprotein E Mutant Mice", *Circulation*, vol. 120, no. 9, pp. 821-822, 2009.
- [91] S. Prajapati, A. Kilcoyne, A. Samano, D. Green, S. McCarthy, B. Blackman, M. Brady, L. Zarzabal, A. Tatiparthi, T. Sledz, T. Duong, S. Ohshima-Hosoyama, F. Giles, J. Michalek, B. Rubin and C. Keller, "MicroCT-Based Virtual Histology Evaluation of Preclinical Medulloblastoma", *Molecular Imaging and Biology*, vol. 13, no. 3, pp. 493-499, 2011.
- [92] J. Silva, I. Zanette, P. Noël, M. Cardoso, M. Kimm and F. Pfeiffer, "Three-dimensional non-destructive soft-tissue visualization with X-ray staining micro-tomography", *Scientific Reports*, vol. 5, no. 1, 2015.
- [93] T. Zikmund, M. Novotná, M. Kavková, M. Tesařová, M. Kaucká, B. Szarowská, I. Adameyko, E. Hrubá, M. Buchtová, E. Dražanová, Z. Starčuk and J. Kaiser, "High-contrast differentiation resolution 3D imaging of rodent brain by X-ray computed microtomography", *Journal of Instrumentation*, vol. 13, no. 02, pp. C02039-C02039, 2018.
- [94] J. Albers, M. Markus, F. Alves and C. Dullin, "X-ray based virtual histology allows guided sectioning of heavy ion stained murine lungs for histological analysis", *Scientific Reports*, vol. 8, no. 1, 2018.
- [95] N. Jeffery, R. Stephenson, J. Gallagher, J. Jarvis and P. Cox, "Micro-computed tomography with iodine staining resolves the arrangement of muscle fibres", *Journal of Biomechanics*, vol. 44, no. 1, pp. 189-192, 2011.
- [96] A. de Crespigny, H. Bou-Reslan, M. Nishimura, H. Phillips, R. Carano and H. D'Arceuil, "3D micro-CT imaging of the postmortem brain", *Journal of Neuroscience Methods*, vol. 171, no. 2, pp. 207-213, 2008.
- [97] O. Aslanidi, T. Nikolaidou, Jichao Zhao, B. Smail, S. Gilbert, A. Holden, T. Lowe, P. Withers, R. Stephenson, J. Jarvis, J. Hancox, M. Boyett and Henggui Zhang, "Application of Micro-Computed Tomography With Iodine Staining to Cardiac Imaging, Segmentation, and Computational Model Development", *IEEE Transactions on Medical Imaging*, vol. 32, no. 1,

- pp. 8-17, 2013.
- [98] C. Hsu, L. Wong, T. Rasmussen, S. Kalaga, M. McElwee, L. Keith, R. Bohat, J. Seavitt, A. Beaudet and M. Dickinson, "Three-dimensional microCT imaging of mouse development from early post-implantation to early postnatal stages", *Developmental Biology*, vol. 419, no. 2, pp. 229-236, 2016.
- [99] B. Nieman, M. Wong and R. Henkelman, "Genes into geometry: imaging for mouse development in 3D", *Current Opinion in Genetics & Development*, vol. 21, no. 5, pp. 638-646, 2011.
- [100] P. Granton, S. Pollmann, N. Ford, M. Drangova and D. Holdsworth, "Implementation of dual- and triple-energy cone-beam micro-CT for postreconstruction material decomposition", *Medical Physics*, vol. 35, no. 11, pp. 5030-5042, 2008.
- [101] C. Badea, X. Guo, D. Clark, S. Johnston and C. Marshall, "Dual-energy micro-CT of the rodent lung", *American Journal of Physiology-Lung Cellular and Molecular Physiology*, vol. 302, no. 10, pp. 1088-1097, 2012.
- [102] R. Molthen, J. Weaver, C. Badea, N. Befera, D. Clark, Y. Qi and G. Johnson, "Dual-energy micro-CT imaging of pulmonary airway obstruction: correlation with micro-SPECT", *Proc. of SPIE*, vol. 9038, pp. 90380U, 2014.
- [103] J. Ashton, D. Clark, E. Moding, K. Ghaghada, D. Kirsch, J. West, C. Badea and T. Kalin, "Dual-Energy Micro-CT Functional Imaging of Primary Lung Cancer in Mice Using Gold and Iodine Nanoparticle Contrast Agents: A Validation Study", *PLoS ONE*, vol. 9, no. 2, 2014.
- [104] C. Badea, K. Athreya, G. Espinosa, D. Clark, A. Ghafoori, Y. Li, D. Kirsch, G. Johnson, A. Annapragada, K. Ghaghada and J. Gelovani, "Computed Tomography Imaging of Primary Lung Cancer in Mice Using a Liposomal-Iodinated Contrast Agent", *PLoS ONE*, vol. 7, no. 4, 2012.
- [105] E. Moding, D. Clark, Y. Qi, Y. Li, Y. Ma, K. Ghaghada, G. Johnson, D. Kirsch and C. Badea, "Dual-Energy Micro-Computed Tomography Imaging of Radiation-Induced Vascular Changes in Primary Mouse Sarcomas", *International Journal of Radiation Oncology*Biophysics*Physics*, vol. 85, no. 5, pp. 1353-1359, 2013.
- [106] R. Bhavane, C. Badea, K. Ghaghada, D. Clark, D. Vela, A. Moturu, A. Annapragada, G. Johnson, J. Willerson and A. Annapragada, "Dual-Energy Computed Tomography Imaging of Atherosclerotic Plaques in a Mouse Model Using a Liposomal-Iodine Nanoparticle Contrast Agent", *Circulation: Cardiovascular Imaging*, vol. 6, no. 2, pp. 285-294, 2013.
- [107] S. Handschuh, C. Beisser, B. Ruthensteiner and B. Metscher, "Microscopic dual-energy CT (microDECT): a flexible tool for multichannel ex vivo 3D imaging of biological specimens", *Journal of Microscopy*, vol. 267, no. 1, pp. 3-26, 2017.
- [108] M. Moghiseh, R. Aamir, R. Panta, N. de Ruyter, A. Chernoglazov, J. Healy, A. Butler and N. Anderson, "Discrimination of Multiple High-Z Materials by Multi- Energy Spectral CT– A Phantom Study", *JSM Biomedical Imaging Data papers*, vol. 3, no. 1, p. 1007, 2016.

- [109] A. Raja, M. Moghiseh, C. Bateman, N. de Ruiter, B. Schon, N. Schleich, T. Woodfield, A. Butler and N. Anderson, "Measuring Identification and Quantification Errors in Spectral CT Material Decomposition", *Applied Sciences*, vol. 8, no. 3, 2018.
- [110] R. Panta, S. Bell, J. Healy, R. Aamir, C. Bateman, M. Moghiseh, A. Butler and N. Anderson, "Element-specific spectral imaging of multiple contrast agents: a phantom study", *Journal of Instrumentation*, vol. 13, no. 02, pp. T02001-T02001, 2018.
- [111] "Measuring Multiple Contrast Agents Simultaneously", *MARS Bioimaging*. [Online]. Available: https://www.marsbioimaging.com/mars/apps/#_ContrastAgents. [Accessed: 03-Sep.-2019].
- [112] D. Turecek, T. Holy, J. Jakubek, S. Pospisil and Z. Vykydal, "Pixelman: a multi-platform data acquisition and processing software package for Medipix2, Timepix and Medipix3 detectors", *Journal of Instrumentation*, vol. 6, no. 01, pp. C01046-C01046, 2011.
- [113] L. Tlustos, "Performance and limitations of high granularity single photon processing X-ray imaging detectors", Ph.D. thesis, Wien, 2005.
- [114] J. Jakubek, "Semiconductor Pixel detectors and their applications in life sciences", *Journal of Instrumentation*, vol. 4, no. 03, p. P03013, 2009.
- [115] J. Jakubek, J. Dammer, T. Holy, M. Jakubek, S. Pospisil, V. Tichy, J. Uher and D. Vavrik, "Spectrometric properties of TimePix pixel detector for X-ray color and phase sensitive radiography", in *2007 IEEE Nuclear Science Symposium Conference Record*, 2007, pp. 2323-2326.
- [116] A. Thompson and D. Vaughan, "X-ray Data Booklet", *Lawrence Berkeley National Laboratory: Center for X-ray Optics and Advanced Light Source*. [Online]. Available: <http://xdb.lbl.gov/>. [Accessed: 04-Sep.-2019].
- [117] J. A. Seibert, J. T. Dobbins III, J. M. Boone, J. M. Boone, and K. K. Lindfors, "Flat-field correction technique for digital detectors", in *Proceedings of SPIE, Medical Imaging 1998: Physics of Medical Imaging; Volume 3336*, p. 348, 1998.
- [118] J. Jakubek, "Data processing and image reconstruction methods for pixel detectors", *Nuclear Instruments and Methods in Physics Research Section A: Accelerators, Spectrometers, Detectors and Associated Equipment*, vol. 576, no. 1, pp. 223-234, 2007.
- [119] D. Vavrik and J. Jakubek, "Radiogram enhancement and linearization using the beam hardening correction method", *Nuclear Instruments and Methods in Physics Research Section A: Accelerators, Spectrometers, Detectors and Associated Equipment*, vol. 607, no. 1, pp. 212-214, 2009.
- [120] J. Zemlicka, J. Dudak, J. Karch and F. Krejci, "Geometric correction methods for Timepix based large area detectors", *Journal of Instrumentation*, vol. 12, no. 01, pp. C01021-C01021, 2017.
- [121] X. Wu, J. Kalliopuska, M. Jakubek, J. Jakubek, A. Gädda and S. Eränen, "Study of edgeless radiation detector with 3D spatial mapping technique", *Journal of Instrumentation*, vol. 9, no. 04, pp. C04004-C04004, 2014.

- [122] J. Dudak, J. Zemlicka, F. Krejci, S. Polansky, J. Jakubek, J. Mrzilkova, M. Patzelt and J. Trnka, "X-ray micro-CT scanner for small animal imaging based on Timepix detector technology", *Nuclear Instruments and Methods in Physics Research Section A: Accelerators, Spectrometers, Detectors and Associated Equipment*, vol. 773, no. -, pp. 81-86, 2015.
- [123] "3D X-ray Microscopy: Non-destructive 3D imaging based on Micro Computed Tomography", *Bruker*. [Online]. Available: <https://www.bruker.com/products/microtomography.html>. [Accessed: 05-Sep.-2019].
- [124] J. Tous, J. Blazek, J. Zemlicka and J. Jakubek, "Evaluation of a YAG: Ce scintillation crystal based CCD X-ray imaging detector with the Medipix2 detector", *Journal of Instrumentation*, vol. 6, no. 11, pp. C11011-C11011, 2011.
- [125] F. Krejci, J. Jakubek, M. Kroupa, J. Dammer and D. Vavrik, "Enhancement of spatial resolution of roentgenographic methods using deconvolution", in *2008 IEEE Nuclear Science Symposium Conference Record*, 2008, pp. 4124-4129.
- [126] C. Mitja, J. Escofet, A. Tacho, and R. Revuelta, "Slanted Edge MTF", *ImageJ: Image Processing and Analysis in Java*. [Online]. Available: <https://imagej.nih.gov/ij/plugins/se-mtf/index.html>. [Accessed: 05-Sep.-2019].
- [127] J. Dudak, J. Zemlicka, J. Karch, Z. Hermanova, J. Kvacek and F. Krejci, "Microtomography with photon counting detectors: improving the quality of tomographic reconstruction by voxel-space oversampling", *Journal of Instrumentation*, vol. 12, no. 01, p. C01060, 2017.
- [128] J. Dudak, J. Zemlicka, J. Karch, M. Patzelt, J. Mrzilkova, P. Zach, Z. Hermanova, J. Kvacek and F. Krejci, "High-contrast X-ray micro-radiography and micro-CT of ex-vivo soft tissue murine organs utilizing ethanol fixation and large area photon-counting detector", *Scientific Reports*, vol. 6, no. -, p. 30385, 2016.
- [129] "Micro-CT-Bar-Pattern", *QRM: Quality Assurance in Radiology and Medicine*. [Online]. Available: http://www.qrm.de/content/products/microct/microct_barpattern.htm. [Accessed: 05-Sep.-2019].
- [130] R. Zainon, A. Butler, N. Cook, J. Butzer, N. Schleich, N. Ruiter, L. Tlustos, M. Clark, R. Heinz and P. Butler, "Construction and Operation of the MARS - CT Scanner", *Internetworking Indonesia Journal*, vol. 2, no. 1, pp. 3 - 10, 2010.
- [131] F. Noo, R. Clackdoyle, C. Mennessier, T. White and T. Roney, "Analytic method based on identification of ellipse parameters for scanner calibration in cone-beam tomography", *Physics in Medicine and Biology*, vol. 45, no. 11, pp. 3489-3508, 2000.
- [132] . Zhanli Hu. Jianbao Gui. Jing Zou. Junyan Rong. Qiyang Zhang. Hairong Zheng and . Dan Xia, "Geometric Calibration of a Micro-CT System and Performance for Insect Imaging", *IEEE Transactions on Information Technology in Biomedicine*, vol. 15, no. 4, pp. 655-660, 2011.
- [133] H. Yang, K. Kang and Y. Xing, "Geometry calibration method for a cone-beam CT system", *Medical Physics*, vol. 44, no. 5, pp. 1692-1706, 2017.
- [134] T. G. Flohr, J. Y. Lo, T. Gilat Schmidt, M. W. Jacobson, M. Ketcha, A. Uneri, J. Goerres, T. De

- Silva, S. Reungamornrat, S. Vogt, G. Kleinszig, and J. H. Siewerdsen, "Geometric calibration using line fiducials for cone-beam CT with general, non-circular source-detector trajectories", in *Proceedings of SPIE: The International Society for Optical Engineering*, p. 101320I, 2017.
- [135] F. Zhang, J. Du, H. Jiang, L. Li, M. Guan and B. Yan, "Iterative geometric calibration in circular cone-beam computed tomography", *Optik*, vol. 125, no. 11, pp. 2509-2514, 2014.
- [136] F. Vogeler, W. Verheecke, A. Voet, J. Kruth and W. Dewulf, "Positional Stability of 2D X-ray Images for Computed Tomography", in *International Symposium on Digital Radiology and Computed Tomography*, 2011.
- [137] N. Flay, W. Sun, S. Brown, R. Leach and T. Blumensath, "Investigation of the Focal Spot Drift in Industrial Cone-beam X-ray Computed Tomography", *Digital Industrial Radiology and Computed Tomography*, 2015.
- [138] W. Sun, S. Brown, N. Flay, M. McCarthy and J. McBride, "A reference sample for investigating the stability of the imaging system of x-ray computed tomography", *Measurement Science and Technology*, vol. 27, no. 8, pp. 085004-, 2016.
- [139] N. Uhlman, M. Salomon, S. Burtzloff, F. Porsch, W. Johansson, F. Nachtrab and R. Hanke, "Components and Methods for Highest Resolution Computed Tomography", *International Symposium on NDT in Aerospace*, 2008.
- [140] D. Vavřík, I. Jandejsek and M. Pichotka, "Correction of the X-ray tube spot movement as a tool for improvement of the micro-tomography quality", *Journal of Instrumentation*, vol. 11, no. 01, pp. C01029-C01029, 2016.
- [141] A. Sasov, S. Stock, X. Liu and P. Salmon, "Compensation of mechanical inaccuracies in micro-CT and nano-CT", *Proc. of SPIE*, vol. 7078, pp. 70781C-1, 2008.
- [142] J. Dudak, J. Karch, K. Holcova and J. Zemlicka, "X-ray imaging with sub-micron resolution using large-area photon counting detectors Timepix", *Journal of Instrumentation*, vol. 12, no. 12, pp. C12024-C12024, 2017.
- [143] J. Dudak, J. Zemlicka, F. Krejci, J. Karch, M. Patzelt, P. Zach, V. Sykora and J. Mrzilkova, "Evaluation of sample holders designed for long-lasting X-ray micro-tomographic scans of ex-vivo soft tissue samples", *Journal of Instrumentation*, vol. 11, no. 03, pp. C03005-C03005, 2016.
- [144] B. Münch, P. Trtik, F. Marone and M. Stampanoni, "Stripe and ring artifact removal with combined wavelet—Fourier filtering", *Optics Express*, vol. 17, no. 10, pp. 8567-, 2009.
- [145] E. Anas, S. Lee and M. Hasan, "Removal of ring artifacts in CT imaging through detection and correction of stripes in the sinogram", *Physics in Medicine and Biology*, vol. 55, no. 22, pp. 6911-6930, 2010.
- [146] S. Rashid, S. Lee and M. Hasan, "An improved method for the removal of ring artifacts in high resolution CT imaging", *EURASIP Journal on Advances in Signal Processing*, vol. 2012, no. 1, 2012.

- [147] E. Anas, S. Lee and M. Kamrul Hasan, "Classification of ring artifacts for their effective removal using type adaptive correction schemes", *Computers in Biology and Medicine*, vol. 41, no. 6, pp. 390-401, 2011.
- [148] "CT Imaging Phantoms PlastiCreatures", *Smart Scientific Solutions*. [Online]. Available: <http://www.smartscientificsolutions.com/products/>. [Accessed: 31-Aug.-2019].
- [149] G. Schulz, C. Waschkies, F. Pfeiffer, I. Zanette, T. Weitkamp, C. David and B. Müller, "Multimodal imaging of human cerebellum - merging X-ray phase microtomography, magnetic resonance microscopy and histology", *Scientific Reports*, vol. 2, no. 1, 2012.
- [150] F. Pfeiffer, T. Weitkamp, O. Bunk and C. David, "Phase retrieval and differential phase-contrast imaging with low-brilliance X-ray sources", *Nature Physics*, vol. 2, no. 4, pp. 258-261, 2006.
- [151] A. Momose, T. Takeda, Y. Itai and K. Hirano, "Phase-contrast X-ray computed tomography for observing biological soft tissues", *Nature Medicine*, vol. 2, no. 4, pp. 473-475, 1996.
- [152] T. Takeda, T. Kunii, R. Sirai, T. Ohizumi, H. Maruyama, K. Hyodo, A. Yoneyama and K. Ueda, "Ethanol fixed brain imaging by phase-contrast X-ray technique", *Journal of Physics: Conference Series*, vol. 425, no. 2, 2013.
- [153] E. Lein and e. al, "Genome-wide atlas of gene expression in the adult mouse brain", *Nature*, vol. 445, no. 7124, pp. 168-176, 2007.
- [154] A. Petiet, M. Kaufman, M. Goddeeris, J. Brandenburg, S. Elmore and G. Johnson, "High-resolution magnetic resonance histology of the embryonic and neonatal mouse: A 4D atlas and morphologic database", *Proceedings of the National Academy of Sciences*, vol. 105, no. 34, pp. 12331-12336, 2008.
- [155] J. Mrzílková, M. Patzelt, P. Gallina, Z. Wurst, M. Šeremeta, J. Dudák, F. Krejčí, J. Žemlička, V. Musil, J. Karch, J. Rosina and P. Zach, "Imaging of Mouse Brain Fixated in Ethanol in Micro-CT", *BioMed Research International*, vol. 2019, pp. 1-7, 2019.
- [156] R. Zhang, X. Chen and H. Wen, "Improved experimental model of hepatic cystic hydatid disease resembling natural infection route with stable growing dynamics and immune reaction", *World Journal of Gastroenterology*, vol. 23, no. 45, pp. 7989-7999, 2017.
- [157] P. Dubé, "Considerations for rodent irradiation", in *Taconics: Models For Life*. [Online], Available: <https://www.taconic.com/taconic-insights/oncology-immuno-oncology/rodent-irradiation-considerations.html>. [Accessed: 01-Sep.-2019].
- [158] D. Cavanaugh, E. Johnson, R. Price, J. Kurie, E. Travis and D. Cody, "In Vivo Respiratory-Gated Micro-CT Imaging in Small-Animal Oncology Models", *Molecular Imaging*, vol. 3, no. 1, 2004.
- [159] I. Willekens, N. Buls, T. Lahoutte, L. Baeyens, C. Vanhove, V. Caveliers, R. Deklerck, A. Bossuyt and J. de Mey, "Evaluation of the radiation dose in micro-CT with optimization of the scan protocol", *Contrast Media & Molecular Imaging*, vol. 5, no. 4, pp. 201-207, 2010.

- [160] N. Miyahara, T. Kokubo, Y. Hara, A. Yamada, T. Koike and Y. Arai, "Evaluation of X-ray doses and their corresponding biological effects on experimental animals in cone-beam micro-CT scans (R-mCT2)", *Radiological Physics and Technology*, vol. 9, no. 1, pp. 60-68, 2016.
- [161] J. Boone, O. Velazquez and S. Cherry, "Small-Animal X-ray Dose from Micro-CT", *Molecular Imaging*, vol. 3, no. 3, 2004.
- [162] D. Dickerscheid, J. Lavalaye, L. Romijn and J. Habraken, "Contrast-noise-ratio (CNR) analysis and optimisation of breast-specific gamma imaging (BSGI) acquisition protocols", *EJNMMI Research*, vol. 3, no. 1, 2013.
- [163] P. He, B. Wei, W. Cong and G. Wang, "Optimization of K-edge imaging with spectral CT", *Medical Physics*, vol. 39, no. 11, pp. 6572-6579, 2012.
- [164] P. He, B. Wei, P. Feng, M. Chen and D. Mi, "Material Discrimination Based on K-edge Characteristics", *Computational and Mathematical Methods in Medicine*, vol. 2013, pp. 1-6, 2013.
- [165] D. Vavrik, M. Holik, J. Jakubek, M. Jakubek, V. Kraus, F. Krejci, P. Soukup, D. Turecek, J. Vacik and J. Zemlicka, "Modular pixelated detector system with the spectroscopic capability and fast parallel read-out", *Journal of Instrumentation*, vol. 9, no. 06, pp. C06006-C06006, 2014.
- [166] T. Poikela, J. Plosila, T. Westerlund, M. Campbell, M. Gaspari, X. Llopart, V. Gromov, R. Kluit, M. Beuzekom, F. Zappone, V. Zivkovic, C. Brezina, K. Desch, Y. Fu and A. Kruth, "Timepix3: a 65K channel hybrid pixel readout chip with simultaneous ToA/ToT and sparse readout", *Journal of Instrumentation*, vol. 9, no. 05, pp. C05013-C05013, 2014.
- [167] D. Turecek, J. Jakubek and P. Soukup, "USB 3.0 readout and time-walk correction method for Timepix3 detector", *Journal of Instrumentation*, vol. 11, no. 12, pp. C12065-C12065, 2016.
- [168] Q. Bao and A. Chatziioannou, "Estimation of the minimum detectable activity of preclinical PET imaging systems with an analytical method", *Medical Physics*, vol. 37, no. 11, pp. 6070-6083, 2010.
- [169] M. Correia, V. Newcombe and G. Williams, "Contrast-to-noise ratios for indices of anisotropy obtained from diffusion MRI: A study with standard clinical b-values at 3T", *NeuroImage*, vol. 57, no. 3, pp. 1103-1115, 2011.
- [170] J. Dudak, J. Karch, J. Jakubek, M. Jakubek and J. Zemlicka, "Compact four-layer Timepix-based particle tracker WidePIX 3D: the first applications in X-ray CT imaging", *Journal of Instrumentation*, vol. 13, no. 12, pp. C12001-C12001, 2018.